Myosin cluster dynamics and their roles in epithelial wound ring constriction

Alka Bhat

UNIVERSITÉ DE STRASBOURG

ÉCOLE DOCTORALE DES SCIENCES DE LA VIE ET DE LA SANTE

UMR 7104 - Institut de Génétique et de Biologie Moléculaire et Cellulaire (IGBMC)

THÈSE présentée par:
Alka BHAT

Soutenue le**: 18 Septembre 2019**

Pour obtenir le grade de: **Docteur de l'université de Strasbourg**

Discipline/ Spécialité: **Physique Cellulaire**

Les dynamiques d'agrégats de myosine et leurs rôles dans les fermetures d'epithelia

THÈSE dirigée par :
Daniel RIVELINE Directeur de Recherche, Université de Strasbourg, France

RAPPORTEURS :
Benoit LADOUX Professeur, Université Paris Diderot
Franziska LAUTENSCHLÄGER Professeur, Leibniz-Institut für Neue Materialien, Saarbrücken, Allemagne

---

AUTRES MEMBRES DU JURY:

Pramod PULLARKAT Professeur, Raman Research Institute, Bangalore, India
Pascal DIDIER Professeur, Université de Strasbourg, France

UNIVERSITÉ DE STRASBOURG

ÉCOLE DOCTORALE DES SCIENCES DE LA VIE ET DE LA SANTE

UMR 7104 - Institut de Génétique et de Biologie Moléculaire et Cellulaire (IGBMC)

THESIS presented by:

Alka BHAT

Soutenue le**: 18 Septembre 2019**

Pour obtenir le grade de: **Docteur de l'université de Strasbourg**

Discipline/ Spécialité: **Cell Physics**

Myosin cluster dynamics and their roles in epithelial wound ring constriction

THÈSE dirigée par :
Daniel RIVELINE Directeur de Recherche, Université de Strasbourg, France

RAPPORTEURS :
Benoit LADOUX Professeur, Université Paris Diderot
Franziska LAUTENSCHLÄGER Professeur, Leibniz-Institut für Neue Materialien, Saarbrücken, Allemagne

---

AUTRES MEMBRES DU JURY :

Pramod PULLARKAT Professeur, Raman Research Institute, Bangalore, India
Pascal DIDIER Professeur, Université de Strasbourg, France

ACKNOWLEDGEMENTS

Firstly, I would like to thank my supervisor Daniel Riveline, for accepting me as a PhD student in his lab. I was trained as a biologist and had very little knowledge about the field of biophysics while joining this lab. I am very grateful for the opportunity, to discover this field and for his constant support and push, to step out of my comfort zone. It was a great learning experience, both in terms of scientific problem solving and learning new techniques. I learnt a lot from you and I'll always be grateful for these years, thanks a lot.

I would also like to thank my jury members, Benoit Ladoux and Franziska Lautenschläger for agreeing to review my thesis, Pascal Didier and Pramod Pullarkat for being a part of my jury panel.

I got introduced to this dynamic and fascinating part of a cell called 'cytoskeleton', during my master's course. I was grateful to land in the lab. of Pramod Pullarkat (RRI, Bangalore) where I was able to study and manipulate these protein complexes for the first time. Goes without saying, I cannot thank Pramod enough for being a stepping stone for where I am today and for all the much-needed support over the years. I will always be grateful for those formative years under your guidance which motivated me to take decision, to pursue this path.

I am very grateful to present and past lab members for all the support, constructive feedbacks and discussions over these years. Jordi Comelles and Raghavan Thiagarajan for being extremely approachable and patient teachers, your insights into the subject and zest to pass it on, helped me a lot during these years. Amélie Godeau, thanks for all the kindness and interesting discussions over the years, you will always be someone I look up to, in so many ways. David Rodriguez for all the artistic fun, and that enthusiastic smiling face checking up on your well-being time to time, thank you so much. Simon, for all the help regarding physics related concepts in addition to all scientific and non-scientific discussions over these years, I learnt a lot from you, thanks a lot. Michele, for your kindness in addition to all the early morning motivational talks, I am very grateful for your support. Linjie, for all the discussions and food that you brought me ;), It was a pleasure being around you. Tristan, it's such a pleasure knowing you, your knowledge about diverse subjects and the amazing way to impart that knowledge will always stay with me, thanks a lot for all the kindness and support. Pooja, for being that friendly face around and sharing and moments of sharing our day to day troubles, I am so grateful for you being around all these years. Emilie Le Maout, I cannot thank you enough for your kindness and support over these years, for dragging me out of the lab to take a breather and clear my mind, for all the discussions and making me feel at home, I am very grateful for all that and much more.

I would like to thank all the people from imaging facility (IGBMC) for their constant support over the years. My special gratitude for Marcel, Erwan and Elvire for their enthusiasm and help, regarding issues that I brought to them almost every week.

I am very grateful for an amazing bunch of friends I have back home, their support turned out very vital, during these years. Swati, Navneet and Manoraj, thanks to each of you for all the support, and fun times, for travelling each time from different parts of the country, to make sure I was ready for the challenges of the year ahead. Rohit and Yogesh, thanks a lot for all the words of wisdom, and being there as my support system. Megha, Minder and Shweata, I am grateful for all the kindness in addition to checking up on me time to time and motivating me whenever I was down. Kunalika, for being that 'someone' whom I could discuss my work with, and it an wasn't an alien discussion ;) I am very grateful for your support. Thanks to Sushil and Renu, for all the wisdom and discussions over these years. Thanks a lot to Susav, for being my confidant and having my back for all these years, of course in addition to your world famous momos ☺. A very big thanks to Amod, for all the never-ending discussions, motivation and positivity about what we do and what lies ahead. Your presence was crucial for my journey.

I was lucky enough to have some of my dear ones, approachable geographically ☺, in addition to being on the same boat. Shraddha for all the support wisdom and motivation about life, PhD and moving to an unknown place thousands of miles away from home. Your support was crucial over the years, leading up to where I am today, thanks a lot. Deepika for all the fun times, liveliness and positivity. Vrushali, for all the good times and support here in Strasbourg and our discussions of the past 10 years. I cannot thank Shruthi enough, for being my pillar of support for more than a decade. I was lucky enough to make this professional journey from undergrad till now, with you by my side, even with us moving across the country and eventually continents. I am extremely thankful for your undying support and so much more.

I also want to give special thanks to my two-year-old niece (Kiyara Bhat), her smile and baby talks were my constant stress buster, when I needed them the most.

Lastly, I want to thank my family for supporting my decisions including my brothers, sisters' uncles and aunts. A special thanks to my elder brother, for challenging me to do better and always supporting me for the decisions that did seem scary at the first look.

And lastly, none of this would have been possible without my strongest pillar of support, my mother. Thanks for being the iron lady of my life, for all the struggles you went through to see me where I am today. Thanks for the support, regarding all the unconventional decisions taken by me over these years. None of this would have been possible without you.

RÉSUMÉ DE LA THÈSE

Le développement embryonnaire implique des transformations de formes cellulaires. Ces changements sont essentiellement guidés par le cytosquelette d'acto-myosine régulé par les GTPases Rho. La conservation de ce principe entre les systèmes modèles est frappante à cet égard, depuis la mouche *Drosophile* jusqu'à la souris et le poisson Zèbre, en passant par *C. elegans*. Elle ouvre la perspective d'identifier les principes généraux d'auto-organisation de la matière vivante.

A ce jour, les conservations moléculaires sont établies. Cependant, les filaments d'actine et la myosine agissent généralement en groupe pour toutes ces morphogenèses. Une fibre de stress, des anneaux de cytokinèse, par exemple, sont constitués de milliers de filaments aux polarités variées, en interaction avec des milliers de myosine. Comment cet ensemble de partenaires s'organise-t-il pour mener les transformations de forme ?

Les organisations des filaments dans les muscles ont permis d'expliquer des applications de contraintes dans ce cas simple [1][2][3][4]. L'hydrolyse d'ATP et le glissement de filaments de polarités opposées permet de transformer l'énergie chimique en travail mécanique. Ce schéma n'est cependant pas conservé dans les autres systèmes impliqués dans la morphogenèse.

L'équipe de Daniel Riveline a montré que les agrégats de myosine peuvent servir de lecture de sortie simple pour la cytokinèse. Les agrégats fixes dans le référentiel appliquent des contraintes, les agrégats mobiles assurent des activités de transport. Cette règle a été établie par des expériences impliquant biologie cellulaire, microfabrication, physique théorique des gels actifs [5]. Elle permet de comparer des systèmes aussi différents que les levures ou les cellules de mammifères.

De manière frappante, ces agrégats ont été également observés avec des rôles voisins chez *C. elegans* et chez la *Drosophile* [6][7][8]. Des dynamiques similaires ont été rapportées aussi *in vitro* dans des systèmes reconstitués. Ces conservations d'auto-assemblage et de fonctions ouvrent la perspective que ces règles d'organisation régissent les transformations de forme du vivant. Cette hypothèse est d'autant plus intéressante que les théories de gel actif prédisent cette conservation de dynamique et d'auto-organisation.

Le sujet de thèse a consisté à sonder cette règle 'agrégats fixes-stress' et 'agrégats mobiles-transport' dans des monocouches épithéliales *in vitro*. Le travail a impliqué de la biologie cellulaire, de la microfabrication, des approches de biologie quantitative. Nous avons généré des trous de diamètre constants dans des monocouches en imposant des piliers réguliers de dimension contrôlée : des anneaux d'acto-myosine se formaient en bordure pour fermer la

monocouche. Les agrégats suivent bien les règles génériques. Par ailleurs, nous montrons que les proportions d'agrégats mobiles et fixes dictent les vitesses de fermeture. Les cellules de la monocouche contribuent de manière mineure à la fermeture, ainsi que le montrent les cinétiques avec des anneaux de cellules ou des monocouches avec des trous dont les inter-distances varient. Enfin, des expériences avec des ablations laser confirment les forces élevées des agrégats fixes. Pour la signalisation associée aux phénomènes, nous montrons que des contraintes mécaniques permettent de rétablir la présence d'agrégats, suggérant que l'activité de mécanosension de ces anneaux d'acto-myosine est impliquée, ce qui est confirmé par des mesures d'activités Rho locales par FRET. L'ensemble de ces résultats suggère que ces agrégats et leurs dynamiques sont des objets de choix pour prédire les transformations de forme de la matière vivante.

Le texte qui suit reprend les éléments essentiels de ces résultats.

1/ La vitesse de fermeture de la monocouche est imposée par les anneaux d'acto-myosine.

La fermeture des monocouches épithéliales est essentielle pour assurer la continuité du tissu, et le caractère fondamental du phénomène a suscité son étude approfondie [9][10]. Plusieurs mécanismes sont proposés [11], et nous nous sommes intéressés au 'purse-string' dans cette thèse. Nous avons utilisé des cellules épithéliales MDCK avec plusieurs marqueurs fluorescents, en particulier la myosine (MRCL-GFP).

Pour contrôler la localisation et les dimensions des trous, nous avons utilisé des développements récents en microfabrication. Nous avons ainsi préparé des piliers par lithographie [9] de diamètre 50μm et de hauteur 80μm. Nous incubons les cellules qui s'étalent pendant 14h-16h. Après retrait des piliers, des trous contrôlés sont générés.

De manière frappante, les vitesses de fermeture sont les mêmes dans toutes les configurations sondées, en variant les distances entre piliers, ou encore en préparant un anneau de cellules. Ce résultat suggère que l'anneau d'acto-myosine joue un rôle central dans la cinétique de fermeture.

2/ Les dynamiques des agrégats de myosine suivent des règles simples d'auto-organisation.

En regardant de plus près les anneaux d'acto-myosine, nous avons observé que des agrégats se formaient. De manière frappante, leur dynamique peut être classée en deux catégories, les agrégats qui tournent, et les agrégats qui sont fixes/stationnaires. Ces dynamiques sont conservées pour tous les anneaux. Par ailleurs, la vitesse de fermeture est plus faible localement

pour les agrégats qui tournent que pour les agrégats stationnaires. Enfin, la proportion de ces deux dynamiques semble dicter les vitesses de fermeture. Tous ces éléments suggèrent que les dynamiques des agrégats sont étroitement liées aux vitesses locales et globales de fermeture. Ce résultat confirme les prédictions théoriques et rejoignent les observations et mesures sur les anneaux de cytokinèse [5].

3/ Les contraintes associées aux deux dynamiques sont cohérentes avec les prédictions.

Pour déterminer avec précision les contraintes associées aux deux dynamiques, nous avons imposé des ablations laser locales. Cette méthode permet de comparer de manière quantitative des 'stress' associés. La Figure 3 reprend les résultats majeurs : les ouvertures des anneaux sont suivies au cours du temps. En fermeture normale après retrait du pilier, les deux types d'agrégat sont visés, et de manière significative, la vitesse d'ouverture montre que les contraintes des agrégats stationnaires sont bien plus élevées que celles des agrégats tournants. Les mêmes valeurs d'ouverture sont obtenues dans une situation pour laquelle seuls les agrégats tournants sont présents. Ces résultats confirment à nouveau, et de manière quantitative, le schéma d'auto-organisation générique pour la dynamique de agrégats et leurs rôles dans les transformations de formes.

3/ Les agrégats de myosine sont des mécanosenseurs liés à la voie Rho.

Pour sonder les liens entre Rho et les agrégats, nous avons utilisé une condition particulière. Lorsque le pilier est conservé dans la monocouche, de manière frappante, tous les agrégats tournent. Cela suggère que le gel est instable. Par ailleurs, en incubant les cellules avec l'inhibiteur ML7, nous avons fait disparaître l'anneau, et fait varier son diamètre. L'effet est réversible, fermeture et agrégats reprennent après lavage de l'inhibiteur.

L'expérience qui suit a combiné les deux approches. En laissant le pilier et en incubant avec l'inhibiteur ML7, nous avons observé que les agrégats restent. Il semble que la présence d'une barrière physique empêche la disparation de l'anneau et des agrégats. Ces agrégats pourraient dont être des entités mécanosensibles, car la mécanique se substituerait à la signalisation.

4/ La GTPase Rho est active autour de l'anneau de fermeture.

Pour confirmer cette implication de Rho, nous avons utilisé un senseur FRET qui permet d'acquérir les formes GTP de Rho [12][13]. Des études ont en effet montré sur plusieurs systèmes que Rho et myosine sont couplés [14][7]. Nos résultats montrent que la myosine

reconstruit l'anneau après ablation, et par ailleurs, ce recrutement est associé à l'activation de Rho. Cette même activation est présente pendant les fermetures des anneaux. Ces résultats établissent le lien entre activations de cette GTPase centrale et des agrégats caractérisés dans notre étude.

Ces travaux suggèrent une règle simple d'auto-organisation : les agrégats fixes imposent la fermeture, les agrégats mobiles sont liés l'homogénéisation de l'anneau. Ces agrégats sont des mécanosenseurs impliquant l'activation par la GTPase Rho. Cette simplicité inattendue ouvre la perspective de prédire les changements de formes avec cette même lecture de sortie, les agrégats. Ainsi, la morphogenèse pourrait être caractérisée pour tout organisme en développement avec ces règles d'auto-organisation accessibles par suivi en fluorescence d'agrégats.

ABSTRACT

Myosin clusters have been reported in a variety of systems, ranging from *Drosophila* to *C. elegans* and reconstituted *in vitro* systems. However, their integration in a generic framework is still lacking. We recently reported that clusters dynamics are associated with stress generation when still and transport when motile in cytokinetic rings. Here we show that this simple rule holds as well for acto-myosin rings leading the wound closure in epithelial monolayers. By using micro-fabrication, cell biology, and imaging and theoretical physics, we report that still rings are associated with local closure whereas rotating clusters are related to stalled portions of rings. We also show that myosin clusters are mechanosensors regulated by the GTPase Rho. This conserved mechanism suggests that myosin clusters dynamics could be used as generic read-outs for mapping stress in developing embryos with predictive power.

THESIS SUMMARY

It has been previously shown in the lab. that myosin clusters formation and their dynamics are related to their functions [5]. Such observation was made possible by placing the cytokinetic ring parallel to the focal plane yielding unprecedented spatial and temporal resolutions. Focusing on the cytokinetic ring of mammalian (HeLa) and fission yeast cell, it was reported through experiments and theory that myosin self-assembles into clusters in both of these cases. Arrangement and dynamics of these myosin clusters were observed to vary with periodic cluster arrangement in mammalian cell cytokinetic rings. Fission yeast cytokinetic rings showed non-periodic cluster arrangement. Myosin clusters observed in mammalian rings were reported to apply stress during constriction, in contrast to fission yeast rings where clusters were observed to rotate, and proposed to be associated with transport of the wall machinery [5].

This previous study on myosin clusters in single cell systems gave basis to propose that ***cluster dynamics – still and/or rotating - capture the mechanism of ring constriction in general***. Here, still clusters mean the clusters that remain at the same position in the context of the ring, while its constriction. On the contrary, rotating clusters mean, the clusters that rotate in the context of the ring, while its constriction. In this study, we addressed the question whether this cluster dynamics is conserved to multi-cellular system as well. For this, we chose the multi-cellular system of epithelial wounds, where both supracellular acto-myosin ring as well as myosin clusters could be tracked and manipulated. In the present study, still clusters were referred to as radial, and rotating clusters were referred to as tangential clusters.

Wounds in epithelial cells lead to loss of tissue integrity which can in turn lead to infections, because of exposure to the outer environment containing micro-organisms. Closure of such gaps in a multi-cellular environment is vital, for proper functioning and development of the tissue as well as for the organism. For this reason, many of the recent studies have been dedicated to studying the dynamics and factors regulating the phenomenon of wound closure [10][9]. Re-establishment of a wounded tissue involves coordinated motion of cells, towards the wounded zones. Studying this process has revealed two distinct mechanisms that work together in the healing of a wounded tissue. These factors include coordination, mechanical properties and forces generated by the surrounding tissue. Progression of these tissues have been studied under two main mechanisms known as cell crawling and purse-string contraction [15]. Wound closure via crawling cell mechanism involves lamellipodial action. Closure via purse-string-like mechanism involves an acto-myosin cable at the wound edge. Relative

contributions from both mechanisms can differ in different wound configurations and therefore are known to be non-mutually exclusive [15].

We mainly aimed at focusing on the purse-string-like mechanism driven by stress inherent to the acto-myosin cable around the wound ring. For this assay, micro-fabrication protocol was standardised to obtain micro-pillars of controlled dimensions [16]. The ring diameter was fixed to 50μm in most experiments in order to rule out ring closure through cell crawling mechanism. This dimension was chosen to preclude the phenomenon of lamelliopodia-based ring closure mainly observed in larger rings. After attachment of the 50μm diameter micro-pillars with a height of 80μm to the coverglass, cells were plated and allowed to spread around the pillars. Careful removal of pillars gave reproducible damage-free wound rings throughout the monolayer. Cells used in this study were MDCK (Madin-Darby Canine Kidney) epithelial cell line. These cells were stably transfected with Myosin Regulatory Light Chain (MRLC) fused to Green Fluorescent Protein (GFP) to follow live myosin dynamics. Visualisation of these wounds exhibited acto-myosin accumulation in the form of a *ring*, as well as *myosin clusters* around the wound perimeter. These structures are referred to as *acto-myosin ring* and *myosin clusters* in the text throughout this study. To understand dynamics of these structures, we first started by characterising the acto-myosin ring around the wounds. We used the powerful method of micro-fabrication in order to control characteristics of the cell monolayer forming these wounds. And we tracked wound closure dynamics as a readout.

First, we determined, ***if the cell number contributed to wound closure***. We prepared three types of PDMS micro-pillar motifs with increasing inter-distance between pillars, *i.e.* 30μm, 100 μm and 200 μm. Cells plated at *constant density* around these pillars presented wounds with varied cell number between them, and we kept constant the cell density in all experiments. The higher was the inter-distance, the higher was the number of cells between neighbouring wounds. We characterised the difference by analysing the speed of wound ring closure in each case. Wound closure dynamics was evaluated after removing of pillars referred to as *open ring configuration*, in the following of the text. Interestingly, we observed that even with increasing cell number, the ring closed at the same rate of ~0.3μm/min. To further confirm this result, we prepared micro-fabricated O-ring shaped motifs of similar diameter 50μm. We micro-contact-printed one of the extracellular matrix protein *fibronectin*. With this process, we were able to obtain 'doughnuts' of rings with minimal surrounding cell number. Surprisingly, the rate of ring closure in this case had no significant difference with the closure rates amongst the monolayer rings. This suggested that cells were not the main contributors of the wound ring closure.

Therefore, we looked next at the active component of closure, *i.e.* the acto-myosin accumulation observed around the wound edge.

Higher acto-myosin density was seen around the wound edge, when compared to the to the basal myosin intensity in the cell cytoplasm. This was referred to as an acto-myosin ring. As compared to the myosin density in the cells cytoplasm, density within the ring was evaluated to be ~ 1.8 – 2 times higher which was representative of the acto-myosin cable. We assume that interaction of actin and myosin filaments at the wound edge defines activity of this active gel, closure of these wounds is further referred to as *constriction* in the following text.

Next, as a readout for myosin concentration, we evaluated ***dynamics of temporal myosin intensity at the wound rings***. The total myosin intensity was shown to decrease during constriction. This seemed obvious since the wound ring loses perimeter progressively with time. Interestingly, even though the total myosin intensity was observed to be reducing with time, mean ring intensity was measured to stay constant. This suggests that myosin concentration is constant throughout the process of ring closure. We also propose that the system has ***myosin conservation over time***. To evaluate this further, we took 'halo' of myosin intensity around the ring as a readout of myosin concentration. By plotting this intensity associated to the decrease in diameter during ring constriction, we indeed saw a constant myosin loss with time. This suggests that there is a constant loss of myosin during ring constriction. These results showed that this acto-myosin ring maintained a constant concentration of myosin during ring closure, and the lost myosin is conserved and distributed nearby in the cells.

Acto-myosin ring consists of non-sarcomeric, stochastic arrangement of polar actin filaments and myosin motors [17]. Force balance of contractions and extensions in such a system should cancel out each other and therefore would lead to stalling of the ring. Contractile acto-myosin rings during developmental stages are predominantly observed to constrict progressively rather than stalling. This progressive constriction is a consequence of ***myosin motors self-organising into transient and/or long-term structures*** and their subsequent interaction with actin filaments. These self-organised arrangements have been observed in various developmental processes, in the form of myosin high-density foci [5][18][6][8], referred to as *clusters* in this study. They were also predicted theoretically.

Next, we looked for these self-organised myosin arrangements in our system of epithelial wounds. Similar to previous study in the lab. about key roles of clusters in cytokinetic rings of mammalian and fission yeast cells [5], we also observed myosin *clusters* at perimeter of multi-cellular wound rings. In addition, their temporal dynamics also appeared to be similar as for the clusters characterised in cytokinetic rings [5].

Motivated by this observation, we focused on determining whether cluster characteristics and dynamics observed in single cell cytokinetic ring will correlate with multi-cellular acto-myosin wound rings. First, we characterized these myosin clusters and subsequently their potential role in ring constriction. We characterised the ***cluster contrast*** with respect to the myosin intensity of the ring. This parameter indicates myosin concentrations in these clusters. The average myosin cluster contrast was evaluated to be constant throughout its time of persistence. This showed that myosin concentration within clusters was maintained in a temporally stable manner. Next, we evaluated number of clusters existing at the ring perimeter. This was determined by evaluating temporal ***cluster density*** *i.e.* number of clusters per unit length during the process of ring constriction. This evaluation showed that similar to cluster contrast, cluster density was also maintained constant during the process of ring constriction, in turn showing higher cluster number in larger diameters as compared to smaller diameters. On an average, ~3 clusters were observed at the start of ring constriction process observed at a starting diameter of 50µm.

Having characterised clusters, we next investigated ***myosin cluster dynamics*** during constriction. Two types of dynamic clusters were reported and characterised in single cells, and they were referred to as *radial* and *tangential* corresponding to mammalian and *fission yeast* cell cytokinesis, respectively. Interestingly, we observed that both types of cluster dynamics co-exist in our multi-cellular system.

In addition, we observed that local closure rates of the ring curvatures were related to the local types of cluster. Rings consisting of purely tangential clusters closed much slower than rings containing purely radial clusters, typically by a factor of 5. These observations showed that ***radial clusters are related to a local fast closure compared to tangential clusters***. This observation was further quantified by correlating the closure rate with the relative fraction of still and moving clusters within a ring. It was clearly seen that whenever the relative fraction of radial myosin clusters was higher, the closure rate increased and vice versa. This suggests a difference in stress related to these two types of dynamic clusters, and that ring closure could be led by cluster dynamics.

To further test the hypothesis of distinct stresses associated with types of clusters, we decided to ablate them with a laser. First, we asked the question if there exists any stress difference associated with a cluster and the homogeneous myosin ring portion. For this, we used multi-photon laser ablation setup to ablate both these distinct portions of the acto-myosin ring. Ablating these different portions of the acto-myosin ring indeed depicted an initial fast 'snapping' of both ablated portions, with higher snapping for clusters. Evaluating the

snapped/retracted distance and subsequently the retraction velocity gave us an indicative stress measurement of the ablated portions. We clearly saw that when the ablation was applied locally on the ring, the snapped distance and subsequent initial retraction velocity were much higher than for homogeneous portion, by a factor of 1.6. This indicates a ***higher stress associated with the clusters as compared to the homogeneous ring portion***. Also, fluorescent recovery after photobleaching (FRAP) analysis of clusters showed less to almost no myosin recruitment, as compared to homogeneous ring portions. This result suggests a stress-dependent stability in clusters as compare to homogeneous acto-myosin ring portions.

To test our hypothesis of stress difference related to the types of cluster dynamics, we followed the same protocol to ablate and subsequently evaluate their retracted distance and velocity of retraction. Since our hypothesis stated that that radial clusters have higher stress compared to tangential clusters, we first identified them to persist through at least a time period of ~6-7min. Next, we ablated them and evaluated their snapped distance and subsequent retraction velocity. A clear difference in both readouts was observed, with radial cluster having an increased retraction velocity by a factor of ~1.5 compared to tangential cluster. This was further evaluated by fitting a nonlinear exponential decay curve for the data points [19], where the retraction velocity corresponding to the associated stress for radial clusters was evaluated to be 2.19 ± 0.61 µm/s, compared to 0.71 ± 0.18 µm/s for tangential clusters. Initial velocity corresponds to tension associated with myosin clusters. These results show that indeed radial clusters have higher initial tension compared to tangential clusters. Hence, these results altogether validated our hypothesis that ***radial clusters have higher stress compared to tangential clusters***. This suggests that this difference in stress could be responsible for faster acto-myosin ring constriction of the corresponding portion of the ring. In addition, it also explained the observation of faster ring constrictions with relatively higher percentage of radial clusters as compared to tangential clusters.

All these experiments were performed in open ring configuration *i.e.* when the pillars were removed and rings were allowed to constrict. Similar ablation studies were also done in closed ring configuration *i.e.* with pillars left inside the wound ring, acting as a physical barrier for ring constriction. Interesting observations came out of this specific configuration and its laser ablation studies. First, it was observed that ***all clusters in closed ring configuration predominately followed tangential cluster dynamics***. Although ablation of homogeneous ring portions in this configuration showed comparatively lower retraction velocity to the tangential cluster, these clusters showed similar retraction velocities compared to their counterparts in

open ring conformation. Therefore, these results indicated that ***there exist concrete correlations between cluster dynamics and the corresponding initial stress associated with them***.

Since we observed tangential clusters, rotating with ~1° min^{-1} which added up to more than 90° in the course of 60 min evolution in an open ring configuration, we wondered if these clusters were able to cross cell-cell junctions. For this, we used an MDCK cell line stably expressing Myosin Regulatory Light Chain (MRLC) and E-cadherin (E-cad) for simultaneous visualisation of myosin and cell-cell junction, respectively. It was observed that these junctions acted as a barrier to these clusters and hence, acto-myosin ring at each cell edge behaved as an individual segment.

To further investigate the stress associated with myosin clusters, we inhibited their activity via ***myosin light chain kinase inhibitor*** (ML-7) in an open ring configuration. Within minutes of exposure, this led to the disappearance of clusters and acto-myosin ring. Interestingly, this disappearance was associated to the ***subsequent stalling and opening of the ring*** which was potentially indicative of the stress associated with the acto-myosin ring. The acto-myosin devoid ring stayed in this state throughout the incubation time with drug. We checked if the phenomenon was reversible, *i.e.* if the activity of myosin could be restored after wash-out. Myosin clusters as well the myosin ring reappeared after the drug washout within 5min, leading to subsequent normal ring constriction. This supports that myosin clusters are indispensable for the normal ring constriction.

Interesting, ***inhibiting myosin light chain kinase in a closed ring conformation led to myosin cluster rescue*** instead of cluster disappearance. This suggested that myosin clusters as a whole could act as mechanosensors. Since RhoA could be one of the actors playing a crucial role in myosin activation through Rho-associated kinase (ROCK), we prepared a cell line co-expressing MRLC and FRET biosensor. By ratiometric analysis, we showed that indeed there exits an ***increased RhoA activity around the wound ring*** in both closed and open ring configurations, when compared with the surrounding cell monolayer. Also, through laser ablation of these rings and subsequent ratiometric analysis, we showed that ***high RhoA activity was correlated with myosin recruitment*** during ring recovery after ablation. These results are consistent with the study reporting myosin recruitment and RhoA activity in *Xenopus* single cell embryo ablation [20]. We are further analysing our results for RhoA activity in closed and open ring configuration, to look for possible mechanotransduction pathways existing in these acto-myosin rings.

Finally, mesoscopic mechanisms for changes in cell shapes have been previously shown in the Lab. However, resolution has been limiting to determine the organisation of actin filaments and

myosin motor proteins. Therefore, in order to obtain better resolution of clusters, we initiated new collaboration with A. Honigmann Lab. (MPI-CBG Dresden), and designed experiments with STED super-resolution microscopy. We were able to observe a resolved sub-structural arrangement of the acto-myosin wound ring. These sub-structures were observed as evenly distributed MRLC bands with alternating actin bands visualised by phalloidin staining. This orderly arrangement within the ring perimeter depicted an organisation which was observed to be reminiscent of the periodic arrangement of actin and myosin in muscle contraction units as well as being consistent with the myosin stack formation in non-muscle cells [21]. This indicated a novel mechanism for self-organisation of the acto-myosin cytoskeleton in non-muscle cells at a tissue level.

Finally, we also took advantage of correlative light electron microscopy (CLEM) in the Lab. in order to try and determine the arrangement of actin and myosin filaments within the cluster region in terms of numbers. We observed sub-clusters within one cluster formation. This approach provided us with spatially resolved myosin clusters, depicting ~10 sub-clusters within one cluster, in addition to ~10 dense filament like structures depicting actin filaments in single cuts. We are further analysing these results to obtain numbers and organisations for myosin and actin filaments within clusters in rings.

In conclusion, results of this study, demonstrated self-organised myosin clusters and their dynamics in multicellular system, providing a simple explanation for wound healing. They are consistent with dynamics reported for cytokinetic rings of mammalian cells *i.e.* radial clusters and tangential clusters, demonstrating stress variations. In addition, these myosin clusters are reported in a variety of systems in development, for example in *Drosophila* and in *C. elegans*. We propose that clusters dynamics could serve as a powerful readout for morphogenesis with the simple rule still/stress and moving/transport. Changes in shape of living matter could be inferred through tracking and quantification of myosin clusters which would serve as generic readouts. Theory and our experiments support so far, this simple and testable framework.

LIST OF MOVIES AND LEGENDS

Movie 1: Ring closure of spontaneously formed wounds in epithelial cell (MDCK) monolayer expressing MRLC GFP. Scale bar 50µm. Time in hh:mm:ss.

Movie 2: Closure of micro-fabricated MDCK wound rings, of 50µm diameter and 30µm interdistance between wounds. Phase contrast and fluorescence (MRLC-GFP) images shown. Time in hh:mm:ss.

Movie 3: Closure of micro-fabricated MDCK wound rings, of 50µm diameter and 100µm interdistance between wounds. Phase contrast and fluorescence (MRLC-GFP) images shown Time in hh:mm:ss.

Movie 4: Closure of micro-fabricated MDCK wound rings, of 50µm diameter and 200µm interdistance between wounds. Phase contrast and fluorescence (MRLC-GFP) images shown. Time in hh:mm:ss.

Movie 5: MDCK cells were segmented with the help of a custom-made macro, to analyse ring characteristics on phase contrast images. Time in hh:mm:ss.

Movie 6: 'O' ring closure with diameter maintained at 50µm. Acquisition showing phase contrast and fluorescence (MRLC-GFP) images of the ring closure dynamics. Duration 4h. Time in hh:mm:ss.

Movie 7: *Radial cluster* dynamics at the ring perimeter during evolution of wound ring, in an open ring configuration. Fluorescence images of MRLC-GFP shown. Time duration of 80 mins followed. Time in hh:mm:ss.

Movie 8: *Tangential cluster* dynamics during evolution of wound ring, in an open ring configuration. Time duration of 30 mins followed. Fluorescence images of MRLC-GFP shown. Time in hh:mm:ss.

Movie 9: *Radial cluster* (MRLC-KO1, red) dynamics, acquired for a duration of 7min. Cells expressing MRLC-KO1 and E-cadherin mNG (green). Acquisition done in open ring configuration. Time in hh:mm:ss.

Movie 10: Retraction of cable ends, acquired after *radial cluster* ablation for a duration of 70s after the first cut. Cells expressing MRLC-KO1 and E-cadherin mNG (green). Acquisition done in open ring configuration. Time in hh:mm:ss.

Movie 11: Recovery of ablated ring after ablation at the *radial cluster* for a duration of 15min. Cells expressing MRLC-KO1 and E-cadherin mNG (green). Acquisition done in open ring configuration. Time in hh:mm:ss.

Movie 12: *Tangential cluster* (MRLC-KO1, red) evolution, acquired for the duration of 6min. Cells expressing MRLC-KO1 and E-cadherin mNG (green). Cells expressing MRLC-KO1 and E-cadherin mNG (green). Acquisition done in open ring configuration. Time in hh:mm:ss.

Movie 13: Retraction of cable ends, acquired after *tangential cluster* ablation for a duration of 120s after the first cut. Cells expressing MRLC-KO1 and E-cadherin mNG (green). Acquisition done in open ring configuration. Time in hh:mm:ss.

Movie 14: Recovery of ablated ring after ablation at the *tangential cluster* for a duration of 4min. Cells expressing MRLC-KO1 and E-cadherin mNG (green). Acquisition done in open ring configuration. Time in hh:mm:ss.

Movie 15: *Tangential cluster* dynamics in a closed ring configuration, acquired for a duration of 14h. Phase contrast and fluorescence (MRLC-GFP) images shown. Time in hh:mm:ss.

Movie 16: Retraction of cable ends, acquired after *cluster* ablation for a duration of 70s after the first cut. Cells expressing MRLC-KO1 and E-cadherin mNG (green). Acquisition done in closed ring configuration. Time in hh:mm:ss.

Movie 17: Recovery of ablated ring after ablation at the *cluster* for a duration of 26min. Cells expressing MRLC-KO1 and E-cadherin mNG (green). Acquisition done in closed ring configuration. Time in hh:mm:ss.

Movie 18: Retraction of cable ends, acquired after ablation at the *homogeneous ring portion*, for a duration of 70s after the first cut. Cells expressing MRLC-KO1 and E-cadherin mNG (green). Acquisition done in closed ring configuration. Time in hh:mm:ss.

Movie 19: Recovery of ablated ring after ablation at the *homogeneous ring portion*, for a duration of 3min. Cells expressing MRLC-KO1 and E-cadherin mNG (green). Acquisition done in closed ring configuration. Time in hh:mm:ss.

Movie 20: Wound ring, in closed configuration imaged for 40min. Afterwards, pillars were removed and ring evolved for 40min. Next, ML-7 was introduced for 1h and then washed out. Time in hh:mm:ss.

Movie 21: Wound ring, in closed configuration imaged for 40min. Next, ML-7 was introduced for 2.5h and then washed out. Time in hh:mm:ss.

Movie 22: Tangential clusters followed in an open ring configuration, with cells expressing MRLC-KO1 and E-cadherin mNG for a duration of ~3h. Time in hh:mm:ss

Movie 23: Ring constriction dynamics with visible myosin loss to adjacent cells. Cells expressing MRLC-KO1. Duration of acquisition in the open ring configuration 85min. Time in hh:mm:ss.

Movie 24: Two cell divisions at the ring edge, slowing down the constriction dynamics to ~6h. Cells expressing fluorescence MRLC-GFP. Duration of acquisition in the open ring configuration ~11h. Time in hh:mm:ss.

Movie 25: Fluorescent recovery after photobleaching (FRAP) for a cluster. Cells expressing MRLC-KO1. Acquisition at 1s interval for 60s and 60s interval for 30min. Time in hh:mm:ss.

Movie 26: Fluorescent recovery after photobleaching (FRAP) for a homogenous ring portion. Cells expressing MRLC-KO1. Acquisition at 1s interval for 7min. Time in hh:mm:ss.

Movie 27: Ratiometric RhoA FRET analysis (CFP/YFP couple) for acto-myosin ring dynamics in an open ring configuration. Both MRLC-mCherry and FRET (calibration: grey levels) channel are shown. 1 min interval for a duration of 90min. Time in hh:mm:ss.

Movie 28: Ratiometric RhoA FRET analysis (CFP/YFP couple) for acto-myosin ring dynamics in a closed ring configuration. Both MRLC-mCherry and FRET (calibration: grey levels) channel. 1 min interval for a duration of 10min. Time in hh:mm:ss.

Movie 29: Ratiometric FRET analysis (CFP/YFP couple) during myosin recruitment to ablated site for recovery. Both MRLC-mCherry and RhoA FRET (calibration: grey levels) channel are shown. 1 min interval for a duration of 37min. Time in hh:mm:ss.

Movie 30: Wound ring constriction in an open ring configuration with cells expressing non-phosphorylatable (AA) MRLC-GFP. Duration of acquisition 14h. Time in hh:mm:ss.

Movie 31: Wound ring constriction in a closed ring configuration with cells expressing non-phosphorylatable (AA) MRLC-GFP. Duration of acquisition 8h. Time in hh:mm:ss.

Movie 32: Wound ring constriction in a closed ring configuration, with cells spreading and showing myosin clusters as soon as contact with the pillars. Cells expressing non-phosphorylatable (AA) MRLC-GFP. Duration of acquisition 15h. Time in hh:mm:ss.

Movie 33: Transmission Electron Microscopy of a myosin cluster at the epithelial wound edge showing 4 ‘z’ slices of 80µm thickness, from bottom of the coverslip.

Movie 34: NOA cavities with diameter 22µm and height 12µm, checked for being through-hole by putting beads at the bottom, prior to cavity preparation. Rotation of the movie in ‘Y’ direction.

Movie 35: NOA cavities with diameter 22µm and height 12µm, checked for being through-hole by putting beads at the bottom, prior to cavity preparation. Rotation of the movie in ‘X’ direction.

Movie 36: A tilted HeLa cytokinetic ring inside cavities, immunostained for MRLC, showing 'z' step size of 0.2μm and resolved myosin clusters around the ring.

Movie 37: HeLa cell cytokinetic ring constriction inside cavities showing cortical rotation. Duration 90s. Time in hh:mm:ss.

Movie 38: HeLa cell cytokinetic ring dividing on a coverslip with fibronectin, showing cortical rotations. Duration ~9min. Time in mm:ss.

Movie 39: Fission yeast cytokinesis on glass coverslip with lectin, showing myosin clusters coalescing to form the cytokinetic ring. Duration ~12min. Time in hh:mm:ss.

Movie 40: Wound ring in closed ring conformation during exposure with Y27632, ROCK inhibitor Duration ~1h. Time in mm:ss.

Movie 41: Wound ring in closed ring conformation during exposure with C3 transferase, Rho inhibitor Duration ~1h. Time in mm:ss.

TABLE OF CONTENTS

1.Ph.D. MOTIVATION

Understanding acto-myosin ring dynamics has been so far based on the sarcomeric concept of actin and myosin arrangements, where forces generated by sliding filaments are analogous to sarcomeres.

Acto-myosin rings have in principle random arrangement of polar actin filaments. Given the presence of thousands of such filaments in a ring, stochastic organisation of parallel and anti-parallel filaments precludes the idea of constant contraction in these rings. In such configuration, forces from single filament extensions would oppose the forces produced by contractions, and hence lead up to stalled rings. And surprisingly, acto-myosin rings are always observed to be constricting.

Constant contractions within these stochastic configurations could be brought about by molecular motors such as myosins. Myosin-II has been studied widely to self-organise relative to actin filaments thereby modifying the network architecture with experiments performed in close connections with theory.

Myosin clusters	**Velocity of cluster ($\mu m\ s^{-1}$)**	**Velocity of ring constriction**	**Duration of the process**
***in vitro* reconstituted actin asters**	~ 0.06	-	~15 min [22]
***Drosophila* (germband extension) cell intercalation**	~ 0.11	-	~0.6 min (junctional shrinkage for cell intercalation) [6]
***C. elegans* (1-cell stage) A-P polarity**	~ 0.05	-	~5 min [7]
Mammalian cytokinetic ring	~ 0.05	2.5µm/min	8mins (20µm diameter)[5]
Fission yeast cytokinetic ring	~ 0.001	0.1µm/min	40 mins (4µm diameter)[5]

Table 2.1: Myosin cluster velocities during different biological processes.

One of the highly prevalent self-organised form of myosin *i.e.* clusters, has been conserved throughout different systems. These myosin clusters are known to produce stress within the network, leading to its proper evolution in morphogenesis.

Cluster formations are shown to be indispensable for the process of cytokinetic acto-myosin ring constriction. This was previously reported in the lab, in context of fission yeast and mammalian cells. Two types of dynamic clusters were studied, radial and tangential, associated with distinct stresses and therefore functions. Velocity of ring constriction (Table 2.1) correlated with distinct cluster dynamics, and these results were supported by theory.

This gives a basis for us to hypothesise that **cluster dynamics – still and/or rotating - captures the mechanism of ring constriction in general**.

Myosin molecule measuring ~100 nm, forms similar self-organised clusters across scales spanning ~4µm diameters for fission yeast cytokinetic rings, 20µm mammalian cell cytokinetic ring to 200µm contractile ring during *Drosophila* dorsal closure. Although dynamics of these clusters might differ from one system to another, the underlying interactions are conserved. Rules for active gels could be generic and conserved across scales and between species.

In this study, we focused on answering the question whether this cluster dynamics is conserved to multi-cellular system as well. If correct, myosin clusters could serve as simple readouts for shape transformation using fluorescent microscopy for any model system.

2. INTRODUCTION

2.1 Morphogenesis

Development process of a multicellular organism from a collective ball of cells to a fully functional organism follows a highly dynamic progression of morphogenesis. The concept of morphogenesis was famously predicted and described in the work of D'Arcy Thompson where he focused on analysis of the physical limitations to the growth and structure of organisms. He primarily argued in his work regarding entanglement of growth and form where former can't be described without reference to the latter.

As the name suggests, *morphogenesis* (*genesis;* formation, *morpho;* shape), is transformations leading to emergence of shapes. This process starts from evolution of a mere cell collection giving rise to tissues. Elaborate shapes in these tissues form organs and eventually a fully functional organism with its three-dimensional body structure. This dynamic process is later followed by formation of a much complex fully functional organism. Hence, the process from cell divisions inside a fertilized egg followed by attaining complex shapes in an organism is studied under the concept of *morphogenesis*.

First steps of *morphogenesis* termed as *embryogenesis* involves different levels of biological organisation; genes, cells, tissues inside a developing embryo. Functional development of an embryo depends on local activities of cell proteins translating to whole cell activity where interactions between these individual cells give rise to tissues.

Epithelia are compact tissues forms consisting of adjacently placed cells as a mechanical barrier between the body and its environment. Morphogenesis of epithelia is mainly observed during embryogenesis. Being the first step of evolution into an organism, embryogenesis involves dynamic epithelial morphogenesis during its progression.

Hence, for a better understanding of the epithelial morphogenesis, analysis integrating genetic regulations as well as active mechanics at different scales in cells and tissues are approached. For example, gene expression patterns at the tissue level can facilitate the emergence of planar cell polarity. This allows propagation of global directional information generated by these

spatial cues. Such instance was observed via transcription factors targeting of Toll-like receptors, in drosophila germ band extension establishing identities of body segments [23]. Although dynamic changes in tissues are genetically encoded, key insights from studying different model organisms have emerged with the idea that their accomplishment is essentially a mechanical event. Although there are multiple gene regulations involved in the activity of a cell, to explain the mechanisms of morphogenesis through them has been challenging. Genetic analysis of various model organisms such as *zebrafish*, *drosophila* and *C. elegans* have brought forward hundreds of mutations affecting certain steps in morphogenesis such as differentiation and cell fate determination. Although very small proportion of mutations have been reported to specifically affect the process of morphogenesis.

There exists a vast variety of animal forms both in terms of external appearances and internal variations among cells tissues and organ anatomies. Generic rules that explains such interactions remain largely elusive. Basic rules determining the events, in this complex phenomenon has been a challenge in the field. Continuous efforts are been put through for past two decades to elaborate this complexity in various model organisms. Although detailed analysis of morphogenetic events studied in various model organisms have made it possible to outline certain conserved mechanisms leading to tissue deformation.
Tissue deformation is driven via contributions from different cell scaling processes, leading to epithelial morphogenesis. These events can be broadly classified into *cell division*, *cell rearrangement* and *cell shape changes* [24].

These cellular events are observed to be followed in different combinations and sequences, to bring about tissue deformation in a multicellular developmental process. Starting from embryogenesis and throughout adult life, there is a continuous growth and regeneration of epithelia. These individual cell shape changes consequently translate to the tissues bringing about their deformation.

The property that allows cells to change their shapes divide and rearrange with respect to each other, is due to the assembly of certain proteins. These proteins polymerize into different types of organisations including short- and long-range filaments. The collective mesh of these network filaments giving the cell its shape and mechanical property, is termed as *cytoskeleton*. Cytoskeleton of a cell, primarily consists of filaments of proteins; actin, myosin and tubulin arranged in the form of branched and crosslinked bundles. Interaction between actin and myosin

filaments forms a contractile assembly termed *acto-myosin*. Contractile behaviours of the acto-myosin assembly are a result of motor property of myosin proteins (described in later sections). Rearrangements of the cytoskeletal network proteins help individual cells in events such as shape alterations, division and migration.

Insights in single cell dynamics allows to follow long range tissue deformations. Active tissue rearrangements at single cell level can be brought about by events such as cell divisions and cell extrusions (T2 transitions). Another single cell deformation leading to epithelial morphogenesis includes T1 transition where cells undergo neighbour exchange, leading to their rearrangement and cell shape changes. Such active rearrangements are known to play a key role in processes such as tissue stretching, which is one of the driving forces of embryonic development.

Cell cytoskeleton (2.3) is known to be anisotropically distributed within different sub-cellular compartments such as the cytoplasm and cortex. These anisotropies can therefore be extrapolated to tissues which are comprised by such cells. Dynamic interactions of the cytoskeletal components within each other are responsible for forces exerted by these cells within a given tissue. Anisotropies in this cytoskeletal distribution arise as a result of cell-substrate and/or cell-cell interactions, driving changes in tissue contractility through cellular force distribution. These cellular forces are therefore responsible for mechanical properties of a tissue, in turn providing the driving force behind several key morphogenetic events such as cytokinesis, cell extrusions and cell neighbour exchange to name a few. All these events are important in maintaining the tissue homeostasis and rely on remodelling of junctional E-cadherin proteins and forces transmitted through cell acto-myosin cytoskeleton (2.4).

Epithelial tissue deformations during embryogenesis, visualising specific protein distribution and their dynamics have been made possible by several high-end microscopy techniques. Also, for understanding the dynamics of tissues, in addition to dissecting through the complexities of the system, *in vitro* approaches have become highly recognised. This has been made possible due to availability and ease of secondary culture maintenance of epithelial cells. These *in vitro* approaches and biophysical techniques dedicated to accessing mechanical properties have proven to be an ideal setup for studying stress evolution, and their effects on cellular dynamics.

2.2 Forces in morphogenesis; molecular actors

Force is defined as a push or pull that causes a particle or the system in study to accelerate or deform with respect to its original position and shape respectively. Although the modest force in everyday experience, 1N (S.I. unit; Newton) is 10^{12} larger than the force exerted by molecular elements inside a cell (~10^{-12} N) which is in the range of piconewtons (pN) [25].

The constituent molecular elements brought together, generating such force within a cell is referred to as *cytoskeleton*. As the name suggests (*Cyto*: cell, *skeleton*: supporting framework) this is a multi-protein scaffold that functions as a supporting framework for cells, in order to maintain a stable yet dynamic state. Animal cells lack cell wall and depends on the presence of a fluid-like plasma membrane to support its complex cellular morphologies. The primary function of the cytoskeletal network is to provide the cell its shape in addition to resistance against and/or contributing towards deformation. Apart from giving overall structure and internal organisation, these protein filaments determine the mechanical properties of a cell. Assembly and organisation of cytoskeletal is observed to be spontaneous hence referred to as self-organisation. The assembly of these proteins is often in the form of filaments in the order of 1-1000 μm which assemble and disassemble leading to shape changes and movement in cells. The proteins of this network involve Actin, myosin and tubulin. Post polymerisation and self-organisation of the monomers these proteins give rise to actin filaments, myosin clusters or mini-filaments and microtubules respectively. Although, how these proteins self-organise as designated building blocks of such an assembly remains an outstanding problem in cell biology.

In case of polymerised form of cytoskeletal elements maintained at equilibrium would not account for any force applied within and/or to the system. However, above critical concentration of monomers in their vicinity will lead to flux of monomers onto the polymers. Hence, the polymerisation-depolymerisation of cytoskeletal filaments, as well as their interaction with each other, owns to the non-equilibrium mechanics of active cytoskeleton [26].

Forces mediated by cytoskeletal elements inside a cell translates to tissue dynamics. These changes generate tissue wide deformations observed during morphogenesis an embryo during its development. The developmental steps for attaining shapes in multi-cellular organisms are typically generated through involvement of molecular motors such as, *dynein kinesin* and

myosin referred to as cytoskeletal motors. Amongst the three cytoskeletal motors dynein and kinesins are associated with microtubules to help transport cell cargo towards or away from the nucleus. The third type of cytoskeletal motor 'myosin' in synchrony with 'actin' is responsible for generating *cellular tension* in addition to muscle contraction and intracellular cargo transport. The combined self-organised assembly of these two cytoskeletal elements is referred to as *acto-myosin* complex.

Cellular tension is generated via acto-myosin network, accounting for the force per unit area of the cell. These forces generated via acto-myosin network in a cell are transmitted through cytoskeletal elements and adhesion molecules within and between them. Involvement of acto-myosin network and adhesion proteins has been studied in single cell [5][19] as well as multi-cellular systems [27] involving developmental stages of an embryo [28].

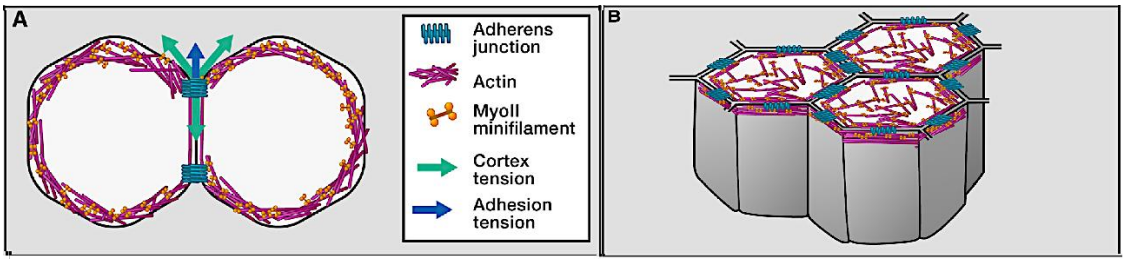

Figure 2.1: Schematic representing positional self-organisation of cytoskeletal elements: *actin, myosin and adherens junctions involved during force generation. Depending on forces associated with acto-myosin contractility (green arrow) as well as adherens junctions (blue arrow), leads to shape changes in single cells (A) and multi-cellular tissue arrangement (B).* [28]

Studies pertaining to signalling networks has proven to be helpful in tracing back the cytoskeletal changes contributing to appropriate mechanical cues. These mechanical cues then act on instructing cell and tissue deformations, for e.g. during embryonic development [29]. In this context, Rho pathway has provided a versatile means regulating cytoskeletal dynamics [30]. Although these mechanisms do shed light on synchrony between signalling molecules (e.g. Rho, Rac, Cdc42) and cytoskeletal dynamics, it ignores the remarkable capability of self-organisation in these cytoskeletal elements, actin, myosin, tubulin and cadherins (Figure 2.1) are responsible for force induced shape changes during embryonic development.

2.3 Cytoskeleton

Cytoskeleton is a scaffold of polymeric network existing in a eukaryotic cell. It enables processes such as movement of sperm cells, crawling of fibroblasts, contraction of muscle units,

extension and maintenance of axons in neuronal dynamics. Cytoskeleton also plays a vital role in plant cell plate positioning, intercell communication as well as plant cell development [31].

Apart from maintaining the cellular structure, it also contributes in several vital processes such as division [32], migration [33][34] and membrane trafficking [35]. Cytoskeleton is involved in dynamics related to single cells and also plays a key role in multicellular processes within tissue monolayers *in vitro* [36] as well as *in vivo* during embryo development [37].

These processes are known to require stress generation [38], centered around the behaviour of three main cytoskeletal components referred to as actin filaments, intermediate filaments and microtubules. These cytoskeletal elements contribute in several different ways to the cellular mechanics and therefore dynamics of cells and tissues. Amongst them, *actin filaments* are known to be a key player in cell migration and cell-shape changes. *Intermediate filaments* are established to provide mechanical strength and resistance to shear stress. *Microtubules* are known to provide tracks for inter-cellular organelle transport, regulating the position of membrane-enclosed organelles. Although these filaments are supposed to be ineffective without the set of accessory proteins linking these filaments to other components and to each other. Apart from the three main cytoskeletal filaments, there exists a class of proteins referred to as *myosins*, known as molecular/myosin motors. These motor proteins can move organelles along actin filaments as well as trigger relative sliding of filaments with respect to each other. Taking functional reference of a human body, where actin and myosin filaments serve parallel to bones and muscles for a cell, intermediate filaments serve as ligaments. Scaffold made up of polymers from the three main cytoskeletal networks can persist or alter their organisation according to the functional need basis of the cell.

Cytoskeletal structures often span an entire cell length spanning a distance from tens to hundreds of micrometres, though the dimension of individual protein molecule is around few nanometres in size. Most of these filaments are formed by repetitive assembly of large numbers of monomers or smaller subunits. The cytoskeletal filaments undergo rapid structural reorganisations due to subunits being under constant flux.
In the following subsections, I will briefly explain the characteristics related to the main cytoskeletal components.

2.3.1 Microtubules

Microtubules are polymer filaments with an outer diameter of ~24-25nm, formed from subunits of protein known as tubulin spanning 100nm-5mm in length. These filaments are composed of alternating globular α and β subunit of tubulin molecules polymerized to form protofilament (figure 2.2). Microtubule filaments are known to be made up of 13 protofilaments running parallel to each other forming its hollow cylindrical structure [39]. There exists longitudinal (α-β) as well as lateral (α-α and β-β) contacts between the subunits, making the protofilaments energetically stable giving rise to a regular helical lattice of microtubule filaments. Presence of alternating subunits naturally provides them with a structural polarity where '+' end is designated as the growth end (Figure 2.2). G proteins are involved in the dynamics of microtubules. These are family of guanosine nucleotide-binding proteins which act as molecular switches within cells, for transmitting signals from outside to inside of a cell and vice versa. Their activity is regulated by their ability of hydrolyse guanosine triphosphate (GTP) to guanosine diphosphate (GDP). These components belong to a larger class referred to as GTPases and their activity stay 'on' while bound to GTP and 'off' while bound to GDP.

Both α and β subunit have binding sites and affinity for GTP molecule. When α subunit is attached to GTP molecule, it behaves as a cap on the tubulin heterodimer since it cannot be exchanged. In contrast, GTP bound to the β subunit is hydrolysed and hence exchangeable.

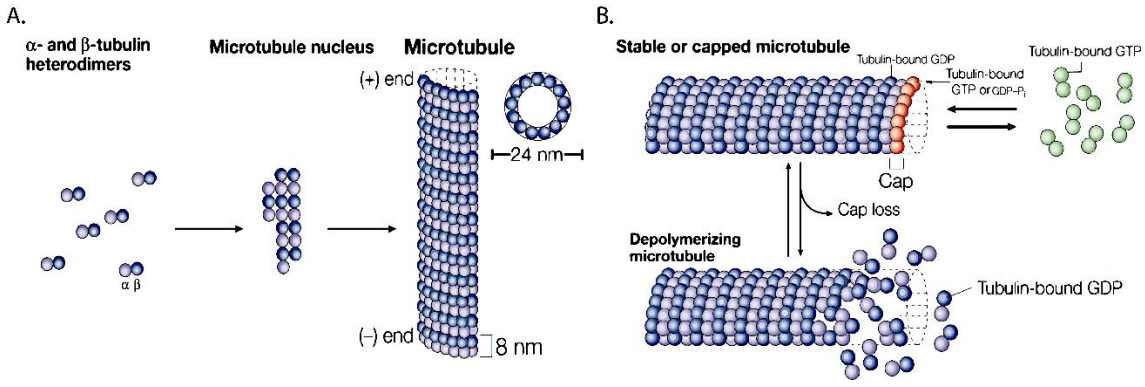

Figure 2.2: *(A) Schematic representing α and β tubulin heterodimer giving rise to protofilament followed by generation of hollow microtubule filament. (B) Polymerisation and depolymerisation dynamics of microtubule polymer via hydrolysis of GTP bound tubulin heterodimer.* [40]

Owing to the possibility of both GTP and GDP bound nucleotide on the β tubulin, this side of the polymer is responsible for both polymerisation and depolymerisation process (Figure 2.2), also known as dynamic instability [39]. Shrinkage of microtubule filaments is achieved by depolymerisation of monomers from the polymeric form. When GTP-bound to the tubulin monomer at the filament end is hydrolysed, depolymerisation process begins. Therefore, the GTP-bound tubulin at the filament end behaves as a cap preventing the depolymerisation process. Alternating phases of such polymerisation-depolymerisation is known as dynamic instability [39]. The process of dynamic instability allows a cell to maintain the overall filament length and hence its structure. Therefore, in response to change in external conditions or internal signalling, cell can change its structure rapidly. The polarity of these filaments contributes towards directional movement of motor proteins such as dynein and kinesin which are responsible for organelle transport in a cell in addition to its role in chromosome segregation during mitosis.

2.3.2 Intermediate filaments:

Intermediate filaments are extremely thin structures with a typical diameter of ~10nm and length lesser than 1μm. One of the most diverse intermediate family filaments are keratins found in hair and nails - in addition to epithelial cells. Arrangement of intermediate filaments include follows both self-associated forms as well as crosslinking entity for accessory proteins. This cytoskeletal component forms a structural scaffold providing mechanical support to the inner face of nuclear envelope for protecting the cell's DNA and in the form of twisted cables holding epithelial sheets together. They are especially important in maintaining mechanical strength in the epithelial tissues [39].

2.3.3 Actin

Actin is the most abundant protein in cytosol, contributing to around 5-10% of the total protein in the cytoskeletal network. These cross-linked actin filaments play a crucial roles such as resisting cell deformation, force transmission, cell migration and reinforcing the plasma membrane via presence in the cell cortex [41]. These properties help cells to change their shapes, move through narrow spaces, divide and adapt to their environment. Actin is present inside cells in both globular (G) and filamentous forms (F) referred to as G-actin and F-actin respectively.

G-actin is the 'monomeric form' which assembles in dimers and trimers giving rise to double-helical arrangement referred to as F-actin which is the 'polymeric form' [39]. Binding of ATP to the G-actin facilitates the change in its monomeric structural conformation, allowing subsequent binding of the actin subunits. This monomeric conformational change forming a polymeric structure is involved in providing the actin filament its polarity. Binding of ATP bound G-actin to each other gives rise to trimers which is referred to the 'seed' that initiates polymer filament extension [39] (Figure 2.3; upper panel; actin filament nucleation). Hydrolysis of bound ATP during assembly, gives bi-products ADP and inorganic phosphate (P_i). Inorganic phosphate dissociates leaving behind core actin subunits with tightly bound ADP.

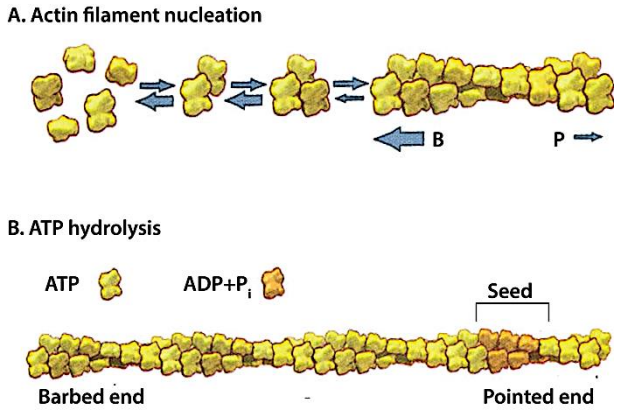

Figure 2.3: *Actin filament nucleation and growth via ATP hydrolysis.* [42]

The helical structures represented by actin filaments are in the form of a right-handed geometry with both ends structurally and dynamically different, assembling as polar polymers. The two dynamically distinct ends of the filament are referred to as (+) barbed end and (-) pointed end (Figure 2.2 lower panel, ATP hydrolysis). Barbed ends of the filaments are comparatively more dynamic than the pointed ends; elongating 10 times faster at a rate of $11.6\mu M^{-1}s^{-1}$ [43].

Polymerisation and depolymerisation of actin filaments contribute to efficient reorganisation of actin cytoskeleton [44]. Growth and shrinkage of actin filaments results from addition and loss of subunits from the polymer ends, a phenomenon known as *treadmilling*. Since both ends have different rates, the *polymer length* dynamics depends upon the available concentration of the monomeric pool of G-actin above the critical concentration reported to be 0.1µM at barbed ends and 0.6µM at pointed ends [45].

Apart from balanced polymerisation depolymerisation rates, filament length steady-state and bundling of these filaments occur through regulation of filament dynamics, and also by *actin-binding proteins*.

2.3.4 Actin binding proteins

Actin-binding proteins also known as ABP, facilitates maintenance of the actin network architecture, regulating assembly and dynamics of the actin cytoskeleton. More than 60 families of actin-binding proteins regulate the assembly and disassembly leading to dynamics of these proteins inside the cell cytoplasm. These accessory proteins fall into different categories such as polymerisation, depolymerisation/destabilizing and stabilizing/crosslinking, depending on their contribution [39].

Actin depolymerizing factor ADF/cofilin inhibits nucleotide exchange by binding and destabilizing ADP actin filaments. It does so by severing the polymer by binding on the side of ADP bound actin filaments. Another actin binding protein contributing in depolymerizing of filaments referred to as gelsolin severs the filament from the pointed end. This gives rise to the formation two by-products a new pointed end and a capped barbed end.

Polymerisation of filaments barbed ends is promoted by another ABP referred to as profilin which stimulates nucleotide exchange factor, recycling ADP bound monomers to ATP bound monomers in turn used for polymerization. The ABP profilin is present in abundance inside a cell, playing an important role in actin filament dynamics and homeostasis for *de novo* actin assembly [46]. Actin nucleation factors such as protein complex known as Wiskott-Aldrich syndrome (WASP), contribute to catalysing the formation of these new actin filaments by forming the ‘seed’ trimeric configuration leading to the polymer filament extension (2.3.3).

Cellular nucleation leads to rapid filament elongation at the free (+) barbed end, in turn preventing polymerisation at the (-) pointed end. This differential elongation rates, in the presence of ABP such as formin, provides polarity to the actin architecture [33]. Actin assembly takes place at the (+) barbed, while ‘formin’ binds to the barbed end facilitating elongation as well as crosslinking/ bundling. Arp2/3 complex interacts with the actin filament sides, leading to its branching.

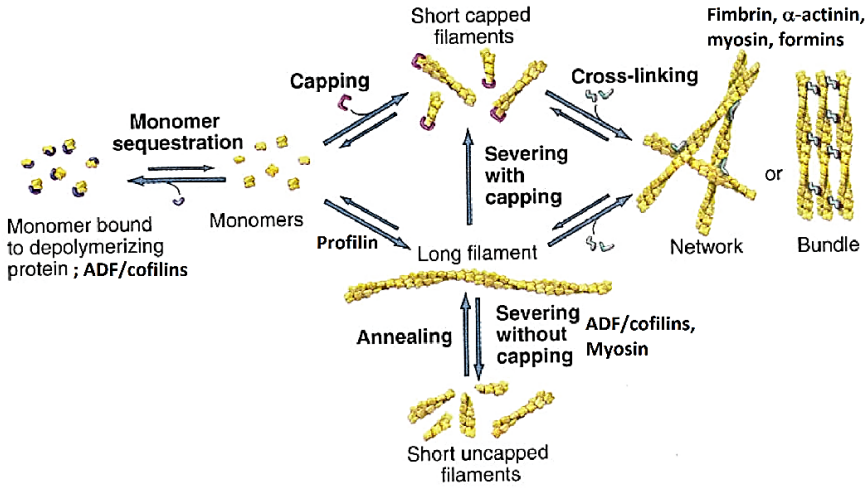

Figure 2.4: *Several actin-binding proteins involved as building blocks of actin filament regulation.* [42].

Actin filament stabilizing ABPs (for example, CapZ) binds to filament ends and prevents polymerisation. Actin filament stabilizing ABPs include α-actinin, filamin, fascin and fimbrin.

All these proteins work in coordination for regulating actin filament length, their bundling properties and therefore actin network architecture through interactions of ABPs such as formins, α-actinin, fimbrin, fascin as well as myosin II motor proteins (Figure 2.4).

2.3.5 Myosin and other motor proteins

Myosin proteins also known as *molecular motors* bind to the double helical polar (+)/(-) actin filament ends.

Molecular motors move along cytoskeletal filaments via energy derived from cycles of ATP hydrolysis [39]. There are different types of motor proteins which are primarily classified according to the type of cytoskeletal filament they bind to actin or microtubule, in addition to their 'cargo' transport properties and their directional movement towards a specific filament end.

They are classified into *microtubule-based* and *actin-based* motor proteins. Microtubule based motor proteins include kinesin and dynein. These proteins move along microtubules, transporting membrane enclosed organelles; 'cargo' such as Golgi complex, mitochondria and secretory vesicles from one location to another inside a cell. Among the microtubule-based

proteins, dyneins are pointed (-) end-directed while kinesins are primarily barbed (+) end-directed motor proteins [39].

Actin based motor proteins are identified under members of myosin superfamily. This superfamily of proteins has been reported to comprise more than 20 families interacting with actin filaments [47]. Myosin superfamily consists of a conserved head domain and a divergent tail domain. The divergent tail domain harbour the unique properties differentiating all super-families [48].

Adenosine triphosphate (ATP) is made up of adenosine molecule and three inorganic phosphates. Loss of one of the phosphates releases energy, used by the cell for its crucial reactions and in the process gives, adenosine diphosphate (ADP). Myosins move along the actin filaments directionally, using energy derived by adenosine triphosphate (ATP) hydrolysis (Figure 2.5; B). With the involvement of ATP, myosin proteins can generate spontaneous dynamics in actin filament network. The most widely studied myosin involved in different biological phenomenon is myosin II which moves directionally along the barbed (+) end of the actin filament.

Myosin II molecule structurally comprises two heavy chains and four light chains. Each heavy chain could be further characterized into a head domain and a tail domain [49] (Figure 2.5 A). The coiled tail domains are involved in dimerization of myosin molecules forming *thick filaments* (Figure 2.5; B) consisting of several hundred myosin heads which are oriented in opposite direction from one end to another forming a functional unit for interaction with numerous actin filaments. The neck region connects the head and tail domain, and consists of light chain domains, referred as essential light chain (ELC) and regulatory light chain (RLC). The phosphorylation of RLC is essential for myosin activity, leading to directional movement of the associated myosin heads towards the barbed (+) ends of actin filaments (Figure 2.5 B). This in turn leads to movement of actin filaments in opposite directions.
Functionally directional movement of myosin involves five steps [39], explained below for single head domain (Figure 2.5, B):

The movement of actin filaments with respect to myosin filaments, depends upon the instantaneous conformations of myosin heads.

1. At the beginning of the cycle, myosin heads are bound to the actin filaments due to their rigor conformation lacking the bound nucleotide (ATP).
2. Next, an ATP molecule binds to the cleft of myosin head, further from the side attached to the actin filament. This leads to change in conformation of the head domain with actin binding affinity. This altered conformation has lower affinity for the actin filaments and in turn releases the pre-existing filament attachment.

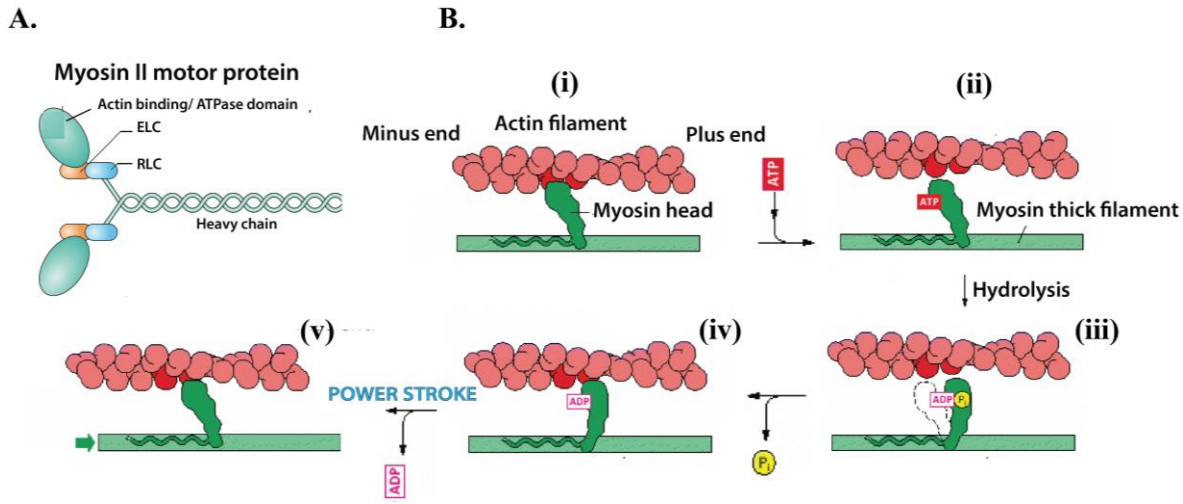

Figure 2.5: *A. Myosin II molecule showing globular head; actin binding domain with essential light chain (ELC) and regulatory light chain (RLC).* [49]. *B. Schematics representation of steps (explained in the text) of myosin activity via ATP hydrolysis, w.r.t to an actin filament.* [42].

3. The cleft closes due to the bound ATP molecule, leading to a strong conformational change. Such conformational change allows the myosin head to move ~5nm along the actin filament. This step concludes with completion of ATP hydrolysis releasing adenosine diphosphate (ADP) and inorganic phosphate (P_i). Inorganic phosphate molecule remains attached to the myosin head at the end of this step.
4. The inorganic phosphate is released after the myosin head has made (weak) attachment to another site on the filament in turn leading to the stronger interaction between them. This release triggers force generating conformational change of the myosin head. This process is referred to as the *power stroke*.
5. During the power stroke, myosin head regains its original conformation (Figure 2.5; B. step1) losing the attached ADP, in turn returning to the start of a new cycle, with myosin head tightly bound to a new position on the actin filament.

Myosin molecules crosslink with other myosin molecules by tail region and form myosin thick filaments. Actin monomers along the polar actin filament, do not bear any stoichiometric spatial correlation with myosin molecular spacing, in an interacting thick filament. Therefore, a directional motion of myosin filaments with respect to actin filaments, is selected by a symmetry breaking event. One such proposed mechanism explains the sliding of actin filaments, with respect myosin filaments, driven by fluctuations and Brownian motion. These fluctuations are associated with myosin heads, during their interaction to actin filaments. Hence, rather than stoichiometric travelling of myosin heads on actin filaments, the phenomenon involves a dynamic phase transition which characterises the behaviour of myosin motors in collection [50].

Myosins are other such directional movement of myosin motors, converts chemical energy (ATP) into mechanical movement. This controls motion of actin filaments leading towards stress generation in cytoskeletal filament networks. Basic interaction rules of actin and myosin II were well established by studying the muscle contraction unit [2][3][4]. Such configuration presented a simpler arrangement of organized filament network. Double globular headed myosin II is found to be processive, with an ability to travel longer distances on an actin filament without detachment.

This network is often referred to as *contractile* for the presence of myosin motor heads pulling on actin filaments via ATP hydrolysis, in turn sliding actin filaments in the opposite direction. This contractile system is also referred to as an active gel.

2.3.6 Active gels

The polymer network of *polar* actin filaments interacting with myosin motor proteins as a dynamic viscoelastic material is referred to as an active gel (Figure 2.6) [51][52][53]. Viscoelasticity is related to transient connections between the network fibres.

As mentioned in the earlier section 2.3.4, differential elongation rates via ABPs such as profilin and formin provides filament *polarity* to the actin architecture involving force generation during cell shape changes. Polarity of actin filaments contributes in distinct network architecture parallel and antiparallel filaments. *Parallel actin filaments* have (+) barbed ends pointing towards the same direction. Such structures are found in cell-based structures such as filopodia, mostly facing the cell membrane and contributing in cell migration [54].

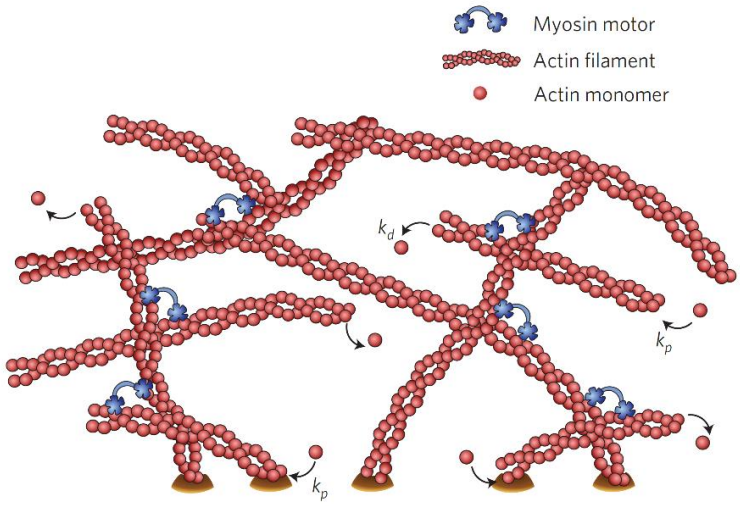

Figure 2.6: *A. Schematic of an active gel* [51], showing actin filaments assembled from actin monomer assembly and cross-linked by myosin motors, depicting polymerisation and depolymerisation (treadmilling) process via k_p and k_d respectively.

Antiparallel actin filaments are arranged with orientation of actin filaments in the opposite direction with respect to each other. This orientation is mainly found in contractile networks with actin and myosin. Tight packing of actin filaments via ABP (for example fimbrin) in pure parallel filaments, refers also to muscles or sarcomeric arrangement. This works in contrast to lose packing of pure antiparallel actin filaments resulting from ABP binding (for example, α-actinin) which allows myosin II to enter the bundle. Such configurations gives rise to *contractile acto-myosin* arrangement working in a collective manner in association with their protein environment [39]. Electron micrographs of this polar actin gel has been shown to involve large number of entangled filaments [55] crosslinked with proteins [56].

2.3.6.1 Mesoscopic description of the actin gel

Most cellular processes depend on the mechanical properties of the cytoskeleton [39]. For example, a cell rounding up before mitosis involves acto-myosin dynamics at the cortical layer, just below the plasma membrane. Apart from this, other cellular and subcellular phenomenon such as cell motility and cell adhesion respectively are clearly related to mechanical properties of the cytoskeleton. Quantitative description of the mechanical properties is necessary to describe these cellular processes.

Sub-cellular acto-myosin interactions are different from the macroscopic collective behaviours seen at a multi-cellular level [57], i.e. they do not add up simply. It is worth noting also that living matter works at ‘low Reynolds number’. Such situations are described with negligible

inertial forces, and dominant viscous forces [57]. This means that the force experienced by the network is purely determined by the exerted external force and not due to memory of any past force exerted. The Reynolds number is given by $R = av\rho/\eta$, where ρ denotes the density and η denotes the viscosity of the fluid. Velocity and length of the particle are given by v *and* a, respectively [58].

The surrounding medium of (acto-myosin) polar gel cannot be neglected while understanding the dynamics of the system. To do so, *hydrodynamic* approach has been used to address spontaneous generation of flow in these active gels coupled to motor proteins [53][59]. Hydrodynamic approach considers interactions following large length- and time-scales rather than individual filament interactions of the viscoelastic network depicting non-linear responses. This approach includes variables such as conserved quantities, system order and following dynamic relations between them [53]. For example, the active gel is in the presence of solvent and free monomers of actin and crosslinking proteins that constitute the system. These crosslinking proteins gives the network its viscoelastic nature. Hence this approach mainly depends on the symmetries, rather than microscopic components involved in this active gel such as structural polarity of actin filaments. So, by considering the inherent activity of the system with respect to structural polarity, filament treadmilling and directed ATP related motor activity can be explained. This in turn can illustrate the mechanics of the cytoskeleton.

Myosin II interaction with actin filaments fuelled by ATP hydrolysis generates internal stress inside the network. These stresses are involved in contraction of the actin meshwork, considered to be out-of-equilibrium due to constant energy (ATP) hydrolysis [53]. Hence, description of this active gel cannot rely on energy minimization based on thermodynamic approach [60]. To have a correct description for this active system, two approaches are followed; dynamic theory relying on local force balance equations of acto-myosin interactions, and coarse-graining of these phenomenon over larger length scales to determine the mechanical property of this active gel.

Actin network can generate significant forces together with polymerisation, depolymerisation and filament crosslinking alone, hence considered as semi-flexible polymers [60]. Elasticity of such semi-flexible network, is controlled by a parameter referred to as *mesh size,* ξ . This represents mesh size of the branched actin filament network. This property is controlled by the available pool of monomeric actin and capping proteins, together with availability of

crosslinking proteins such as Arp2/3 complex. Higher network density by change in filament length L_p, considerably increases the stiffness of the mesh by decreasing the mesh size. This affects the *elastic modulus (E)* of the network, given by $E = kTL_p/\xi^4$. 'k' represents the Boltzmann constant and temperature is denoted by T.

2.3.6.2 Active gel theory

Configuration of actin monomer binding and effective actin filament treadmilling by ATP hydrolysis provide to the network its polar architecture. This actin filament polarity is denoted as barbed (+) and pointed (-). Filament polarity allows the myosin motor proteins, to move in a directional manner on these actin filaments. Myosin II moves towards the (+) barbed end of the filament. This directional movement of myosin heads towards the barbed filament end is initiated and maintained by constant cycles of ATP hydrolysis. This facilitates constant interaction of actin and myosin filaments (Section 2.3.5, Figure 2.6). These acto-myosin network also referred to as *active gel* contributes in various cellular structures such as cell cortex, cytokinetic ring, stress fibres, filopodia and lamellipodia action. In an acto-myosin cytoskeleton, actin filaments undergo treadmilling to form a viscoelastic gel by ATP hydrolysis and interaction with myosin motors. Given the polarity in these filaments, acto-myosin cytoskeleton can be considered as a polar gel with interacting crosslinking proteins. Depending on the crosslinking time, the property of the active gel varies over time [60].

At short time scales, this active gel behaves as a viscoelastic material with an elastic modulus of 10^3-10^4 Pa [61], in contrast to longer time scales, where it behaves as gel with flow property of finite viscosity η. This viscosity is described by Maxwell relation associated with the elastic modulus E and the relaxation time τ, given as $\eta = E\tau$ [60].

At longer length and time scales, the system requires macroscopic variables such as stress (σ) and the velocity gradient (μ). Stress exhibited by a liquid is given by $\sigma = 2\eta\mu$ where η is the viscosity described by Maxwell relation (explained in the previous paragraph). Based on the material properties of the active gel (actin and myosin) and for larger length and time scales, the behaviour of the polymer gel was described using hydrodynamic theory (explained under mesoscopic description) [53]. As mentioned earlier, there exists a polarity in this network and therefore consideration of both flow properties as well as polarization dynamics are to be taken into account [60]. To consider the fluxes of ATP consumption rate, free energy $\Delta\mu$ is

considered. Energy consumption is given by the difference between hydrolysed ADP and non-hydrolysed ATP states; $\Delta\mu = \mu ATP - \mu ADP - \mu P_i$, where increase in ATP concentration leads to increase in available free energy and vice versa. This free energy works as the driving force for the active process of cytoskeletal reorganization.

Therefore, active stress in the system (σ) is given by $\sigma = 2\eta\,\mu + \nu\,h - \zeta\Delta\mu$ where it describes linear dependency on velocity gradient (μ), viscosity of the active gel denoted by η, free energy change ($\Delta\mu$). Filament polarization term is included with the help of their filament orientational field (h) and the coefficient (ν) obtained from linear hydrodynamic equations. Stress within the active gel also has linear dependency on activity, denoted by $\zeta\Delta\mu$, where ζ indicates the myosin activity to the corresponding viscous material property of the active gel. This property also incorporates the motor activity and energy consumption during the treadmilling of filaments.

2.4 Acto-myosin

Interaction of cytoskeletal filaments, actin and myosin and their presence in the form of a network is referred to as acto-myosin complex. In the process of embryonic development, epithelial tissues undergo extensive remodelling. This remodelling is orchestrated by cell shape transformations and mediated by self-organisation of acto-myosin cytoskeleton. Apart from playing an indispensable role in embryo morphogenesis, interaction among this dense protein network determines cell shape and its resistance to deformation. This leads to stabilisation of the tissues composed by these cells. Even after extensive remodelling and stabilisation, cells and tissues faithfully maintain their polarised network architecture. This network is notably referred to as an active gel (Section 2.3.6.) The reason for such a reference is because this network is primarily composed of polar acto-myosin filaments behaving as a dynamic viscoelastic material maintained in a non-equilibrium state.

Contractile property of the network enables force generation at subcellular levels such as cytokinetic ring during cell division [5].

Majority of the force-driven processes in the cells and tissues have an active involvement of acto-myosin cytoskeleton. Assembly and regulation of this widespread cytoskeletal network poses an important question, as how this network self-organises into different architecture such as hotspots, rings, cables, meshwork etc. It is interesting to study how these network

architectures are regulated, to assemble and/or disassemble at specific place and time, inside cells and tissues.

Acto-myosin network might differ in their localization, supporting components, organisation and connections with cellular structures, whilst maintaining its core components i.e. actin and non-muscle myosin II. This network is capable of generating contractile forces in by interactions between these core components. Forces generated by this interaction play a critical role in dynamics at subcellular, cellular and tissue levels. These contractile assemblies are involved in subcellular dynamics such as retraction of plasma membrane blebs and clathrin-mediated endocytosis. Contributions of the acto-myosin network at the cellular and tissue level include cortical symmetry breaking, cytokinesis, cell migration and gastrulation, germ band extension, respectively to name a few phenomena.

Architecture of the acto-myosin network is a key determinant in its function. Polymerisation, turnover and crosslinking of actin filaments in addition to contractility driven self-organisation through localised myosin activation are the key factors contributing in building and maintaining the acto-myosin architecture. Apart from the *network architecture*, specific localization of *Rho GTPase regulators* and its close association with *adherens junctions* are key components of acto-myosin network. All these factors determine the spatiotemporal regulation of these networks at cell and tissue levels. These concepts are further described in the following sections.

2.4.1 Acto-myosin architecture

Interactions of actin and myosin-II filaments combine to form different architectures of acto-myosin complex. This complex is inherently contractile given the presence of myosin motors and its interaction with actin filaments.

We use muscles every day to do several different activities from breathing, blood circulation to moving around our body. Smooth muscle and cardiac muscle cells are under involuntary control, as opposed to skeletal muscles which fall under voluntary control. These skeletal muscles are composed of many myofibrils which in turn forms the contractile units known as sarcomere. This sarcomeric arrangement contains periodic arrangement of actin and myosin

filament which run adjacent to each other along the length of a myofibril. They contract or relax by stimulus from the nervous system which is translated in the form of calcium ions.

Basic interaction rules for actin and myosin was established seven decades ago, by describing it in a muscle contractile unit or sarcomere [2][3][4]. These contractile units consist of alternating myosin thick filament and actin think filament proteins (Figure 2.7). Muscles contract when these filaments slide past each other. Myosins motor proteins move along the actin filaments through ATP hydrolysis (Section 2.3.5, Figure 2.5). Most myosins are monomeric and hence poorly processive and hence exhibiting little activity.

Although, once assembled in bipolar filaments these myosins pull on actin filaments, walking towards the plus end of the polar actin filament (Section 2.3.3).

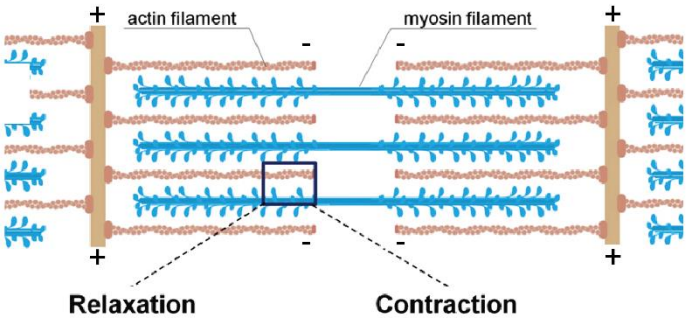

Figure 2.7: *A. Schematic of a sarcomeric contraction unit where contraction and relaxation cycles are achieved by relative movement of actin and myosin filaments.* [62]

In this configuration, both filament types (actin and myosin) are anchored, hence providing them a highly arranged periodic organization. Myosin thick filaments are anchored at the centre, known as *M line* and actin filaments are anchored at their plus ends known as the *Z line*.

Bundles of these acto-myosin structures are also present in non-muscle cells contributing in different biological processes, such cell division and embryonic development (described later). Arrangement of actin filaments and myosin-II motors in non-muscle cells, rarely shows periodic arrangements. Hence, relative orientation of actin and myosin-II filaments with respect to each other dominates the outcome of the dynamic interactions of this acto-myosin network.

Since actin monomers polymerize into polar filaments, two distinct filament ends referred to as, plus (+) and minus (-) end are generated. Arrangement of filaments with similar (+/+, -/-)

and/or opposite (+/-) orientation coming together is referred to as, parallel and/or anti-parallel filaments respectively. Acto-myosin networks lacking sarcomeric structure, have been shown to contract, *in vitro* [63] as well as *in vivo*.

In theory, depending on the relative filament position, myosin motor induced sliding of filaments can either general contractile, or extensile forces. Contractile forces will lead to shortening of the filament pair. As such, extensile forces are never observed, which could be an outcome of filament buckling or bending [64]. Although in simulation, extensile forces will result in filament pair lengthening.

Such activity can be described with a simple configuration of an actin filament pair. Sliding of this filament pair with respect to a monomeric myosin molecule would be achieved by their interaction. Outcome for such configuration will result in stress generated through balance of motor forces, in addition to frictional forces over the entire length of actin filaments. These forces are applied through 'power stroke', at the position where the myosin motor head binds to actin filament. The combined stress profiles $\boldsymbol{\sigma}$ exerted on both filaments, averaged and displayed as a function of their position **x**, shows contractile, extensile or stable filament dynamics (Figure 2.8).

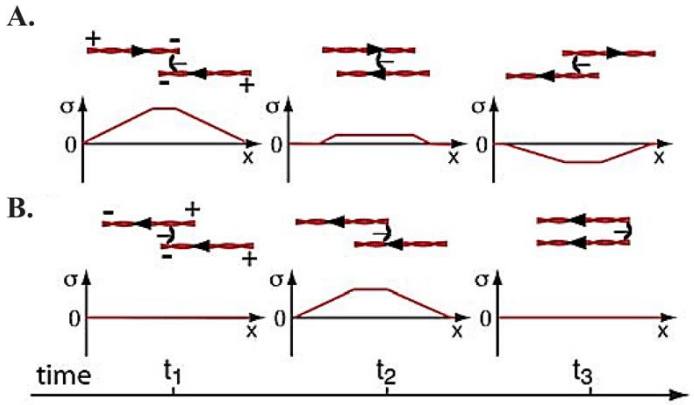

Figure 2.8: *A. Stress profiles in actin and myosin interacting in different filament arrangements, followed through time*. [17]

By averaging the stress values, contraction results from shifting of the centre of mass while filaments sliding towards each other. This leads to positive or contractile stress on an average. Stress profiles followed through time in parallel and anti-parallel filaments, can be studied in three different stages. In parallel filaments, myosin-II monomer walks towards the positive filament end, in turn sliding both actin filaments with respect to each other. This leads to high stress and hence, contraction (Figure 2.8, B, Left). In the second and third stage, movement of filaments with respect to each other leads to lesser stress and finally negative stress

corresponding to relaxation and/or lengthening respectively (Figure 2.8, B middle and right). Similarly, within parallel filaments, stress followed through time can be described with contraction or steady states (Figure 2.8 A). These states are again a consequence of myosin-II position with respect to the actin filament end. Hence, interactions of these filaments with respect to each other through myosin filament position and their processivity, can describe the overall outcome of an acto-myosin bundle.

As explained earlier, acto-myosin arrangement in muscle cells is very periodic. This is in contrast with arrangements found in non-muscle cells, where they are more versatile. These arrangements include bundles which are observed in the form of linear filament bundles or in the form of rings. In both these cases, the arrangement of filaments can be either parallel or anti-parallel arrangement, with respect to each other. Since these filaments do not have any periodic anchorage like in muscle cells, it is given that these filaments have to be arranged in a stochastic manner. This stochasticity is presented with respect to the actin filament orientation throughout the acto-myosin bundle (Figure 2.9, A)

Taking into consideration the stochasticity of filament orientations as well as myosin head positions, it is challenging to decipher the outcome of such a structure (Figure 2.9).

In order to explain this dynamic system, a possible mechanism based on relative sliding of polar actin filaments of opposite orientations with respect to myosin motors, was proposed couple of decades ago [1].

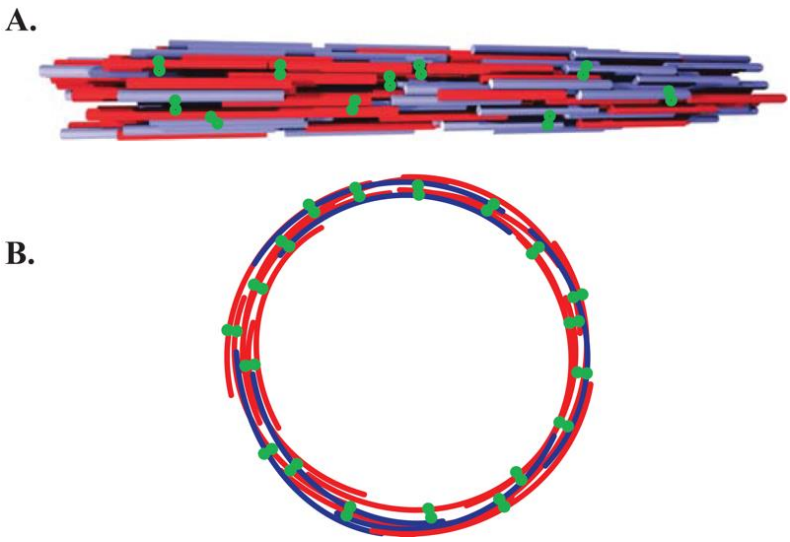

Figure 2.9: *Schematics depicting stochastic actin and myosin filament arrangement with plus ends to the left indicated by red, and to the right indicated by blue. Myosin in green, showing A. acto-myosin bundle* [17] *and B. acto-myosin ring.*

These interactions were described to be responsible for stress generation in a contractile ring. Although, considering the stochasticity of filament arrangement in an acto-myosin ring, average forces on filaments should be cancelled out (Figure 2.9, B).

In this scenario, net stress generated during the process should add up to be zero. This would lead to a stable, rather than contracting ring dynamics observed during e.g. *cytokinesis*. Cytokinetic acto-myosin rings amongst other rings found in nature, are always seen to be under constant contraction [5]. Therefore, to achieve such scenario, acto-myosin network needs to overcome the stochasticity. This is shown to be achieved in various acto-myosin networks across systems, with the help of self-organised myosin structures referred to as *clusters*.

2.4.2 Building and maintenance of acto-myosin architecture

Key steps in formation and maintenance of these distinct acto-myosin architectures are based on interactions and dynamics within actin filaments. These include, polymerisation, turnover and connectivity. Since actin proteins work closely with myosins, self-organisation of these motor proteins within the actin cytoskeleton is another factor that determines the acto-myosin architecture. Considering all the previously mentioned factors, in addition to acto-myosin anchorage by junctional proteins, altogether determines the final outcome of the acto-myosin contraction.

Actin turnover is another factor that contributes towards the architecture of acto-myosin complex and therefore contractility. As compared to muscle architecture where the filaments are known to be very stable, non-muscle acto-myosin architecture is known to be highly dynamic. This includes continuous polymerisation as well as depolymerisation of the filaments also known as turnover. Turnover of filamentous actin by depolymerising factors, such as cofilin, plays a major role towards regulation of acto-myosin contractility.

Actin polymerisation imparting filaments with their polar conformation, is catalysed by nucleation as well as elongation factors. Architecture of the filaments formed often depends on the type of nucleation factor involved. For example, linear arrays of actin filaments are formed facilitated by formins or VASP proteins, and Arp2/3 complex. Formins are responsible for actin polymerization in general, and Arp2/3 complex facilitates formation of branched actin networks [65]. These nucleation factors are known to work independently as well as in cooperation with multiple actin assembly nucleation factors. Therefore, these nucleating factors contribute in

actin architecture and therefore in acto-myosin contractility. Continuous actin polymerisation would lead to stiffer networks. Stiffer networks are needed when the system has to withstand a compression or stretch, as loosely organised networks will be reorganised due to the applied forces. However highly stiff networks will lead to stuck networks and incapable of contractions or reorganizations, necessary for cellular dynamics. For example, stabilising actin filaments with cell permeable jasplakinolide, has been shown to halt acto-myosin contractility in epithelial cells by increasing actin polymerisation [66].

Mechanical forces generated through this contractile network architectures alone cannot result in cellular behaviours [48]. This echoes with the fact that cell cytoskeleton has an active interaction with its surrounding, through cell adhesion complexes at the plasma membrane. These complexes which contain mechanosensitive properties help the cell to regulate its dynamics through cytoskeletal remodelling.

2.4.3 Acto-myosin network and adherens junctions

Acto-myosin network has connections to cell membrane and nucleus, in addition to connections with the neighbouring cells and also the cell environment. These adherens junctions provide the means to sense the external environment of the cells and tissues, in turn remodelling the acto-myosin network. Hence, they act as mechanosensors as well as force transmitters. These protein complexes are primarily classified into *cadherins* and *integrins.* These both are transmembrane protein complexes with its regulators and filament binding ability at the intra-cellular sites. Cadherins and integrins act as mechanosensors and regulators of cell-cell and cell-ECM mediated interactions respectively.

Cadherins are transmembrane cell-cell junction proteins. Cadherins fall under the category of calcium dependent cell adhesion molecules which modulate tissue specific cell-cell adhesion seen in early vertebrate tissues [39].

E-cadherin is best characterized amongst different types of classical cadherins. Apart from being found concentrated in adherens junctions of epithelial cells, it is also known for its role during mammalian developmental steps. Cytoplasmic tail of the cadherin molecule binds to a family of anchor protein complex called *catenins.* Amongst this protein family, *β catenins* help in linking cadherins to the actin cytoskeleton. The interaction of E-cadherin to the actin

cytoskeleton is essential for efficient cell-cell contacts holding the cells together in a multi-cellular tissue environment.

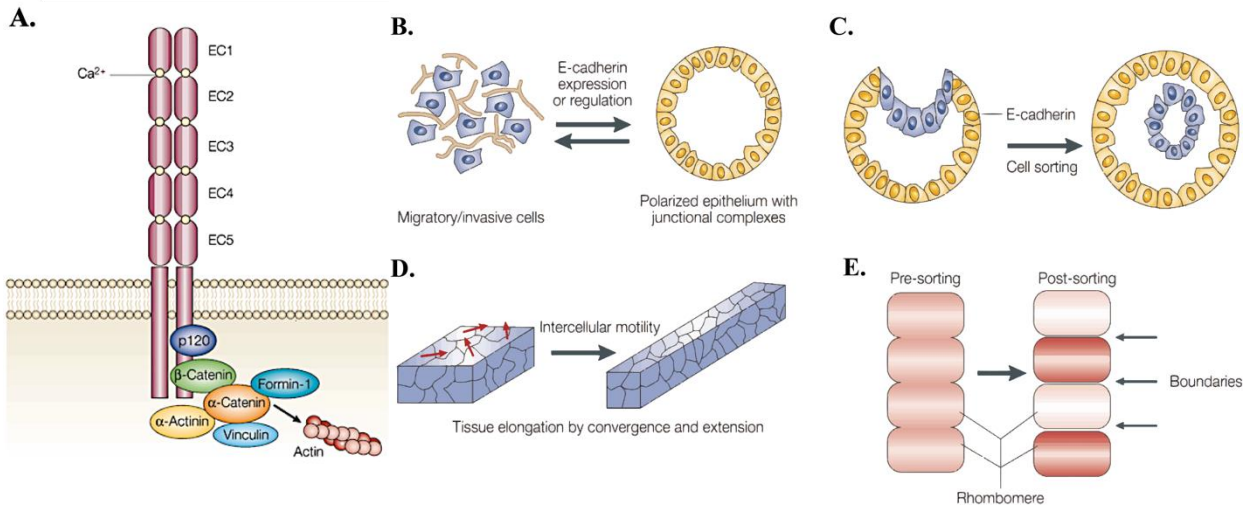

Figure 2.10: Cadherins and their effectors*: Schematic representation of (A) cadherin protein complex and its organisation for cytoskeletal association. (B) Involvement of this complex in tissue morphogenesis such as the epithelial-mesenchymal (EMT) transition. (C) Cell sorting due to differential expression of cadherin in cells during embryonic development, (D) cell rearrangements driven tissue morphogenesis and (E) selective adhesion strengths leading to compartmentalisation in tissues during vertebrate hind brain development.* [67]

Regulation of cadherin expression by catenins plays a key role in several developmental processes such as epithelial to mesenchymal (EMT) transition, cell sorting, tissue compartmentalisation and rearrangements, during embryo morphogenesis (Figure 2.10) [67].

Adhesion complexes have been demonstrated to promote efficient force transmission within epithelial cells, in *Drosophila* dorsal closure. It was shown that disruption of cell-ECM adhesion affected cell, and in turn tissue deformations. This led to impeded dorsal closure in *Drosophila* with apical force transmission and inversely correlated with basal adhesion [68]. Apart from *cadherins, integrins* also mediate anchorage to the ECM, providing constrains to the tissue shape. Cell-substrate interations through extra-cellular matrix proteins not only facilitates processes such as cell migration and cell extrusions, but also facilitates active ECM remodelling during various morphogenetic events in the developing embryos [68][69].

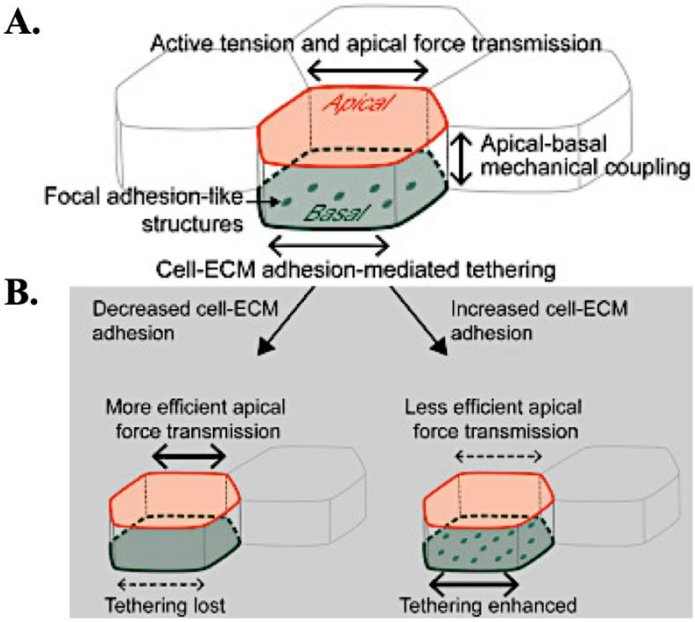

Figure 2.11: *Schematic representation of cell-ECM adhesion mediated tissue morphogenesis in Drosophila, where A. represents normal morphogenesis and B. represents disrupted morphogenesis due to increased or decreased cell-ECM adhesion* [68]

Anchoring points of cell-cell and cell-matrix adhesion sites provide force transmission between cells and tissues. Apart from this, these adhesion sites also actively regulate acto-myosin contractility. Cell-ECM adhesion complexes are involved in acto-myosin contractility, through cortical acto-myosin and its interaction, driving the formation of *Drosophila* tracheal tube actin rings (Figure 2.11). There also exists instances where these adhesions play an antagonistic role towards acto-myosin contractility. It was reported that excess of E-cadherin at the embryonic wounds prevents accumulation of acto-myosin assembly at the wound edge. This led to delayed wound healing, in contrast to eliminating E-cadherin from the wound site, which led to myosin-II recruitment crucial for the wound closure [70]. Such mutual exclusiveness among myosin-II and E-cadherin has also been observed in *C. elegans* embryo, where E-cadherin knockdown led to increased cortical myosin-II [71] .

Regulation of myosin-II and consequently Rho levels have also been reported, during basal cell contractions driving *Drosophila* egg chamber elongation [72], apart from correlations between myosin recruitment and RhoA activity levels during *Xenopus egg development.*

2.4.4 Regulation of acto-myosin contraction by Rho GTPases

Apart from adherens protein complexes, cells have another set of machinery to regulate the acto-myosin network architecture, in turn increasing or decreasing its contractility. This includes a set of membrane associated regulators which can tightly control and modulate the

acto-myosin network architecture both spatially as well as temporally. These membrane-associated regulators of acto-myosin contractility, are controlled by small GTPases Rho, involved in signalling pathway referred to as *Rho signalling pathway*.

A cell senses its environment not only by external stimuli such as cell-ECM interactions (2.4.3), but also by soluble cell-signalling molecules, such as growth factors and cytokines. These soluble factors have been studied to be highly efficient, for example in recruiting macrophages and neutrophils at the site of a tissue injury. This recruitment is known to be highly efficient, both spatially and temporally at a timescale of couple of seconds. Similarly, in response to soluble factors acting as external stimuli, these signals can regulate actin cytoskeleton at specific sites inside a cell and tissue, through Rho proteins [30].

Rho belongs to the *Ras* superfamily of small GTPases. These are monomeric signalling G proteins function as molecular switches. These G proteins are therefore responsible for turning "on" and "off" the signal transduction pathway modulating the acto-myosin cytoskeleton in response to chemical and/or mechanical stimuli (Figure 2.12). Being a key regulator of acto-myosin re-organisation, Rho-GTPases play an important role in cellular dynamics such as cytokinesis, cell polarity, cell adhesion and cell migration [73] [74].

Amongst 20 identified members of this superfamily, Rho, Rac and Cdc42 are key regulators of cytoskeletal re-organisation. Amongst these, Rho-GTPases are found to be highly conserved, throughout all the studied eukaryotic organisms.

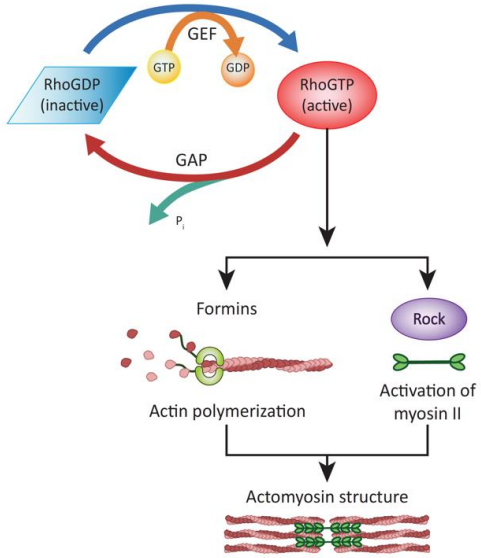

Figure 2.12: Schematic representation of Rho signalling pathway *leading towards regulation of acto-myosin contractility* [72]. *Explained in the text.*

Regulation of Rho-GTPases plays a key role in multi-cellular environmental processes, such as tissue remodelling and wound closure during embryonic development. Interplay between Rho-GTPases through its upstream regulators and downstream effectors modulate cytoskeletal re-organisation.
Rho GTPases have several different targets, regulating multiple signal transduction pathways and consequently contributing towards diverse cellular functions [75]. Two major effectors of Rho, contributing in contractility of acto-myosin have been identified as *formins* such as mDia and *Rho-associated protein kinase (ROCK).*

Activation of Rho-GTPases cycles between an inactive GDP-bound form to an active GTP-bound form and is regulated by Rho-GEFs (Guanine nucleotide exchange factors) exchanging GDP to GTP and Rho-GAPs (GTPase activating proteins) (Figure 2.12). Distinct localisation of these regulators GEFs and GAPs within a tissue can regulate the otherwise inefficient Rho-GTPase enzyme [76]. GEFs are known to be activators and GAPs as inhibitors of Rho-GTPases. This Rho signalling pathway can subsequently modulate the acto-myosin reorganisations at those particular locations, leading to a specific biological output. They do so by being targeted to the cell membrane, stabilized thereby its lipid moiety. In addition to these two regulatory proteins, guanine nucleotide dissociation inhibitors (GDIs) and GDI displacement factor (GDF) are also essential regulators of Rho-GTPases. While GDIs sequester Rho-GTPases from the cell membrane through masking its lipid moiety, GDFs bind to the inactive form and prevents its further activity. Masking the lipid extensions of GTP-bound Rho subsequently facilitates cytoplasmic solubility of the GTPases [76]. An activated form of this GTPase when bound to the cell membrane can interact further with its downstream pathway effectors. These interactions in turn leads to re-organisation of acto-myosin cytoskeleton.

Active form of Rho-GTP binds to formins, and Rho-associated protein kinase (ROCK). Through binding to Rho-GTP to formins, it regulates actin polymerisation. Activating ROCK through Rho-GTP, consequently activates myosin-II regulatory light chain (MRLC), by elevating its phosphorylation. This activation contributes towards assembly and contractility of acto-myosin structures [76].

Organisation and contractile activities of myosin-II filaments are regulated by phosphorylation-dephosphorylation cycles, occurring at the regulatory portion of myosin-II light chain.

Assembly and activity of Myosin-II filaments leading to acto-myosin contractility is regulated by dynamic phosphorylation-dephosphorylation cycles. Phosphorylation of myosin light chain 2 (MLC2) is a critical step which takes place primarily at highly conserved residues of Thr18 and Ser19 residues, activating Myosin-II. This process is regulated by calcium-calmodulin pathway. Upstream to calcium-calmodulin activity, ROCK also regulates MLC2 phosphorylation by inhibiting MLC phosphatase, therefore maintaining MLC in an active phosphorylated form.

Therefore, Rho-GTPases regulate acto-myosin contractility by regulating both, actin polymerization by formins and/or by regulation at the level of myosin light chain kinase (MLCK) and ROCK.

Acto-myosin contractile rings has been studied in varies biological processes from single to multi-cellular levels, spanning from cytokinesis, wound closure to complex developmental processes involving tissue rearrangements and folding [72]. Subsequent studies regarding Rho-GTPases in these processes has revealed that that regulation of these 'G' proteins, directs acto-myosin response during wound healing.

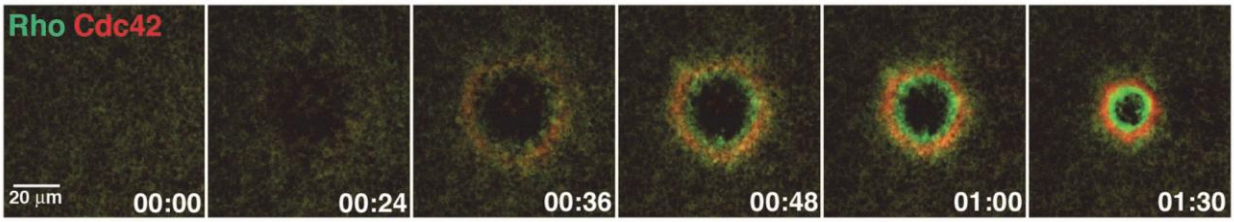

Figure 2.13: Schematic representation of GTPase response to a single cell wound. *Time course showing individual frames (Z projected) following active Rho (green) and active Cdc42 (red) during Xenopus oocyte wound response. Time in mm:ss* [20]

One such study focused on spacial and temporal localization of active Rho, in single cell wound models of *Xenopus* oocytes. Wounds induced by laser cutting inflicted in these embryos showed activation of both Rho and CDC42, with a tight temporal control of a 20s post laser exposure [20]. Initially the local activation of Rho and CDC42 was seen to be homogeneous and overlapping with each other spatially. This was followed by a clear segregation of the two zones in a concentric manner (Figure 2.13).

It was proposed in this study that concentration of Rho activity on the interior of the concentric circle of active zone ensures MLC phosphorylation and hence Myosin-II mediated contraction of the wound ring. Conversely the outer zone of active Cdc42 activity directs the actin assembly/disassembly in that region. Epithelial wound edges are known to accumulate acto-

myosin network in the process of re-epithelialisation. This network, being contractile in nature, has been demonstrated to induce mechanical forces therefore closing the wounds. The fact that these concentric zones of activated regions preceded the onset of actin accumulation, indicated recruitment of myosin-II by Rho-GTPases.

Studying occurrence of these Rho active regions in single cells also showed zones of high Rho activation at the contractile cytokinetic ring. Activation/inactivation cycles of Rho-GTPases through its regulators GEFs and GAPs was observed to be restricted to the equatorial plane of the dividing cell. This restriction prevented the movement of Rho-GTPases outside the equatorial zone, confining the region of Rho signalling [77]. Rho activation dynamics was observed to be coinciding with myosin-II accumulation. Another study depicting the correlation between Rho activity and myosin-II made use of optogenetics, where light mediated control of Rho activity was observed in non-contractile anaphase HeLa cells [12]. This induced Rho activation of mid-anaphase cells was shown to induce furrow and contractile ring formation at the midzone similar to cells at beginning of the telophase.

Study pertaining to myosin recruitment via activated Rho, was performed during early cell cycle stage in *C. elegans* embryo [7]. Previously, chiral myosin cortical dynamics was reported during first cleavage, suggesting an intrinsic chirality in the system [78]. In the current study under description, pulsatile myosin-II foci were observed throughout the early cell cycle stage embryo [7]. Flows in these pulsatile cortical myosin foci depicted chiral symmetry breaking, with anterior and posterior parts counter-rotating relative to each other. Interestingly, assessment of active RhoA also depicted foci-like arrangement in these early stage embryos. It was shown that both foci co-localised spatio-temporally, relative to each other (Figure 2.14).

Analysis of this study revealed an active RhoA mediated recruitment of myosin to these pulsatile foci, important in breaking the left-right symmetry. This analysis was supported by inhibiting RhoA early on in the embryos, revealing homogenization of the myosin-II foci rendering them non-pulsatile.

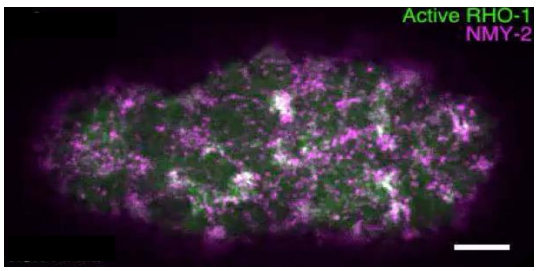

Figure 2.14: Active RhoA and myosin co-localization *seen in a single plane of early C. elegans embryo. Scale bar 5µm* [7]

As described earlier, Rho-kinase regulates myosin light chain (MLC), dynamics of which is key in the process of wound closure. To test the spatio-temporal localisation of Rho-kinase and myosin light chain in MDCK epithelial cell monolayer, wounds were created by laser ablating this epithelial cell monolayer. Accumulation of MLC was shown (Figure 2.15, in red) at the wound edge, with simultaneous accumulation of Rho-kinase (Figure 2.15, green). Although accumulation of Rho-kinase was observed to be apico-lateral as compared to baso-lateral accumulation of MLC.

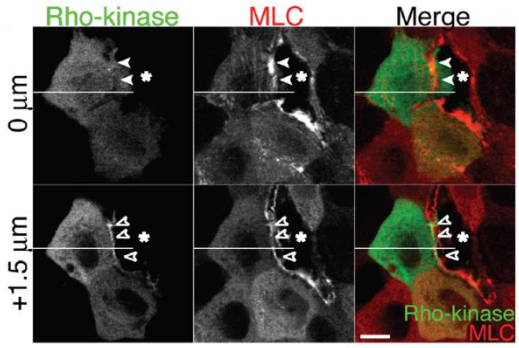

Figure 2.15: Accumulation of Rho-kinase at epithelial cell wound edge *was observed to be comparatively apico-lateral (GFP), compared to baso-lateral colocalization of myosin light chain (RFP), at the wound edge. Scale bar 10µm* [15]

In this case, Rho-kinase was seen to colocalise as well as move with the acto-myosin ring during the wound closure. This indicates the essential role played by Rho-kinase during the contractile activity of this acto-myosin ring around the wound edge. These observations correlated with concentric active zones of Rho, observed around wound closure in *Xenopus* oocytes [20].

2.4.5 Regulation of acto-myosin contractility by mechanotransduction

Mechanotransduction is a step-wise process which converts mechanical stimuli into chemical and hence biological output, regulating cell behaviour and its function. This is made possible due to the cell mechanosensors interacting closely with its environment, providing the cell with its external stimuli. It is a key regulator in cell morphology during development, coupling and transforming external transient mechanical stimuli into reorganization of the cytoskeleton [72]. Such mechanical stimuli include substrate rigidity and/or cell stretching leading to cell shape changes. This is made possible through signals transmitted via integrin molecules to the cell cytoskeleton. This in turn leads to emergence of chemical and mechanical signals, regulating cell behaviour and function [79].

A long time known micro-environment factor sensed by a cell regulating its dynamics, has been identified as cytokines. Apart from such soluble chemical factors, dynamic interaction between the cell-cell, cell-extracellular matrix (ECM) is also sensed by the cells by forces applied ‘by’

and ‘to’ them. These factors therefore act as mechanosensors, responsive to counterforces from matrices as well as other neighbouring cells [72]. Similar mechanosensors can have various effects on cells, persisting in environments with different cell-surface adhesions, and therefore differences in mechanical properties of the cell.

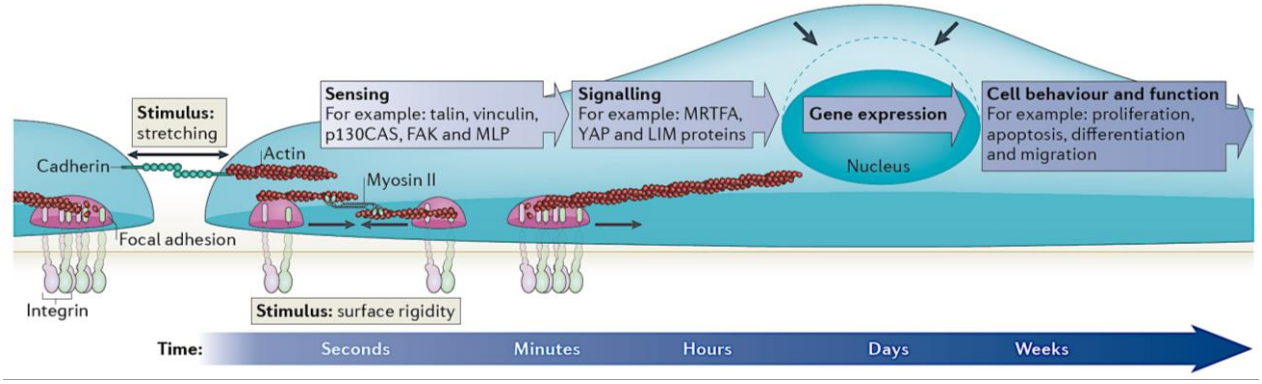

Figure 2.16: Key mechanosensors and their interacting partners: *Cell-cell and cell-matrix interactions are regulated in response to mechanical stimuli, in the short duration of seconds to longer time period of days through various mechanosensors.* [79]

Two decades ago, rapid strengthening of the cytoskeleton was observed, by applying force to the cells through integrin coated beads [80]. Recent advances in the field has established that, forces generated over larger distances are the key elements, for downstream signalling through cadherins and integrins (Figure 2.16). Forces sensed by these cell-cell and cell-matrix mechanosensors, in turn reorganizes the acto-myosin cytoskeleton within seconds or minutes. Downstream effects of these force sensing mechanisms, not only affect cellular processes such as cell migration but also sub-cellular gene expression, in turn leading to cell shape dynamics (Figure 2.16).

Tissue rearrangements in developing embryos are known to involve mechanosensors such as cadherins and their targets, acto-myosin cytoskeleton. Time frame for these rearrangements span from tens of minutes to couple of hours. Reorganisation of acto-myosin cytoskeleton is central in short- and long-term tissue reorganizations, during development of an organism. Myosin motors are responsible for this rearrangement by exerting forces on actin filaments in an acto-myosin network. The acto-myosin cytoskeleton is anchored to the cell-cell or cell-matrix adhesion by cadherins and integrins respectively. Therefore, cellular tension by acto-myosin contractility, is transmitted through these junctional proteins behaving as mechanosensors. These mechanosensors enable force generation at tissue scales, regulating cell and organ shapes.

Acto-myosin contractility and its interaction with cadherins have been reported to play key role during tissue rearrangements in developing embryos. These tissue rearrangements utilise pulling forces, which can either elongate, stabilise or fracture the system. During tissue rearrangements in developing embryos, acto-myosin driven contraction of one region containing cells, often stretches the neighbouring tissues. These local contractions have been studied to be driven by 'induced' acto-myosin activity.

Acto-myosin feedback mechanisms have been studied regulated by cell-cell adhesions during the first steps. One such example is studied in epithelial cells of *Drosophila* during its development. Pulling force generated by ingressing acto-myosin ring of a dividing cell, leads to myosin-II accumulation at the adjacent cells edge [81] (Figure 2.17).

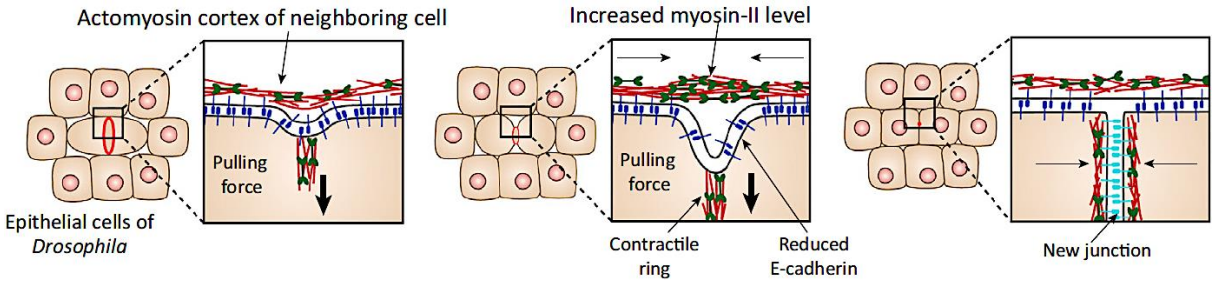

Figure 2.17: Schematic representation of positive (myosin recruitment) mechanical feedback: *Pulling force (black arrow) generated by cytokinetic acto-myosin ring, leading E-cadherin (dark blue) dilution at the previous cell-cell junction. This promotes junctional remodelling and formation of new junctions (cyan) between divided and neighbouring cells* [72]**.**

In response to the pulling force, dilution of E-cadherin promotes junctional remodelling, and therefore formation of new junctions between divided and the neighbouring cells (Figure 2.17). This describes a positive feedback regulation, ensuring a persistent signal, and therefore a self-sustained evolution of the system.

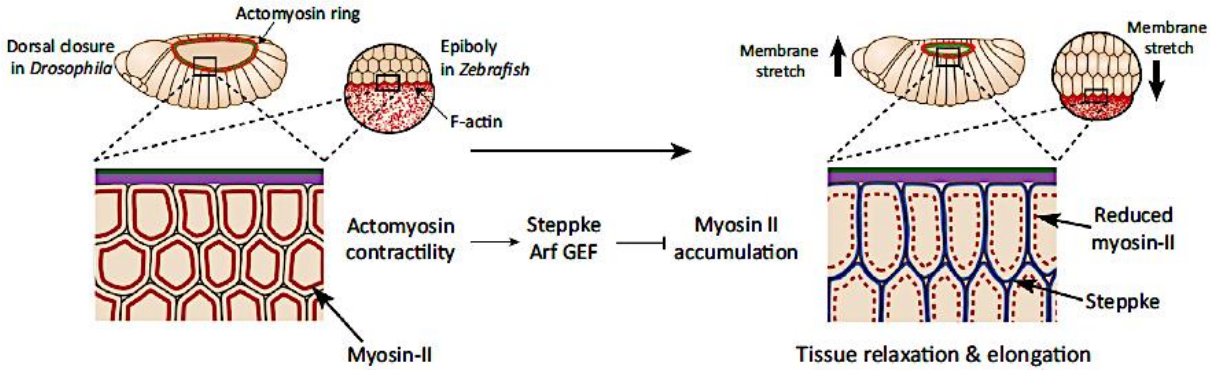

Figure 2.18: Schematic representation of negative (myosin dispersion) mechanical feedback: *Stretching of epithelial tissues during Drosophila dorsal closure and Zebrafish epiboly leads to recruitment of GEFs (Arf GEF and Steppke: blue) to the cell-cell junctions. This causes relaxation and therefore elongation of the epithelia* [72].

Similarly, negative feedback regulation via acto-myosin contractility at the cell-cell junctions has been observed in developmental stages of *Drosophila* and *Zebrafish* tissue elongation [82]. This negative feedback regulation led to lower myosin-II concentrations around the cell-cell junctions. Lower myosin-II recruitment or myosin dispersion from the site, eventually relieved the mechanical stress during tissue elongation. This was brought about by acto-myosin driven recruitment of small 'G' protein' (GEFs), referred to as Arf and Steppke [82]. During the time scale of minutes, acto-myosin enrichment led to recruitment of the GEFs at the junctions of the leading epithelial cells. Acto-myosin enrichment driven recruitment of the GEFs in turn antagonizes further myosin-II accumulation at the adherens junctions. This leads to relaxation of the cell-cell junctions and prevents tissue disruption in the process (Figure 2.18).

Also, myosin dependent negative feedback, on myosin-II recruitment, has been observed during contraction-relaxation cycles of a cells during germband extension in *Drosophila* development.

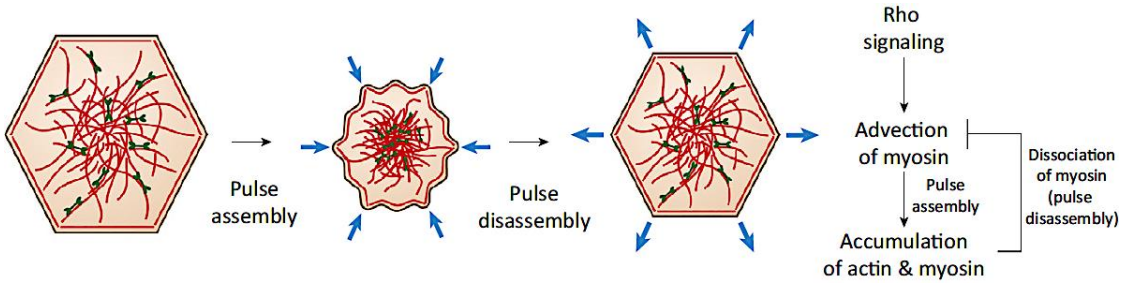

Figure 2.19: Schematic representation of myosin-dependent contractility and feedback: *Pulsatile contractility of the medio-apical acto-myosin network during germband extension in Drosophila, regulated by feedback mechanism of myosin recruitment and dissociation via Rho signalling* [72].

Oscillations in acto-myosin networks has been observed as a conserved phenomenon during developmental stages of several organisms. These oscillations are known to occur as a result of pulsatile acto-myosin contractility. Feedback loop of an activator inhibitor system was found to be responsible for such pulsatile contractility. In this case, myosin advection towards the medio-apical centre was observed to recruit myosin-II at the cell centre. Accumulated myosin-II was in turn observed to negatively feedback and hence reduce the myosin advection, leading to disassembly of the pulse and therefore relaxation of the cell boundaries. A cycle of Rho activation and inhibition via Rho-GEFs and GAPs respectively, has been described earlier (Section 2.4.4). F-actin and myosin-II activity being the downstream effectors of this signalling pathway, regulates their combined activity. This maintains a self-organized and self-regulated system for myosin recruitment and disassembly via negative feedback regulation (Figure 2.19). Such feedback regulations, describes an efficient way towards robust and self-organizing system where mechanical signals driven by acto-myosin contractility coordinate processes during tissue morphogenesis.

Another self-organised structure of acto-myosin network is present in the form of rings and/or cables contributing to force generation and subsequent ring constriction.

2.5 Acto-myosin complex; cables and rings

2.5.1 Rings in single cell system

Acto-myosin has been widely studied widely studied in cytokinetic ring at the last phase of the cell cycle referred to as mitotic 'M' phase. In the final event of cytokinesis, the furrow ingresses, generating two separate cells. (Figure 2.20).

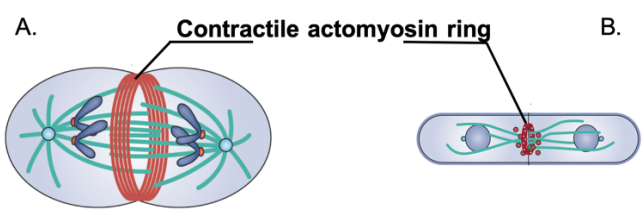

Figure 2.20: Schematic representation of cell division in animal cells: *Contractile acto-myosin ring (red) forming at the cell centre of (A) mammalian and (B) fission yeast cell, constricting and giving rise to two daughter cells. Microtubules and the spindle are shown in green.* [83]

This requires coordinated action of membrane systems and cytoskeleton which are known to be controlled in space and in time. The overall approach of cell division is conserved between

animal species, *e.g.* fission yeast and mammalian cells [83]. The last step of cytokinesis requires coordinated action of cytoskeleton and membrane system, in order to divide the cell into two. These steps of are known to be precisely controlled over space and time in all animal cells. Fluorescence and electron microscopy of dividing cells in, developmental stage embryos such as *C. elegans* as well as cultured mammalian and fission yeast, have shown accumulations of actin and myosin-II and actin associated proteins in the cytokinetic ring [5]. Even though distinct arrangements of this acto-myosin network exists during cytokinesis of different species [83][5], the network is known to be conserved and indispensable during the process of cell division.

2.5.2 Rings in multi-cellular system

Rings have been identified for acto-myosin networks across systems. As seen in earlier text, this acto-myosin network is observed to form accumulated bands around cell junctions, contributing to tissue morphogenesis (Figure 2.18). Similar cable formations at different sub-cellular locations have also been identified during developmental stages of several organisms [84].

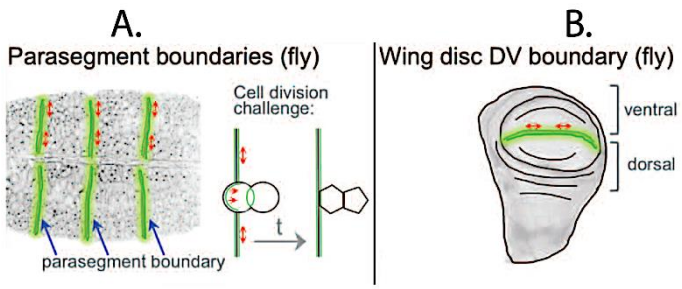

Figure 2.21: Schematic representation of acto-myosin cables during development: *Linear cables at the cell boundaries in (A) embryonic epidermis of Drosophila, (B) Dorso-ventral boundary in Drosophila wing disk. Green line indicating cables. Double-sided arrows (red) indicates tension generated in the cables.* [84]

These cables are supra-cellular arrangements of acto-myosin networks that appear to span over many cell diameters. Below, I describe principles that have emerged from analysis of these cables.

These acto-myosin cables are relatively stable, also under tension but do not constrict in contrast with acto-myosin rings. Such cables serve important developmental functions of compartment 'identity'. This restricts intermixing of cells with different fates present during early developmental stages [84]. Examples of such compartments segregated by acto-myosin cables

include para-segmental boundaries of embryonic epidermis (Figure 2.21). This prevents cell mixing when boundaries are challenged by cell divisions. Acto-myosin cable with similar property is also identified in larval wing disk, compartmentalising dorso-ventral and anterio-posterior boundaries (Figure 2.21 B.). These cables have tension associated with them, and have also been identified to drive *Drosophila* germ-band extension and chick neural tube folding and extension, to name few morphogenetic phenomena [84].

Apart from the linear cables, circumferential cables (rings) were also identified at the tissue edge, in cultured epithelial cells and developmental stages of organisms [85]. Acto-myosin ring was first identified three decades ago, during epidermal wound healing in embryonic buds of chicken wing disk [86]. These rings have been extensively studied since then, and have shown to constrict in a purse sting-like manner.

Acto-myosin contractile rings have been shown to assemble at the cell edges, facing the wounds and/or an empty space. These rings form rapidly around the wound edge within timescales of seconds, and subsequently lead to centripetal tension mediated wound closure. Such tension driven wound healing phenomenon, has been identified in damaged centres of *Drosophila* and *Zebrafish* embryos.

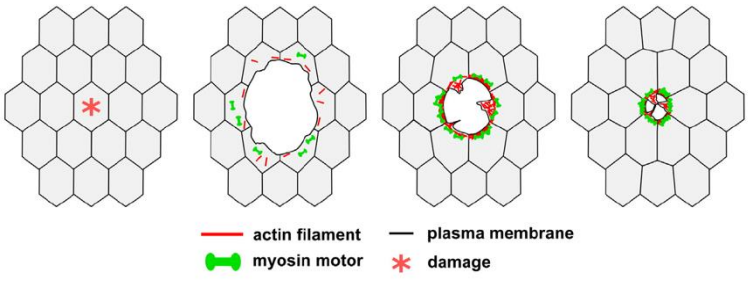

Figure 2.22: Schematic representation of cytoskeletal rearrangement during damage induced wound ring closure: *Actin (red) and myosin (green), forming a contractile ring during wound repair in Drosophila embryo cell sheets.* [87]

This was demonstrated by laser cutting of the epithelia, where coordinated cell movements participated in re-sealing the epithelial discontinuity (Figure 2.22). Cytoskeletal remodelling contributed to the wound closure.

The tension works in conjugation with other mechanisms such as adherens junction remodelling, through its upstream regulators Rho and Cdc42 (Section 2.4.4). This in turn directs acto-myosin cable assembly and dynamics at the wound edge.

More examples have been identified *in vivo*, such as dorsal closure in *Drosophila* embryos where epidermis moves to cover the region previously occupied by a layer of extra-embryonic tissue (Figure 2.23). Multiple cellular processes are known to involve in dorsal closure such as apical constriction of amnioserosa cells, constriction of supracellular acto-myosin purse string/cable, filopodial extension for the zipping process and apoptosis in amnioserosa cells. Out of these, contractile forces from myosin activity within the amnioserosa cells and the acto-myosin purse-string at the lateral epidermis are known to be the key contributors. These two processes pull the lateral tissue margin to the dorsal midline, closing the epidermis [88].

Organisation and contraction-driven closure of this supra-cellular acto-myosin ring suggests the presence of a functional contractile cable.

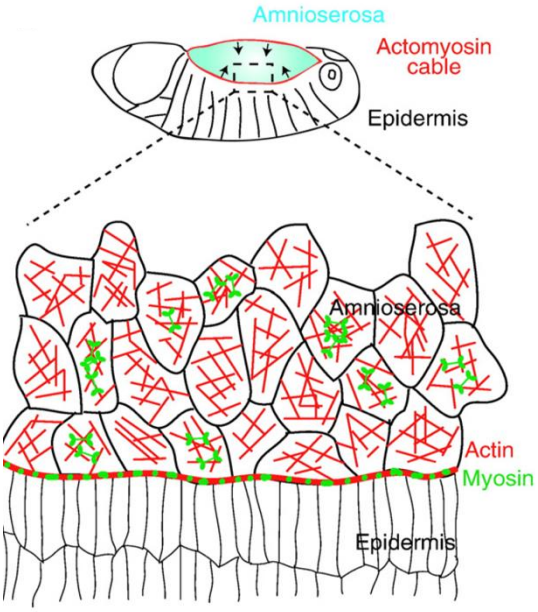

Figure 2.23: Schematic representation cell sheet extension during Drosophila dorsal closure: *Acto-myosin (red-green) dynamics in amnioserosa cells and acto-myosin cable at the edge leads to dorsal closure* [88].

At early stages of dorsal closure, assembly of acto-myosin cable pulls the edge leading to epidermal cell contraction. Epithelia are made of layers of cells composing their corresponding organs or tissues. Maintaining the integrity of this epithelial is of utmost importance in order to prevent pathogen invasions, in addition to inappropriate growth factor signalling and therefore inflammation. Maintaining the health of these tissues include turnover by apoptosis and subsequent high rate cell divisions to cover that space. Majority of cancer cases arise at epithelial sites, should the cell turnover machinery be misregulated. Cell death is the primary determinant of cell turnover. It potentially creates gaps within the epithelium via extrusion of the cells from the cell monolayer. Cell turnover via cell death drives normal homeostatic

environment of an epithelium. Crowded epithelial region lead to cell extrusion, critical for promoting tissue homeostasis.

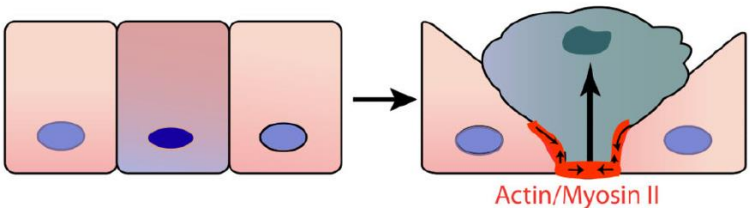

Figure 2.24: Schematic representation of acto-myosin ring during cell extrusion: *Basolateral acto-myosin contraction, squeezing the dying cell out of the epithelia apically, maintaining the barrier function.* [89]

Acto-myosin rings are vital in the process of cell extrusion. Cell death of an epithelial cell induces actin filaments in the surrounding cells to accumulate forming an actin ring. Subsequent Rho activity leads to myosin-II phosphorylation and activation, resulting in the contraction of this acto-myosin ring at the basal side [15]. This acto-myosin ring contracts and shrinks circumferentially along the basolateral surface of the cell sheet, subsequently pushing the dying cell out of the cell sheet (Figure 2.24). Therefore, cell extrusion via acto-myosin contraction leads to subsequent reformation of the intercellular junctions between the new neighbours, maintaining the tissue integrity. Such basal extrusion has also been observed in developing *Drosophila* epithelium [89].

Gaps in multi-cellular tissues are observed to occur naturally during lifetime of an organism. These gaps can either have a natural physiological origin such as in *Drosophila* dorsal closure and zebrafish epiboly, or it can be a consequence of damaged epithelia with disease prognosis.

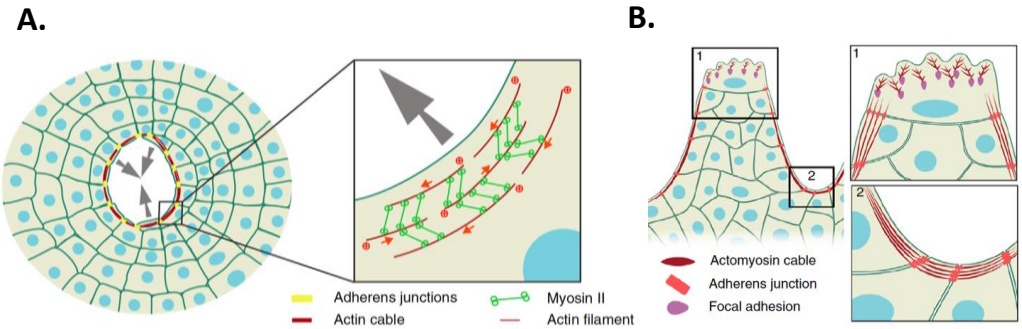

Figure 2.25: Schematic representation of gap closure: *A. Gap closure via purse-string mechanism primarily involving contractile acto-myosin ring with adherens junction ensuring ring continuity. B. Lamellipodia at the wound border showing finger-like protrusion organised at the leader cell edge.* [90]

For the gap closure during epithelial healing, two mechanisms have been reported, referred to as crawling mechanism and purse-string mechanism of gap closure. Both mechanisms are significant for closing epithelial gaps and most importantly, mutually non-exclusive. Both mechanisms are known to co-exist during the process of wound closure in epithelial cells [91]. Factors favouring one mechanism over another may include, geometry and size of the gap. *In vitro* systems involving epithelial cell monolayers, have provided essential insights in understanding the biological and mechanical factors involved epithelial gap closure. It has been reported that model wounds via scratch assays lead to the formation of lamellipodia and subsequent crawling mechanism-based closing of the gap (Figure 2.25 B). Therefore, local curvature of the gap was determined as one of the key determinants, for the specific mode of mechanism followed for the gap closure. Negative curvature, *i.e.* concave border was related to acto-myosin ring assembly leading to subsequent purse-string based closure. On the contrary, positive curvatures that depicts convex borders favours crawling cell mechanism [10]. Essentially purse-string and crawling mechanisms operate together at circular wounds (negative curvatures), thus leading to faster gap closure. Hence, coexistence and interaction between these two mechanisms are responsible for efficient wound ring closure, with relative contributions depending on the local curvature of the wound.

Purse-string based closure has been reported to form a supra-cellular acto-myosin ring around the cell edge at the wound border (Figure 2.25 A). Since the acto-myosin filaments span the whole wound border, these filaments are linked with the neighbouring cells, presumably by adherens and/or tight junctions. These connections help in maintaining tension across several cells.

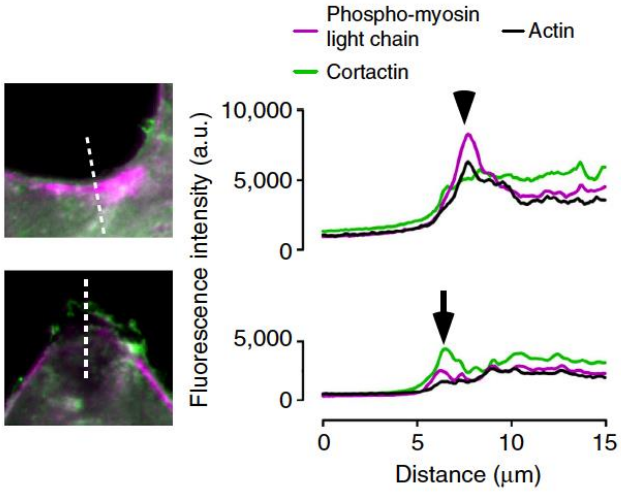

Figure 2.26 Myosin accumulation at different wound curvatures: *Differential myosin accumulation and corresponding intensity profiles at negative (concave: upper panel) and positive (convex lower panel) curvatures.* [10]

Contraction of this acto-myosin ring drives the collective movement of cells around the wound edge, into the gap and therefore closing the gap/wound. Higher intensity of phospho-myosin indicative of higher myosin-II accumulation and purse-string driven closure, was observed at

concave wound curvatures (Figure 2.26, upper panel). In contrast, lower accumulation of myosin-II was observed at convex curvatures, primarily driven by cell crawling mechanism of gap closure (Figure 2.26, lower panel). It was also observed that reduced purse-string contractility was sufficient in releasing the crawling motion at convex portions of the ring.

Focal adhesions are known to play a crucial role in mechanical force and regulatory signal transmission between cell and the extra-cellular matrix. Distribution analysis of these force transducers revealed orientations, tangential to the wound edge close to concave curvatures, as opposed to perpendicular orientations at the convex borders (Figure 2.27).

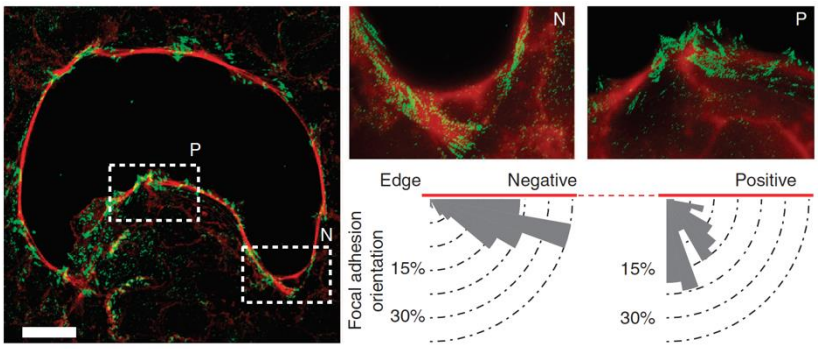

Figure 2.27: Actin and paxillin localisation in wound rings: *Staining of acto-myosin wound ring. Left panel showing actin in red and focal adhesions, paxillin in green. Right panels showing zoomed view of positive and negative curvatures with their corresponding focal adhesion orientation. Scale bar 20µm*

[10]

In agreement with focal adhesion distribution, transient force dipoles parallel to the wound edge were observed in negatively curved regions. This was attributed to the acto-myosin ring at the wound edge. In contrast, positively curved regions were evaluated to show backward pulling forces. This showed mechanical coupling of the two mechanisms where focal adhesions were shown to be coupled to both protrusive as well as contractile bundles [10]. Also, in agreement with the focal adhesion distribution, highest traction forces were shown to be concentrated at the wound edge, rather than (>15µm) behind it.
This distribution illustrates the fact that there is indeed higher tension associated with the acto-myosin ring when compared to the surrounding cell monolayer.

Other than forming ring structures, acto-myosin has also been observed to form of self-organised ‘foci’ in several developmental processes. Such occurrences and their related characteristics are described in the section below.

2.6 Acto-myosin complex: myosin clusters

In contrast to the well-organised muscle contraction unit, organisation of the network within such rings is fairly random. Although basic interaction rules of this active gel can be translated throughout systems [72], its stochasticity [17] poses a challenge to investigate the network in molecular details.

This stochasticity is often broken by spontaneous self-organisation of myosin in the form of clusters. Such myosin clusters have been observed throughout various systems and visualised to be temporally dynamic [6][7]. Presence of myosin clusters have also been observed in acto-myosin rings from single cell contractile rings [5] to multi-cellular acto-myosin cable in *Drosophila* tissue morphogenesis [8].

2.6.1 Myosin clusters: Multi-cellular system

Acto-myosin self-organised network in the form of 2D or 3D networks has been observed within the cell cortex, underlying the plasma membrane in majority of animal cells. This network has vital roles in many developmental processes.

Early stage developing embryo of *C. elegans* demonstrates two distinct types of ingressions. First, a pseudo-cleavage furrow which establishes antero-posterior polarity at the single cell stage level. This is followed by the cytokinetic furrow, that leads to the division of a 1-cell stage embryo into two.

Breaking left-right symmetry of a developing embryo is a key step in morphogenesis. This step determines the body symmetry and organisation of the fully-grown organism and its respective tissue arrangements. In *Drosophila* early embryo, gradient of a chemical factor known as Hunchback protein has been observed to contribute towards breaking the A-P polarity [92].

Although the same process of A-P polarisation in *C. elegans* embryo is shown to follow a mechanical-based as opposed to chemical-factor approach, this mechanical based factor involved acto-myosin network. Cortical flows of myosin-II clusters were observed to precede anteroposterior (A-P) polarisation of the embryo (Figure 2.28).

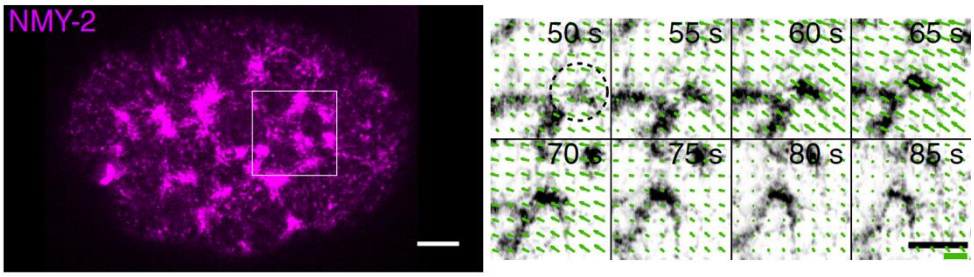

Figure 2.28: Non-muscle myosin-II foci in* C. elegans *embryo: *A. Myosin-II clusters (magenta) observed in early stage embryo. B. Time course of myosin assembly patterns showing coalescing clusters in a flow velocity map. Scale bar 5µm, Velocity scale bar 0.4µm/s.* [7]

Chiral flows of myosin-II foci were shown to break the symmetry of the early embryo. By quantifying the cortical flow velocity though particle image velocimetry (PIV), it was shown that the flow proceeds mainly through the A-P axis. Next, these chiral cortical flows were found to precede whole cell rotations, breaking the chiral symmetry of a 1-cell stage embryo and therefore determining the A-P polarity. The A-P portions of the cortex were shown to counter-rotate relative to each other with a 2 times faster velocity of rotation for the anterior portion as compared to the posterior one (Figure 2.29, D: black). Also, the fact that these cortical rotations were observed to be preceding the chiral whole cell rotation, illustrated them as the driving force for the process.

Also, reduction the myosin activity through mlc-4 showed reduction in both A-P myosin flows as well as chiral counter-rotation velocity of the whole cell. The reduction in whole cell chiral rotation was reduced from -2.9 ± 0.3 µm/min in wild type to -1.1 ± 0.4 µm/min in RNAi condition (Figure 2.29, C, non-RNAi: black, mlc-4 RNAi: orange respectively).

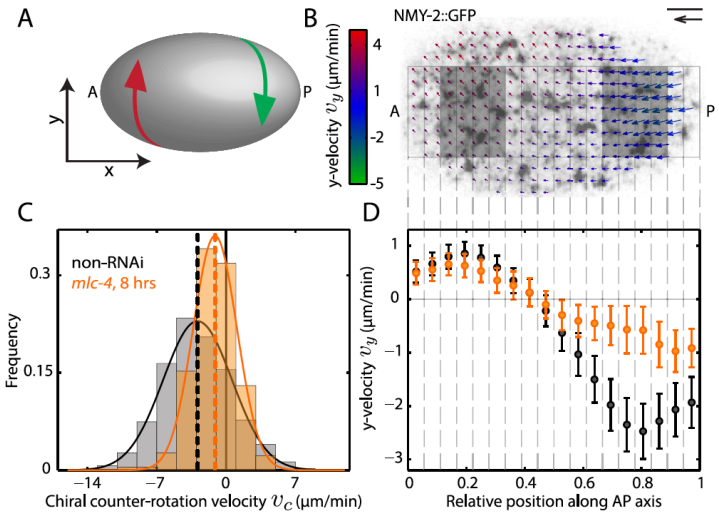

Figure 2.29: Chiral cortical myosin flow depending on myosin activity, in* C. elegans *embryo: *A. representation of a* C. elegans *embryo depicting A-P axis and relative counter-rotations. C. Time averaged cortical flow fields corresponding to the B. representative image of embryo portion at the top (A: anterior, P: posterior). Arrows indicating 'y' velocities, spatially averaged over left and right areas to give v_c, i.e.*

chiral counter-rotation velocity. Velocities along the AP axis for non-RNAi (black) and mlc-4(RNAi). Scale bar 5µm, velocity scale bar 20µm/min [7]

Hence these results showed that myosin-II cluster flow is a major determinant for *C. elegans* embryo L-R asymmetry. It was shown to be responsible for both A-P polarizing chiral flows as well as subsequent chiral counter-rotation of the two *C. elegans* embryo cells relative to each other.

Another example of myosin cluster activity in developmental stages was evident in *Drosophila* germband extension. This process occurs ~20min after the onset of gastrulation, primarily involving cell intercalation and subsequent tissue shape changes.

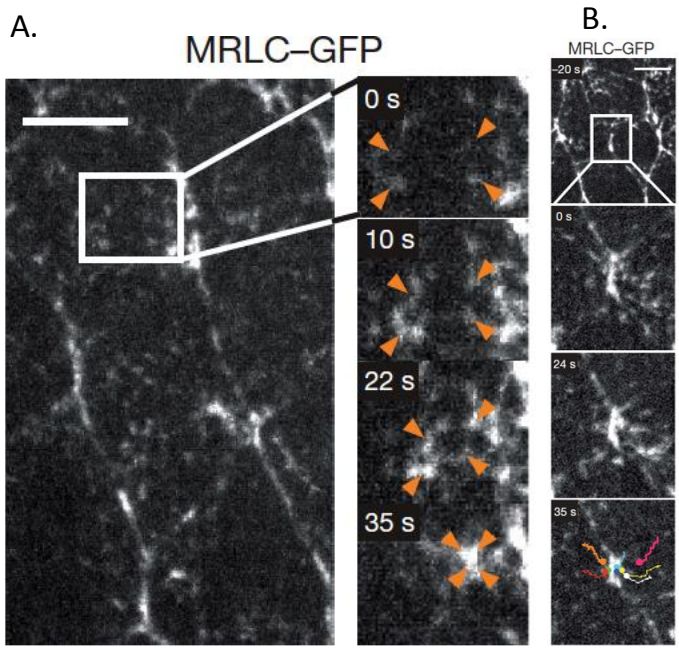

Figure 2.30: Pulsating pools of acto-myosin leading to cell Drosophila germband extension: *Cells expressing myosin regulatory light chain, showing A. medial myosin-II cluster dynamics (zoomed: temporal dynamics) and B. junctional myosin-II flow depicting cluster coalescence (color traced) at the cell-cell junction leading to intercalation. Scale bar 5µm* [6].

These shape changes were observed in the form of tissue elongation, shown to be driven by cell intercalation. This process was observed to be driven by dynamics of self-organised myosin-II clusters. Activity of these clusters was important in remodelling the cell-cell junctions, in turn leading to cell intercalation. These clusters were observed to concentrate at the vertical junctions, leading to increased tension, and therefore junctional shrinkage (Figure 2.30, B.). The flow speed was evaluated to be 0.11 ± 0.03µm/s. Apart from junction flow of myosin-II clusters, another population referred to as medial pool of myosin-II was observed

to contribute towards cell intercalation. This specific myosin-II cluster pool, slightly apical to the junctional flow, was shown to display anisotropic flows feeding the vertical junctions. When compared, medial pulsed flows were visualised to precede the junctional flow by ~8s showing a tightly coordinated and hierarchical flow patterns. Hence medial pulsed flows of myosin clusters feed and fuse with junctional myosin clusters to drive the adjacent junctional polarity and cell intercalation.

Therefore, not myosin-II distribution alone, but its dynamics such as clustered (pulses) and flows are responsible for the deformations of a cell.

Another developmental stage where this myosin clustered morphology is known to exist is during dorsal closure. The phenomenon of dorsal closure in *Drosophila* embryo is influenced by dynamic forces from cells positioned at the amnioserosa, as well as the lateral epidermis. These forces are contributed by dynamic myosin foci within the amnioserosa cells as well as acto-myosin cable observed at the interface of these two tissues (Figure 2.31, red and green arrows respectively).

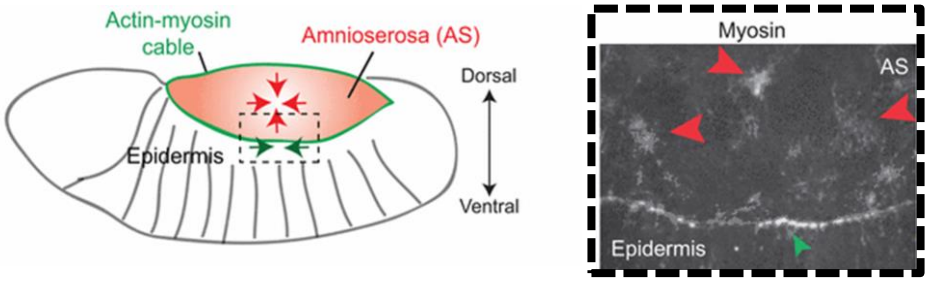

Figure 2.31: Organisation of myosin-II clusters during Drosophila dorsal closure: *Left, representation of dorsal closure in Drosophila, driven by myosin activity in amnioserosa cells (red arrows) in addition to leading edge acto-myosin ring contraction (green arrows). Dashed box showing zoomed view.* [6]

Punctate arrangement of myosin-II is observed both in apical constriction of amnioserosa cells as well as around the contractile acto-myosin cable. Clustered arrangement of myosin-II around the contractile acto-myosin ring is shown to alternate with α-actinin, suggesting a sarcomeric organisation [88]. Despite the tension evaluation by laser ablation studies, the average distance between these myosin-II clusters was shown to be unchanged after initial straightening of the leading edge. Loss of tension in this cable by mosaic myosin-II mutants revealed epidermal cell stretching, illustrating tension generation leading to cell shape stabilization [88]. Apart from clustered myosin-II arrangement at the leading acto-myosin ring, amnioserosa cells are also

shown to undergo pulsatile contractions and relaxation cycles during the process of apical constriction. These pulses lead to cluster formations inside cells resulting in their contraction relaxation cycles and therefore cell shape fluctuations.

Apart from its involvement during *in vivo* development stages, self-organised acto-myosin complex was also observed to form clusters during *in vitro* reconstitution of its core elements, *i.e.* actin and myosin.

2.6.2 Myosin clusters: *in vitro* reconstitution

One such example included reconstituting these proteins on a substrate functionalised with lipids. Linkers were constructed in a way that they contained actin binding domains, in turn able to interact with myosins. The membrane actin linker HYE was used in this configuration, constructed from actin binding domain of ezrin (Figure 2.32). Ezrin is known to be one of the protein participants amongst the ERM protein family. Components of this protein family is known to crosslink actin filaments to the plasma membrane of the cell. Reconstituted minimal system was utilised for addressing the role of acto-myosin, as an active process in spatial organisation and dynamics of cell surface components.

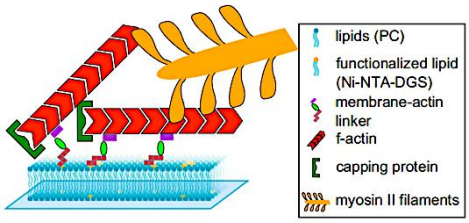

Figure 2.32: Schematic of the reconstituted* in vitro *system in use: *Showing actin an myosin filaments linked to the lipid bilayer through membrane linkers* [22].

These bilayers containing HYE linkers recruited actin filaments to form thin sheets above these lipid bilayers. Fluidity of this lipid bilayer was shown to be unaffected by the actin filament attachments.

Addition of bipolar myosin filaments to the lipid bilayer bound thin actin filaments, produced actin polar asters characterised by islands of actin and associated myosin. This configuration reflected contractile organisation where myosin was found to be clustered at the middle of actin filaments (Figure 2.34, myoII (red)). While clustering, myosin driven contractile flows were

evaluated to be ~0.5-1µm/min. Also, after addition of myosin-II, a lag period was observed before appearance of myosin clusters.

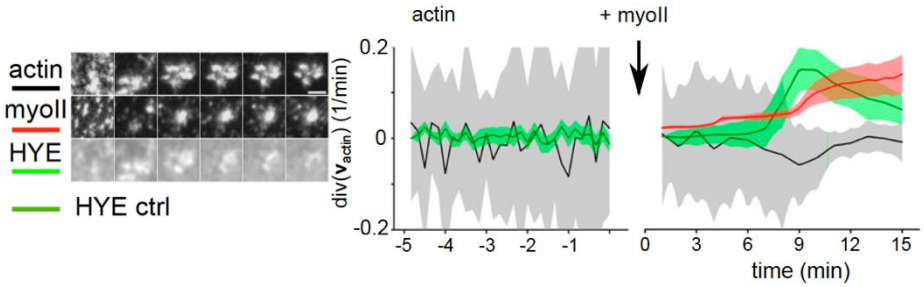

Figure 2.33: Reconstituted* in vitro *system forming self-organised myosin clusters: *Myosin filament induced cluster formation. Left: self-organised myosin (red) clusters observed after adding myosin bipolar filaments to actin filament attached lipid bilayer. This also leads to linker HYE clustering (green), depicting bilayer fluidity. Right: contractile flows evaluated by PIV data shows clustering after addition of myosin.* [22]

This correlates with *in vivo* scenario of homogeneous states, before threshold acto-myosin interactions are achieved leading to clustering [5][7]. Therefore, such reconstituted minimal system illustrated that clustering mechanism relied on actin and myosin interactions, resembling dynamics in live cells.

Another example of such reconstituted acto-myosin network included actin patterned surfaces. In such experiments reconstituted actin filaments, assembling on flat surfaces via UV based patterning was used. This configuration was then further evaluated after addition of myosin motors, to determine their evolution over time.

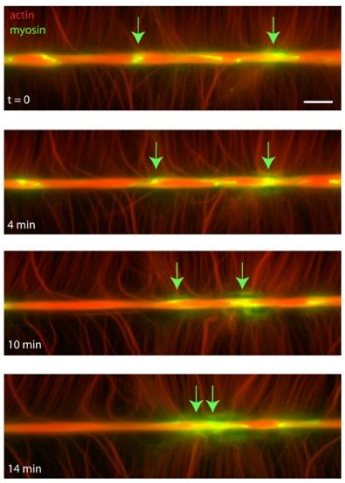

Figure 2.34: Self-organised myosin cluster induced actin mesh contractility on bars: *Actin (red) on patterns visualized with myosin(green). Myosin cluster induced contractility and disassembly of the actin meshwork was observed (t=0 to t=14min)* [93].

Patterned actin networks in the of bars were generated, and myosin-VI was introduced. Myosin-VI is an unconventional myosin, moving towards (-) end of actin filament.
Actin orientation-based network contractility and disassembly was observed in this case, where parallel filaments remained unaffected, but the branched filaments on the actin meshwork contracted.

Interestingly self-organised myosin clusters were responsible for such contraction and disassembly of the actin network (Figure 2.34, myosin green).
Another example of self-organized myosin cluster appearance leading to contraction was observed on ring shaped micro-patterns of actin network. Filaments assembled into branched meshwork form on a full ring pattern. Myosin introduced in this configuration led to constant contraction of the ring. Visualising the myosin channel interestingly showed self-organised cluster dynamics while constricting the ring (Figure 2.35, bottom panel, myosin high density).

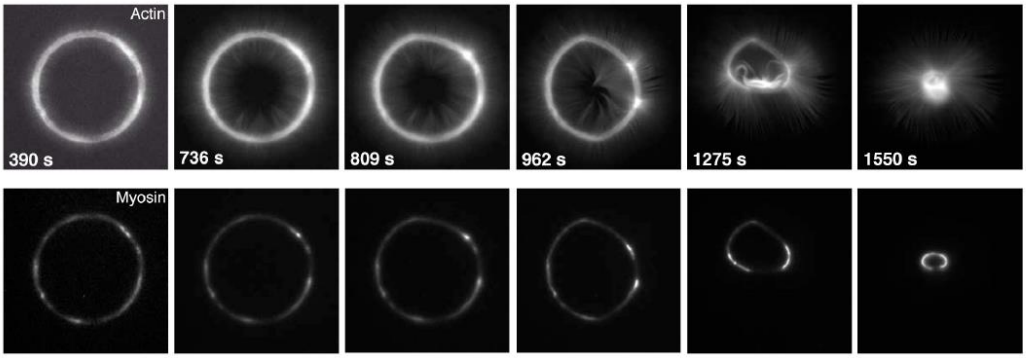

Figure 2.35: Self-organised myosin cluster induced actin mesh contractility on rings: *GFP tagged myosin-VI, showing actin and myosin signal during full ring contraction after addition of myosin* [93].

Moreover, in another configuration used in the same study, acting nucleating regions were created in a dot-like manner. This dotted ring specifically formed anti-parallel filaments between the dots. Myosins accumulated on these rings without any network deformation. This lag period was followed by deformation, above a critical myosin concentration. Actin network contraction in such a configuration of broken symmetry, showed twice as faster ring constriction, compared with rings without any actin nucleating regions. These results indicate that selective contraction and disassembly in actin cytoskeleton can be illustrated by spatially controlled acto-myosin contractility.

Moreover, apart from their existence myosin clusters also showed dynamics behaviour in such a reconstituted system (Figure 2.35, bottom panel: rotating myosin clusters). This result was consistent with cluster dynamics observed in single cell cytokinesis.

2.6.3 Myosin clusters: Single cell system

Organisation of actin and myosin is an unsolved problem in the field of cell cytoskeleton. These proteins are known to form several organisations and have been known to generate forces via those configurations. Different in forces indicate distinct internal organisations.

Studies relating to filament polarity using myosin decoration have shown that cytokinetic ring consists of mixed polarity rather than a sarcomeric arrangement [94]. Myosin self-organisations in the form of clusters have provided some clear indications regarding network assembly in different systems. Instantaneous dynamics of these myosin clusters were illustrated to be a reliable readout for such differences. These distinct dynamics were found to be involved in different functions during the cell cytokinesis.

One such study from our lab., illustrated this in mammalian and fission yeast cell cytokinesis.

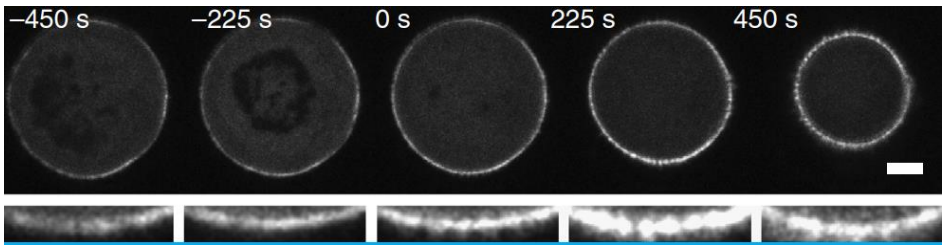

Figure 2.36: Early stages of cytokinesis in mammalian cells: *Time lapse images of cytokinesis in HeLa cells inside cavities. Homogeneous distribution of myosin seen before the start of process (-450s to -225s), eventually leading to myosin clusters observed around the ring perimeter during the process of constriction (225s to 450s). Scale bar 5µm* [5].

Dividing cells were placed inside cavities to obtain orientation of full rings in focus. Entire circumference of the cytokinetic ring was visualised in this case.

Visualising myosin for mammalian (HeLa) cell cytokinesis illustrated homogeneous region of myosin distribution just before the start of cytokinesis (Figure 2.36). As soon as cytokinesis started, myosin clusters were seen to appear throughout the ring perimeter. These clusters were seen to be periodically placed at an inter-distance of ~0.8µm. During constriction, these clusters

were observed to persist at the same position in the framework of the ring (Figure 2.37, right: kymograph).

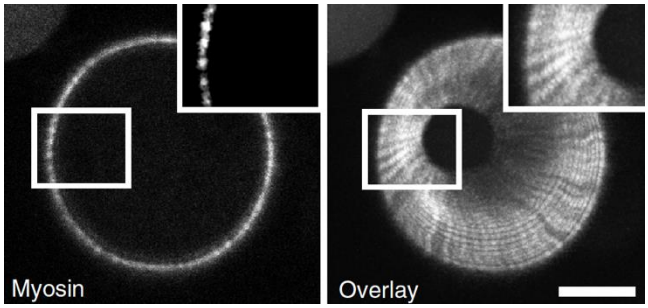

Figure 2.37: Still/radial clusters during mammalian cell cytokinesis: *(Left) HeLa cell cytokinetic ring showing myosin clusters around the ring perimeter. (Right) Time projection of image frames (interval 10s) showing dynamics of the clusters: still/radial. Scale bar 5µm* [5].

Similarly, fission yeast cytokinesis was also followed inside cavities. Interestingly, this system also had myosin clusters. However, the dynamics of these clusters was different from mammalian cells. Myosin clusters in fission yeast cytokinesis followed rotating or tangential dynamics (Figure 2.38).

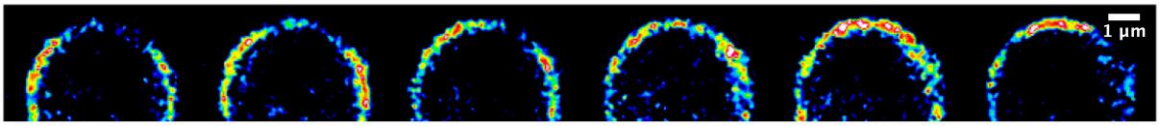

Figure 2.38: Rotating/tangential clusters during fission yeast cytokinesis: *Fission yeast cytokinetic ring showing myosin clusters (heat colours) around the ring perimeter showing rotating/tangential dynamics with the time of constriction. Time interval 24s* [5].

The mechanisms of these pattern formations were first supported by a physical model, considering the basic rules of interactions between the polar actin filaments (Figure 2.8). In order to capture the cluster formations *in silico*, presence of bipolar filaments was also introduced in the theoretical description (Figure 2.39). Assumption of bipolar filaments was illustrated by the presence of two polar filaments of fixed lengths, assembling (+) end to (+) end by an actin binding protein (Figure 2.39). This configuration gave an easy and perceivable configuration for myosin clustering at the junction of two interacting polar filaments. Theoretical analysis determined that sliding velocities of parallel filaments (α) with respect to the bipolar filaments was the limiting factor contributing to cluster formations. Bipolar

filaments were described to assemble and disassemble at rates denoted by ω_c and ω_d respectively (Figure 2.39).

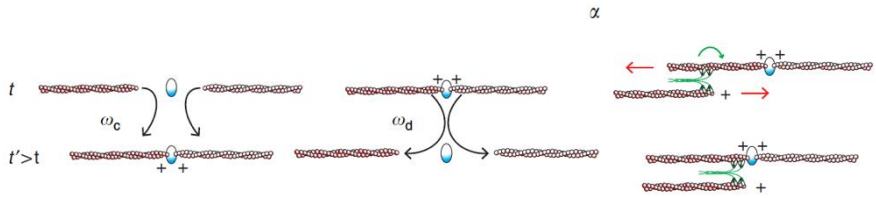

Figure 2.39: Bipolar filament assembly and dynamics: *(Left) Showing assembly and disassembly of bipolar filaments. (Right) Dynamics of bipolar filaments with parallel filaments leading to myosin accumulation at the center, given by velocity α.*

Physical framework in [5] revealed that a critical value of sliding velocities of parallel filaments α_c pushed the system from its homogeneous myosin distribution state, to a state with myosin clusters. This was found out to be weakly dependent β. The two cluster states were recapitulated by the theory where higher values of ω_d lead to rotating clusters as compared to lower values where clusters appeared to be stationary (Figure 2.37 and 2.38 respectively). This was shown with a phase diagram for both the cluster dynamics studied (Figure 2.40 C.). This physical framework *in silico* could also recapitulate the dynamics in the form of kymographs similar to experimental data in fission yeast and mammalian cell cluster dynamics (Figure 2.40 A.)

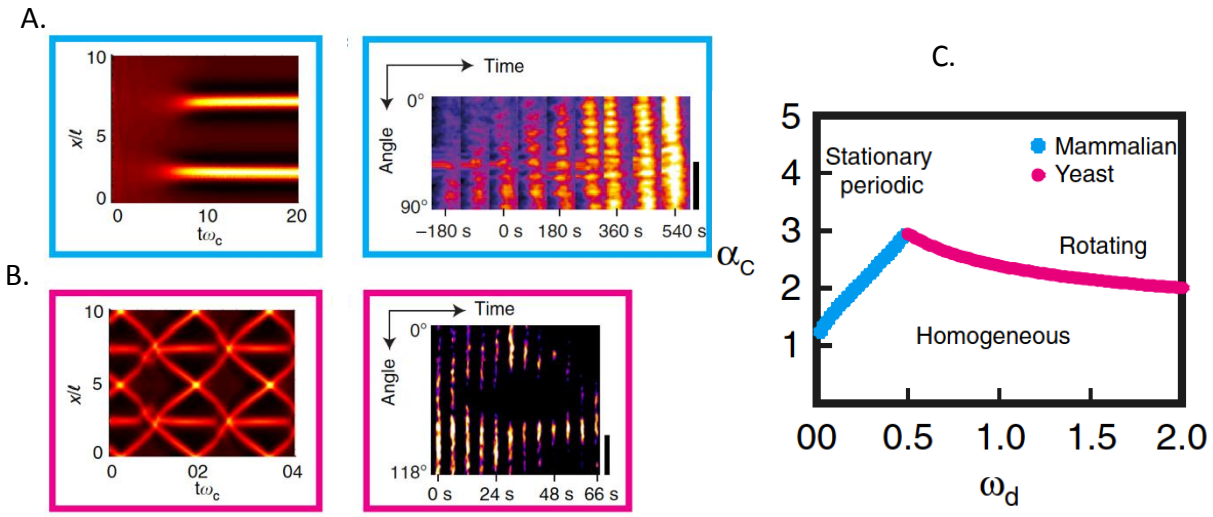

Figure 2.40: Theoretical validation for myosin cluster dynamics during cytokinesis: *Kymograph obtained by theoretical predictions (left) and experimental data (right), for A. still clusters in HeLa cells and B. in fission yeast cell cytokinetic rings. Clusters are shown as heat colours. C. Phase diagram for myosin cluster states.* [5]

Theoretical analysis also predicted differences in respective stresses generated by these clusters in their corresponding systems. Confirming these results with experimental data, distinct functional roles were suggested for these distinct dynamics. Still clusters in mammalian cells were suggested for being associated with higher stress and therefore contraction, on the contrary, rotating clusters were associated with lesser stress and transport of wall machinery.

3.MATERIALS AND METHODS

In this section, I will introduce the experimental techniques used in this study.

I will start with introducing the protocol for constructing micrometre dimension structures through UV photolithography, also known as micro-fabrication. This will be followed by protocols for sample preparation in order to introduce these cells in/around the fabricated micron structures. Lastly, I will describe experimental methods and imaging techniques utilised to for high spatial resolution imaging.

First, I will start with introducing photolithography used to fabricate micrometer scale structures made of photoresist (SU-8). This process follows the first steps of obtaining motifs used in the study; epithelial cell wound rings, *'O' rings* and orientating of single cell (HeLa and fission yeast) cytokinetic rings.
Next, these structures are replicated to PDMS (Sylgard 184) for being used in the experimental setups directly, or replica mold to serve as a master for preparing the motifs (PDMS) used in the experimental procedure.
Afterwards, I will detail the cell lines used in this study and their culture conditions.
Finally, I will describe the experimental procedure followed to obtain shape controlled *epithelial wound rings* in cell monolayers, *isolated 'O' rings* of epithelial cells and vertically oriented dividing cells (HeLa and *fission yeast*) inside cavities.

3.1 Photolithography

Photolithography is a widely used process followed in micro-fabrication. This process is used to fabricate micrometer scale structures by means of a photosensitive resin. In our study, an epoxy-based photoresist SU-8 2025 (MicroChem) is used for this purpose. The SU-8 photoresist is conventionally exposed with UV (350-400nm) radiation. This process is essentially performed in a clean room with a dust free environment. Such environment assures fabrication of well resolved microstructures. The process requires a clean and dust free silicon (Si) wafer. For this purpose, the Si-wafer is cleaned following a two-step solvent process. First, the wafer is cleaned with acetone and then with ethanol. Silicon wafers are dried after each solvent cleaning, using a nitrogen stream. The two-solvent cleaning method assures complete

removal of dust, oils and organic residues from the surface of the wafer. After this step, wafers are heated at 200 °C for 15min. This ensures removal of humidity from the surface of the wafer. Fabrication of SU-8 motifs used to obtain *rings of epithelial cell monolayers, isolated epithelial 'O' rings* and vertically oriented cells (HeLa and *fission yeast*) are described below**.**

3.1.1 Designing the photomask

Clewin (Freeware) and Autocad® software were used to design the photomasks with required motifs. The motifs are then printed on a plastic mask used as photo-mask in the steps of micro-fabrication.

3.1.2 Micro-fabrication protocol for obtaining multicellular rings

1. Liquid photoresist (~2ml) is poured over the wafer. Any existing air bubbles trapped in the poured photoresist are removed with the help of a plastic dropper. This is a necessary step to avoid inhomogeneity in the spin-coated SU-8 layer.
2. After the bubbles are removed, the assembly is spin-coated (WS-650-23 Spin Coater; Laurell Technologies corporation, rotor details kept throughout for micro-fabrication) with the parameters optimal for obtaining the target thickness of the motifs on the Si-wafer (Figure 3.1 (i), Figure 3.2 (i)).
3. A two-step spinning process is set on the spin-coater. Parameters are set to first spin at 500rpm for 10s (acceleration 300rpm/s) in order to homogenize the photo-resist layer over the wafer and then at 1000rpm for 30s (acceleration 500rpm/s) for reaching the target thickness of 80µm, for epithelial cell *monolayer rings* or 3000rpm for 30s (acceleration 1000rpm/s) for reaching the target thickness of 25µm for epithelial cell *'O' rings*.
4. Next, pre-bake (before exposure) of this assembly is done on a levelled hot plate maintained at 65°C for 5min followed by 95°C for 10min for the target thickness of 80µm and only at 5°C for 5min for obtaining the target depth of 25µm.
5. After obtaining the target thickness, photomask with desired printed photo-mask is carefully placed on the photoresist layered Si-wafer and exposed for 5.5s for the target thickness of 80µm and 4s for the target thickness of 25µm. Exposure time depends on the recommended exposure energy (200mJ/cm^2; 80 µm, 150mJ/cm$^{2;}$ 25µm) and power of the UV source, (40mW/cm^2; in our case). UV exposure will pass through the photomask and eventually crosslink the areas which are transparent on the photomask as compared to the portions

corresponding to the dark areas which will remain un-crosslinked (Figure 3.1 (ii), Figure 3.2 (ii)).

6. Next, a two-step post-bake (after exposure) is done on a levelled hot plate maintained at 65°C for 2min followed by 95°C for 8min for the target thickness of 80µm and at 65°C for 1min followed by 95°C for 5min for the target thickness of 25µm. With an optimal exposure parameter, a latent image is revealed on the wafer (in a couple of seconds) after being placed on the hot plate for post-bake.

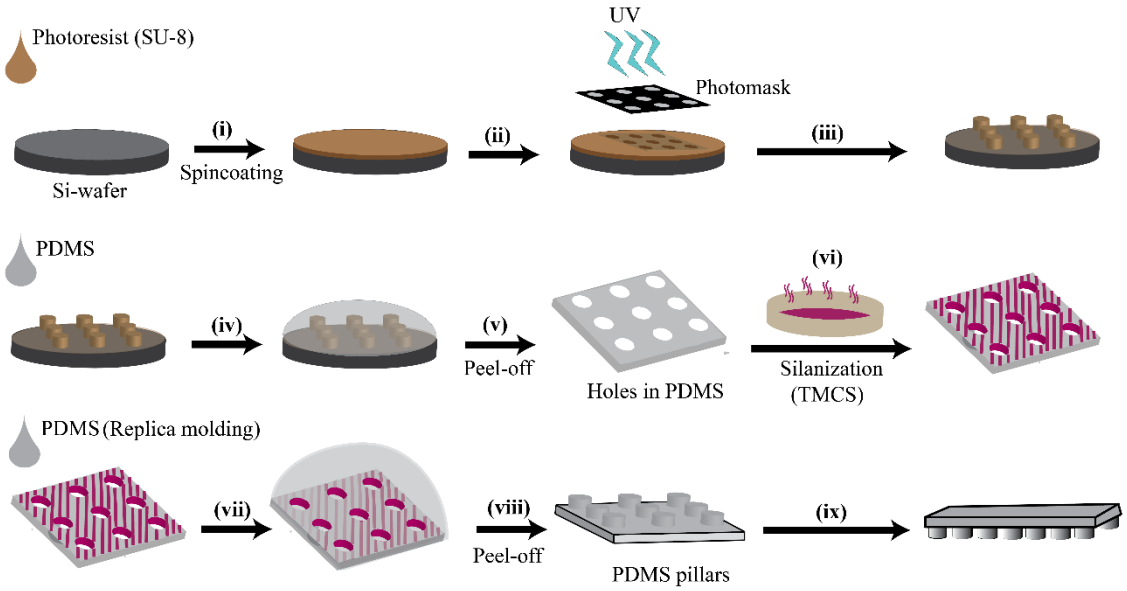

Figure 3.1: Schematic representation of micro-fabrication process followed to obtain shape controlled circular rings of cell monolayer: *Photoresist is spin-coated over Si-wafer with speed corresponding to obtain motif height of 80µm (i). After pre-bake, photomask with desired printed motifs is placed on the wafer and exposed to UV light (ii). After post-bake and developing process, Si-wafer with pillars of photoresist is revealed (iii). PDMS (base: crosslinker; 10:1) is poured over the Si-wafer with pillars (iv) and incubated for heat crosslinking at 65°C for at least 4h. Peeling off this PDMS layer gives replica of the Si-wafer with holes inside the PDMS block referred to as master 1 (v). PDMS master 1 with holes inside is incubated with silane vapors (TMCS;pink) under enclosed conditions for 30min to give a silanised PDMS surface (vi). Next, replica molding of PDMS master 1 is performed by pouring PDMS over the silanised master (vii) and peeling it off after heat crosslinking (vii). This gives PDMS block with pillars of required height used further in the experiment setup.*

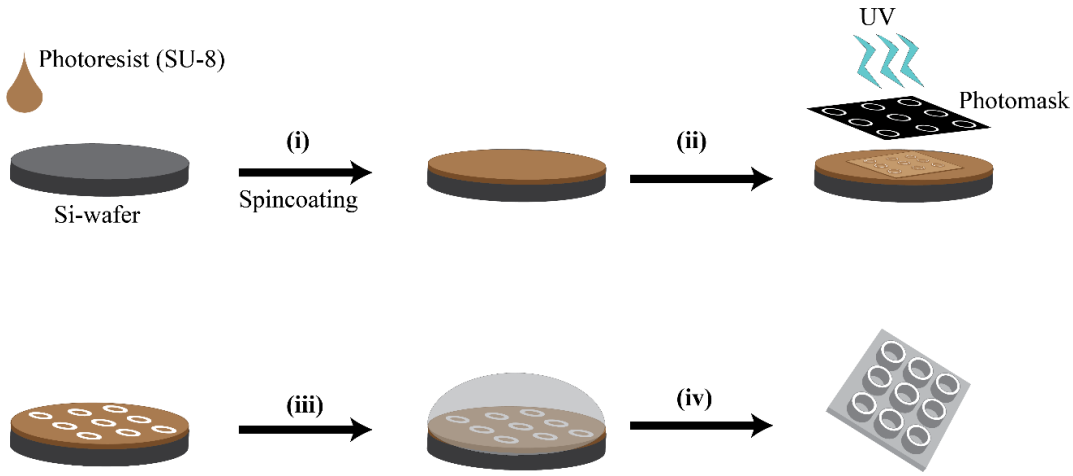

Figure 3.2 Schematic representation of micro-fabrication process followed to obtain isolated epithelial cell 'O' rings: *Photolithography process is followed where Si-wafer is spin-coated with photoresist to obtain the required height of 25µm (i). After pre-bake photo mask with desired printed motifs is placed over the wafer and exposed to UV (ii). After post-bake and development process Si-wafer with 'O' ring shaped holes is revealed inside the photoresist (left, iii). PDMS (base: crosslinker; 10:1) is poured over the Si-wafer with holes (right; iii) and incubated for heat crosslinking at 65°C for at least 4h. Peeling off this PDMS layer gives PDMS stamps with 'O' ring shaped pillars (iv).*

7. After the two-step post-bake, un-crosslinked areas are stripped off with the help of SU-8 developer. Wafer is put inside a solution of developer for a 1-2min followed by washing with Isopropyl Alcohol (IPA) for 10s. Rinsing with IPA revealing a white film stripping off the wafer, indicates towards underdevelopment of the unexposed photoresist. In such a case the wafer should again be put inside the SU-8 developer solution. This process should be repeated until no white film is seen stripping off the photoresist layer on the wafer leading to complete development process.
8. Proper development will reveal desired SU-8 motifs on the Si-wafer. SU-8 pillars (height 80µm) are used for preparing rings of epithelial cell monolayer and SU-8 'O' ring holes (depth 25µm) are used for preparing epithelial cell 'O' ring.
9.

3.1.3 Micro-fabrication protocol for obtaining single cell rings

3.1.3.1 Protocol for mammalian cell cytokinetic rings

After two-step solvent cleaning process, the silicon wafer is dried and heated at 200 °C for 15min, ready to be used for photolithography.

1. Liquid photoresist (~2ml) is poured over the wafer. Any existing air bubbles trapped in the poured photoresist are removed with the help of a plastic dropper. This is a necessary step to avoid inhomogeneity in the spin-coated SU-8 layer.
2. After the bubbles are removed, the assembly is spin-coated (WS-650-23 Spin Coater; Laurell Technologies corporation, rotor details kept throughout for micro-fabrication) with the parameters optimal for obtaining the target thickness of the motifs on the Si-wafer.
3. A two-step spinning process is set on the spin-coater. Parameters are set to first spin at 500rpm for 10s (acceleration 300rpm/s) in order to homogenize the photo-resist layer over the wafer and then at 3000rpm for 30s (acceleration 1000rpm/s) for reaching the target thickness of 25µm.
4. Next, pre-bake (before exposure) of this assembly is done on a levelled hot plate maintained at 65°C for 5min for obtaining the target depth of 25µm.
5. After obtaining the target thickness, photomask with desired printed motif (white dots with dark background) is carefully placed on the photoresist layered Si-wafer and exposed for 4s for the target thickness of 25µm. Exposure time depends on the recommended exposure energy (150mJ/cm^2 for 25µm) and power of the UV source, (40mW/cm^2; in our case). UV exposure will pass through the photomask and eventually crosslink the areas which are transparent on the photomask as compared to the portions corresponding to the dark areas which will remain un-crosslinked.
6. Next, a two-step post-bake (after exposure) is done on a levelled hot plate maintained at 65°C at 65°C for 1min followed by 95°C for 5min. With an optimal exposure parameter, a latent image is be revealed on the wafer (in a couple of seconds) after being placed on the hot plate for post-bake.
7. After the two-step post-bake, un-crosslinked areas are stripped off with the help of SU-8 developer. Wafer is put inside a solution of developer for 1-2min followed by washing with Isopropyl Alcohol (IPA) for 10s. Rinsing with IPA reveals a white film stripping off the wafer. This is an indicator for underdevelopment of the unexposed photoresist. In this case, the wafer should be placed inside the SU-8 developer solution for another 2min. This process should be repeated until no white film is seen stripping off the photoresist layer from the wafer.
8. Proper development will reveal SU-8 pillars of 25 µm height, eventually used to prepare both NOA and PDMS cavities.

3.1.1.1 Protocol for Fission yeast cytokinetic rings

Microcavities for fission yeast was previously designed in the lab. Cavities were fabricated with a conical bottom, using deep ion etching method [95][96][97][98]. The diameter and height of these microcavities were chosen based on the cell type (~ 5 µm diameter and ~ 15 µm height).

3.2 PDMS motif preparation

3.2.1 Motif preparation for multicellular rings

The following steps are followed for obtaining PDMS motifs used in experimental procedures for obtaining multicellular epithelial cell contractile rings.

3.2.1.1 PDMS motifs for wound rings in epithelial cell monolayer

For preparing rings of epithelial cell monolayer, PDMS stamp with pillars of 80µm height are required. For this purpose, photolithography is followed to obtain SU-8 pillars on the Si-wafer. Next, liquid PDMS (Polydimethylsiloxane, base: crosslinker; 10:1, v/v) mix is prepared by thoroughly blending the constituents with the help of a glass rod.

1. After mixing base and the crosslinker, it is poured over the wafer containing the desired motifs (prepared through photolithography). This is exposed to vacuum inside a desiccator until air bubbles trapped inside the polymer mix are removed (Figure 3.1 (iii)).
2. After obtaining a clear polymer layer over the wafer, it is incubated at 65°C for at least 4 hours for the polymer to cure.
3. After PDMS layer is cured, it is carefully peeled off the wafer revealing cavities inside the PDMS mold, hence denoted as *master 1* from here on.
4. Next, a soft lithography technique known as *replica molding* is followed where master 1 is activated under oxygen plasma using a plasma activator (power 3.5, O_2 flow 4.4, 20s) followed by silanisation with chlorotrimethlysilane (TMCS) for 30min inside an enclosed space.
5. After silanisation liquid PDMS mix is poured over master 1 and exposed to vacuum inside a desiccator to remove air bubbles trapped inside the polymer mix. This step ensures that PDMS fills all the microstructures (holes) inside the master 1.
6. After obtaining a clear polymer layer over the wafer, it is incubated at 65°C for at least 4 hours for the polymer to cure.

7. Cured polymer layer is carefully peeled off the PDMS master 1 revealing PDMS pillars on the replica.
8. This PDMS replica stamp (with pillars) is used to prepare for experiments studying rings in epithelial cell monolayer.

3.2.1.2 PDMS motifs for epithelial cell O rings

PDMS stamp with holes of 25µm deep are required. For this purpose, photolithography is followed to obtain SU-8 holes on the Si-wafer. Next, liquid PDMS (Polydimethylsiloxane, base: crosslinker; 10:1, v/v) mix is prepared by thoroughly mixing the constituents with the help of a glass rod.

1. This mix is then poured over the wafer containing the desired motifs (prepared through photolithography) and exposed to vacuum inside a desiccator until the air bubbles trapped inside the polymer mix can be removed. This step ensures that PDMS fills all the microstructures (holes) inside the Si-wafer (Figure 3.2 (iii)).
2. After obtaining a clear polymer layer over the wafer, it is incubated at 65°C for at least 4 hours for the polymer to cure.
3. Next, the cured PDMS layer is carefully peeled off the wafer revealing pillars of 'O' rings on PDMS replica.
4. These pillars are then used in a process known as *micro-contact printing* in order to prepare for the experimental procedure of creating epithelial cell 'O' rings (described below).

3.2.2 Cavity preparation for single cell rings

3.2.2.1 Protocol for mammalian cell cytokinetic rings

The following protocol was used to obtain PDMS/NOA-74 cavities, to orient cytokinetic rings parallel to plane of visualization.

3.2.2.1.1 PDMS cavities with bottom (polymer) layer

PDMS base and the curing agent are mixed in a ratio of 9:1 (v/v). This liquid PDMS is poured over the silicon master obtained via photolithography.

1. Liquid PDMS poured over the silicon wafers containing SU-8 pillars post-photolithography, is degassed (removing trapped air inside the liquid polymer) and cured at 65°C overnight.
2. After curing by heat, the PDMS layer is peeled off from the wafer surface. This peeled off layer is considered as Master 1, with holes in the PDMS block. This is used as replica mold to fabricate pillars used as final motifs for the preparation of cavity (Figure 3.3 (A)).
3. PDMS stamp with pillars is hydrophilized under oxygen plasma and incubated with TMCS to passivate the surface for 7min under vacuum.
4. A small amount of premixed liquid PDMS (~50µl) is poured over the motifs with subsequent spin-coating (and vacuum to hold the PDMS block) with 500rpm for 10s (to homogeneously distribute the liquid PDMS drop) and 1700rpm for 45s to obtain the preferred height (~ 40µm). (KW-4A Spin coater; SPI supplies). This thickness will be corresponding to the polymer layer at the bottom of glass coverslip (25mm; #1) (Figure 3.3 (A), i).
5. This combination of uncured PDMS block (containing pillars) is then incubated at 65°C overnight for curing (Figure 3.3 (A), ii).
6. Cured PDMS block and 25mm glass coverslip #0 (80-130µm thickness) are activated under oxygen plasma. In addition, PDMS block is bonded with the glass coverslip (coated side down). This configuration is pressed for several seconds to ensure tight bonding between them.
7. This coverslip-PDMS 'sandwich' is incubated at 65°C overnight. Longer exposure to heat helps the bonding to be stronger between PDMS and coverslip.
8. Next, coverslip is held on both sides of the PDMS block, while peeling it off carefully. This avoids the risk of coverslip breakage during the process.
9. Peeling off reveals a thin bottom layered PDMS sheet (~ 40µm), with cavities on top (Figure 3.3 (A), iii).

Even though cells are oriented in the right orientation with a good match between cell and cavity dimensions, an elastomer layer at the bottom leads to loss in resolution. This loss is related to a blurring effect due to distortion of light, caused by thin PDMS layer at the bottom. Therefore, for such configurations, upright microscopy is a preferred choice. Visualizing cells in this configuration increases spatial as well as temporal resolution, in order to capture subcellular dynamics occurring at short timescales (e.g. for cytokinesis in HeLa cells).

In order to visualise cellular dynamics with higher resolutions, cavities without polymer layer at the bottom are fabricated. Cells are placed inside these cavities and imaged using STED super-resolution microscopy.

3.2.2.1.2 Through-hole NOA-74 cavities.

Cells directly 'touching' the glass surface - without any polymer layer at the bottom - have a significant advantage to gain in resolutions during image acquisition [99]. In addition, this configuration also provides higher freedom of objective working distance as well as the ease in using both upright and inverted microscope setups. Through-hole cavities are achieved with both polymers mentioned earlier, PDMS and NOA-74.

1. Steps 1 and 2 from section 3.2.1.1 are repeated to obtain master 1 (PDMS block with holes).
2. To obtain PDMS pillars (final motifs for cavity preparation), Master 1 is activated under oxygen plasma. Next, it is passivated with chlorotrimethylsilane (TMCS) under a desiccator for 20-30 mins. Post-silanisation PDMS is poured over the Master 1 (with holes), degassed and cured at 65°C overnight.

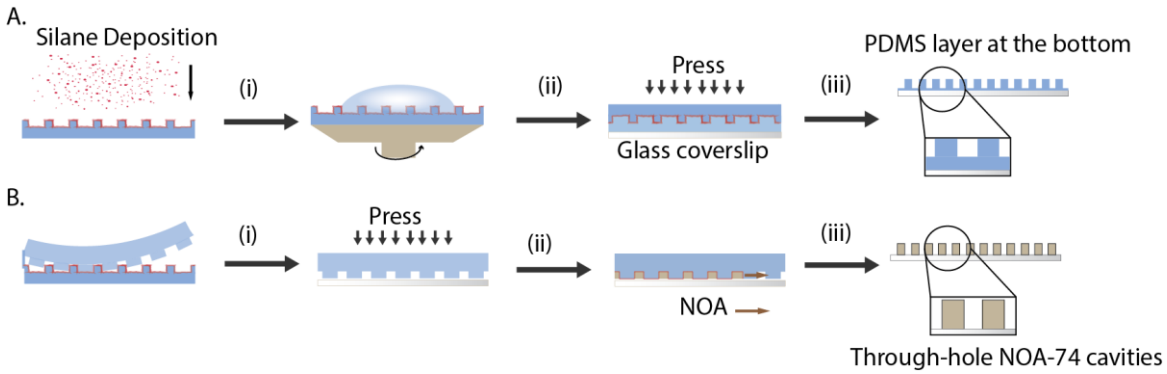

Figure 3.3: Schematic representation of cavity preparation. *After micro-fabrication process using photo-mask of desired dimensions, cavities are prepared with the help of PDMS block containing pillars. A. For preparing cavities with polymer layer at the bottom, first TMCS is deposited on the PDMS master to passivate the surface and later spin-coated with PDMS (base: crosslinker; 1:9) to obtain the desired PDMS thickness (i). Post crosslinking at 65°C for 4h or overnight, the PDMS assembly and a clean coverslip is activated under oxygen plasma and bonded with each other by pressing the assembly uniformly (ii).* Post incubating the assembly at *65°C overnight, PDMS block is peeled off carefully revealing cavities left behind on the coverslip (iii). B. For preparing through-hole cavities, first a PDMS mold with pillars is obtained through replica molding of master1 and plasma bonded with a clean glass coverslip (i). After incubating assembly at room temperature for 1h, NOA-74 is introduced from the sides of the assembly (ii). After UVA crosslinking of NOA-74, the PDMS block is carefully peeled off revealing through-hole cavities (iii).*

3. After curing, PDMS is peeled off the Master 1 (PDMS with holes) revealing PDMS block with pillars of target height.
4. To obtain cavities without PDMS layer at the bottom, first, blocks of PDMS with pillars (0.5cm X 0.5cm) are cut and sonicated (5min) with 70% ethanol to remove any dirt and residual silane.
5. These PDMS blocks (with pillars) are used for the preparation of cavities for fission yeast cells, as well as through-hole NOA-74 cavities for HeLa cells.
6. Surfaces of PDMS pillars are activated under oxygen plasma, along with the glass coverslip on which pillars are to be bonded (Figure 3.3 (B), i).
7. Activated PDMS block with pillars is now turned (activated side down) and put on top of the activated coverslip. The assembly is carefully pressed to ensure proper bonding. Inadequate bonding would lead to non-through-hole cavities. Excessive strong bond will result in blocked cavities. Care is taken that the pressure does not tilt these pillars.
8. The assembly is then incubated for passivation with TMCS in a desiccator for 20-30 mins. Passivation is done to prevent irreversible bonding of PDMS pillars with the introduced polymer (NOA-74).
9. Post-passivation: the polymer (NOA-74) is introduced as a drop on one side of the assembly. Capillary action pulls the polymer into the assembly. Speed of polymer flow throughout the assembly is dependent on height of the pillars as well as viscosity of the polymer. For example, NOA-74 is less viscous than PDMS and will 'travel' through the assembly quicker and more efficiently than PDMS. Desiccator can be used for 5-7 min for efficient and homogeneous filling of pillars, removing any air bubble trapped inside the assembly (Figure 3.3 (B), ii).
10. Polymer NOA-74 incubated assembly is then placed for curing (crosslinking) inside a chamber with UV-A source for minimum 4-6 hours.
11. After curing, pillars are carefully peeled off the surface of coverslip. Through-hole NOA-74 cavities are revealed, directly attached to the glass coverslip without any polymer layer at the bottom (Figure 3.3 (B), iii).

3.2.2.2 Protocol for fission yeast cytokinetic rings

Imaging of dividing yeast cells can be done by orienting the cytokinetic rings either parallel (on coverslips) or perpendicular (inside cavities) to the plane of visualisation.

1. For imaging the rings parallel to the plane of visualization, cells are placed inside PDMS cavities prepared via deep ion etching method [96][100][98] of silicon wafers to obtain "V" shaped bottom, columnar micro-cavities. The diameter of the cavities is chosen to be ~5 µm and height is chosen to be 6-10 µm.
2. Next, through soft lithography, replica of this wafer is prepared by pouring liquid PDMS (base: crosslinker; 1:9), degassed under vacuum and incubated at 65°C overnight. After PDMS is crosslinked, molded "V" shaped pillars on the PDMS is carefully peeled off the surface of the silicon wafer.
3. After obtaining the PDMS stamps with "V" shaped bottom columnar pillars, the motifs are plasma activated and silanised with TMCS under vacuum for 30min.
4. Next, 25mm glass coverslip #0 is hydrophilised via activation under oxygen plasma and spin-coated with a drop of un-crosslinked PDMS (base: crosslinker; 1:9) at 1500rpm for 30s for a thickness of around 50 µm. Also, a small piece of crosslinked PDMS piece (holder) is glued to the side of the coverslip, by placing it with small drop of un-crosslinked PDMS.
5. Simultaneously a drop of TMCS is put on top of PDMS stamp with "V" shaped columnar pillars, silanised prior with oxygen plasma and is let to evaporate for ~5min. This will passivate the surface against any un-crosslinked PDMS coming in contact with its surface.
6. Next, the silanised stamp placed face (containing pillars) down on the PDMS spin-coated coverslip and pressed gently once to make sure that stamp is parallel to the coverslip surface.
7. The assembly is put inside an oven maintained ta 65°C for 4-6h/overnight.
8. Next, the PDMS stamp is gently peeled off, revealing cavities with "V" shaped bottom.
9. Coverslip with cavities is cleaned by sonicating it for ~5min immersed under ethanol. The motifs are dried under stream of N_2 and is ready to use for placing fission yeast cells inside for studying the cytokinetic ring.

3.3 Cell culture

3.3.1 Mammalian cell culture

Mammalian cells are cultured inside Petri dish (60 x15mm). Petri dishes with cells are incubated inside a temperature and humidity-controlled chamber, maintained at 37°C with 5%. Both cell types are cultured till 60-70% confluency. Trypsin 0.25% EDTA is used for replating cells. Antibiotics are added to the medium with cells expressing tagged proteins. Below mentioned are cell lines are used in the study:

Cell lines	Fluorescent markers	Source	Complete media
MDCK **wild type (WT)**	--	Prof. S. Yonemura RIKEN, Japan	DMEM LG[1] + 1% antibiotics[2] + 10% FBS
MDCK MRLC GFP	*Wild type* ***M****yosin* ***r****egulatory* ***l****ight* ***c****hain* - GFP	Prof. S. Yonemura RIKEN, Japan [101]	DMEM LG + 1% antibiotics[2] + 10% FBS + 400 µg/ml Geneticin
MDCK MRLC AA	*Non phosphorylatable* *MRLC* - GFP	Prof. S. Yonemura RIKEN, Japan[101]	DMEM LG + 1% antibiotics + 10% FBS + 400 µg/ml Geneticin
MDCK MRLC KO1 **Ecad mNG**	*Wild type* *MRLC* – KO1 *E-cadherin*- mNG	Prof. S. Yonemura RIKEN, Japan	DMEM LG + 1% antibiotics + 10% FBS + 400 µg/ml Geneticin
MDCK FRET	FRET Donor: acceptor (CFP/YFP[13])	Riveline lab	DMEM LG + 1% antibiotics + 10% FBS + 250 µg/ml Hygromycin B
MDCK FRET **MRLC mCherry**	FRET Donor: acceptor (CFP/YFP[13]) MRLC - mCherry	Riveline lab	DMEM LG + 1% antibiotics + 10% FBS + 250 µg/ml Hygromycin B
Hela **wild type (WT)**	--	Prof. A. Hyman MPI-CBG, Dresden	DMEM HG[3] + 1% antibiotics + 10% FBS + 2mM L-Glutamine
Hela MHC GFP **LifeAct mCherry**	MHC-GFP LifeAct mCherry	Prof. A. Hyman MPI-CBG, Dresden	DMEM HG+ 1% antibiotics + 10% FBS + 500 µg/ml Geneticin + 2mM L-Glutamine
MDCK E-cadherin-GFP	E-cadherin GFP	Nelson lab.	DMEM HG+ 1% antibiotics + 10% FBS + 500 µg/ml Geneticin + 2mM L-Glutamine

[1] 1g/L glucose
[2] 100 µg/ml Penicillin Streptomycin (PenStrep)
[3] 4.5 g/L glucose

Table 3.1: Cell lines used for the study

3.3.2 Fission yeast culture conditions

Schizosaccharomyces pombe also known as *fission yeast* is a unicellular fungus with rod-like shape. It is a widely used model organism to study cell division. Culturing of this organism can be done on a laboratory bench near a Bunsen burner flame to avoid aerial microbial contamination.

3.3.2.1 Culture media

Fission yeast cells are cultured in autoclaved yeast extract (YE+5S) medium and/or Edinburgh minimal enrichment medium (EMM+5S) according to the application [102][103]. Cells are cultured and maintained in YE5S media broth and/or on YE5S agar plates. EMM media is filtered (rather than autoclaved) to be used for imaging purpose. This ensures absence of auto-fluorescence emerging due to charring of glucose in the media. We followed the culture protocols as suggested in the Nurse lab manual [102].

3.3.2.2 Freezing and thawing of yeast cells

Cells to be expanded from filter paper strip (containing yeast cells) needs to be placed on top of a YES agar plate with few drops of autoclaved water to soak the paper strip. Next, this water-soaked strip containing yeast cells, is dragged through the YES agar plate and eventually maintained at 32°C for 2 days to obtain yeast colonies.

Thawing: Using a 5mm diameter loop, cells are scraped from a frozen vial and streaked on one side of the YES agar plate as a source for obtaining yeast colonies. Next, with a help 2mm diameter loop, cells are streaked as straight vertical lines with respect to the original streaked portion. To further spread the cells better, the same 2mm loop is passed vertically on to the previous straight lines. Two-step streaking process makes sure of obtaining isolated yeast colonies, to be used in further steps of culture expansion, freezing and experimental setups. After maintaining the streaked YES agar plates at 32°C for 2-3 days, one isolated colony is picked up and re-streaked on a fresh YES agar plate in a similar way as described earlier. This ensures appropriate recovery of the frozen stock by providing sufficient time after un-freezing and synchronisation of the culture to some extent. This plate is referred to as mother plate and can be stored at 4°C for 10 days for further usage for culture expansion and experiments.

Freezing: Cells passaged at least twice on YES agar plates can be used for freezing. After the second passage, isolated single colony is picked up with a 5mm diameter loop and streaked on a YES plate without any break, to obtain a monolayer of cells on the YES agar plate. The plate is incubated for 3 days at 32°C. Next, all the cells are scrapped and released into a cryovial filled with ~1.5ml of yellow freezing mix (YES5S + Glutamic acid + 30%glycerol)[102] The vial with cells in thoroughly agitated to prevent cell clumping inside the vials. Prepared cryovials can be stored at -80°C for several years.

3.4 Transfection

Transfection is performed by liposome mediated technique using Lipofectamine 2000 reagent (Invitrogen). Following Protocol for transfection was performed inside a 6 well plate (volume 2ml)

1. 24h before the transfection process, cells are trypsinized from a 60-70% confluent plate (60 x 15 mm) and seeded inside a 6-well plate (dilution; 1:10).
2. Cell culture medium is changed (from 10% FBS) to medium with 1% serum (FBS).
3. Two Eppendorf vials with 150 µl of Opti-MEM media are prepared.
4. Plasmid DNA (1µg) of interest is diluted inside one of the vials containing Opti-MEM.
5. Lipofectamine reagent (~7µl) is diluted in the second vial containing Opti-MEM.
6. Both vials with mixture (DNA**:** Opti-MEM, Lipofectamine**:** Opti-MEM) are incubated for 5min at room temperature.
7. Diluted DNA is added to the Lipofectamine vial and incubated at room temperature.
8. After 10mins the DNA-Lipofectamine mixture is added to the well with spread cells.
9. After 4-6h cell culture medium is changed to the standard culture medium (10% serum; FBS).

3.5 Sample preparation

3.5.1 Sample preparation for multicellular rings

3.5.1.1 Sample preparation for obtaining cell monolayer wound rings

The following steps are followed to obtain shape and size controlled wound rings. This protocol was adapted from [16].

1. PDMS stamp with pillars is peeled off the silanised PDMS master 1 and cut in 0.5x0.5cm dimension. It is made sure that stamp is cut, close to the pillars. This assures liquid to enter the assembly easily through capillary action.
2. Prepared PDMS stamps is sonicated with 70% ethanol. This ensures any residual silane to be removed from the PDMS pillars.
3. PDMS stamps are dried inside an oven maintained at 65°C, for 10min.
4. Glass coverslip and dried PDMS stamp (replica of master 1) with pillar side up is activated under oxygen plasma.

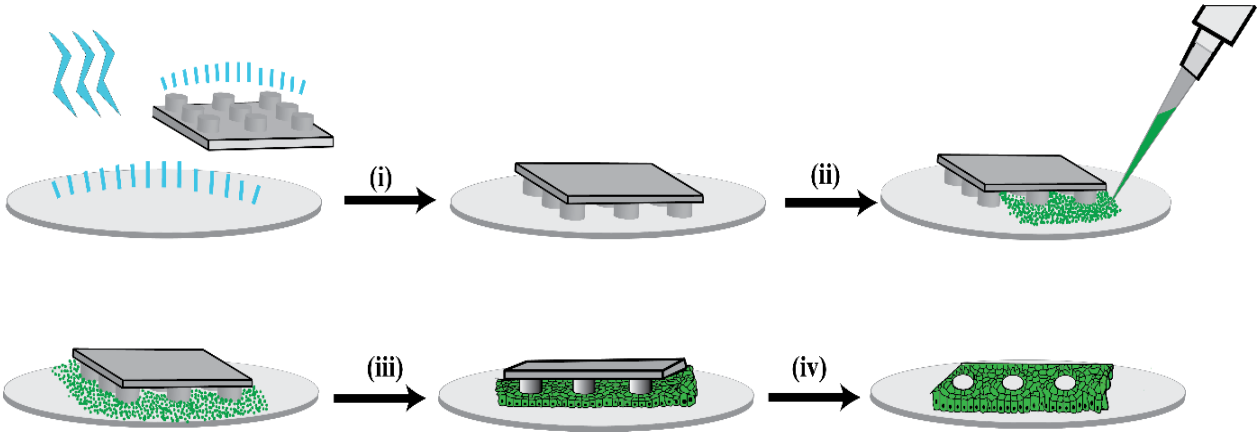

Figure 3.4: Schematic representation of protocol followed to obtain rings in epithelial cell monolayer: *First the glass coverslip and the PDMS stamp with pillars is plasma activated, carefully bonded with each other and left at room temperature for 1h (i). After passivation with Pluronic acid for 1h, cells are introduced from all sides to ensure an even distribution (ii). Next, the assembly is incubated for 12-16h at 37°C and 5% CO_2.*

5. Both entities are bonded with each other and the assembly is pressed gently to assure good attachment.
6. The assembly is passivated with ~ 100µL of 0.2% pluronic acid (in Milli-Q). This ensures that the spread monolayer does not peel off later, during stamp removal.
7. The assembly is incubated with pluronic acid for ~1h. After the incubation is over, passivation solution is drained out of the assembly.
8. The assembly is left to dry at room temperature (for 30mins) or an incubator maintained at 37°C (for 10mins).
9. Next, the assembly is exposed to vacuum inside a desiccator to get rid of air trapped between pillars and the coverslip. The assembly (glass coverslip: PDMS stamp) is placed inside a Petri dish (35 x 10 mm).
10. Next, a confluent plate (60 x 15 mm) of spread epithelial (MDCK) cells is trypsinized using trypsin-EDTA (0.25%) solution.

11. Cells are harvested and seeded at a density of 21500 cells/µl ($2X10^7$/ml) from all sides of the assembly. Seeding from all sides ensures a homogeneous distribution of cells on the coverslip between the pillars. This assembly with cells is incubated for 1h inside a temperature-controlled chamber maintained at 37°C with 5% CO_2. This ensures cell attachment to the glass coverslip.
12. Next, 2ml of complete DMEM culture medium is put inside the Petri dish (35 x 10 mm) holding the coverslip with cells. Cells are incubated for ~12-14h inside a temperature-controlled chamber maintained at 37°C with 5% CO_2.
13. After ~14h cells can be seen to have formed a monolayer with circular wounds at the place of attached PDMS pillars.
14. Next, PDMS stamp with pillars is carefully removed from the glass coverslip with the help of a pair of tweezers. Removal of PDMS pillars should be performed very carefully without disturbing the epithelial cell monolayer around the pillars.
15. Removal of the PDMS pillars leaves behind circular wound rings, inside the epithelial cell (MDCK) monolayer.
16. Ring closure dynamics is acquired on the microscope setup with appropriate objective under controlled temperature conditions of 37 °C inside self-buffered L-15 medium with 10% FBS.

3.5.1.2 Sample preparation for obtaining epithelial cell 'O' rings

3.5.1.2.1 Micro-contact printing

It is widely followed soft-lithography technique used to transfer proteins of interest onto a surface in the form of patterns, for e.g. on glass surface in our case. Such environments when exposed to cells, can impose cell shape changes [104] and can provide important insights in studying single cell motion [105] as well as monolayer dynamics.

Following are the steps to obtain patterned glass surface for studying ring constriction with controlled cell number. We use patterns of fluorescent fibronectin (TRITC; red); an extracellular matrix protein.

3.5.1.2.2 Coverslip silanization

1. First, the coverslips are treated with *Piranha* solution (Sulphuric acid: Hydrogen peroxide [7:3]) for 10min. This ensures freeing up of the –OH groups through hydrolysis of the glass coverslip. This process in turn leads to formation of bubbles on the glass surface. Coverslips are kept immersed inside the solution, throughout this process. This step should be cautiously performed under the fume hood (Figure 3.5, (i), left).
2. Rinse the glass coverslip with Milli-Q water, put them inside glass beakers and sonicate for 5min. Hold the clean coverslip with the help of a tweezer and dry it under a nitrogen stream.
3. Next, put them inside an oven maintained at 65°C for 10min.
4. Place the *piranha* cleaned coverslip inside a vacuum environment via desiccator, incubated in the presence of 100µl of 3-(mercapto) propyltrimethoxysilane (MPTMS) for 1h (Figure 3.5, (ii), left).
5. Leave the silanised coverslip inside an oven maintained at 65°C for at least 90min (up to 4h).

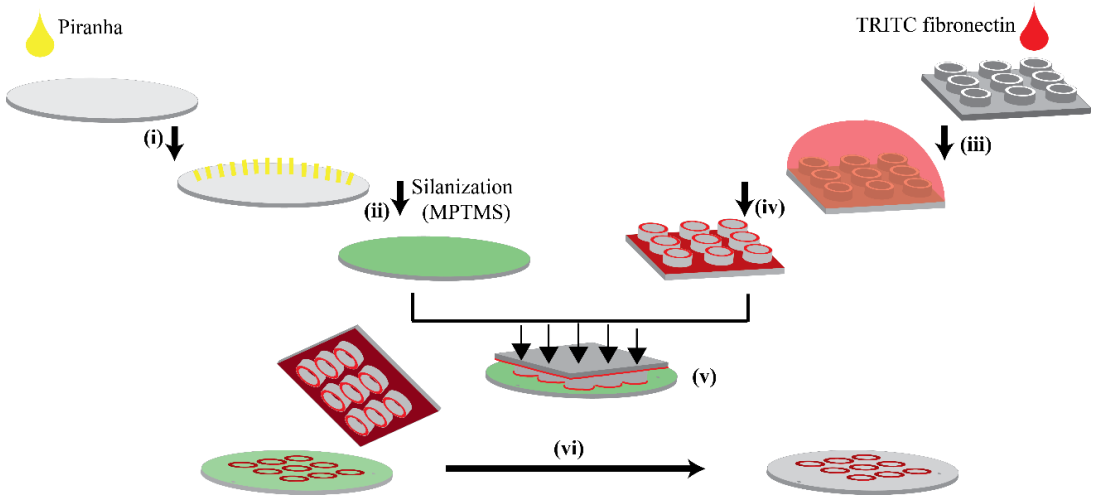

Figure 3.5: Schematic representation of the microcontact printing process: *Glass coverslip is cleaned and activated through incubation in Piranha solution followed by silanisation with MPTMS vapor (i, ii) and placed at 65°C. In parallel, PDMS stamp with 'O' ring shaped pillars is activated through oxygen plasma and incubated with TRITC tagged fibronectin solution for 30min (iii). Next, this solution is removed from the PDMS stamp and dried carefully (iv). Next, fibronectin is stamped on the silanised coverslip (v). After careful removal of the stamp, 'O' ring patters of fibronectin can be revealed on the glass coverslip (vi). This should be stored in Milli-Q water at 4°C.*

3.5.1.2.3 Stamp preparation

1. PDMS stamp with 'O' ring pillars is peeled off the Si-wafer containing SU-8 'O' ring holes.
2. Care is taken to cut the edges of PDMS stamps straight in 1cm x1cm dimension. This is essential for a later step, to hold off the fibronectin liquid drop on top of it.

3. Sonicate the PDMS stamps containing ‘O’ rings; obtained via photolithography, in ethanol for 5min and dry them with a nitrogen stream. Keep it inside an oven maintained at 65°C for 10min.
4. Activate the dried PDMS stamps (‘O’ ring pillars side up; face) with Oxygen plasma. This will ensure hydrophilicity of the surface suitable for protein binding.
5. Incubate plasma activated PDMS stamps with a ~100µl drop of 10µg/ml solution of fluorescent (TRITC) fibronectin for 1h placed at a levelled surface. This assembly is covered with an opaque and humid cover to avoid evaporation of the drop (Figure 3.5, (ii), right).
6. After the incubation remove the drop with a pipette and dry it with a nitrogen stream or leave it at room temperature for 5min. This step is critical for the optimal quality of patterns transferred on to the glass coverslip.

3.5.1.2.4 Protein Stamping

1. Dried PDMS stamps are put face down on the silanised coverslip. Put a weight of ~50g on top of it, ensuring optimal transfer of the patterns. Incubate this assembly for 30mins at room temperature. (Figure 3.5, (v)).
2. Next, gently remove the weight and the PDMS stamp from the coverslip revealing the ‘O’ ring patterns. The quality of the patterns is checked to be homogeneous, with a fluorescence microscope setup using a 4X/10X objective.
3. Coverslip with protein patterns can be stored inside Milli-Q water at 4°C for several days.

3.5.1.2.5 ‘O’ ring preparation

The following steps are followed to obtain shape and size controlled epithelial cell wound rings.

1. Coverslip with fibronectin ‘O’ ring patterns obtained via stamping is incubated with a 100µl drop of 100µg/ml PLL-g-PEG, placed face down on a flat parafilm sheet.
2. This assembly is covered with an opaque and humid cover incubated for ~20min.
3. After 20min this coverslip can be stored inside a Petri dish with PBS, until cell seeding.
4. Next, a confluent plate (60 x 15 mm) of spread epithelial (MDCK) cells is trypsinized using trypsin-EDTA (0.25%) solution.

5. Cells are harvested, centrifuged and resuspended in 500µl of DMEM culture medium with 1% FBS. Reduced serum concentration facilitates weaker attached of cells outside of the 'O' rings and reduced cell division.

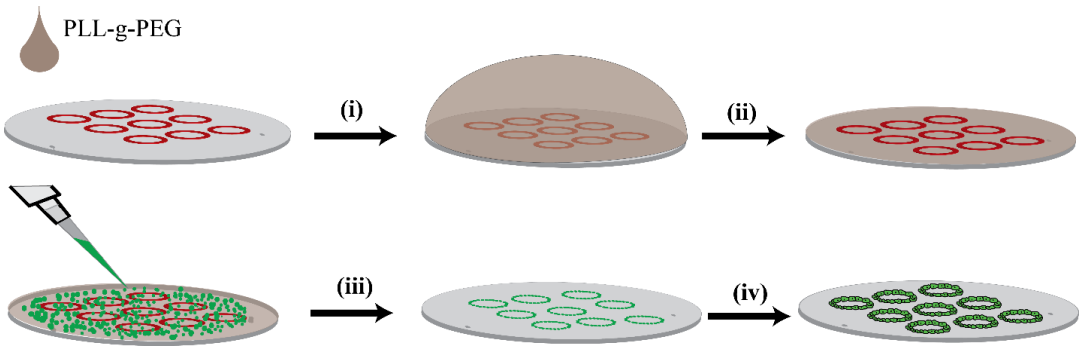

Figure 3.6: Schematic representation of protocol followed to obtain epithelial cell 'O' rings: *First the fibronectin (FN) patterned glass coverslip is incubated with PLL-g-PEG (i) for 20min to passivate the surface outside and inside the FN 'O' rings (ii). Next, epithelial (MDCK) cells are seeded on the coverslip and incubated for 1h in low serum (1% FBS) DMEM culture medium. After 1h, the coverslip is washed with new medium to remove the loosely attached cells settled on the passivated parts of the coverslip (iii). Next, the cells are allowed to spread for 30min inside an incubator maintained at 37°C with 5% CO_2, forming epithelial cell 'O' rings (iv).*

6. Patterned and passivated coverslip is carefully fitted inside a metal holder to be used for imaging.
7. Harvested ~2x10^6 cells in 500µl of culture medium is put on top of the coverslip and incubated for 1h inside a temperature-controlled chamber maintained at 37°C with 5% CO_2 (Figure 3.6, (ii)).
8. Incubation of the fibronectin (FN) pattered coverslip with high cell density will increase the probability of cells to settle down on the FN patterns.
9. After 1h incubation, remaining unattached cells are pipetted out of the metal holder containing the coverslip.
10. Passivation via PLL-g-PEG and incubation with low serum medium will avoid strong attachment of cell settling outside of the 'O' rings. Nonetheless, some cells invariably attach in the vicinity of 'O' rings and should be removed carefully by pipetting up and down with a 200µl tip (Figure 3.6, (i)).
11. Carefully removing the loosely attached cells on the coverslip reveals attached cells, on the FN ring patterns.

12. Next, the cells are allowed to spread for 30min inside an incubator maintained at 37°C with 5% CO_2 revealing epithelial cell 'O' rings (Figure 3.6, (vi)).
13. Ring closure dynamics is acquired on the microscope setup with appropriate objective under controlled temperature conditions of 37 °C inside self-buffered L-15 medium with 10% FBS.

3.5.2 Sample preparation for single cell rings

3.5.2.1 Sample preparation for orienting mammalian cell cytokinetic rings

3.5.2.1.1 Cell cycle synchronization of HeLa cells

HeLa cells are seeded inside 75cm^2 flasks (2-3 flasks) at a concentration that allows to have a 60-70% confluent flask surface at the day of seeding. Moments prior to cytokinesis, cells round up from their earlier spread state. Attributing to the round shape, cells at 'M' phase have weaker attachment to the substrate as compared to their counterparts (spread cells).
Taking advantage of this property, such cells were harvested from a 75cm^2 flasks by mechanical shake-off and concentrated via centrifugation at 500rpm for 3min and resuspended into 1ml culture medium [95]. This concentrated population of cells is ready to be placed inside the cavities or on a glass coverslip in order to visualize dynamic cytokinetic ring components.

3.5.2.1.2 Orienting cytokinetic rings parallel to the focal plane

1. Small rectangular piece of PDMS is attached to the side of the coverslip with cavities. The PDMS piece is attached with a drop of un-crosslinked PDMS. This assembly is incubated inside an oven maintained at 65°C for 4h. Such PDMS block will serve as a holder to handle the cavities with help of tweezers in the subsequent steps.
2. Cavities are plasma activated under oxygen plasma.
3. Cavities are further immersed in 10 μg/ml fibronectin solution inside a culture plate for 4h incubated at room temperature.
4. Cylindrical PMMA piece is introduced inside 50ml tube.
5. Culture media; 6ml is introduced into the tube until it forms a thin layer over the PMMA piece.

6. Coverslip with cavities is handled carefully with the help of tweezers, holding the rectangular PDMS block attached to them. It is placed carefully inside the tube over the PMMA piece.
7. Harvested cells (3.5.2.1.1) are centrifuged at 500rpm for 3min. Cell pellet is resuspended in 2ml of culture media and placed over coverslip inside the 50ml tube.
8. This assembly is centrifuged at 1500-2000rpm for 2min. The process is repeated three times. Between each repeat, media containing cells is carefully mixed to dissociate any cell clusters formed during the process of centrifugation. This step ensures a better filling percentage.
9. After the centrifugation steps, cavities are carefully removed and fitted inside a metal holder with selected culture medium, and the sample is ready for acquisition under a microscope.

3.5.2.1.3 Cytokinetic rings on flat surface

1. Clean and dry coverslip is taken and a small PDMS piece is glued to the side via un-crosslinked PDMS. The assembly is incubated inside an oven maintained at 65°C for 4h or overnight. Following this step, coverslips are ready to be handled with the help of a tweezer, necessary for the following steps. Such PDMS block will serve as a holder to handle the coverslip via tweezers in the subsequent steps.
2. Next, the coverslip with PDMS holder is hydrophilized under oxygen plasma and incubated with 10 µg/ml fibronectin solution for 3h inside a culture plate at room temperature or at 4 °C overnight.
3. Next, the coverslip with cells at 'M' phase is obtained as described in *section 3.5.2.1.1*

3.5.2.2 Sample preparation to orienting fission yeast cytokinetic rings

3.5.2.2.1 Yeast culture preparation

1. A well-defined isolated single colony is selected from the YE5S agar mother plate and with a plastic loop and released into a culture tube containing 5ml of YE5S media marked as starter culture. The tubes in use should have movable caps which will ensure proper gas exchange with the environment.
2. The starter culture is incubated at room temperature for 3 days until a white precipitate can be seen settled at the bottom of the tube.

3. The tube is thoroughly vortexed to get the cell pellet distributed evenly in the media. Next, dilution is made from the starter culture into a flask containing 10 ml of YE5S media by adding 5, 10, 20 and 30 µl of the starter culture.
4. The flask is covered with aluminium foil (avoiding aerial contamination) and kept for shaking inside an incubator shaker maintained at 32°C and 200rpm for 18-28h. Different dilutions through the procedure) is chosen to ensure proper range of OD at different time points. Flasks containing 30µl 20µl 10µl 5µl will reach desired optical density (OD) of 0.2-0.8 at 18, 20, 24 and 28h post inoculation respectively.
5. The flask is shaken thoroughly and the OD of 1ml culture is determined. This measurement is done with a spectrophotometer. First, the system is calibrated with a cuvette containing 1ml of YE5S media (blank). Next, OD for all the flasks with yeast culture is determined. Flask with the most appropriate OD; 0.2 - 0.4 is chosen. This ensures the culture to be in the exponential phase with maximum number of dividing cells per volume of the media during the time of inoculation.
6. Next dilutions are done in EMM5S media incubated at 27°C. This temperature shift is to ensure the culture adaptation to the imaging conditions which also includes EMM5S (filtered) media at 27°C. The chosen flask is again thoroughly shaken and 1ml of is this media is centrifuged in an Eppendorf tube. Leaving the cell pellet, YES5S media is removed and replaced with 1ml of EMM5S media.
7. Dilutions of 100µl 300µl 500µl 700 µl are made in fresh flasks with 10ml of EMM5S media. Flasks containing 700, 500, 300 and 100 µl will reach desired OD of 0.2-0.8 at 15, 18, 20 and 24h post inoculation.
8. After reaching the desired OD yeast cells can be used to study dynamic cytokinetic ring constriction.

3.5.2.2.2 Orienting cytokinetic rings parallel to the focal plane

For imaging the cytokinetic rings parallel to the focal plane, cells are placed vertically inside the “V” shaped columnar PDMS cavities.

1. Place the PMMA hollow cylindrical piece fitting inside the 50ml Falcon tube.
2. Introduce 13ml of EMM5S media inside the Falcon. Next, with the help of a tweezer, take the ethanol cleaned coverslip containing cavities and place is carefully inside the falcon. At this stage the coverslip should be covered with a thin layer of EMM5S medium.
3. Next, introduce 5ml of EMM5S medium with yeast cells measured to be at the desired OD.

4. Centrifuge the assembly at 4000rpm for 3 min. Next remove the Falcon tube and swirl the medium to detach the cells settled on the coverslip outside the cavities.
5. Repeat step 4, 3 times. This ensures maximum filling percentage of cells inside the cavities.
6. Remove the coverslip containing cavities from the Falcon carefully with the help of a tweezer and put it inside the metal holder (used for imaging). Clean the coverslip, removing the unattached yeast cells by washing the coverslip with 1ml of filtered EMM5S media 3 times and finally filled with 2ml fresh EMM5S medium.
7. This will make sure that the surface of PDMS cavity is clean and therefore dynamic cytokinetic rings can be visualized inside a temperature-controlled chamber, maintained at 27°C.

3.5.2.2.3 Cytokinetic rings on flat surface

For imaging the rings perpendicular to the focal plane, the cells are placed on a glass coverslip.

1. Fission yeast cells placed directly on an uncoated glass coverslip get displaced with time due to thermal fluctuations. To ensure the stable positioning of yeast cells over time, glass coverslip is coated with lectin (ConA) binding glycoproteins of the yeast cell wall. For this purpose, a 200 µl drop of lectin (100 µg/ml) is introduced in the middle of the coverslip surface and allowed to dry. Such lectin coated coverslips can be maintained at room temperature for 20-30 days for further usage.
2. Yeast cells from an exponential culture inside EMM5S media is introduced over the dried lectin spot fitted inside the metal holder (for imaging). Cells are allowed to settle down on the glass surface for 10min.
3. Next, the metal holder with filled with 2ml of filtered EMM5S medium and proceeded for acquisition of cytokinetic ring constriction.

3.6 Drug experiments for multicellular rings

To investigate the role of cytoskeletal elements and the factors upstream and downstream to them following drugs were used:

Name	Effect	Incubation time (h)	Washout	Working concentration
ML7	MLCK inhibitor	1.5/10h	Y/N	100µM
C3	Inhibition of Rho proteins (A, B, C)	1.5/10	N	1 µM
Y27632	Inhibition of Rho associated kinase (ROCK)	10	N	50 µM

Table 3.2: Drugs used and their corresponding concentrations and incubation times.

Some of the drugs were tested with conditions with and without washout. This has been indicated in the table as Y (yes; washout) and N (no washout). For washout, the original media was removed and the drug with desired concentration was introduced, diluted in 2ml of L-15 medium with 10% FBS. After the incubation is over, the drug containing culture media is removed carefully (while on the microscope setup) and washed 3 times with fresh L-15 medium. Next, fresh 2ml of L-15 medium with 10% FBS is introduced for further acquisition. All drugs were dissolved in DMSO.

3.7 Immunostaining

3.7.1 Staining protocol for multicellular rings

Immunostaining is used followed for studying protein localization during cell frozen state achieved via paraformaldehyde (PFA) treatment.

1. Culture media is aspirated from the plate with coverslip containing epithelial cell monolayer wound rings removed from the incubator maintained at 37°C with 5% CO_2.
2. Prewarmed 4% PFA in 1X PBS maintained at 37°C, is added on top of the coverslip containing cells. It is incubated at room temperature for 8min. This would lead to crosslinking of proteins in their original state as existed during *'live'* conditions.
3. Next, the sample is washed with 1X PBS, 3 times to remove any trace of the fixative (PFA).
4. The cells are permeabilized with 2ml 0.5% of Triton (in 1XPBS) for 3 min.

5. After this, Triton solution is aspirated and washed 3 time with 1X PBS to remove any trace of permeabilising agent.
6. Next, the sample is incubated with blocking solution; 5% BSA (in 1XPBS) for 1h. This allows the blocking of surface for any non-specific binding during the antibody (primary 1°, secondary 2°) treatment.
7. Primary and secondary antibodies are diluted in blocking solution in the concentration of 1:100 and 1:400 respectively. First, primary antibody is prepared in 150 µl final solution.
8. For staining, a Parafilm sheet is spread flat on the bench with a few drops of water at the bottom.
9. Next, 1° antibody drop; 150 µl is pipetted out on the parafilm and the coverslip with treated cells are flipped upside down on to the antibody drop.
10. The sample is incubated for 90min at room temperature under a covered box with a water-soaked tissue paper on its roof. This is to ensure humid conditions to avoid evaporation of the antibody solution. Primary antibody incubation can also be done overnight at 4°C.
11. Next, the coverslip is carefully picked up with a help of tweezer from the Parafilm strip and placed cells side up on a plate and washed 3 times with 1X PBS to strip off the remaining primary antibody from the surface.
12. After the washing, cells are incubated with 2° antibody in the same manner as step 10 for 60min.
13. The coverslip is carefully picked up with a help of tweezer from the parafilm strip and placed cells side up on a plate and washed 3 times with 1X PBS to strip off the remaining secondary antibody from the surface.
14. Next, the cells can be stored for 2-3 days in 1XPBS at 4°C before imaging or the sample can be mounted on a microscope glass slide with 20 µl of PBS: glycerol solution (1:1).
15. After careful mounting, excess mounting solution is removed from the coverslip edges with the help of a tissue paper and sealed with nail polish.
16. Slides are allowed to dry at the room temperature and are ready to be imaged. Samples can be stored at 4°C later.

3.7.2 Staining protocol for mammalian cell (HeLa) cytokinetic rings

1. Clean and dry coverslip is taken and a small PDMS piece is glued to the side via un-crosslinked PDMS. The assembly is incubated inside an oven maintained at 65°C for 4h or

overnight. Following this, coverslips are ready to be handled with the help of a tweezer, necessary for the following steps.

2. Coverslip is hydrophilized under oxygen plasma and incubated with 10 µg/ml fibronectin solution for 3h inside a culture plate at room temperature or at 4 °C overnight.
3. Next, the cells harvested at 'M' phase (3.5.2.1.1) are centrifuged on a clean fibronectin coated coverslip with/without cavities as described in section 3.5.2.1.2*; steps 4-9*.
4. For immunostaining process, similar steps are followed as described in section 3.7.1 with an exception for the usage of 3% PFA. These conditions were standardised for HeLa cells.

3.8 Sample preparation: improving spatial resolution

For this purpose, two methods were followed named CLEM: Correlative Light Electron Microscopy and STED: Stimulated Emission Depletion Microscopy.
Here, I will explain the sample preparation for both methods.

3.8.1 Sample preparation for CLEM (Correlative Light Electron Microscopy)

This method utilizes Electron Microscopy (EM), of the region of interest (ROI). This region is correlated to the fluorescent microscopy image of the same ROI.
First, the region of interest is identified by epi-fluorescence microscopy and next, the sample is processed for electron microscopy.

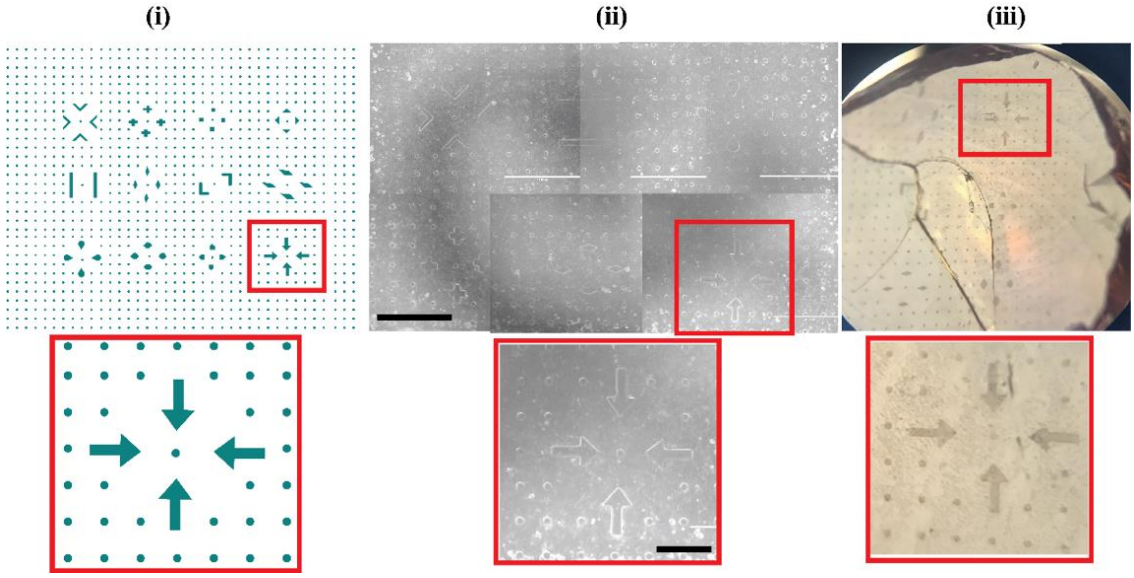

Figure 3.7: Stamp preparation for electron microscopy: *(i) Photo-mask with several different geometrical shapes around circular rings, are prepared (ii) After following the protocol for preparing wound rings (3.2.1.1), cells spread around circular rings and different geometrical shapes (zoomed view showing arrow pattern). (iii) The same area as (i) shown in a resin block, after embedding and peeling off the resin block from the coverslip. (Scale bar (ii) 1mm, (i: zoomed) 250µm).*

Here, we wanted to visualise epithelial cell wound rings and myosin clusters around the perimeter of these rings, with higher spatial resolution. Wound rings prepared through micro-fabrication are symmetrical in geometry (Figure 3.1). Therefore, it is challenging to identify a specific ring followed by a specific cluster at its perimeter.

Motifs utilized for preparing epithelial wound rings consist of circles of desired diameter, at regular intervals. Therefore, in order to trace back a specific ring of interest, it is imperative to break the

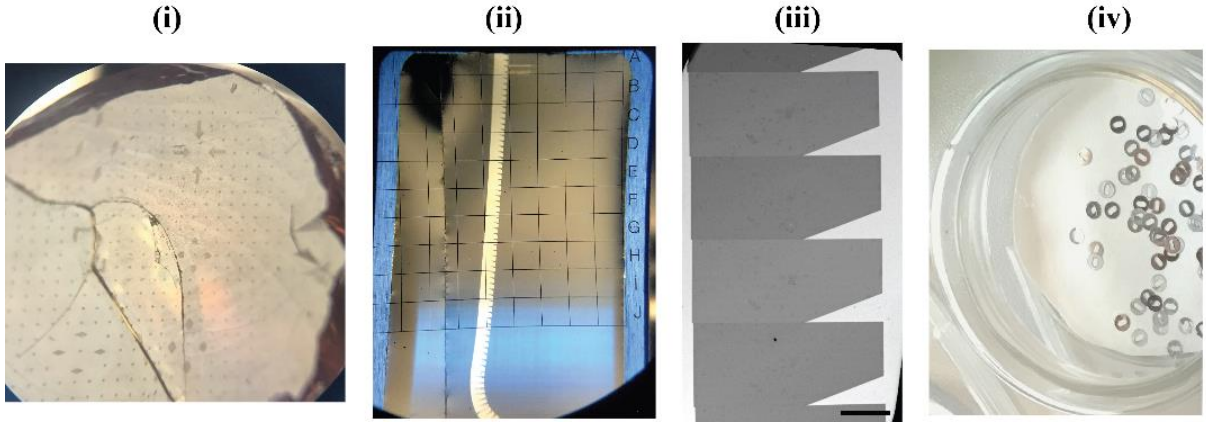

Figure 3.8: Sample preparation for electron microscopy of wound rings: *(i) Resin block showing different geometrical patterns surrounding the rings, after peeled off from the coverslip. (ii) Resin block is serially sectioned with a thickness of 80nm, (iii) placed in the correct order from bottom most section, to the top (Scale bar: 200µm). (iv) Visualisation of these sections attained by placing them on EM grids of 3mm, containing 2mm hole for holding the sections.*

symmetry of these motifs. This was achieved by designing a photo-mask consisting of different geometrical patterns (arrows, tear drops, diamonds etc.) around these circular motifs (Figure 3.7 (i) top). With this geometry, it was easier to trace back to our region of interest which was selected in advance, by epi-fluorescence microscopy.

After obtaining the rings of epithelial cell monolayer, we performed the following steps [106]:

1. The region of interest is chosen by epi-fluorescence microscopy with a high N.A ~1.4 objective. We use an oil emersion objective (40X) for this purpose.
2. Presence of oil residues hinder in preparation of clean dust free samples for EM. Hence, after the selection of area of interest, the bottom of the coverslip should be cleaned thoroughly with 70% ethanol to remove all traces of oil.
3. Next, the sample is processed for electron microscopy following the protocol described in [106]. Fixation of the monolayer is done using 2.5% glutaraldehyde and 2.5% formaldehyde in 0.1M cacodylate buffer for 2h at 4°C.
4. After washing, the samples are post-fixed for 1 hour in 1% osmium tetroxide [OsO4] reduced by 0.8% potassium hexacyanoferrate (III) [K3Fe(CN)6] in H_2O at +4°C.
5. Post extensive rinses in distilled water, samples are post-stained by 1% uranyl acetate for over-night at +4°C, and rinsed in water. Samples are dehydrated with increasing concentrations of ethanol (25%, 50%, 70%, 90% and 3x100%), and embedded with a graded series of epoxy resin. Samples are finally polymerised at 60°C for 48 hours.
6. Ultrathin serials sections (80nm) were picked up on 1% pioloform (Polyvinyl butyral resin) coated copper slot EM grids and imaged.

3.9 Optical setups

3.9.1 Optical setups for mammalian cells (multi-cellular rings)

Different optical setups and configurations used in this study for single cell cytokinetic ring study and dynamic multicellular ring study are detailed below.

3.9.1.1 Acquiring temporal dynamics

For acquiring temporal dynamics in multicellular rings for phase contrast and fluorescence imaging, epifluorescence inverted Olympus CKX41setups was used. All the microscope setups

were enclosed inside a temperature-controlled chamber stably maintained at 37°C. The samples were mounted either on a Marzhauser stage with a stepper motor with Tango controller, enabling multi-position acquisitions.

The optical path to the samples was controlled with the help of shutters by (Uniblitz VCM-D1 / VMM-D1 or ThorLabs SC10) to prevent phototoxicity in case of continuous exposure. Fluorescence excitation lamp (Leica E6000) with mercury metal halide bulb and a white light delivery optical fibre was used, with a cooled charge-coupled device (CCD) (Hamamatsu C4742-95 / C8484-03G02). White light was used in coordination with filters corresponding to the required acquisition channel. The devices were controlled by custom made scripts in the interface of (Hamamatsu) micromanager.

The objectives were selected based on the required field of view and structure resolution. For ring closure experiments Olympus phase contrast air objectives 20X (0.4 N.A) or 40X (0.9 N.A) was used. Acquisition was done with 500ms exposure and 1min frame interval to capture the temporal dynamics.

To prevent evaporation of the media, the samples were covered with two differential sized clean lids. First, the lid belonging to 35X35 mm culture plates and next, from a 100X100 mm culture plates.

It was vital to maintain a humidified chamber by constant storage of water inside the temperature-controlled microscope setup.

3.9.1.2 FRAP and laser ablation

FRAP experiments were performed using a confocal spinning disk microscope (Nikon; Yokogawa CSU-X1 Confocal Scanner; Roper iLas FRAP system) for high speed multidimensional acquisition. High Numerical aperture objective was used for this purpose;100X Oil APO N.A 1.49. Bleaching was achieved using visible light laser (561nm) and the recovery was acquired using both 488 and 561 laser line to image E-cadherin and MRLC respectively. Acquisition was done using Photometrics Evolve 512 back-illuminated EMCCD.

Laser ablation experiments were performed using TCS SP5 Inverted microscope setup under temperature-controlled environment with a Z-galvo stage. FRAP module was used in synchrony with pulsed MP (Coherent Chameleon Ultra II; 800nm; 4MW) laser for ablation. Fluorophore excitation was performed using argon (488nm; E-cadherin) and DPSS 561

(MRLC) laser line. The minimum frame interval that could be chosen was 1.2s pre and post ablation.

3.9.1.3 FRET

Inverted Leica confocal microscope (SP5) equipped with a Z-galvo stage, MP excitation and temperature control (whole microscope). Standard or resonant scanner (8000 Hz, 8000 lines/s) was used for fast imaging. Argon laser (405nm, 15%) was used for excitation of the stoichiometric FRET couple (CFP/YFP) expressing cells. CX PL APO 40x/1.25-0.75 OIL objective was used for acquisition. Acquisition was done with photo-multiplier tube (PMT) detectors at an interval of 1 min.

3.9.1.4 Improved spacial resolution

CLEM (Correlative Light Electron Microscopy)

Fluorescent microscopy images were first acquired on an inverted Leica confocal microscope (SP5) equipped with a Z-galvo stage with temperature control (whole microscope). Standard or resonant scanner (8000 Hz, 8000 lines/s) was used for fast imaging. DPSS 561 (561nm, 10%) and argon (488nm, 10%) laser was used for excitation for cells expressing, MRLC-KO1 and Ecad-mNG respectively. CX PL APO 40x/1.25-0.75 OIL objective was used for acquisition. Acquisition was done with photo multiplier tube (PMT) detectors an interval of 1 min.

Electron microscopy images for CLEM were acquired using a Philips CM12 TEM electron microscope (Philips, FEI Electron Optics, Eindhoven, Netherlands) operated at 80kV and equipped with an Orius 1000 CDD camera (Gatan, Pleasanton, USA).

3.9.2 Optical setups for mammalian cells (single cell cytokinetic rings)

3.9.2.1 Acquiring temporal dynamics in single cell cytokinetic rings:

Inverted confocal microscope (SP5) equipped with a Z-galvo stage with temperature control (whole microscope) was used. Standard or resonant scanner (8000 Hz, 8000 lines/s) was used for fast imaging. The objectives were selected based on the size and field of view of the cell structure under observation. Studies on cytokinetic rings and were done using 25X (cells inside cavities) or 63X (on plain coverslips) 0.95 NA Leica using Z stack slices of 0.5µm.

3.9.2.2 Improved spatial resolution inside cavities

STED (Stimulated Emission Depletion Microscopy)

Confocal and STED imaging, on fixed samples, was performed using an Abberior 3D-2 Color-STED system (Abberior Instruments, Göttingen) with a 100x/1.4 NA oil objective (Olympus). Star580 was imaged with a pulsed laser at 560 nm, and excitation of Abberior Star Red and SiR-actin probe was performed at 640 nm. The depletion laser for both colors was a 775 nm pulsed laser (Katana HP, 3W, 1ns pulse duration, NKT Photonics).

3.9.3 Optical setups for Fission yeast cells

Optimised acquisition of the formation of cytokinetic rings was used to capture the myosin cluster coalescence. Spinning disk confocal system was used for this purpose. This allowed acquiring quality images of rings with an exposure time of 500 ms. The setup consists of a Yokogawa CSU22 spinning disk unit mounted on a Leica DMI6000 inverted microscope equipped with Andor iQ 1.9.1 acquisition system and a cooled CCD camera 96 (Andor iXon 897 BI). The spinning disk rotates at a chosen speed, 5000 rpm. The sample was mounted on x – y motorized and axial (z) piezo driven stage, and imaged with excitation lasers of range 488 nm. The objective was APO TIRF 100x oil objective (N.A 1.49 Leica). Experiments were performed with a temperature control unit maintained at 27°C.

4. RESULTS

4.1 MYOSIN CLUSTER DYNAMICS IN MULTI-CELLULAR WOUND RINGS

In this chapter, I will discuss, self-organisation of acto-myosin complex. This active gel will be discussed in the context of epithelial wound rings.

Using techniques to control cell number and hence ring environment, we studied wound ring dynamics through self-organised *acto-myosin ring* and *myosin clusters*. In this study, we establish active force mediated wound ring closures by the dynamics of myosin clusters. We also shed light on acto-myosin remodelling coupled to mechano-transduction and putative signalling pathway during the wound ring closure. Finally, we investigate these self-organised structures: acto-myosin ring and myosin clusters, by high resolution microscopy (STED[4] and CLEM[5]) to elucidate their corresponding organizations.

In the process of embryonic development, epithelial tissues undergo extensive remodelling. This remodelling is orchestrated by cell shape transformations and mediated by self-organisation of acto-myosin cytoskeleton. Even after extensive remodelling and stabilisation, cells and tissues are capable of faithfully maintaining their polarized network architecture. This is referred to as an *active gel (2.3.6).*

An important component of this network architecture, referred to as 'acto-myosin network' has been observed in the form of *rings* across biological systems. These networks are known to be involved in force generation during several biological processes, both at single [45][5] and multi-cellular level [107][36][88][28]. Such rings are referred to as 'contractile acto-myosin ring' and have been widely studied in cytokinetic rings and cables observed during *Drosophila* dorsal closure.

[4] Stimulated emission depletion microscopy
[5] Correlative light-electron micoscopy

In contrast to its involvement in the well-organised muscle contraction unit, organisation of the network within such rings is fairly unknown. Although basic interaction rules of this active gel can be translated throughout systems [88], its stochasticity and poor characterisation [17], poses a challenge to investigate the network in molecular details.

The myosin network often appears in the form of self-organised clusters. Such myosin clusters have been observed throughout various systems and visualized to be temporally dynamic [108][7]. The presence of myosin clusters have also been observed in acto-myosin rings from single cell contractile rings [5] to multi-cellular acto-myosin cable in *Drosophila* tissue morphogenesis [8].

It has been previously shown in our lab using single cells, that myosin cluster formation and their dynamics are related to their functions [5]. Cluster formations are shown to be indispensable for the process of cytokinetic acto-myosin ring constriction. This was previously reported in the lab., in context of fission yeast and mammalian cells. Two types of dynamic clusters were studied, radial and tangential, associated with distinct stresses and therefore functions. Velocity of ring constriction (Table 2.1) correlated with distinct cluster dynamics, and these results were supported by theoretical analysis.

In this study, we focused on answering the question whether this cluster dynamics is conserved to multicellular system as well. If correct, myosin clusters could serve as simple read-outs for shape transformation using fluorescent microscopy for any model system.

To achieve this, we focussed on wound ring constriction in multi-cellular sheets of kidney epithelial cells, MDCK (Madin-Darby Canine Kidney).

First, I will describe the cellular system in use *i.e.* MDCK wound rings. I will follow by its study in controlled cell environment for the study of myosin cluster dynamics and its role in ring constriction.

4.1.1 Epithelial wound rings as model system for studying constriction dynamics

The closure of epithelial gaps, both during tissue injury or developmental process are essential in order to maintain the tissue integrity. Two types of mechanisms have been illustrated, contributing to the closure in epithelial cell monolayer: crawling and purse string mediated wound closure [90]. The former is known to be driven primarily by lamellipodia mediated collective cell migration [9]. The purse-string constriction is driven by acto-myosin interactions and force generation around the ring [90][109].

Here, I will describe the phenomenon of 'ring constriction' with respect to force applied by self-organised myosin clusters in supra-cellular acto-myosin cable [84] in epithelial wound rings.

4.1.2 Spontaneous wound rings

Canine kidney epithelial cells (MDCK) stably expressing *myosin regulatory light chain* (MRLC) coupled with green fluorescent protein (Table 4.1) were used in this study. Cells were plated on a plain glass coverslip (#1, 25mm diameter) with culture media (Table 4.1) and incubated at 37°C for 12-16h, allowing them to spread on the flat substrate. After spreading, the cell monolayer can be visualized on a coverslip with occasional and spontaneous *'wounds'* of varying geometry. These wounds were formed at the boundaries of merging cell colonies. One such spontaneous wound can be visualised in the following montage (Figure 5.1, Movie 1).

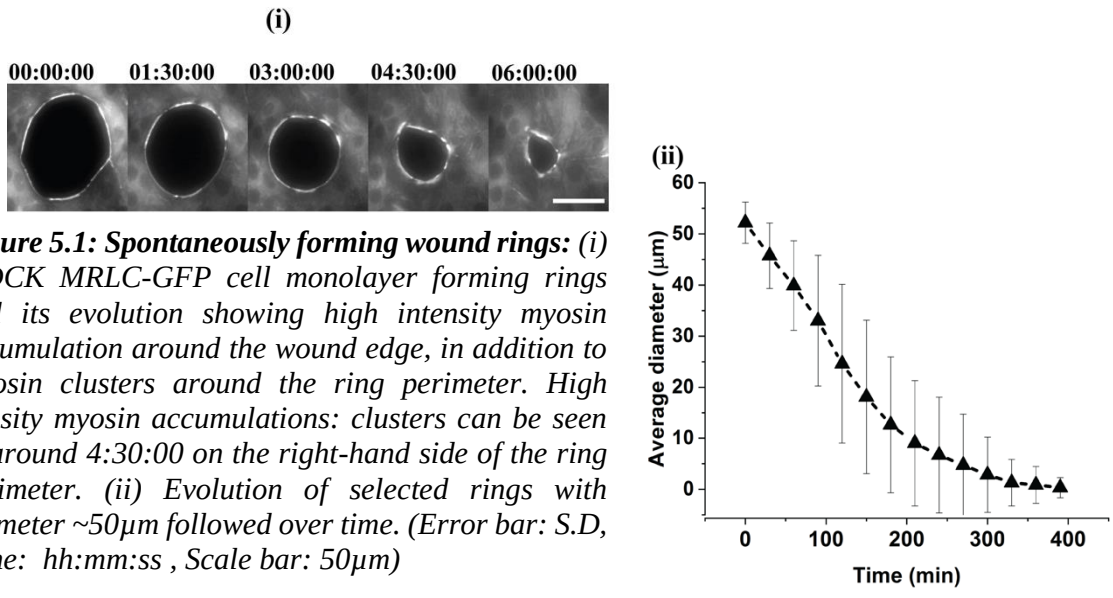

Figure 5.1: Spontaneously forming wound rings: *(i) MDCK MRLC-GFP cell monolayer forming rings and its evolution showing high intensity myosin accumulation around the wound edge, in addition to myosin clusters around the ring perimeter. High density myosin accumulations: clusters can be seen at around 4:30:00 on the right-hand side of the ring perimeter. (ii) Evolution of selected rings with diameter ~50µm followed over time. (Error bar: S.D, Time: hh:mm:ss , Scale bar: 50µm)*

Myosin is an abundant protein and is distributed in polymeric 'filamentous' and monomeric forms inside the cell. Accumulation of myosin in different forms can be seen around the cell cortex, in stress fibres and throughout the cell cytoplasm.

In this study, we follow dynamics and distribution of MRLC[6] coupled to GFP[7]/ mKO[8] by fluorescent microscopy. In the following sections reference to 'myosin' is consistently indicative of 'MRLC' and therefore used interchangeably. Distribution of this myosin subunit can be followed spatially and temporally by following the fluorophore intensity distributions.

Epithelial wound edges of MDCK cells expressing MRLC-GFP/KO1 displayed a high intensity cable around the wound edge [101] with occasional accumulations of myosin in the form of high density spots, referred to as *clusters*/*myosin clusters* henceforth in the text.

Myosin is a motor protein, studied extensively to be involved in force generation at the molecular level, eventually translating to the dynamics of the cell as a whole. In this study, we aim at describing the dynamics of these *clusters* and its role in wound closure driven by purse string constriction.

Wound rings of larger diameters (>60µm) were observed to show lamellipodial activity at the wound edge during the course of wound closure. Wound closure with such activity results in cell migration-based constriction. In order to avoid this and maintain acto-myosin driven wound closure, care was taken to obtain rings of optimal diameter. Wounds of circular geometry with diameter not greater than 50µm were selected and analysed throughout the ring constriction. Clusters of myosin were observed surrounding the ring perimeter in the form of high intensity spots (Figure 5.1 (i)). The ring constriction is determined to be linear in nature with certain level of deviations from one ring to another. This is due to the myosin sequestration during cell division and/or myosin cluster dynamics, observed at ring perimeter.

[6] Myosin regulatory light chain
[7] Green fluorescent protein
[8] Kusabira orange

4.1.3 Shape and size-controlled wound rings

For obtaining wound rings of controlled dimensions on a glass coverslip, optimal design of the photomask was prepared (3.1.1, Figure 3.1)

Micro-fabrication was performed on a silicon wafer using the photomask, to obtain circular SU-8 pillars of 50µm *'D50*[9]*'* diameter and 80µm height (3.1.2). This was followed by replica molding, to obtain micro pillars on the PDMS block. In the following text D50 will refer to as the chosen diameter for all wound experiments. Diameter of 50µm was chosen in order to limit lamellipodial dynamics at the wound edge [9].

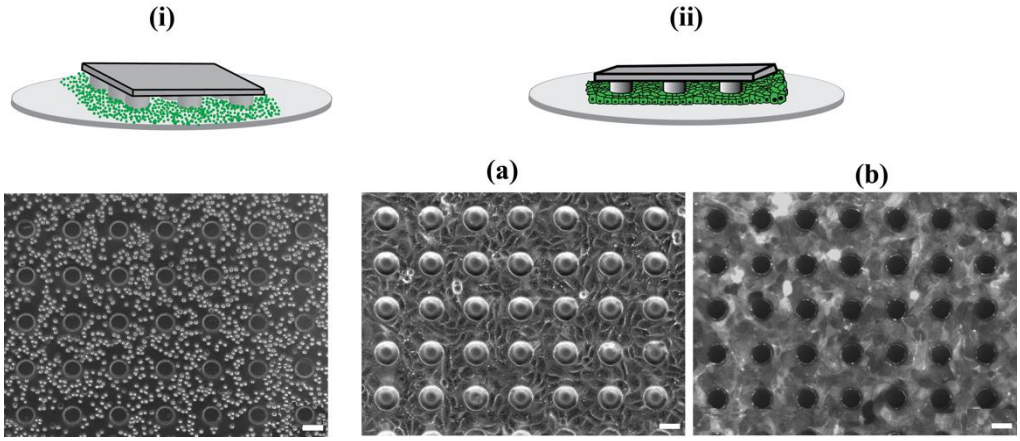

Figure 5.2: Damage free wound rings: *Illustration and phase contrast image (i) showing evenly distributed cells on a coverslip with plasma-bonded PDMS micro-pillars. After 12-16h of incubation at 37°C and 5% CO_2, phase contrast imaging shows spread cells (ii a) around the micro-pillars which can be clearly visualised by fluorescence imaging of MDCK cells (i b) stably expressing MRLC-GFP showing circular wound boundaries. Scale bar 50µm.*

After following optimal plasma bonding protocol, both coverslip and PDMS block with micro-pillars (pillar side: face down) were bonded with each other and prepared for cell seeding (Figure 3.4). Cells were seeded at a specific concentration of $2x10^7$ cells (21500 cells per µl) and ensured to be evenly distributed around the micro-pillars as shown in 'phase contrast' image (Figure 5.2 (i), illustration). After appropriate incubation for 12-16h at 37°C with 5% CO_2, cells were observed to be evenly spread around the PDMS micro-pillars acting as a physical barrier (Figure 5.2, illustration: ii) and therefore forming circular wounds around the micro-pillars, shown by phase contrast and fluorescence images (Figure 5.2 ii (a) and ii (b)).

The wound is surrounded by cells, and therefore there exists a specific number of cells between the wound rings at a given concentration of cell plating. We adapted three different

[9] Diameter = 50µm

configurations for determining the potential role of these cells, during the process of wound closure. Following configurations are described below.

4.1.4 *Potential* role of cells between wounds in ring constriction

In order to address the contribution of cell number during the process of wound closure, two different approaches were followed. First, I increased cell number around the wound rings by changing interdistance between rings (3.1.2). Next by patterning of 'O' rings with controlled cell number. In all configurations ring diameter was maintained D50 with constant cell density.

4.1.4.1 Dynamics of constriction: increase in cell number

Three different configurations of pillar distribution were chosen in order to vary the cell number between wound rings. This was achieved by varying the interdistance *'ID'* between PDMS micro- micro-pillars: ID30, ID100 and ID200. In the following text of this section, 'interdistance between the micro-pillars' will be referred to as ID.

After cell spreading, the PDMS block with micro-pillars was carefully detached from the coverslip, leaving behind circular wounds (Figure 5.3 illustration). These wound rings were surrounded by increasing cell number following the configuration of D50 ID30, 100 and 200 respectively (Movie 2, 3, 4).

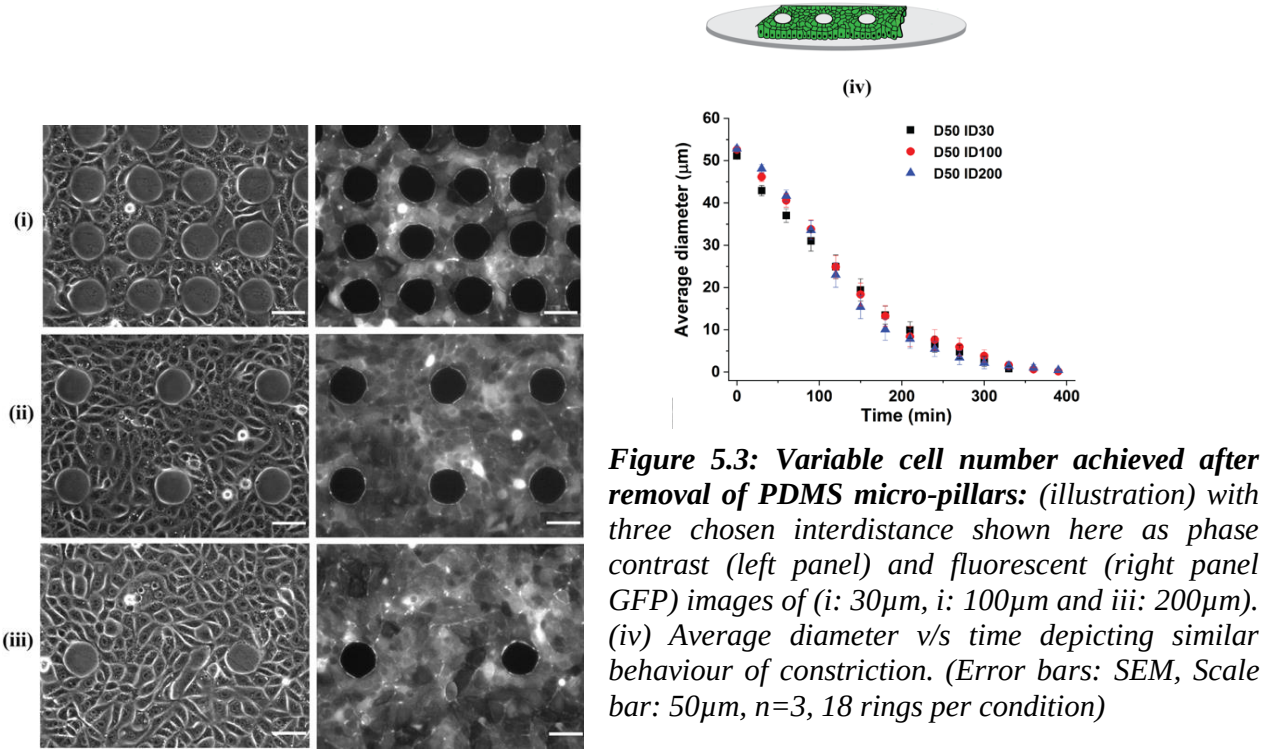

Figure 5.3: Variable cell number achieved after removal of PDMS micro-pillars: *(illustration) with three chosen interdistance shown here as phase contrast (left panel) and fluorescent (right panel GFP) images of (i: 30µm, i: 100µm and iii: 200µm). (iv) Average diameter v/s time depicting similar behaviour of constriction. (Error bars: SEM, Scale bar: 50µm, n=3, 18 rings per condition)*

All three configurations are depicted below, by phase contrast (Figure 5.3, left panel (i, ii, iii)), and fluorescence imaging (Figure 5.3, right panel (i, ii, iii)) showing epithelial wounds rings. Ring 'closure' and ring 'constriction' will be used interchangeably in the following sections, referring to closure of circular gaps in MDCK epithelial monolayer.

Evolution of ring diameter was plotted against elapsed time, by averaging diameters over single time points. All three configurations (IDs) were observed to follow similar dynamics, depicting comparable time for complete ring closures i.e. ~380 - 400min. Rings were segmented with the help of a macro created in-house with the help of Marcel Boeglin (IGBMC, imaging facility) (Movie 5).

4.1.5 Speed of wound ring closure

Although the average wound ring closure for all IDs were observed to follow similar dynamics (Figure 5.3: iv), still some rings were visualized to close faster than the others. Therefore, to confirm our hypothesis of minimal cell contribution between wounds, we analysed ring closure rates in all 3 IDs conditions, with an additional approach of minimizing the cell number around wound rings.

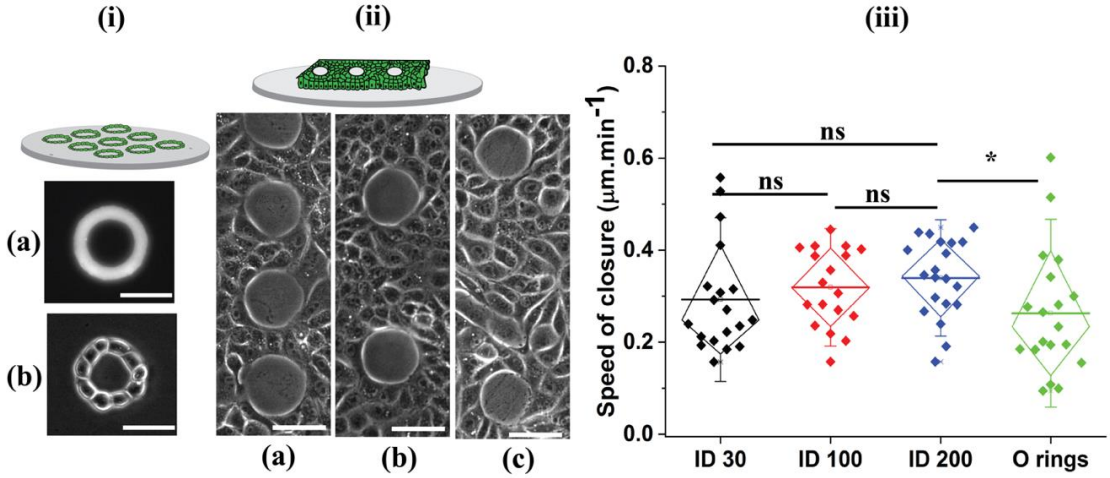

Figure 5.4: Speed of wound closure*: evaluated by varying the contributing cell number in the vicinity by 2 different approaches: plating cells on micro-contact printed 50µm 'O' rings (i: illustration, a: fibronectin printed 'O' ring, b: ring of cells) and changing pillar interdistance (ii a: 30µm, b:100µm and c:200µm). (iii) Rate of ring closure in their corresponding conditions. Each point in (iii) represents speed of closure of a single ring in its corresponding condition. The mean closure speed (horizontal line) is comparable in all conditions: ~0.3 µm min^{-1}. Error bars: S.D, Test: 2-way ANNOVA p>0.05, Scale bar: 50µm, n=3/N=18 rings per condition.*

For this, we used the process of microcontact printing (Figure 3.5) of 'O' rings (Figure 5.4, (i) illustration: a). Diameter of these rings were maintained to be D50 and thickness of the ring

was set to be ~15µm in order to have wound rings of 1 cell thick layer (Figure 5.4 i: b, Movie 6)

Comparing all conditions, we concluded that even though distribution in closure rates had variations from one ring to another, the mean closure rate was maintained at ~0.3µm min^{-1}.

This result strongly suggests that cells in-between the wounds do not play a significant role during its closure.

Dividing cells at the immediate ring vicinity sequesters available myosin from the ring, and subsequently stalls the constriction. Ring constriction does not revive unless the doublet has been spread and the acto-myosin ring has regained its continuity. According to the number of divisions occurring at the ring perimeter, constriction dynamics is slowed down. To preclude any artefacts associated to this phenomenon, such rings were left out of the evaluation.

Next, we looked at the active cytoskeletal component of the acto-myosin ring itself. This ring formed a cable-like structure. This cable was observed to span all the cells surrounding the wound, hence referred to as supra-cellular acto-myosin ring [84].

4.1.6 Characterisation of acto-myosin ring

In this section, I will explain the characterization of acto-myosin ring around the wound edge, during the process of wound closure.

First, I will explain this acto-myosin ring in terms of its intensity profile, indicating on myosin concentration/density around the wound edge. Next, I will describe and characterize self-organised myosin clusters, at the ring perimeter.

4.1.6.1 Intensity profile of the acto-myosin ring

The intensity of MRLC-GFP was measured as an indicative of myosin concentration/density around the wound ring. The cable was visualised by of GFP fluorescence showing a *cable* like structure around the wound edge, referred to as an acto-myosin cable [84].

Myosin accumulation in the cable was measured by line intensity plot and was found to be ~ 1.8 – 2 times higher (Figure 5.5) as compared to the basal myosin intensity around it (Figure 5.5, plateau left and right). Basal myosin intensity is representative of the myosin distribution in the cell cytoplasm, surrounding the cable.

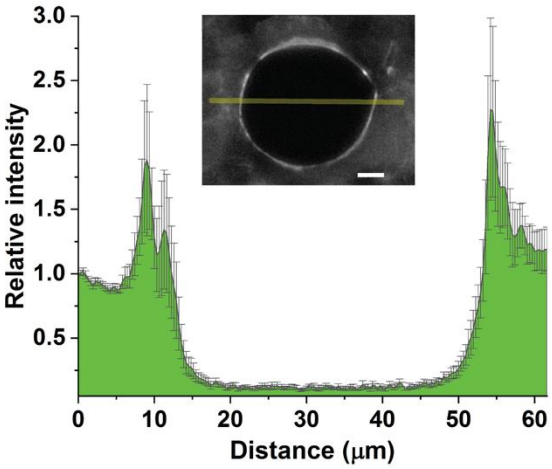

Figure 5.5: Intensity profile of myosin cable: *Left and right: basal myosin intensity of the surrounding cell. Intensity peaks: cable intensities relative to the intensity of surrounding cell (Error bars: SEM, Scale bar: 10μm, n=12 rings)*

4.1.6.2 Intensity measurement around the ring perimeter

In order to characterize the fluorescence intensity profile corresponding to myosin accumulation, cable intensities were followed over time. Thickness of this acto-myosin cable was traced to be ~2μm, corresponding to ~6 pixels in our acquisition used as a standard setting.

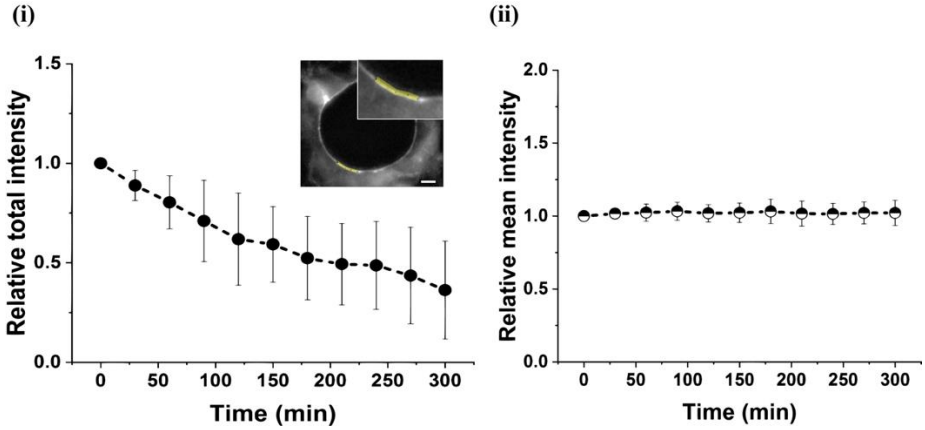

Figure 5.6: Acto-myosin ring intensities corresponding to myosin concentrations: *Intensities of the closing wound rings evaluated by tracing the full ring perimeter with ~2μm in thickness. Total intensity of ring (in grey values) relative to the first time point measured to decrease, with subsequent decrease in diameter with time (i: inset showing full ring and zoomed view of the tracing). Although mean intensity of the same rings, relative to the first time point found to be constant over time (ii). n=3/N=50 rings. Error bars: SEM, Scale bar: 10μm*

Cable intensities were traced over time for a closing ring. Decrease in ring diameter was observed to correlate corresponding to the decrease in measured total intensity of the cable. Values are represented with respect to the measured intensity at the first time point. This demonstrates the relative change in intensities over time (Figure 5.6 (i)).

Next, we measured the mean intensity of the cable as above. The relative mean intensity was constant over time. This indicates that myosin concentration is conserved over time. This suggests that myosin is redistributed in the cell cytoplasm/cortex.
To test this hypothesis, we took following approaches, first by quantifying the intensity of myosin lost during the ring closure, and by quantifying myosin turnover by fluorescent recovery after photobleaching (FRAP). These two approaches are described in later sections.

4.1.7 Characteristics of myosin clusters

Apart from the cable formation, accumulation of myosin high density regions was observed around the ring perimeter after the removal of the PDMS pillar. These regions are referred to as *myosin clusters* or simply clusters throughout the text, observed during ring constriction. Configuration obtained after removal of pillars will be referred to as open ring configuration throughout the text.

Myosin clusters were observed to be 1-2µm in size predominantly circular/elliptical geometry (Figure 5.8, inset). To analyse the patterning of these clusters we quantified cluster contrast and their density in the acto-myosin cable surrounding the wound ring.

4.1.7.1 Cluster density

The number of clusters existing at the ring perimeter were followed over time. First, this was done by following the cluster number for different ring sizes. This analysis showed linear decrease in cluster number with corresponding decrease in diameter (Figure 5.7 (i)). This was also illustrated by plotting the average number of clusters over time which showed a similar trend. The average number of clusters was analysed to be ~3 for initial time points (50µm dimeter) and primarily decreased to ~1 by the end of closure.
Cluster density distribution around the ring perimeter was analysed over time giving mean cluster density to be ~0.02 μm^{-1} (Figure 5.7 (iii)). This corresponded to ~3 clusters at the

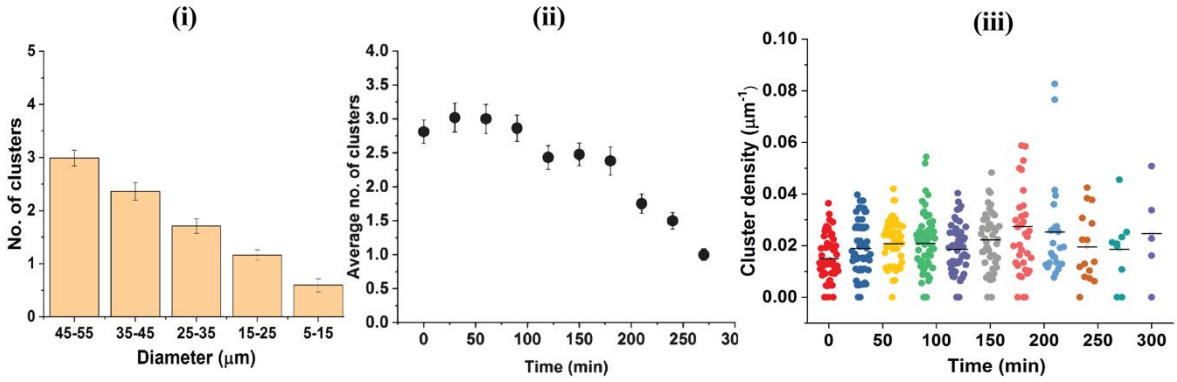

Figure 5.7: Cluster Density*: Evaluation of absolute cluster number revealed decreasing trend with decreasing ring diameters (i). Decrease in average cluster number observed with closing rings over time (ii). Cluster density is constant over time (each colour represents cluster density of a particular ring at a particular time of closure). Error bars: SEM, n=3/N=55 rings.*

beginning of the closure. Over rare occasions, ~4-5 clusters were also observed, which is depicted by higher cluster density values during ring closure (Figure 5.7 (iii) time point 150-200min).

4.1.7.2 Cluster contrast

Intensity of myosin accumulations referred to as *clusters* were observed to be of higher in intensity, compared to the cable (Figure 5.1: right-hand side of ring perimeter at time *'4:30:00'*). These clusters were visualised to be temporally dynamic, with radially and/or tangentially moving clusters (described later in the text).

In order to determine whether the myosin concentration inside clusters varied with time, cluster contrast was analysed during ring constriction. Analysis of cluster contrast was done by extracting cluster intensity with respect to mean intensity of the ring.

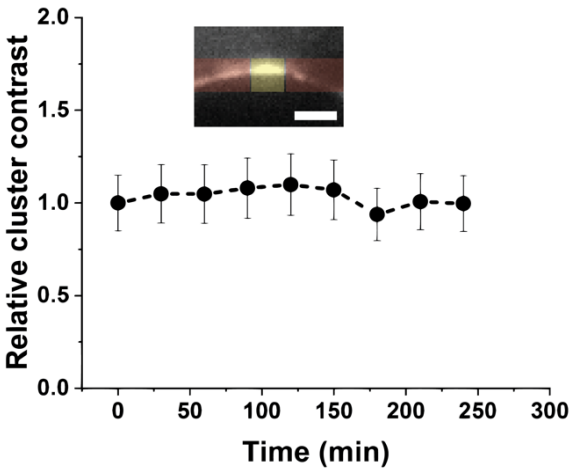

Figure 5.8: Cluster contrast: *determined by (inset: yellow) intensity calculations with respect to the background of ring (inset: red) during constriction. The relative values were calculated with respect to the first time point. n=3/ N=44 rings. Error bars: SEM, Scale bar 5μm*

Relative cluster contrast exhibited a constant dynamic, during ring constriction (Figure 5.8). These results, depicting constant ring mean intensity, in addition with constant cluster contrast and density during ring constriction, strongly suggesting myosin redistribution during acto-myosin ring constriction.

Next, we characterised the self-organised myosin clusters around the wound ring perimeter.

4.1.8 The two types of myosin cluster dynamics, after *removal of PDMS pillars*

Careful removal of PDMS micro-pillars from the epithelial monolayer, releases the physical barrier allowing the onset of wound ring constriction (Figure 5.3). This configuration is followed by wound ring constriction will be referred to as *open ring configuration* in the following text.

Since cells between the rings were evaluated to be non-essential for the rate of closure (Section **Error! Reference source not found.**), we focussed on reviewing whether self-organised myosin clusters around the ring could play a leading role in ring closure.

There were two types of cluster dynamics, characterized in the study relating to acto-myosin ring closure (cytokinesis) in fission yeast and mammalian cells: rotating/tangential and still/radial respectively [5].

We observed similar cluster dynamics, in our multi-cellular acto-myosin rings. We refer to it as radial and tangential clusters, illustrating their trajectories with respect to the ring centre. These trajectories were characterised with respect to their dynamics in cartesian and polar coordinates. The maximum degree of rotation for radial clusters in polar space was evaluated to be far less: 0.2-8° as compared to tangential clusters: 3-30°. This evaluation was done during ~60min period with an acquisition interval of 5min (Figure 5.9, (i), radial: magenta, green: tangential).

Movement of these clusters was also visualised in cartesian space, with ring centre as the reference. This analysis showed correlated dynamics of clusters corresponding to the local ring

perimeter showing radial clusters contributing to faster closures as compared to tangential clusters (Figure 5.10 (ii)). Visual representation of these differences in polar and cartesian space dynamics of radial and tangential clusters are shown in representative kymographs (Figure 5.10 (i) a, b, c)

Typically, both radial and tangential clusters was observed to coexist in the same ring. On rare occasions, rings with exclusive presence of radial (Figure 5.8 (i) a) or tangentially dynamic (Figure 5.8 (i) c) clusters were observed.

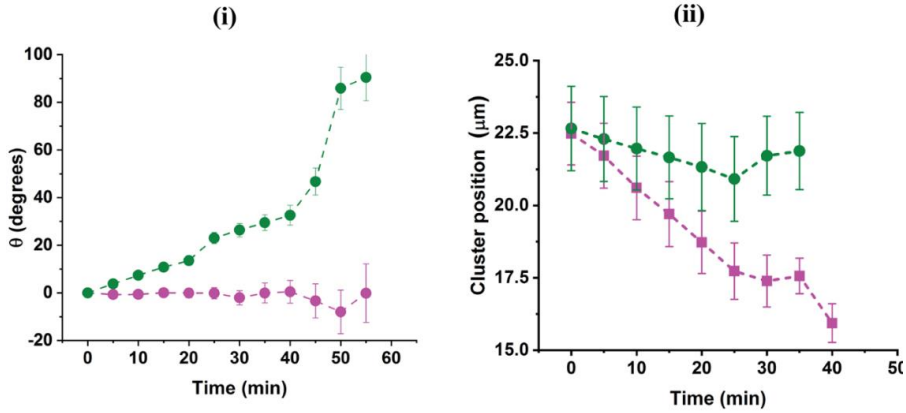

Figure 5.9: Movement of clusters in polar and cartesian coordinate: *(i) Rotational evolution of radial cluster showing minimal instantaneous angle of ~5 °(max: 10 °total evolution, magenta) and for tangential ~30 °(max: 100 °total evolution, green) clusters over time. (ii) Radial (magenta) and tangential (green) cluster position w.r.t to the centre of the ring.*

Characterising the myosin cluster dynamics in the wound ring closure, we observed that the local closure rates of the rings were related to the type of dynamic cluster persisting in that respective ring segment (Figure 5.9 (i) b). Rings consisting of purely tangential/rotating clusters (Figure 5.9 (i) c) closed much slower than rings containing purely radial clusters (Figure 5.9 (i) a). These clusters seem to have similar and very specific effects on the closure rate, even though persisting for a finite amount of time in the ring (Figure 5.10, (i) b). Thus, a radial cluster is correlated to a local fast closure when compared to tangential cluster. Radial and tangential cluster dynamics are shown in the following movies respectively (Movie 7, 8).

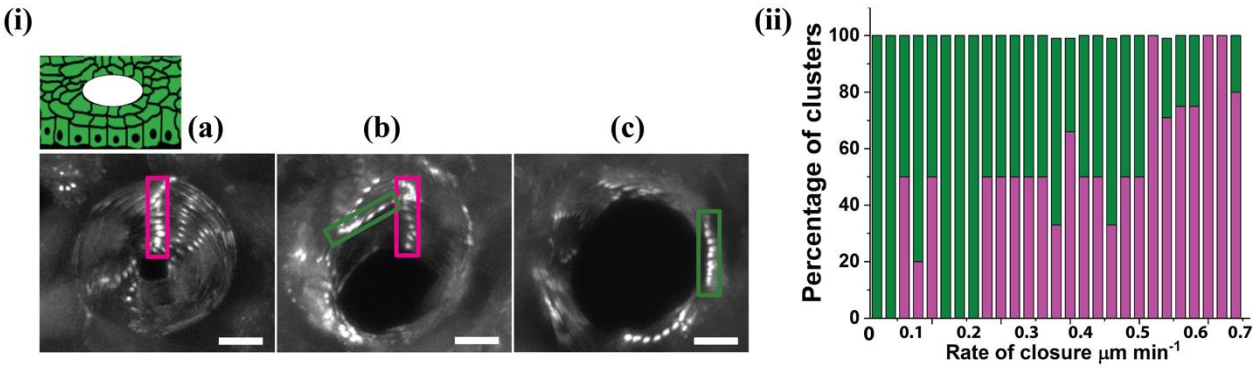

Figure 5.10: Myosin cluster dynamics*: Wound rings after pillar removal. (i) (illustration) depicting kymographs of ring and corresponding cluster evolution at 5 min interval for 40 min, with the exclusive presence of radial (a: magenta) and tangential (c: green) clusters, in addition to rings with coexistence of both (b). (ii)The percentage of coexistence, of types of clusters correlated with the rate of closure. n=3/N=27rings. Scale bar 10µm*

This observation was further quantified by correlating the closure rate with the relative fraction of radial and tangential clusters within a ring. It was clearly seen that whenever the relative fraction of radial myosin clusters was higher as compared to the fraction of tangential clusters, the closure rate increased and vice versa (Figure 5.10 ii).

This suggests a difference in stress associated with radial and tangential clusters. Differences in wound ring constriction suggests that radial clusters are associated with higher stress as compared to tangential clusters. This was evaluated further, by releasing the stress associated with these clusters through ablation.

Next, we evaluated the stress associated with respective cluster dynamics, radial and tangential.

4.1.9 Stress evaluation in acto-myosin ring and myosin clusters

To evaluate the stress associated with these clusters we first repeated the process of creating damage free epithelial wounds with the help of PDMS micro-pillars. According to our hypothesis, release of this physical barrier exposes the wound edge to forces extended via the acto-myosin ring in addition to the forces exerted by the myosin clusters. As shown earlier, radial and tangential cluster dynamics led to different ring constriction rates (Figure 5.10).

To further test our hypothesis, we evaluated the stress associated with these clusters, in order to describe the differences in constriction rates, related to the two cluster dynamics.

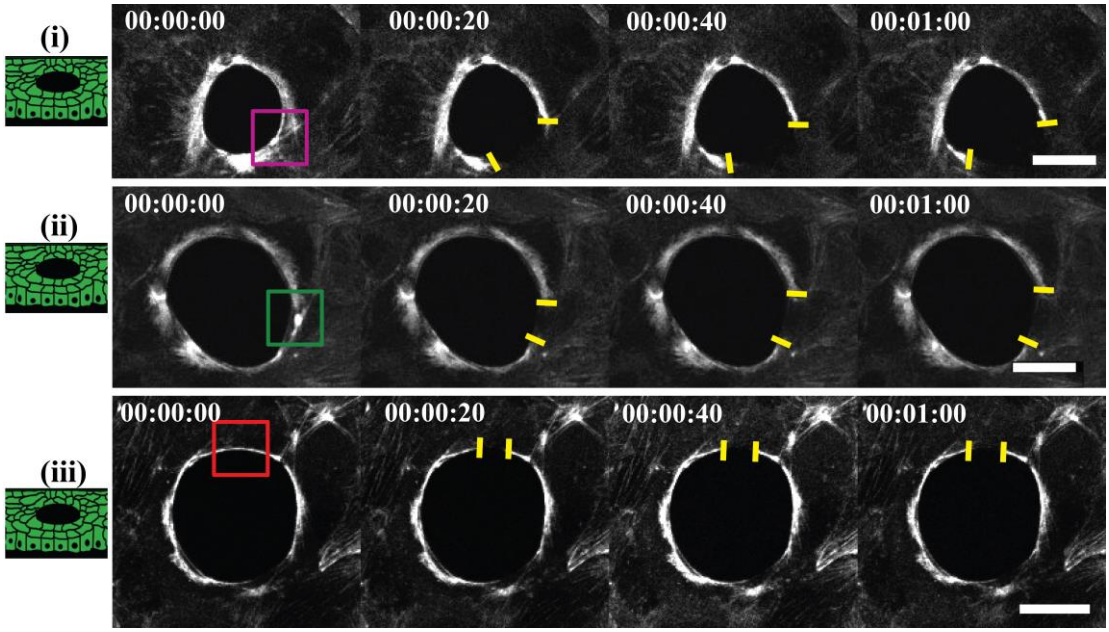

Figure 5.11: Acto-myosin ring and cluster ablation in open ring conformation: *After pillar removal, tracking ablated ends of (i) radial and (ii) tangential clusters. Leaving the pillars inside wound rings, tracking ablated ends of (iii) tangential clusters within wound ring perimeter. Coloured rectangles showing distinct clusters in different configurations: After pillar removal (i) magenta: radial cluster, (ii) green: tangential cluster. While pillar inside (iii) red rectangle: homogeneous portion. Yellow bar, tracking ablated ends. Time hh:mm:ss , Scale bar 20µm.*

For this, we chose to perform laser ablation of these clusters in an *open ring configuration* (Figure 5.11 (i, ii)). Cells stably expressing MRLC as well as E-cadherin were chosen for this experiment. This precluded analysis of any damaged cell, since retracted ends of acto-myosin ring maintained their adjacent cell-cell contacts. To be able to follow and subsequently ablate a myosin cluster, the persistence time was set to be ~5-6 mins. Hence, clusters persisting for at least 6min were considered for the analysis. After choosing a cluster *e.g.* the one persisting radially, the cluster was ablated using a multi-photon laser ablation setup (4mW). Ablation of this cluster led to snap opening of the ring at the point of ablation and subsequent retraction. Immediate opening of the acto-myosin ring at the point of cluster ablation indicates towards stress associated with the cluster. Next, we did similar procedure for tangential clusters and the homogeneous potion of the ring. Ablation of tangential clusters and homogeneous portion, also showed immediate snapping and subsequent retraction of the snapped ends similar to the radial clusters. This snapping behaviour was acquired every 1.2s and continued for 40-50s. This is the

time taken for the snapped ends to stop retracting, and therefore stabilize. These retracted ends were stabilized and recovered subsequently, visualized by cells expressing E-cadherin GFP together with MRLC KO1. Evolution of these clusters, retraction after ablation and subsequent recovery are shown in the following movies, for radial and tangential clusters respectively.

Movie 9, Movie10, Movie11
Movie12, Movie13, Movie14

Post ablation, the instantaneous opening was evaluated by tracking the two retracting ends. When plotted with respect to time, it showed larger first snapped distance in case of radial, as compared to both tangential clusters and homogeneous portions of the ring (Figure 5.12 (i) magenta, green and black respectively).

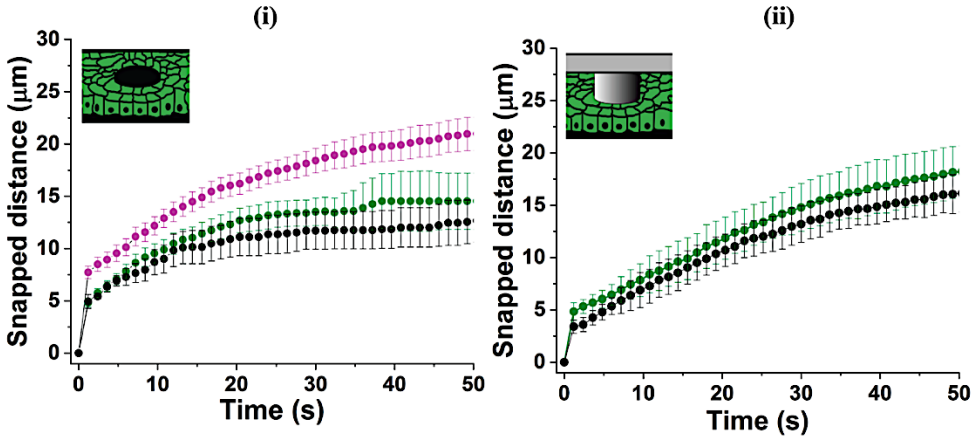

Figure 5.12: Snapped distance traced after laser ablation in open and closed ring configuration: *Snapping acto-myosin ring ends, traced after laser ablation of (i) radial cluster: magenta (ii) tangential cluster: green and homogeneous ring portion: black during open ring configuration. Snapping acto-myosin ring ends, traced after laser ablation of (ii) tangential cluster: green and homogeneous portion: black in a closed ring configuration. (i) n=7/ N=11rings: green and N=14 rings: magenta. (ii) n=3/ N=10 ring: green and n=2/ N=9rings: black.*

The first instantaneous opening after ablation, indicates stress associated with the specific portion. This initial opening after ablation, was observed to be 1.5 times larger for radial clusters as compared to the rest. Although initial opening for tangential clusters and homogeneous portions were comparable, the final retracted distance was slightly larger for the former than the latter. Retracted ends after ablation of radial clusters was observed to be the largest. Retracted ends opened the ring twice as large, compared to homogeneous portion of the ring *i.e.* ~ 20µm. This distance sometimes spanned almost one full cell length, *i.e.* from its one cell-cell junction to another. Cells contributing to the ablated portion of the acto-myosin ring maintained their cell-cell junctions while doing so. These observations in the *open ring*

configuration showed higher stress associated with radial clusters, as compared to tangential clusters and homogeneous acto-myosin ring portions.

Closed ring conformation poses a physical barrier in terms of the PDMS pillar, hindering the acto-myosin ring to move ahead in space and therefore achieve ring constriction. One can imagine that the forces sensed by the acto-myosin ring will be very different in this case, as compared to when this barrier is removed [10]. We observe the presence of acto-myosin ring as well as clusters in the closed ring configuration (Figure 5.11 (iii) 0:0:0). We wanted to compare how this change in configuration could affect the stress associated with these acto-myosin structures. Therefore, we also performed similar ablations for, clusters and homogeneous ring portions in a *closed ring configuration*. Clusters to be ablated were chosen stochastically in this case, given that majority of the clusters in closed ring conformation were observed to follow tangential cluster dynamics (Movie 15).

Initial snapped distance and subsequent retracted distance was observed to be higher for the cluster (tangential) as compared to the homogeneous ring portion (Figure 5.12 (ii) green and black respectively). Interestingly, *tangential clusters in closed ring conformation* were evaluated to follow similar retraction dynamics as *tangential clusters in open ring conformation*. These results can be summarised in two-fold statements. First, clusters have higher stress associated with them as compared to the homogeneous acto-myosin ring in both open and closed ring conformation. Also, tangential clusters in both closed and open ring conformations seem to depict similar snapping dynamics. This indicates towards the fact that, there exists concrete correlations between cluster dynamics and the corresponding stress associated with them.

Next, we went a step further, and evaluated the stress in terms of initial retraction velocity in all conditions tested above for both open and closed ring conformations.
For open ring conformation, the average retraction velocity for radial clusters was evaluated to be 1.6 times higher as compared to tangential clusters (Figure 5.13 (i) magenta and green respectively).

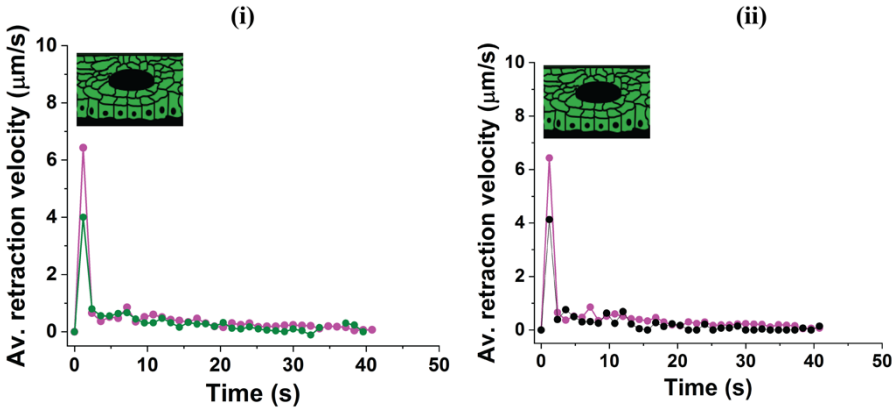

Figure 5.13: Retraction velocity evaluated after laser ablation in open ring configuration: *Average retraction velocity evaluated after laser ablation of (i) radial cluster: magenta and tangential cluster: green, compared with (ii) homogeneous ring portion: black, overlaid with radial cluster retraction velocity curve. n=7/ N=11rings: magenta, n=7/ N=14rings: green, n=2/ N=4rings: black.*

Homogeneous portion of the ring showed similar initial retraction velocity, compared to tangential clusters in open ring conformation (Figure 5.13 (ii: black and i: green respectively)). Although the initial retraction velocities were comparable for the *homogeneous ring portion* and *tangential clusters*, subsequent retraction rates were observed to be slower in the former case, as compared to the latter.

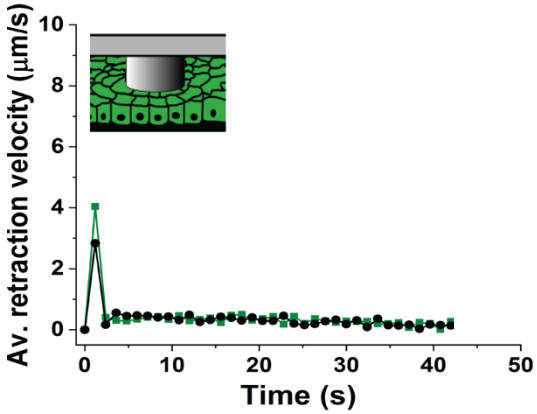

Figure 5.14: Retraction velocity evaluated after laser ablation in closed ring configuration: *Evaluated average retraction velocities after laser ablation of homogeneous ring portion black, overlaid with tangential cluster: green. n=3/ N=10rings: green, n=2/ N=9rings: black.*

Similarly, evaluation of initial retraction velocity of cluster (Movie 16, Movie 17) and homogeneous ring portion (Movie 18, Movie 19) was also performed for the *closed ring conformation* (Figure 5.14, cluster: green, homogeneous portion: black). In agreement with the snapped distance data, retraction velocity in this case showed comparatively higher rate for clusters (tangential) as compared to the homogeneous portion of the ring. Also, similar to snapping distance, retraction velocity of *tangential clusters* in *open ring conformation* were comparable to *tangential clusters* in *closed ring conformation* (Figure 5.13 (i green) and figure 5.14 green, respectively).

These results indicate higher stress associated with radial clusters when compared to tangential clusters. Also, clusters have higher stress as compared to homogeneous ring portions, in both open and closed ring conformations. Altogether, this indicates the fact that, there exists concrete correlations between cluster dynamics and the corresponding stress associated with them.

Acto-myosin ring and the clusters consists of dynamic network of crosslinked actin and myosin filaments. These myosin motors generate active stresses driven by ATP hydrolysis. Hence we can consider the post ablated, retracting acto-myosin ring as in active viscoelastic material [53]. Such viscoelastic material shows elastic behaviour at short time scales, for example the relaxation after laser ablation is fast as compared to viscoelastic relaxation that arises from turnover. Retraction response to ablation corresponds to stress stored within the acto-myosin ring, and is representative of total mechanical tension prior to ablation.

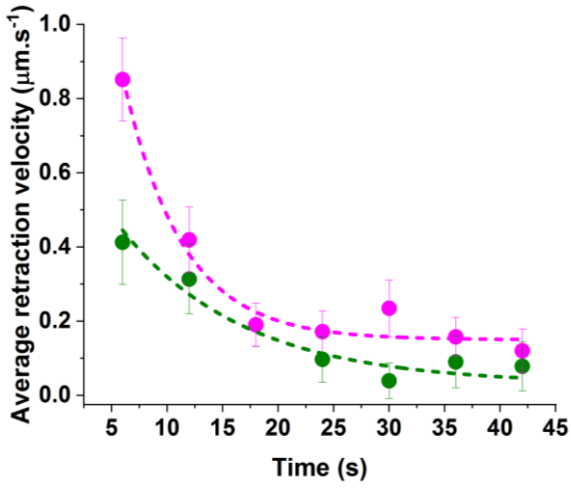

Figure 5.15: Stress evaluation corresponding to radial and tangential clusters in open ring configuration: *Evaluation of stress via fitting the data for nonlinear exponential decay.*

To evaluate further our hypothesis that, still clusters are associated with higher stress as compared to tangential clusters, we fitted out data with nonlinear exponential decay curve given by the equation: $v = -\frac{T0}{\zeta} e^{-t/\tau}$. Here, $-\frac{T0}{\zeta}$ referred to as 'A' corresponds to 'tension', where T_0 is the tension prior to ablation and 'ζ' is the damping coefficient.

This characterises frictional loss during acto-myosin network interaction with the surrounding fluid. Since composition of culture media throughout the system is constant, ζ is expected to be uniform. Also, decay constant 'τ' is inversely proportional to the stiffness of the acto-myosin ring.

Therefore, ratio of initial velocity equates to ratio of the tension as a readout for laser ablation. When the data was fitted by iterations for convergence, relative initial velocity for radial cluster ablation A_{Radial}, was evaluated to be 2.19 ± 0.61 µm/s and for tangential clusters, $A_{Tangential}$ was evaluated to be 0.71 ± 0.18 µm/s. Since initial velocity corresponds to the tension associated with the myosin clusters, these results show that indeed radial clusters have higher tension as compared to tangential clusters.

Current stress evaluation corroborates with previous results, where we saw faster constriction of rings showing higher percentage of radial as compared to tangential clusters (Figure 5.9).

Hence, these results altogether explain that, higher stress associated with radial clusters is responsible to faster acto-myosin ring constriction of the corresponding ring portion.
Earlier sections described the characteristics, spatio-temporal dynamics and the evaluation of stress associated with myosin clusters. Next, we wanted to evaluate the importance of acto-myosin ring as well as myosin clusters in the process of wound ring closure. To this extent, we inhibited the active form of myosin, myosin regulatory light chain (MRLC) in the cells.

4.1.10 Myosin cluster rescue

To evaluate the characteristics of myosin clusters, we followed two approaches: mechanically constraining the ring closure and observe the network dynamics and inducing changes in the network with specific myosin related inhibitor.
The idea was to determine the dynamics of acto-myosin ring and associated myosin clusters in these conditions.

4.1.10.1 Myosin inhibitor mediated cluster rescue

To investigate the stress associated with acto-myosin ring and the network, the system was allowed to evolve in an open ring conformation. (Figure 5.16, (ii) illustration).

After letting the system evolve for around 20 min (Figure 5.16, (i) Control, showing part of the ring), we introduced a myosin light chain kinase (MLCK) inhibitor drug, ML-7 into the epithelial monolayer. ATP competing inhibition of MLCK leads to disappearance of the acto-myosin ring as well as myosin clusters, within minutes of exposure (Figure 5.16, i, ML-7 treatment). Both myosin clusters as well the

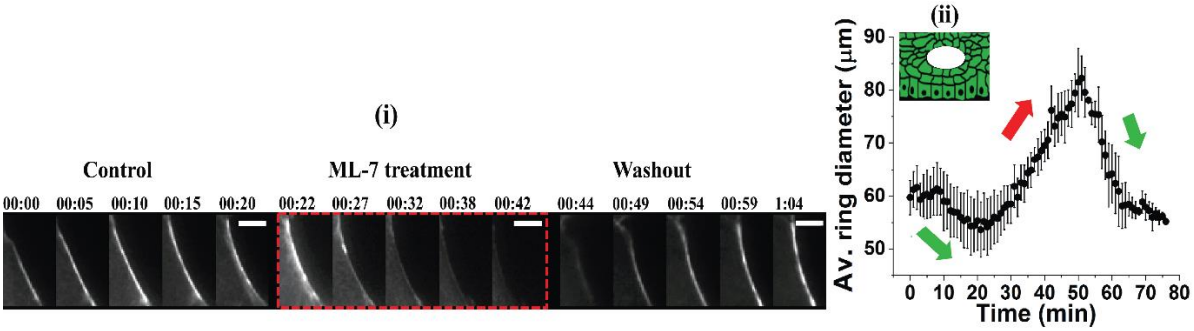

Figure 5.16: Myosin rescue after ML-7 washout*: (i) Ring and cluster evolution after pillar removal (Control) followed by MLCK*[10] *treatment leading to disappearance of acto-myosin ring and myosin clusters from the ring perimeter (ML-7 treatment: 20mins, 40μM) followed by subsequent reappearance and evolution (Washout)of acto-myosin ring and myosin clusters. (ii) Three step ring evolution illustrated by shrinkage in ring diameter during (i: control, ii: left green arrow) followed by opening of rings (i: ML-7 treatment, i: red arrow) and subsequent ring constriction after reappearance of acto-myosin ring and myosin clusters (i: Washout, ii: right green arrow). Error bars: SEM, Scale bar 5μm*

acto-myosin ring reappeared after the drug washout (Figure 5.16, (i), Washout)
leading to subsequent normal ring constriction (Figure 5.16, (ii): green arrow, Movie 20).

All three steps of the ring evolution in the presence and absence of the kinase inhibitor are represented in Figure 5.16 (ii). Left green arrow represents the loss in diameter due to ring closure before drug treatment and right green arrow represents the closure dynamic after drug washout. Disappearance of self-organised myosin structures follow subsequent opening of rings (Figure 5.16 (ii) red arrow). This is indicative of the inherent stress in the myosin ring as well as clusters.

4.1.10.2 Mechanical ring constraint driven cluster rescue

Mechanical constraint on the wound rings was achieved by leaving the PDMS micro-pillars inside the epithelial monolayer (Figure 5.17 illustration). Acto-myosin wound rings with spatially distributed myosin clusters were visualized in this configuration as well (Figure 5.14 (i)).

[10] Myosin light chain kinase inhibitor: ML-7

Cluster dynamics in this configuration mostly followed tangential trajectories with respect to the ring edge (Movie 15). This was in contrast with two distinct dynamics revealed in rings, within open ring conformation (Figure 5.9).

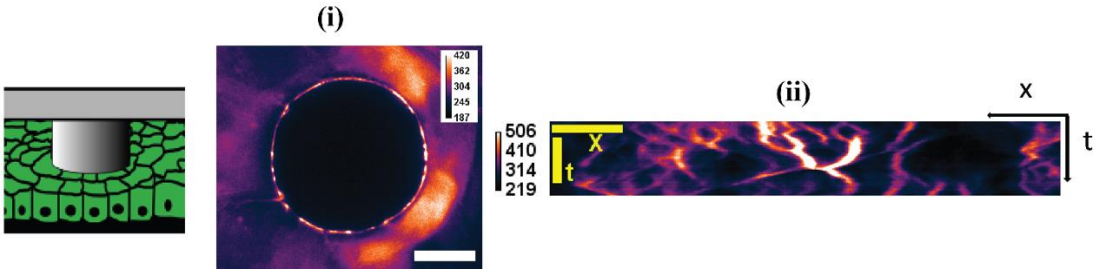

Figure 5.17: Myosin cluster dynamics in closed ring configuration: *illustration. (i) Acto-myosin wound ring showing spatial distribution of myosin clusters (high intensity (white), grey values: calibration bar). (iii) Temporal dynamics of clusters represented by kymograph with wavy lines representing moving clusters. Scale bar: (i) 20µm, (ii) 10µm, time:40min.*

Tangential cluster dynamics are depicted in the kymograph as wavy lines (Figure 5.17, ii, calibration bar: grey values).

Interestingly when such configuration (pillars inside) of rings were left to evolve in presence of myosin regulatory light chain inhibitor (MLCK) ML-7, clusters still continued to move along the ring perimeter (Figure 5.18: ML-7 treatment). Subsequently the clusters followed their usual rotational dynamics (Figure 5.18, ii) after removal of the drug as well (Figure 5.18: washout, Movie 21).

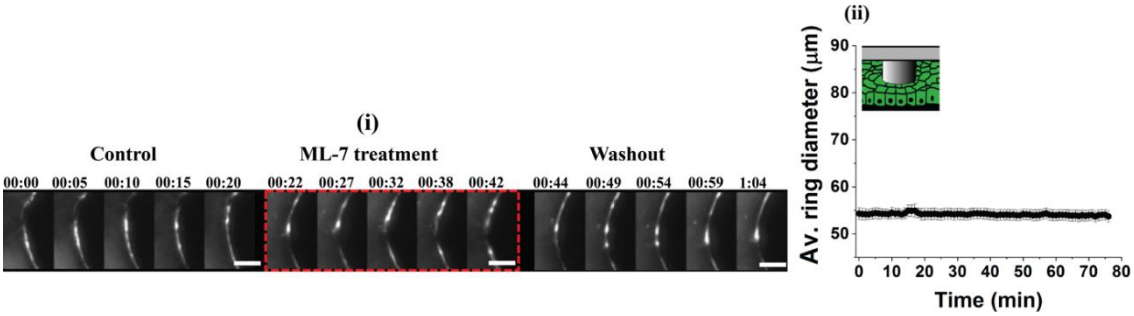

Figure 5.18: Myosin cluster rescue via mechanical constraint*: (i) Cluster evolution while pillars left inside the monolayer (Control) followed by MLCK treatment (ML-7 treatment: 20mins, 40µM) and subsequent (washout), maintaining the cluster dynamics. (ii) Ring evolution illustrated by constant diameter over time due to pillars acting as efficient physical barriers. Error bars: SEM, Scale bar 5µm*

This suggests a putative mechano-transduction of signals leading to myosin cluster rescue which is depicted in following sections (4.1.14, 4.1.13).

These results indicate towards putative role of myosin clusters as mechanosensors in ring constriction.

4.1.11 Boundary conditions for myosin clusters

As described in earlier sections, radial and tangential clusters are observed to be dynamic at short as well long-time scales during ring constriction. Characterized cluster dynamics in polar coordinates showed longer travel range: in specific for tangential clusters: ~30° in 5min and subsequently ~100° in 1h (Figure 5.9).

Epithelial cells surrounding the acto-myosin wound ring are connected to each other by adherens junctions. In order to characterise possible colocalization events between the clusters and adherens junctions, we visualised cells co-expressing markers for both MRLC and E-cadherin. Here, cell-cell junction was visualised by E-cadherin (Figure 5.19 (i) a, (ii) a, marked green) and observed if myosin clusters travel beyond these junctions by crossing them.

We did our observations in both configurations with and without micro-pillars, inside the monolayer (Figure 5.19 (i), (ii), Illustration). Our observations revealed that in both configurations: micro-pillars removed (Figure 5.19, (i) b) and micro-pillars inside (Figure 5.19, (ii) b), clusters do not cross the cell-cell junctions (Figure 5.19, blue arrows, Movie 22).

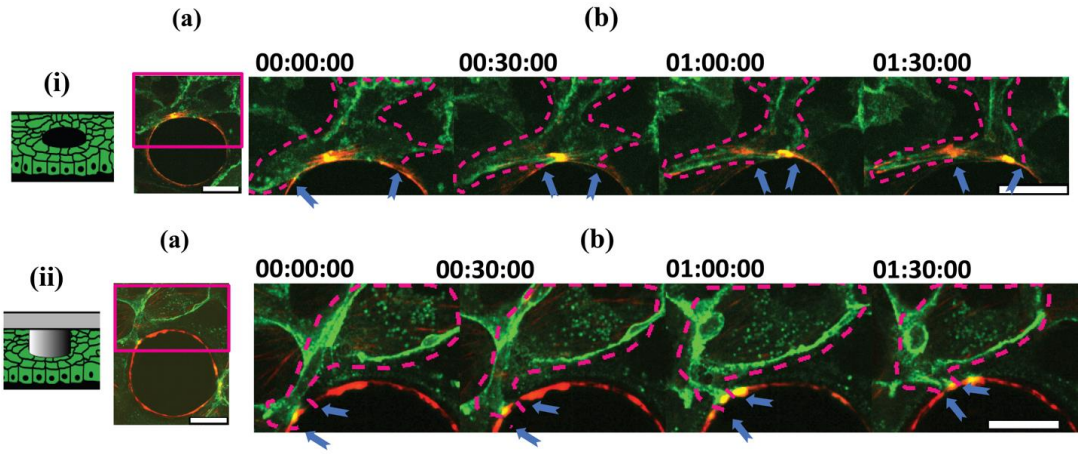

Figure 5.19: Myosin cluster dynamics and corresponding adherens junctions in open and closed ring configuration: *(i) Cells co-expressing E-cadherin-mNG*[11] *and MRLC-KO1*[12] *were plated around PDMS micro-pillars. Cluster dynamics corresponding to junctional movement in (i) open and (ii) closed ring conformations. Blue arrows marking the junctions. Scale bar: 20µm.*

This illustrates that PDMS micro-pillars behave as physical barriers for the cluster movement and hinder their movement past the junctions.

[11] mNG: neon green
[12] KO1: Kusabira orange

As described earlier, mean acto-myosin ring intensity corresponding to myosin concentration was evaluated to be constant throughout the ring constriction (Figure 5.6). This indicated towards constant myosin loss, given that the ring diameter decreases with time, during constriction. We were hence interested in evaluating the myosin flux during the process of ring constriction. For this purpose, we took a two steps approach. Firstly, we determined the myosin loss during the process of ring constriction and secondly, we evaluated the myosin turnover dynamics.

These approaches are described below.

4.1.12 Myosin conservation, and turnover dynamics

If the myosin concentration has to remain constant throughout the course of ring constriction, one can imagine that there has to exist a constant myosin loss, in order to maintain this constant myosin pool. Following this idea, we evaluated the myosin loss in constricting rings.

4.1.12.1 Myosin conservation

A myosin *halo*, around the wound ring perimeter, was almost consistently observed during the ring constriction (Figure 5.20). In a time-lapse image sequence, this can be characteristically observed as myosin waves left behind, adjacent to the cells in the vicinity (Movie 23).

We evaluated this loss relative to the first time point, by thresholding the myosin intensity 'halo' left behind.

By doing so, we indeed observed a constant myosin spanning the ring constriction for time period of ~1h.

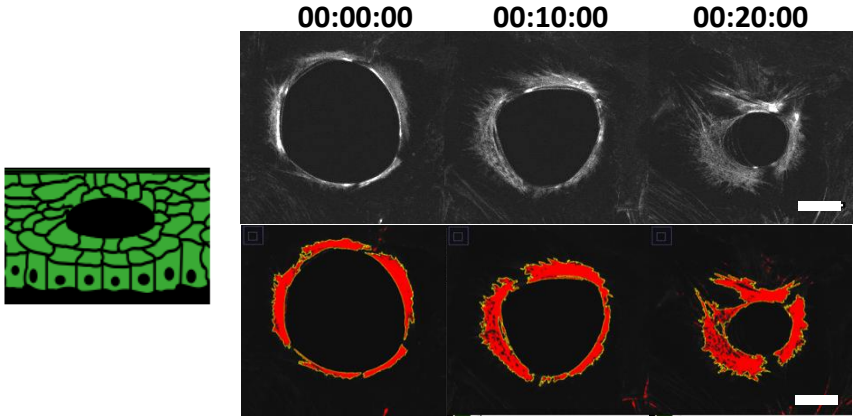

Figure 5.20: Loss of myosin during ring constriction in an open ring configuration: *Instantaneous myosin loss depicted in an open ring configuration, showing (upper panel) halo of myosin lost during ring constriction, (lower panel) thresholded for evaluation through time of ring evolution. Time hh:mm:ss, Scale bar 20µm.*

Short time period of ~1h was chosen to preclude any discrepancy relating to cell divisions close to the acto-myosin ring perimeter. Hence, when relative myosin loss was plotted against loss in diameter, we indeed saw a constant myosin loss with the elapsed time. This constant myosin loss corresponded to the simultaneous loss in diameter during the wound ring constriction. These results explain the dynamics, maintaining constant myosin concentration throughout the process of ring constriction.

Moreover, this characteristic halo was typically absent for *closed ring conformations* (Figure 5.11 (iii)). This was a result of PDMS micro-pillars acting as physical barriers, hindering the ring constriction. In such rings, constant ring intensity corresponding to constant myosin concentration was observed within the elapsed time.

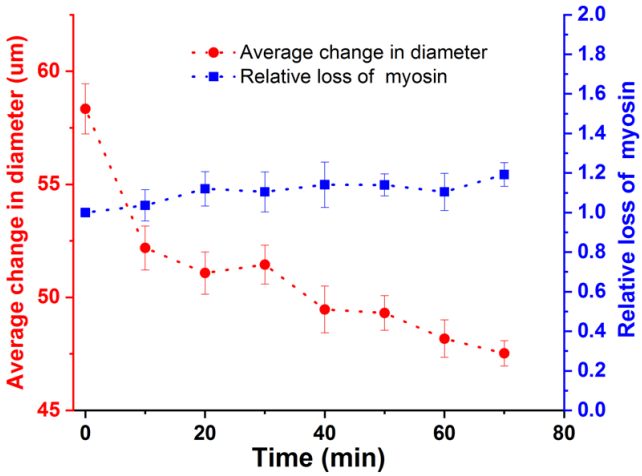

Figure 5.21: Myosin loss during ring constriction: *Relative myosin loss (blue) depicting constant dynamics, with respect to loss in diameter (red) during acto-myosin ring constriction. N=4 rings*

Altogether, constant acto-myosin ring intensity (Figure 5.6), myosin loss (Figure 5.21) during ring constriction, and stalling of rings due to 'adjacent cell division' driven myosin sequestration indicates that ring homeostasis and its dynamic constriction is maintained through constant redistributing of myosin to the adjacent cells (Movie 24).

4.1.12.2 Myosin turnover dynamics

As explained earlier, amount of myosin was found to be conserved, during acto-myosin ring constriction. Apart from the observation that there is a temporal myosin conservation in the

acto-myosin ring, it was observed that there is a flux of myosin being left behind to maintain its constant amount within the acto-myosin ring (Figure 5.6). This was defined in terms of relative mean ring intensity and relative myosin loss, during acto-myosin ring constriction (Figure 5.6 (ii)). Next, we wanted to evaluate if there was myosin exchange from the cell vicinity to the acto-myosin ring.

As described previously by laser ablation study, *homogeneous part* of the ring and the *myosin clusters* have distinct stress associated with them (Figure 5.11 and Figure 5.15). To evaluate existence of myosin turnover within these structures, visible laser induced photo-bleach was performed on the above-mentioned *parts* of the acto-myosin ring.

The method for evaluating fluorescence recovery of these sites is denoted as FRAP: *fluorescent recovery after photo-bleaching*. Fluorescence recovery was corresponded to myosin turnover, at both the bleached sites: homogeneous part and cluster, respectively.

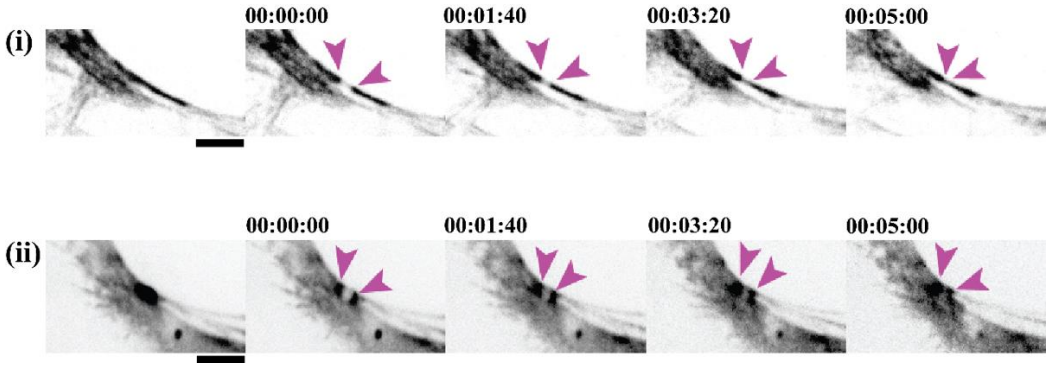

Figure 5.22: Fluorescent recovery after photo-bleaching in rings and clusters: *Acto-myosin ring tagged with MRLC-GFP shown in inverted greyscale, where dark portions indicate to myosin: MRLC accumulation. Long recoveries for (i) bleached part of the rings (left: homogeneous part) depicted in as temporal montage showing myosin recovery through time, and (ii) bleached myosin cluster (left: cluster) depicted as temporal montage showing contraction, rather than myosin recovery through time. Time in hh:mm:ss, Scale bar 5µm.*

Homogeneous part of the ring showed recovery spanning the duration of couple of minutes, after which the fluorescent intensity stabilized to a plateau (Figure 5.22 (i), Figure 5.23 (i)). However, bleached *clusters* showed lesser recovery during same amount of time,

as compared to *homogeneous parts* of the acto-myosin rings (Movie 25 and Movie 26 respectively)

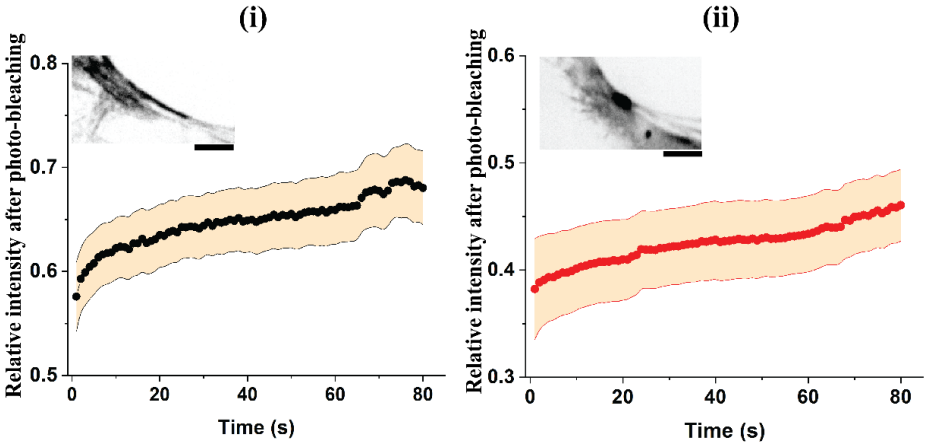

Figure 5.23: FRAP analysis of rings and clusters: (i) *Temporal representation of myosin recovery (fluorescent intensity) in homogeneous parts (inset) of the acto-myosin rings. (ii) Temporal representation of myosin recovery (fluorescent intensity) in clusters (inset) at the ring perimeter. N=3, (i) n=13, (ii) n=9. Acquisition interval:1s, Scale bar 5µm.*

Standardised dimension of the bleach point used was ~1µm. Dimensions of the clusters usually extended from ~1.5 to 2.5µm in length. In such case, laser is capable of bleaching ~50% of the myosin, from the clusters. Often, this leaves behind two adjacent areas myosin rich areas with a bleached region in between (Figure 5.22 (ii), time point 00:00:00). Analysed for similar recovery times, bleached regions of clusters, showed *contraction-driven recovery*. This was in contrast to *myosin recruitment driven recovery*, in homogeneous part of acto-myosin rings (Figure 5.23 (ii)).

Longer time scales depicted the contractile ring behaviour. Therefore, analysis was stopped after 80s, to preclude any discrepancy in recovery rates due to start of ring contraction.

These observations indicate higher myosin turnover in the homogeneous part of the rings, as compared to turnover associated with the myosin clusters. Contraction driven recovery of bleached areas in clusters indicates stability of myosin motors proteins within these temporally dynamic clusters. This stability of myosin molecules could be stress related, since clusters have been evaluated to associate higher stress as compared to homogeneous ring portions (4.1.9).

Since myosin-II activity and recruitment has been correlated with RhoA activity [77], we wanted to test it in our system to uncover any such putative correlations.

4.1.13 Activation of Rho during acto-myosin ring constriction

Conversion of inactive 'GDP, into the active 'GTP associated' form takes place through GEFs (guanine exchange factors). This triggers activation of Rho-kinase, in turn leading to phosphorylation and subsequent activation of myosin. This pathway was demonstrated biochemically, more than two decades earlier. Rho activity has been reported in response to damage wounds, in single as well as multicellular systems. Activity of the Rho pathway has also been shown to relate closely with myosin activity in response to induced wounds as well during developmental stages of embryos.

In order to test the involvement of this pathway, in our system of damage-free wounds, a two-step approach was followed. First, by determining the putative presence of active RhoA around the wound rings and subsequently its correlation with the myosin-II activity.

This was achieved by the technique of fluorescence resonance energy transfer, commonly referred to as FRET. Conventional widefield microscopy allows visualization of the fluorescently labelled proteins, limited to the spatial resolution defined by the Rayleigh principle, i.e. approximately 200 nanometres (0.2µm). However, to visualize and understand the physical interactions between specific proteins partners involved in a biomolecular process, it is necessary to achieve better spatial resolution. FRET, when applied to optical microscopy helps in determining approach between two interacting molecular partners, within the range of several nanometres. To take advantage of this technique for our system, we transfected a RhoA biosensor (Figure 5.24) in MDCK-II wild type (WT) cells. After selecting single clone stably expressing the construct, we co-transfected these cells with MRLC-mCherry. This was done for simultaneous visualisation of myosin regulatory light chain dynamics, together with the RhoA activity.

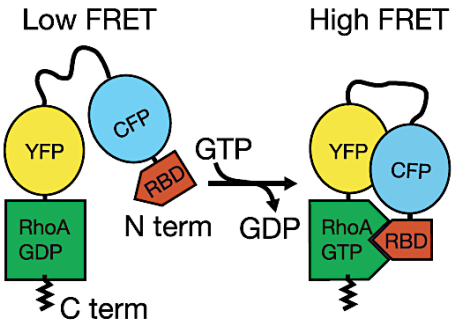

Figure 5.24: RhoA FRET biosensor: *Single chain biosensor with interacting fluorophores upon activation via GTP molecule. FRET levels evaluated via ratiometric analysis of energy transfer from donor to acceptor molecule* [13]. *Construct received from Olivier Pertz lab.*

The utilised probe was designed with donor-acceptor fluorescent pair, placed at the internal portion of the biosensor. Proximity of the effector, Rho binding domain (RBD) to the active GTP bound RhoA conformation allows subsequent proximity of the corresponding fluorophores CFP and YFP. These fluorophores behaving as donor-acceptor pair allow the energy transfer from donor to the acceptor molecule. This proximity dependent energy transfer is used as a readout for Rho activation, at the acto-myosin wound ring. Carboxy terminus of the biosensor is free to bind Rho-GDI (guanosine dissociation inhibitor), important in regulating reversible membrane location of Rho.

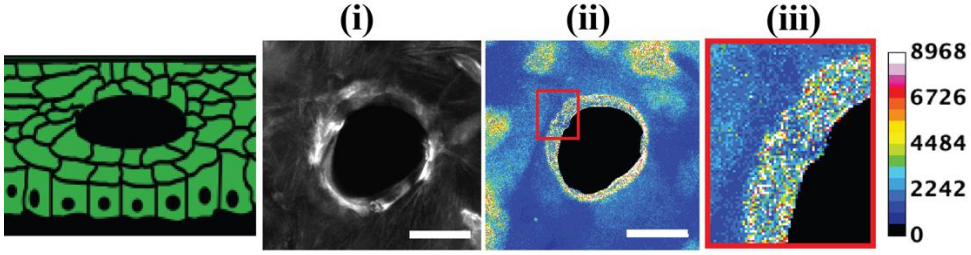

Figure 5.25: Temporal RhoA activity around constricting wound ring in an open ring conformation: *Temporal projection (90min) of wound ring constriction depicting (i) MRLC m-Cherry, showing ring and myosin cluster evolution together with simultaneous (ii) activated RhoA, around the wound ring perimeter. (iii) Zoomed area shown in red rectangle. n=3, N=4 rings. Calibration bar: grey values, Scale bar: 20µm.*

In order to obtain the FRET signal, excitation of the fluorophores was achieved with argon laser line of wavelength 458nm. Simultaneous acquisition was done for CFP and YFP channel with a sequential acquisition of MRLC-mCherry. Areas of high RhoA activation (high FRET) was determined by thresholding and processing the images for subsequent ratiometric analysis (YFP/CFP) [110].

We wanted to test spatio-temporal activity of Rho, around the acto-myosin wound ring. In addition, we also aimed at determining any putative correlation of the Rho activity with the myosin dynamics. For this we plated the doubly transfected cells, with both FRET donor/acceptor couple and fluorescently labelled MRLC, around the PDMS micro-pillars, attached stably to a coverslip. We saw distinct myosin accumulations around wound rings in both open and closed ring conformation (Movie 27, 28)

These myosin accumulations were observed in the form of cable, as well as dynamic radial and tangential myosin clusters. In order to determine any putative correlation between these distinct structures and their dynamics, constricting wound rings were visualized through simultaneous FRET and MRLC channel. Indeed, we saw consistently higher activation of Rho around these

constricting wound rings, as compared to the surrounding cells. Zone of active RhoA around the wound ring was more evident, by temporally projecting the images (Figure 5.25 (ii) and (iii: zoomed)).

Distinct myosin accumulations were observed around wound rings, even with the presence of PDMS micro-pillars inside as the physical barrier for cells. These myosin accumulations depicted cable as well as clusters. These clusters were observed to follow predominantly tangential dynamics. In order to determine any putative correlation between these distinct structures and their dynamics, these wound rings were visualised through simultaneous FRET and MRLC channel.

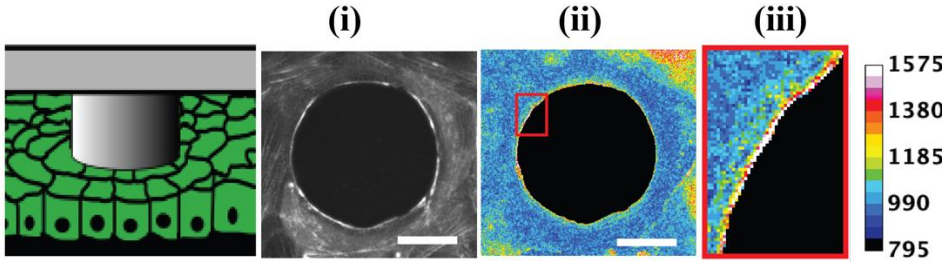

Figure 5.26: Temporal RhoA activity around the acto-myosin ring with closed ring conformation: *Temporal projection (11min) of wound rings with PDMS micro pillars inside, depicting (i) MRLC m-Cherry evolution together with simultaneous (ii) activated RhoA, around the wound ring perimeter (iii) zoomed area shown in red rectangle. Calibration bar: grey values, Scale bar: 20µm.*

In this case as well, we saw consistently higher activation of Rho around wound rings, as compared to the surrounding cells. Active RhoA zone around the wound ring was more evident, by temporally projecting the images (Figure 5.26 (ii) and (iii: zoomed)). Since we observed consistently higher amounts of active RhoA around wound rings, we examined if this had any putative correlation with myosin dynamics.

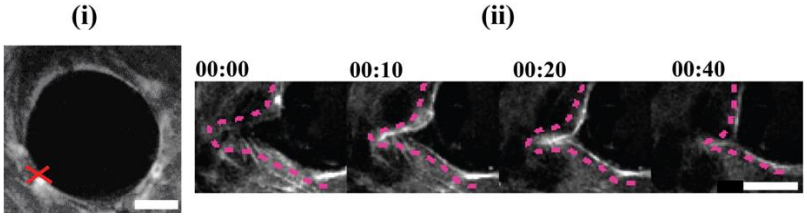

Figure 5.27: Laser ablation of the wound ring expressing FRET biosensor, visualized through MRLC-mCherry: *Ablation of the wound ring at (i) the cluster site was (ii) followed through time, to visualise the myosin recruitment during recovery of the ring. Scale bar: 20µm.*

In order to correlate any putative myosin dynamics with consequent RhoA activity around the wound rings, we first followed the approach of laser ablation of the wound rings at specific site

(Figure 5.27, (i) red cross). Ablation was chosen to be done on a cluster, to impart maximum impact and therefore larger snapped distance (compared in Figure 5.11 (i, ii iii)). This approach was chosen since the recovery of ablated rings, showed consistent recruit of myosin at the ablated sites. Ablation of cluster revealed snapping, and in turn retraction of two myosin cable ends. This was followed by myosin recruitment and recovery at the ablated site (Figure 5.27 (ii), Movie 29).

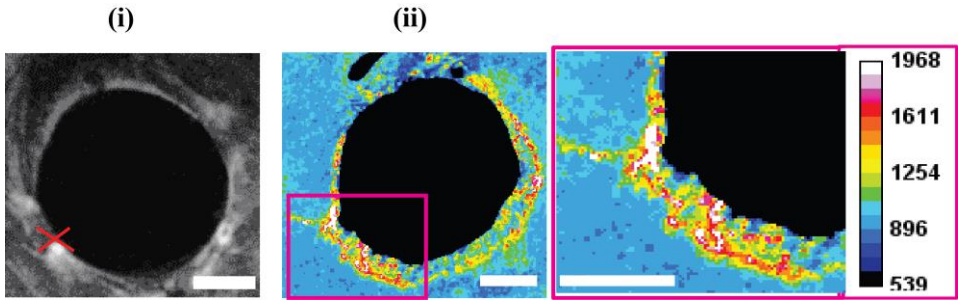

Figure 5.28: Temporal RhoA activity at the ablated site of the wound ring: *Temporal projection (11min) of wound rings with PDMS micro pillars inside, depicting (i) MRLC m-Cherry evolution together with simultaneous (ii) activated RhoA, around the wound ring perimeter (iii) zoomed area shown in red rectangle. Calibration bar: grey values, (i, ii) Scale bar: 20µm, (zoomed) Scale bar 10µm.*

This recovery was followed simultaneously by acquiring FRET, CFP/YFP channel. By analysing FRET and MRLC channel simultaneously, we indeed saw high instantaneous RhoA activation surrounding the recovering part of the acto-myosin cable (Figure 5.28 (ii)). RhoA activity was more evident by projecting the acquired FRET channel over time. This showed higher RhoA activity around the ablated site as compared to the rest of the ring perimeter (Figure 5.28 (iii: zoomed)). This shows that myosin recruitment indeed follows high RhoA activity.

Our results from FRET analysis, so far indicate that RhoA activation is existing at the acto-myosin wound ring and is consistent with myosin recruitment. We are further solidifying our FRET data and investigating the possible correlations of RhoA activation with myosin cluster dynamics. Our main goal is to evaluate possible correlations between RhoA activity, at the sites of radial and tangential cluster.

RhoA activity is known to be involved in regulation *i.e.* activation and maintenance of regulatory light chain of myosin. This is achieved via its downstream effectors, myosin light chain kinases and/or Rho-kinase (ROCK) which inhibits inactivation of MRLC via phosphatases [76][72]. As phosphorylation of MRLC activates myosin-II and its subsequent

involved in acto-myosin contractility, we wanted to determine how inactivated form of this myosin will affect myosin cluster dynamics.

4.1.14Myosin cluster rescue through change in physical environment

To examine the role of MRLC phosphorylation in wound ring constriction, MDCK cell line expressing mutant form of MRLC (nonphosphorylatable) was utilized. In this mutant form, Thr18 and Ser19 residues of MRLC was substituted by Ala. This construct fused with GFP was transfected in MDCK cells, cloned and referred to as MDCK AA [101].

Cells expressing mutant form of MRLC (AA) were plated around the PDMS micro-pillars attached to the coverslip. After cell spreading, pillars were removed carefully and wound ring constriction was studied. No clusters were seen to appear around the wound ring perimeter, during its constriction (Figure 5.29 (i), Movie 30, 31).

This was in contrast with cells expressing wild-type form of MRLC in similar configuration. Such observation was primarily attributed to the contribution of non-active (non-phosphorylatable) MRLC to the wound rings by the surrounding cells

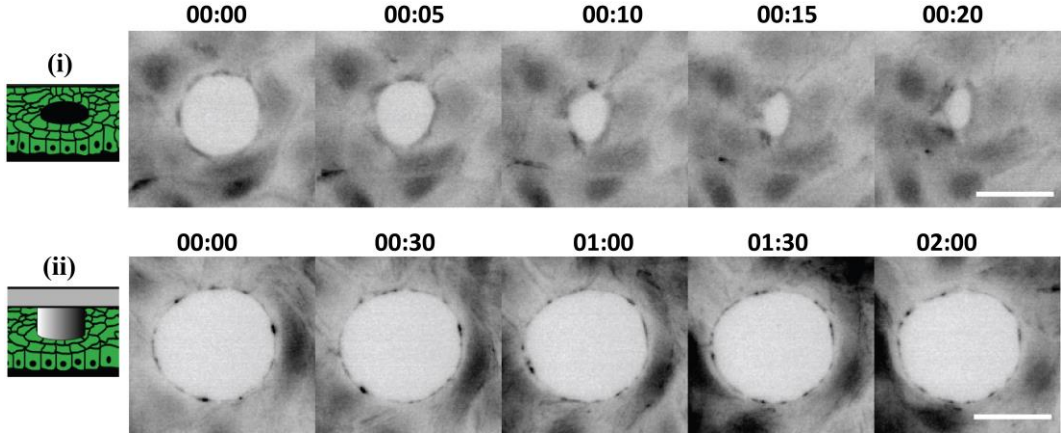

Figure 5.29: Myosin-II dynamics in wound rings expressing nonphosphorylatable MRLC (AA): *Inverted look up table (LUT) of cells expressing MRLC AA-GFP showing (i) absence of myosin clusters during wound ring constriction (ii) rescued with the help of PDMS pillars, acting as a physical barrier to the wound. Scale bar 20µm*

.

Interestingly, when these wound rings were followed through time, without removing the pillars, myosin clusters appeared to be rescued around the ring perimeter (Figure 5.29 (ii)).

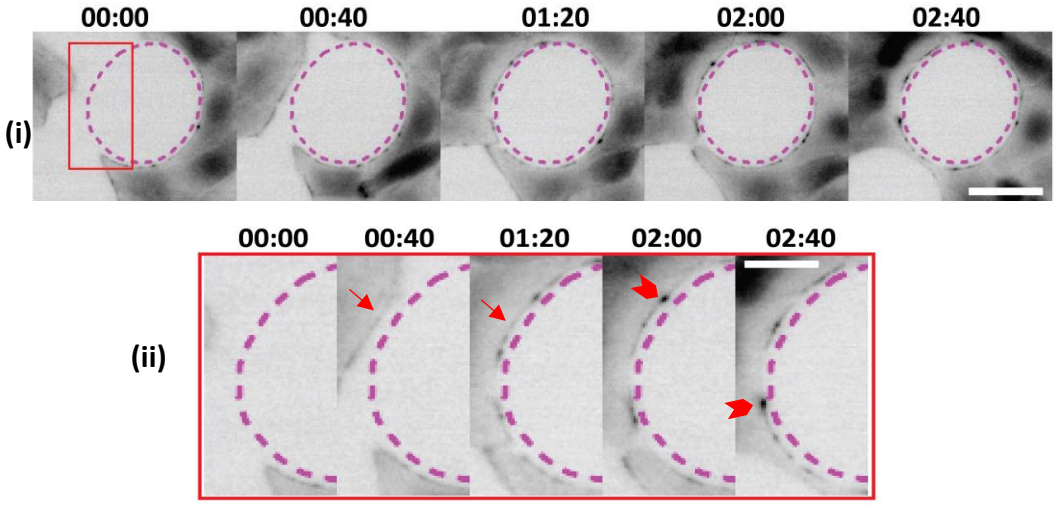

Figure 5.30: Dynamics of myosin cluster rescue in MRLC AA cells in closed ring conformation: *Inverted LUT of time lapse snapshots of (i) cells approaching the pillar surface (dashed magenta) showing (ii: zoomed) instantaneous appearance of clusters (red arrow heads) as soon as cell leading edge (red arrow) physically senses the pillar surface. Scale bar 20µm*

Observing this in real-time indeed showed appearance of clusters, as soon as the cell's leading edge was able to sense the physical barrier (Figure 5.30, (i)). These clusters became more prominent with time, when the wound was formed completely surrounding the PDMS pillar (Figure 5.30, (ii) zoomed, red arrow heads, Movie 32).

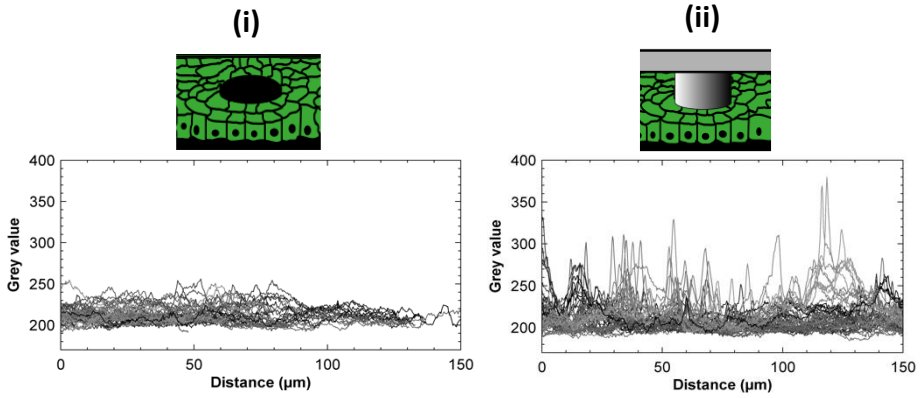

Figure 5.31: Plot profiles of wound rings expressing MRLC AA, with and without physical barrier: *Showing high intensity clusters around the perimeter of rings (right) with pillars inside, as compared to (left) constricting wound rings. n=3, N=5rings.*

Appearance of myosin clusters was quantified with intensity profile plots, tracing the wound perimeter over time (Figure 5.31). Peaks of high grey values, corresponding to the myosin clusters, as compared to wound rings without pillars showing no such cluster appearance (Figure 5.31 (ii and i) respectively). Interestingly, when these myosin clusters were followed

through time, they showed predominant presence of tangential cluster dynamics, with persistent appearance and disappearance at short time scales (Figure 5.32 (ii), white arrows). Sizes of myosin clusters observed in this configuration were similar, as compared to the clusters observed with MRLC wild-type expressing epithelial cell wound rings.

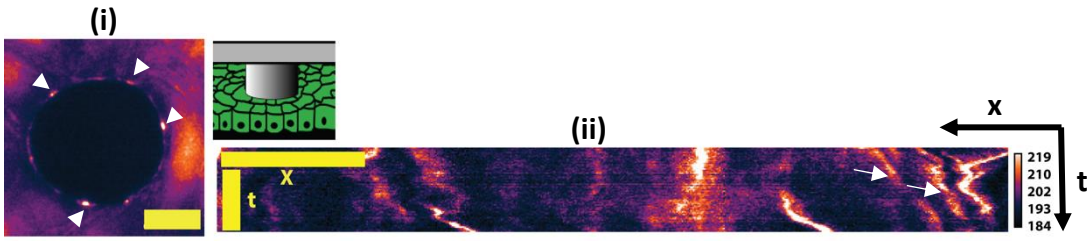

Figure 5.32: Kymograph of myosin cluster dynamics in wound rings expressing MRLC AA with physical barrier: *(i) Snapshot of a wound ring with pillar inside showing multiple clusters (in heat colours, white arrow heads) (ii) kymograph with wavy lines representing rotating clusters. Scale bar 20µm, Kymograph: Scale bar: x 10µm, t 40min*

Wound rings expressing non-phosphorylatable form of MRLC, showing a mechanical barrier induced cluster rescue, indicates involvement of a putative mechano-transduction pathway. Possible mechanism for such dynamics could be perceived as, non-stable actin and myosin interactions inside the acto-myosin cable at the wound edge. In addition to acto-myosin interaction, coordination with putative cell-cell and cell-substrate interactions in addition to Rho activity around these clusters could also be playing a role (2.4.4).

Hence, these results showing predominant presence of tangential dynamics in such configuration, indicates putative instability of these myosin clusters with respect to their binding partners, actin filaments. In addition, these results substantiate our hypothesis that, myosin cluster dynamics i.e. radial and tangential, are regulated by phosphorylated active form of myosin-II.

It is known that Rho-associated kinase inhibits the dephosphorylation of myosin, in turn maintaining it in its active phosphorylated form (p-MRLC). To this extent, we tried to inhibit this path way in closed ring conformation to see if the clusters are still rescued (APPENDIX, A.3.5).

4.1.15 Improved spatial resolution: acto-myosin rings and myosin clusters

Different microscopy-based approaches taken in this study, are corresponding to the type of information under consideration. In the earlier sections, maximum resolution of the images attained was ~0.2µm. With this resolution, we were able to visualise acto-myosin ring and self-organized myosin clusters around it using standard epifluorescence and confocal microscopy.

Constituents of the acto-myosin gel primarily includes actin filaments and myosin motors decorated throughout its length (Figure 2.10). These filaments are in the range of tens of nanometres (2.3.3). Therefore, in order to visualize filament level actin and myosin distribution we turned towards high resolution microscopy such as STED[13] and CLEM[14] where one can attain a resolution of tens of nanometres.

These approaches were taken in order to achieve gain in resolution for self-organised acto-myosin structures around the wound ring perimeter.

4.1.15.1 Correlative light-electron microscopy (CLEM)

As the name suggests, this method utilises visualisation of structures on electron microscopy slices with prior correlated light microscopy images acquired for the same spot [106].

Since this method utilises sectioning of whole cell monolayer, the challenge is to be able to trace back the ring and the cluster of interest, Owing to the symmetrical geometry of wound rings in a monolayer. Tracing has to be done from 'monolayer length' of couple thousand microns to a cluster dimension of around one micrometer. This was overcome by breaking of the monolayer symmetry by two approaches.

First, by specific micro-fabricated motifs developed to break the symmetry of cell monolayer, for recognizing the region of interest (3.8). The second method utilized tracing the clusters with the help of cadherin junctions, around the region of interest. These two approaches turned out to be of great assistance in tracing back our region of interests. Apart from this it was also useful to compare the nucleus position and tentative shape comparison of EM images, with the ones taken by florescence microscopy. This approach was taken in addition to comparing the nucleus shapes around the region of interest.

Cells used in this study, expressed both myosin regulatory light chain domain (MRLC) tagged with KO1 fluorescent protein and E-cadherin protein tagged with mNG (Table 3.1). Myosin clusters and adherens junctions were visualized through MRLC and E-cadherin localisations

[13] STED: Stimulated emission depletion microscopy
[14] CLEM: Correlative light electron microscopy

respectively. After chemical processing and resin embedding of the sample, 'EM grids' containing ultra-thin slices of wound rings are visualized by TEM electron microscope.

First, we tested if the 'monolayer symmetry breaking' and E-cadherin junctional shape, helped in tracing back our region of interests and indeed we were able to do so by tracing back specific acto-myosin ring and myosin clusters by this method (Figure 5.33, blue rectangle: acto-myosin ring and red rectangle: cluster). These observations were a proof of an efficient tracing method.

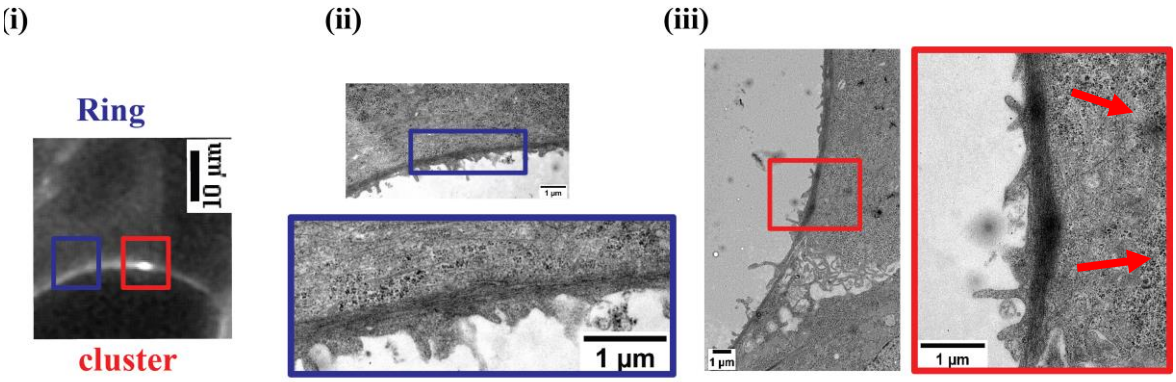

Figure 5.33: Transmission electron microscopy of myosin cluster and wound rings: *Correlative studies of the region of interest (acto-myosin wound ring: blue and myosin clusters: red), first visualised by (i) light microscopy and further correlated by tracking them, on ultra-thin EM sections of ~80µm. (ii) Showing actin filament bundles depicted by dense electron region of an acto-myosin wound ring corresponding to blue rectangle. (iii) Showing actin filament bundles with myosin cluster (zoomed image: showing two sub clusters: red arrows) corresponding to cluster in (i).*

We were able to observe dark bands at the wound edges, corresponding to electron dense regions, depicting dense actin filament bundles (Figure 5.33, blue: dark bands at the edge). These actin filaments were observed to be arranged parallel to the wound edge, as opposed to the filaments in the cytoplasm, with showed a mesh like framework.

After the protocol to trace back and visualise our region of interest was standardized, we repeated the process with additional samples for visualising actin filaments and myosin distribution in clusters as well as the homogeneous part of the acto-myosin ring. This was done to get better insights into the filament number and distribution, in these dense regions.

First, we acquired myosin clusters at the wound perimeter by fluorescence microscopy, visualized both for E-cadherin tagged junctions as well as myosin motor protein (Figure 5.34, (i): cell-cell junctions, (ii): myosin clusters: red arrows). Samples were processed to obtain ultra-thin sections of these areas, later placed on EM grids for image acquisition.

Structures were visualised by transmission electron microscopy showing electron dense regions inside the cluster area corresponding to high myosin accumulations. It was clearly visualised that myosin high density areas, seen almost touching each other near cell-cell junction, were in

principle ~0.5-0.7µm separated from the junctional area (Figure 5.34, right panel). This observation was also in agreement with our data showing that clusters do not cross the cell-cell junctions while showing tangential dynamics (Figure 5.10, (i) b, (ii) b). The structures were evaluated by ultra-thin sectioning of 80µm and visualised by Electron microscopy.

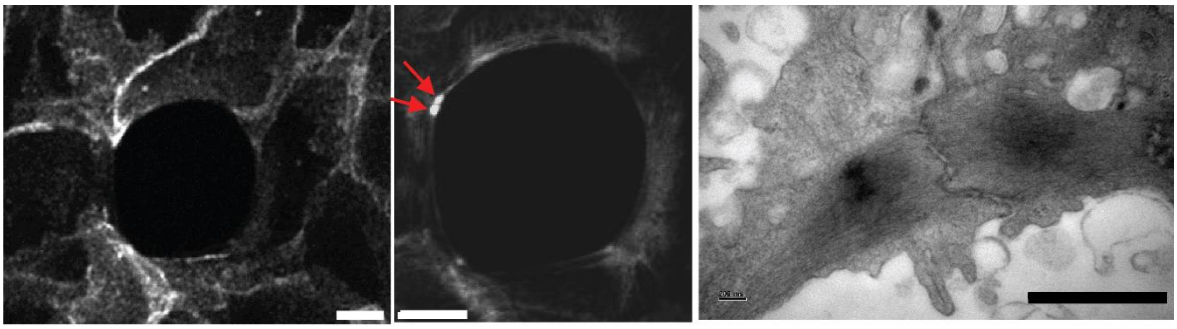

Figure 5.34: Transmission electron microscopy of myosin clusters near cell-cell junction: *(i) Wound rings with corresponding junctions visualized by E-cadherin-mNG. (ii) Two myosin clusters near cell-cell junction, visualized by MRLC-GFP. (iii) TEM image of a single section showing distinct electron density corresponding to myosin accumulation inside the two clusters. Scale bar: fluorescence images:10µm, TEM image:1µm.*

Such thin serial sectioning helped us in determining the position of acto-myosin ring and myosin clusters, by TEM. Information about the section number, showed that myosin clusters and the acto-myosin ring to be present ~1-1.5µm above the surface of the coverslip. Acquisition of bottom most sections showed traces of plasma membrane and absence of the filaments. This demonstrated the fact that acto-myosin ring and the myosin clusters are present ~1-1.5µm above the surface of the coverslip.

Since we could achieve these ultra-thin sections of 80µm, we next established if there were variations of actin filaments and myosin accumulations, among these serial sections. Indeed, we observed that serial EM sections of acto-myosin ring and myosin clusters, both showed differential electron dense areas (Movie 33).

These electron dense areas were illustrated by differential myosin dense regions and actin filament density in and around the clusters respectively (Figure 5.35, (ii): left to right depicting sections from bottom to top).

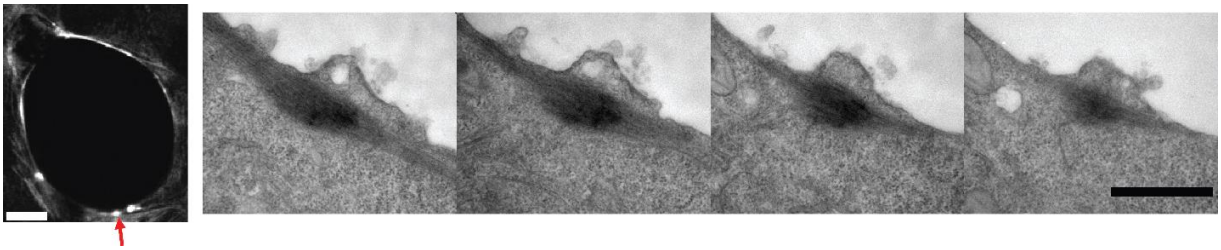

Figure 5.35: Transmission electron microscopy of myosin clusters across sectional thickness: *(i) Myosin cluster and acto-myosin ring visualized by MRLC-GFP showing myosin cluster (red arrow). (ii) Cluster sections with increasing thickness of ~80µm from the bottom of the coverslip depicted in the form of montage (left to right). Scale bar: fluorescence images:10µm, TEM montage:1µm.*

Next, we are interested to get numbers for the actin filament distribution in seen in the acto-myosin ring through EM image analysis by accurate plot profiles. In addition, with higher magnification we saw small myosin foci inside each cluster. Next, we were also interested in extracting the number of these foci inside one myosin cluster to try and characterize their distribution. Our preliminary results are in accordance with the previous data of theoretical analysis [5] where thresholded images for clusters depicted ~10 sub-clusters within a clusters and around similar number of actin filaments in single cuts (analysed by intensity profile).

Both this information will give us unprecedented knowledge about acto-myosin distribution in varying self-organized structures around the wound ring. This information in addition to distinct myosin cluster dynamics: radial and tangential, will help extracting numbers which could be introduced into coarse-grained equations for simulating these dynamics in acto-myosin ring constriction.

Apart from observing the high-density foci inside each myosin cluster, sometimes fluorescence microscopy of one cluster depicted two sub-clusters, when visualized through high resolution EM microscopy. We further took an approach of immunofluorescence of tagged MRLC and actin. We followed this approach together with STED super-resolution microscopy to visualise any such sub-arrangements within a cluster.

4.1.15.2 STED

In order to visualize our region of interest: myosin clusters and acto-myosin rings, we took an approach of recognising proteins with specific antibodies against them. In this case we were interested in actin filaments and activated form of MRLC. Therefore, we used phalloidin dye and phospho(p)-MRLC antibodies, for ‘actin filaments’ and ‘activated form of myosin

regulatory light chain' respectively. Immunostaining protocol was performed in order to visualize localization of our protein of interest (3.7)

First, we co-stained the acto-myosin rings for phospho-MRLC and phalloidin, visualized by secondary antibodies StarRed and AF594 respectively (Excitation: 640nm and 590nm respectively). We often observed a sub-structural organization within these clusters. This organization followed the arrangement where actin filaments and myosins, rather than being arranged uniformly: seemed to accumulate at the centre and at the periphery of a single cluster respectively. This arrangement was reminiscent of one of the arrangements that we observed with CLEM. (Section 4.1.15.1, Figure 5.33 (ii)).

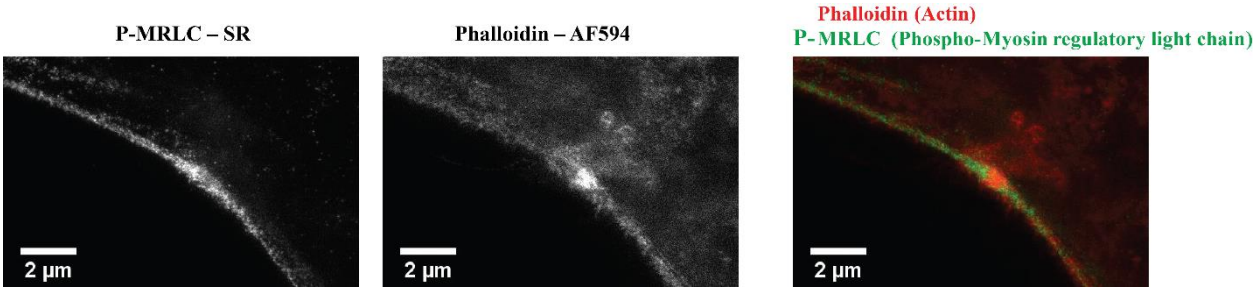

Figure 5.36: STED imaging of actin and myosin within clusters: *Co-staining of wound rings with antibodies against activated form of myosin by p-MRLC-StarRed (left) and actin filaments by phalloidin-AlexaFluor594 (middle), showing differential distribution actin and myosin inside a myosin cluster with actin accumulating in the middle and myosin at the edges of the cluster (merge: right).*

Different actin and myosin arrangements within a cluster observed by STED and CLEM, could be indicative of the putative distinct temporal dynamics: radial and tangential, followed by these clusters (Figure 5.19, 5.21 and 5.22). To test this further, we plan to image these clusters with electron microscopy, correlating them with the radial or tangential dynamics, followed by these clusters.

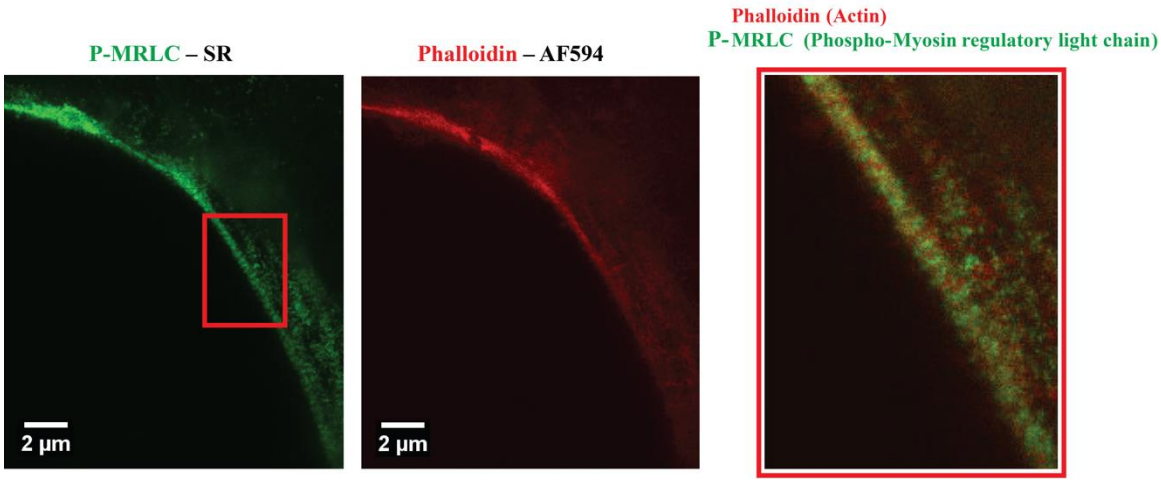

Figure 5.37: STED imaging of actin and myosin within acto-myosin ring: *Co-staining of wound rings with antibodies against activated form of myosin by p-MRLC-StarRed (left) and actin filaments by phalloidin-AlexaFluor594 (middle), sometimes show regular arrangement (rectangle) depicting alternating actin and myosin bundles (right: zoomed, merge).*

Apart from differential actin and myosin arrangement within the clusters, we also observed some peculiar arrangement of this network, within the wound rings. This arrangement depicted an evenly arranged regular organisation (Figure 5.37: right, merge). This kind of ordered acto-myosin arrangement, has also been reported in rat embryo fibroblast cell line. Such ordered arrangement of acto-myosin structures was explained via regulation of filament ordering. This arrangement has been studied to be dependent on coordinated function of actin crosslinking proteins such as tropomyosin and alpha-actinin, in a regulated and competitive manner [111].
These observations of periodic arrangements were done by immunostaining, we would also like to confirm this by electron microscopy to look for any reminiscence of such acto-myosin network arrangements.
Since alpha-actinin is abundant in a cell and directly links actin filaments to adhesion complex, inhibition of it might shed light of their role in such an ordered configuration of filament bundles. In addition, such arrangements were corresponded to lower focal adhesion and tension associated with the cells containing them [111]. This was coherent with our data of lower forces in the wound rings as compared to the clusters (4.1.9)

Until now, I discussed acto-myosin ring and myosin clusters ‘in specific’, applying forces to achieve multi-cellular wound ring constriction.

Similarly, myosin clusters have also been studied to apply forces within the cytokinetic acto-myosin ring during single cell division process. Presence and indispensable involvement of these myosin clusters, have been studied in context of mammalian (HeLa) and fission yeast cell cytokinesis [5].

In the previous sections, I described the distinct myosin cluster dynamics *i.e.* radial and tangential clusters, in terms of multi-cellular acto-myosin rings. This observation mirrored similar myosin cluster dynamics observed during cytokinesis in mammalian and fission yeast cells, respectively [5].

4.2 MYOSIN CLUSTERS: MAMMALIAN CYTOKINESIS

Previous study in the lab described myosin clusters, playing distinct roles during cytokinesis process of both fission yeast and mammalian cells. This was described with respect to stress generation and transport of wall machinery in mammalian cells and fission yeast respectively. Since these clusters seem to be conserved throughout systems, we wanted to evaluate early stages of their spatio-temporal existence. This could impart crucial information regarding their properties across systems.

To this extent, I tried to resolve their spatial and/or temporal dynamics during early stages of acto-myosin ring constriction.

4.2.1 Myosin cluster distribution in cytokinetic rings

In HeLa cell cytokinesis, myosin cluster was observed to be present in an orderly fashion, around the acto-myosin ring perimeter. This observation was made possible with the help of micro-cavities referred to as 'cavities' in the rest of the text.

The need for placement of cells in cavities stemmed from the fact that, cytokinetic rings observed on flat surfaces failed to attain the required resolution to visualise the myosin clusters in focus. Cells at the beginning of their division cycle were plated on glass coverslips, via mechanical shake-off of the flask containing the cells [95]. Full division cycle of a cell can span from 16-18h, although the mitotic (M)-phase lasts only a couple of minutes. Cytokinetic rings imaged on flat surfaces had to be reconstituted through fast 'z' slice imaging where one cell measures ~20µm in diameter.

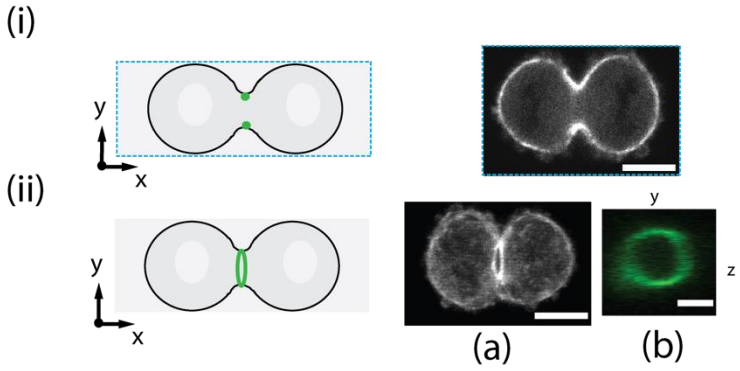

Figure 5.38: Cytokinetic ring visualized on coverslips: *(i) Cytokinetic ring (tagged-myosin heavy chain MHC) visualised on a flat surface with one 'xy' plane showing two-point accumulations. Reconstitution of (a) 'xz' and (b) 'yz', en face plane projections, showing a deformed blurred ring. Scale bars (i and iia 10µm, iib 5µm).*

First, this was not an efficient way of acquisition and second, it does not provide the required resolution for visualizing cytokinetic rings and associated structures. Cytokinetic rings acquired in this manner with single 'xz' plane provided an image with two-point accumulations for the cytokinetic ring (Figure 5.38 (i)). In case of fully reconstituted 'xz' and/or 'yz' planes, spatially distorted rings were obtained (Figure 5.38 (iia, b)).

In this context, micro-fabrication has allowed to prepare 3D environments which are compatible with cell growth and organ designs [112][113]. Shapes in 3D are generated with micrometre resolution using specific protocols (3.1.3). Preparation of these cavities, where cells can be placed vertically with respect to the cover glass was reported earlier by the lab. [114][96][100]. In these 3D configurations, cell division can be observed in a direction perpendicular to the long axis of the cell, and the corresponding cytokinetic ring can be visualised with unprecedented resolutions.

Therefore, in order to visualize the full cytokinetic ring in the same focus, cells were placed inside PDMS cavities of appropriate diameter and height (3.5.2.1.2). By doing so, myosin clusters were visualized depicting a periodic arrangement with an inter-distance of ~0.8µm, around the full ring perimeter [5] (Figure 5.39 (iiia b)). This observation was made with an upright microscope since the cavity configuration we used earlier had PDMS layer at the bottom (Figure 5.39 (i)). This polymer layer gave a blurring ring image when acquired with an inverted microscope setup, due to distortion of light through the polymer layer (Figure 5.39 (iia b)).

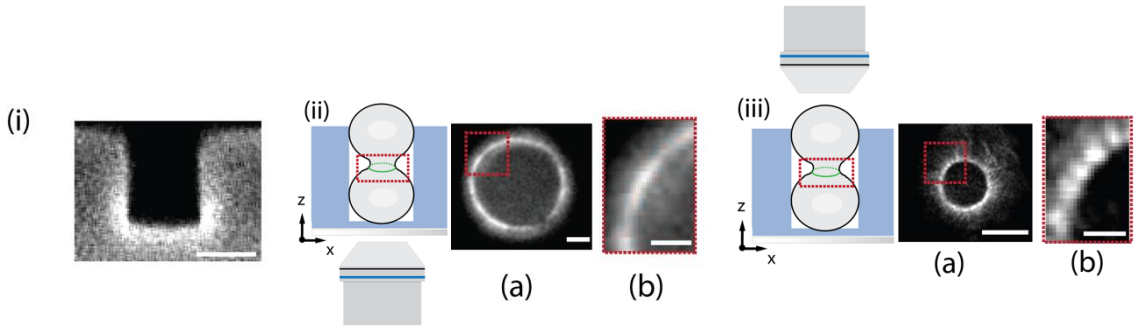

Figure 5.39: Cytokinetic ring visualized inside PDMS cavities: Figure 3: Gain in spatial and temporal resolutions in cavities: *(i) PDMS cavities with polymer (PDMS) layer at the bottom. (ii) Synchronized cells seeded inside cavities visualized with an inverted set-up (illustration) showing (a) blurred cytokinetic ring* [5] *(tagged-MHC) (b) inset: zoomed view showing a blurred portion of the ring. (iii) Better ring resolution attained via imaging with an upright microscope (a) revealing cytokinetic ring with (b) evenly spaced myosin clusters around ring perimeter. Scale bars (i 10µm, iia and iiia 5µm, iib and iiib 3µm).*

To be able to visualize the rings with better resolution and through ease of using an inverted microscope for live samples, we prepared through-hole cavities (Figure 5.40 (i), 3.2.2.1.2, Movie 34, 35).

These through-hole cavities were prepared with the help of UV crosslinking polymer NOA-74. In addition to obtaining optimal resolution, cured form of this polymer has a refractive index closer to glass coverslip (~1.52).

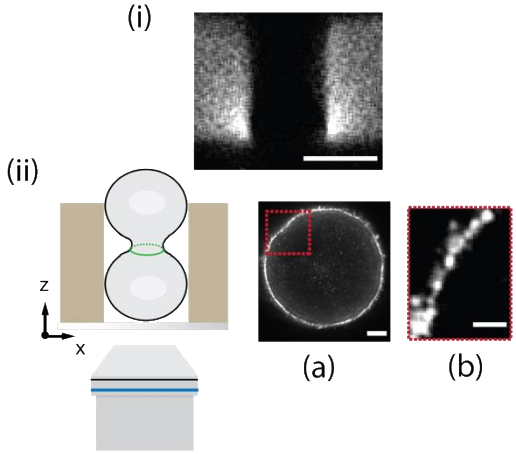

Figure 5.40: STED imaging of the cytokinetic ring inside through-hole cavities: *Gain in resolution on an optimized set-up, (i) NOA-74 through-hole cavities. (ii) Synchronized cells are seeded inside cavities and visualized with an inverted setup. (a) Visualization of cytokinetic ring (b) revealing individual myosin clusters, zoomed view. Scale bars (i 10µm, iia 5µm iib 1µm.*

This minimizes distortion of light due to passage through the polymer layer. Refractive indices of both PDMS (~1.41) and NOA-74 (~1.52) are close to glass, with NOA-74 being a better candidate. By utilising these through-hole NOA74 cavities and visualizing the cytokinetic rings through STED super-resolution we were able to resolve myosin clusters with a better spatial resolution (Movie 36).

This gain in resolution will also bring unprecedented information about temporal resolution of myosin clusters in this configuration and also can be used for other systems providing the necessary 3D environment for cells for studying other cellular processes like lumen formation etc. We are using this configuration in our lab to study several different systems such as MDCK clusters and 3D organoid assembly of mouse pancreatic as well as embryonic stem cells.

4.2.2 Myosin cortical rotations during cytokinesis.

Most of the fully-grown organisms are bilaterally asymmetric with respect to their organ placement. Bilaterally symmetrical embryos are known to break this left-right symmetry, during early stages of the embryonic development [115]. Key factor involved in this symmetry breaking event has been associated with acto-myosin cytoskeleton [116][19]. *In vitro* motility assays have indicated the possible role of myosin motors, by demonstrating rotations in actin filaments around its own axis, due to the myosin motor activity [117]. Such illustrations have strengthened the idea of myosins being one of the key players for chiral asymmetries in early developing embryos. One of the recent studies in *C. elegans* embryo investigated this chiral behaviour of the acto-myosin cortex. By analysing the polarised flow of cortical myosin in early

C. elegans embryo, it was demonstrated that forces from myosin molecular motors can generate turning and twisting of the actin cortex. These local rotations were in turn shown to be responsible for global chiral rotations of anterior half, countering with respect to the posterior half of the embryo. This phenomenon was described to be responsible for asymmetry of the *C. elegans* embryo [19]. These studies were performed in the early embryonic stages *i.e.* 1 and 4 cell stage illustrating that changes in the acto-myosin cytoskeleton of single cells are capable of driving asymmetry throughout the entire embryo.

While studying HeLa cell cytokinesis inside cavities, we observed hints of such chirality in our system as well (Movie 37).

Cells in cavities usually had a portion of cell cortex visible due to occasionally tilted cells. Due to this we were able to observe putative rotations within the cell cortex [5] (Figure 5.41 (ii) white arrows).

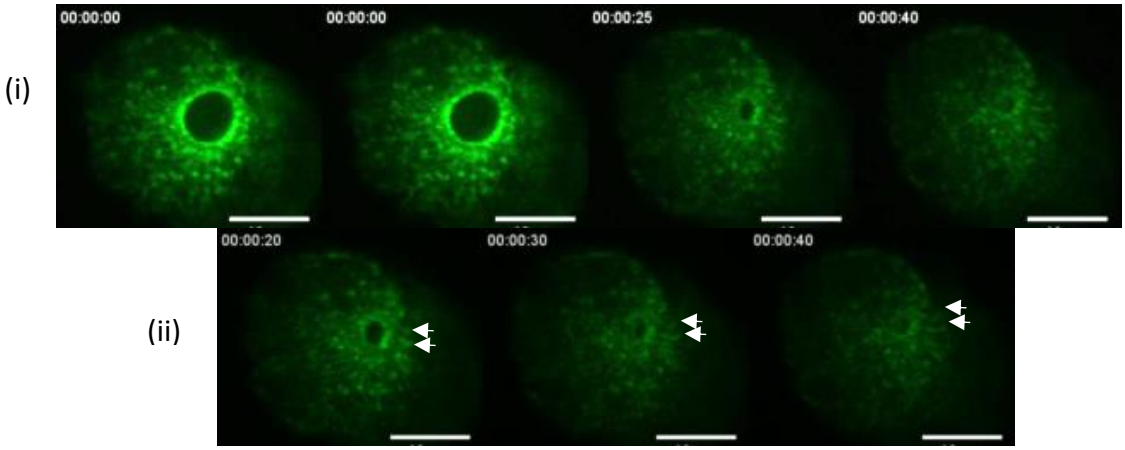

Figure 5.41: Myosin cortical rotations in cytokinetic rings, inside cavities: *Time evolution of (i) full cytokinetic ring constriction observed, inside cavities. (ii) Putative cortical rotations were observed depicted by white arrows marking two cortical strands and their movement anti-clockwise towards the end of ring constriction. Time hh:mm:ss. Scale bars 10µm.*

To be able to further visualize these observations we went back to the configuration of flat surface, using glass coverslips. These rotations died out or were hindered when high

concentration of extra-cellular matrix protein, fibronectin (>10µg/ml) was coated on the coverslips. This was most probably due to stronger cell attachment, to the surface.

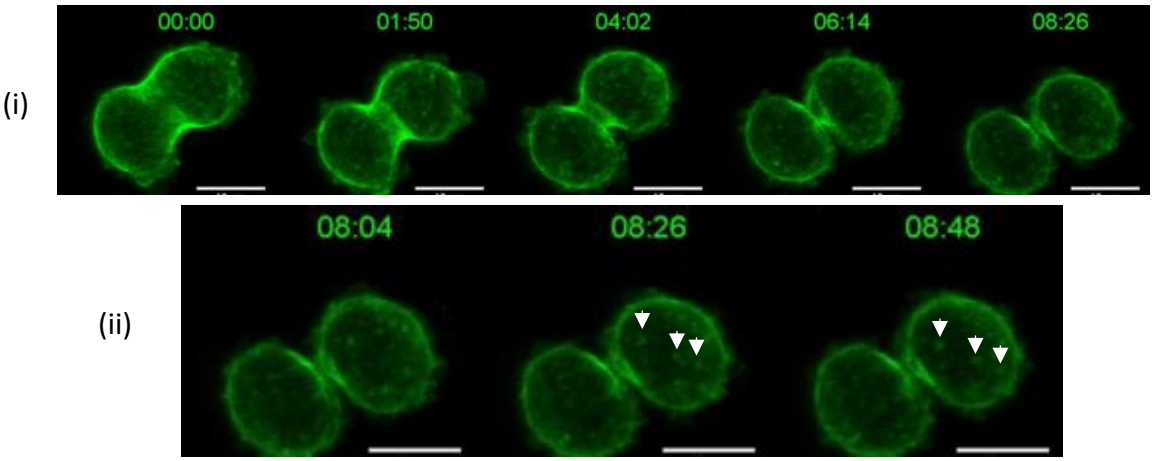

Figure 5.42: Myosin cortical rotations in cytokinetic rings, on coverslip: *Time evolution of (i) full cytokinetic ring constriction observed, on a flat surface. (ii) Cortical rotations were observed depicted by white arrows marking three cortical spots and their movement upwards towards the end of ring constriction. Time mm:ss, Scale bars 10µm.*

Although when low fibronectin concentration was coated on the surface (~8-10µg/ml) dividing cells indeed observed to follow cortical rotations during cell division (Figure 5.42 (i)). These rotations could be traced with the help of myosin clusters arising in the cortical regions (Figure 5.42 (ii, white arrows, Movie 38).

We precluded any environmental flow induced rotation of the cells, by putting fluorescent beads and tracking their movement.

We could not conclude on whether there existed a preferred chirality in the cortex (clock- or anti-clockwise), due to insufficient number of repeats and hence, this is a work in progress.

These results suggest that indeed acto-myosin based cortical rotations are existing conserved throughout different systems and can act as generic readout for their evolution.

4.3 MYOSIN CLUSTERS: FISSION YEAST CYTOKINESIS

Along similar lines, we also tested if there were any conserved chirality of myosin cluster movement, during formation of a fission yeast cytokinetic ring.

Fission yeast cytokinetic ring is observed to take shape via, coalescing myosin clusters in the time span of 4-5min before the start of ring constriction (Figure 5.43). Cells used in this study expressed regulatory light chain (RLC)-mCherry. We coated coverslip with *lectin* in order to stabilize the these yeast cells and visualized them with high speed spinning disk microscopy using 63X, 1.2 N.A objective. This provided us with good temporal resolution to catch this fast phase of coalescing myosin clusters.

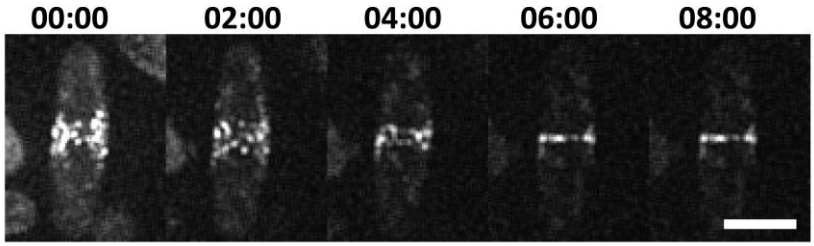

Figure 5.43: Coalescing myosin clusters in Fission yeast cytokinesis: *Clusters of myosin coalescing to form a functional cytokinetic ring, which would eventually lead to diving the cell into two. Time mm:ss Scale bar 2µm*

Coalescence of these clusters has been reported following the *search, capture, pull and release model* [118]. This model described the process as, actin filaments growing from the membrane associated nodes with adjacent nodes capturing the actin filaments and subsequent force applied by myosin-II between the connected nodes. This eventually leads to actin filament breakage and the process continues till these nodes coalesce into the cytokinetic ring in time span of ~10min. Capturing of these nodes was described to be myosin-II dependent, leading to the transient pull on these nodes, in turn forming the contractile acto-myosin ring [83].

We were interested to evaluate any putative chiral rotation in these coalescing myosin clusters. By analysing the 3D reconstructed image on IMARIS software, we tracked these clusters through time ~3-5 min (Figure 5.44).

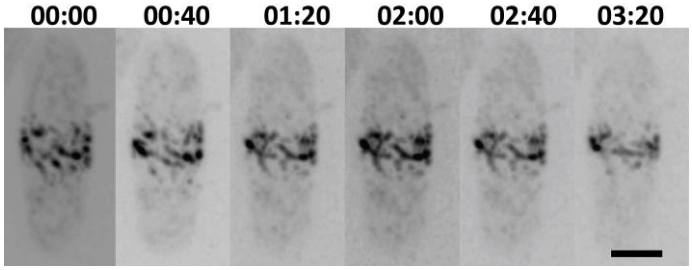

Figure 5.44: 3D reconstruction of fission yeast myosin cluster coalescence during start of cytokinesis: *3D reconstituted 'z' stack images depicting myosin clusters, were traced to look for any putative conserved rotations of these clusters during the process of early coalescence. Time mm:ss. Scale bar 2µm.*

Although we did not see any conserved chiral rotation for these myosin clusters and they seemed to follow a stochastic path towards coalescing into the acto-myosin ring, leading to further constriction (Movie 39).

CONCLUSIONS AND OUTLOOK

On the basis of previous study performed on single cell cytokinetic (acto-myosin) ring [5], we hypothesised that ***still myosin clusters were associated with higher stress as compared to tangential clusters***.

Interestingly, we observed that both dynamics co-exist in our multi-cellular system of MDCK epithelial cells. Therefore, in this study we focused on characterising these two different myosin cluster dynamics, radial and tangential in the context of a multi-cellular ring. Epithelial cells with stably expressing activated form of myosin, myosin regulatory light chain fused with GFP, was utilized in this study using open ring conformation. This conformation corresponded to removal of PDMS pillars from the cell monolayer.

The ring led the closure. This was substantiated by the fact that wound closure/constriction rates were constant and ~0.3μm/min with varied cell number with the same density. Myosin clusters were observed around the ring perimeter. These clusters were observed to be present at constant density throughout ring closure, and hence decreasing number over smaller diameters. Cluster contrast depicting concentration of myosin in the clusters was also maintained to be constant over ring constrictions. These results are similar to data reported for cytokinetic rings.

Distinct cluster dynamics at the acto-myosin wound edge was followed to be the main determinant contributing to comparatively faster or slower closure rates. These cluster dynamics were characterised as radial and tangential clusters, followed over time of ring constriction. These clusters were observed to impact the closure rate, even persisting for a finite amount of time in the ring for typically 6min, sometimes extending up to 30 minutes. The local closure rates were observed to be related to the local type of cluster dynamics existing at that portion. Global closure rates were also evaluated to be dependent on the relative fraction of radial and/or tangential clusters.

Such phenomenon suggested a difference in stress related to these two types of dynamic clusters. Stress evaluation in terms of recoil velocity, recoil distance as well as nonlinear exponential curve fit, depicted higher stress associated with radial clusters compared to tangential clusters. This illustrated faster ring constriction to be related with higher fractional presence of radial clusters and subsequently associated with higher stress as compared to tangential clusters. Similar to cortical myosin clusters observed during *C. elegans* 1-cell stage embryo [7], cortical myosin clusters were also observed during mammalian ring constriction.

This illustrates highly conserved presence of myosin clusters between different systems with potentially shared functions at the mesoscopic scale.

Characterising acto-myosin ring, depicting twice high myosin intensity compared to surrounding cells, depicted putative myosin conservation with time of constriction. Myosin conservation during ring constriction was evaluated via myosin loss from the ring perimeter to the adjacent cells. Myosin turnover dynamics showed lesser turnover and therefore higher myosin stability associated with clusters compared to the ring.

Interestingly, tangential clusters were mainly observed in the closed ring conformation – with pillars still in the monolayer. Possible mechano-transduction in this closed ring conformation was observed via myosin cluster rescue even in the presence of myosin light chain kinase inhibitor (ML-7). This was further evaluated by active RhoA FRET. Indeed, higher active RhoA was observed to encircle the ring in closed conformation, as compared to the adjacent cells. Together with closed ring conformation, open ring conformation also showed higher active RhoA around the constricting rings. As reported in other systems [77], myosin recruitment was shown to be correlated with regions to higher active RhoA.

Using higher resolution microscopy with CLEM and STED, sub-structural organisation of myosin within single myosin clusters was revealed. This depicted ~10 sub-clusters within a clusters and around similar number of actin filaments in single cuts.

Hence, myosin cluster dynamics can be proposed as a generic entity for biological regulation, regulated by self-organisation. Specifically, we characterised rings constrictions in circular wounds in epithelial layers. Clusters dynamics of myosin allow so far to bridge stress generation and morphogenesis in these different systems.

We are planning to correlate our RhoA analysis specifically to radial and tangential clusters in collaboration with Olivier Pertz (University of Bern). This will shed light on any putative RhoA mediated regulation, with respect to distinct cluster dynamics.

We saw radial clusters correlated with higher constriction rates as compared to tangential clusters. Also, cell-cell junctions act as barriers for the movement of these clusters. In this context, we are also evaluating the correlations between cluster dynamics and its adjacent cell movements. This analysis would be helpful in determining if the two dynamics are perfectly correlated, consist a delay and/or which one is leading up to another.

Lastly, we are also working on a theoretical model to explain the dynamics in our system, in collaboration with Karsten Kruse lab. (University of Geneva). Formalisms designed in the study with cytokinetic rings [5] seem to hold true in our multi-cellular system. However new developments in the theory could give new concepts in the self-organisation and the onset of the instability [119]. Also, this ring is composed of segments of acto-myosin cables between cell-cell contacts, and this could lead to other mechanisms.

Altogether, our study would shed light on the dynamics of key phenomena in biological systems, such as wound healing, cytokinesis and embryogenesis in general. Simple epifluorescence microscopy is required to capture the changes in shapes, and this clusters tracking could be implemented in any model systems with standard equipment. Rules determined by studying these clusters in synergy with theory could provide unprecedented knowledge to explain morphogenesis with a predictive power.

APPENDIX

A.1 ABBREVIATIONS

ABBREVIATION	FULL FORM
PDMS	Polydimethylsiloxane
TMCS	Trimethylchlorosilane
MPTMS	3-(mercapto) propyltrimethoxysilane
TRITC	Tetramethyl rhodamine isothiocyanate
MRLC	Myosin regulatory light chain
p-MRLC	Phospho-Myosin regulatory light chain
GFP	Green fluorescent protein
KO1	Kusabira orange1
mNG	Neon green
FRET	Fluorescence Resonance Energy Transfer
MDCK	Madin-Darby Canine Kidney
DMEM	Dulbecco's Modified Eagle Medium
FBS	Fetal bovine serum
PLL-g-PEG	Poly-l-lysine-g-PolyEthylene Glycol
PBS	Phosphate buffer saline
GDP	Guanine Di-Phosphate
GTP	Guanine TriPhosphate
FN	Fibronectin
CLEM	Correlative Light Electron Microscopy
STED	Stimulated Emmison Depletion Microscopy
GDI	Guanine nucleotide Dissociation inhibitors
GEF	Guanine nucleotide exchange factors
AF594	Alexa-fluor 594
SR	Star-Red
ROCK	Rho-associate-kinase
PM	Plasma membrane
MLC2	Myosin Light Chain 2
ECM	Extra cellular matrix

A.2 SUPPLEMENTARY INFORMATION OF PRODUCTS

PRODUCT NAME	BRAND	REFERENCE
DMEM (4.5g/L glucose)	Gibco	4196506
DMEM (1g/L glucose)	Gibco	31885049
Foetal Bovine serum	Fisher	10309433
Penicillin streptomycin (antibiotics)	Fisher	11548876
Leibovitz L-15 medium	Gibco	11540556
Lipofectamine™ 2000 Transfection regent	Invitrogen	11668500
Trypsin (0.25% EDTA)	Gibco	11570626
Fibronectin	Sigma Aldrich	F1141
Petri dish	Greiner Bio-One	628161
Glass coverslip	Deckgläser	0111650
3-(mercaptopropyl)trimethoxy silane (MPTMS)	Fluorochem	S10475
Chlorotrimethlysilane (TMCS)	Sigma Aldrich	92360
SU8-2025 photoresist	MicroChem	-
Silicon Wafer	Si-Mat	PRIME
Photomask	Selba	-
Geneticin	Invitrogen-thermofisher scientific	11548616
TRITC-fibronectin	Cytoskeleton inc.	FNR02
SU-8 developer	Chimie Tech Services	DevSU8/4
NOA 74	Norland Products Inc.	-
PDMS	Sylgard	DC184
Goat a-mouse Star Red (SR) 2	Abberior	2-0002-011-2
Goat a-rabbit Star Red (SR) 2	Abberior	2-0002-011-9
Phalloidin AF594	Thermo-Fisher	A12381
Phalloidin Star red	Abberior	STRED-0100

DRUG	BRAND	REFERENCE
C3 transferase	Cytoskeleton	CTO4-A
Y27632	Sigma Aldrich	Y0503
ML-7	Sigma Aldrich	M-1296

A.3 SUPPLEMENTARY RESULTS

A.3.1 Wound ring constriction in MDCK wild type (WT) cells

Wound ring closure was analysed for wild type cells. Closure dynamics followed similar trend as MDCK MRLC-GFP (4.1.4.1). Although on an average, the final time of closure was increased by ~3h more for MDCK WT, as compared to MDCK MRLC-GFP. This result could because of a certain level of overexpression of activated myosin *i.e.* MRLC leading to comparatively controlled closures.

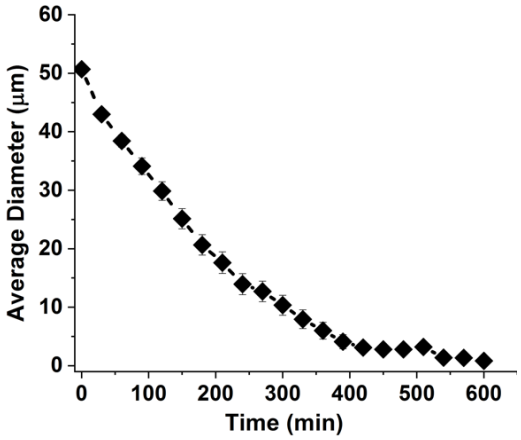

Figure A1: Average ring diameter over time for WT cells. *Error bar: SEM*

A.3.2 Rate of ring constriction for different cell lines used

Wound constriction rates for the three MDCK cell lines WT, myosin regulatory light chain (MRLC-GFP) and non-phosphorylatable myosin regulatory light chain (AA-MRLC-GFP) was evaluated.

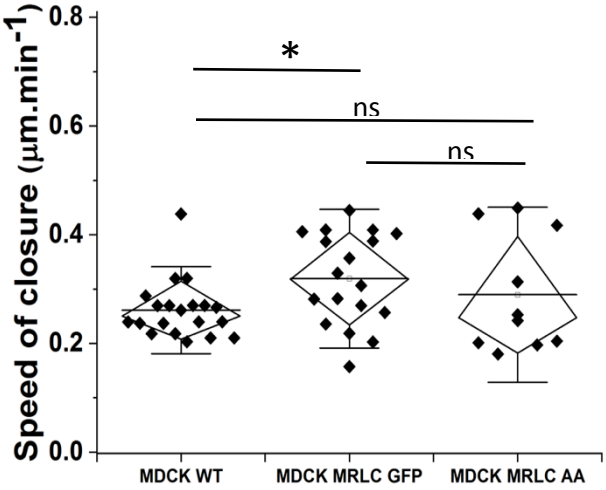

Figure A2: Comparison in rate of constriction for the three cell lines used in this study. *2-way ANNOVA, significance at p-value > 0.05.*

Rate of constrictions were more or less similar for all the cell lines. Although validating the previous result (Figure A1), there was borderline significant increase in closure rates corresponding to MRLC-GFP as compared to wild type cells.
Although it was reported for the cell these lines to have almost similar basal levels of MRLC [101], we believe that the change in closure rates could be due to comparatively higher expression of MRLC in cell lines expressing it. We are evaluating this using Western blots.

A.3.3 Formin staining and visualization by STED microscopy

Throughout the text, we describe wound ring constriction on the basis of acto-myosin contraction.
Actin architecture involves 'formins', which help provide polarity to the actin architecture and for the filament elongation (2.3.4, Figure 2.4). We wanted to visualise how these proteins are arranged at the acto-myosin ring.

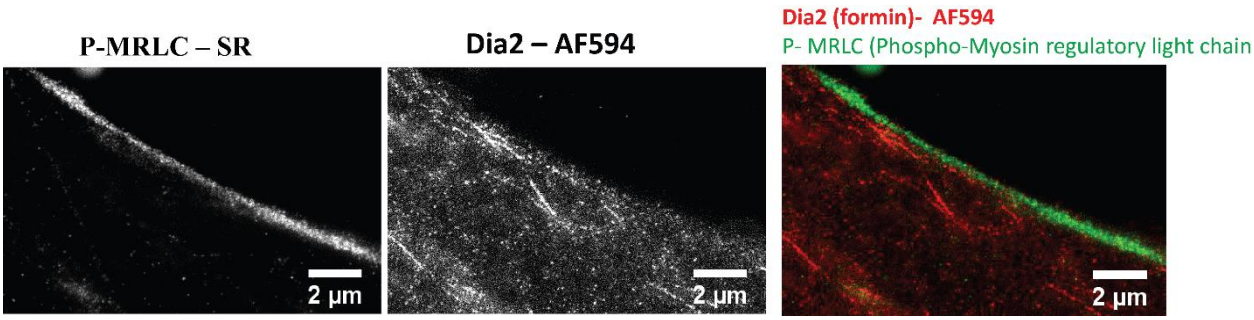

Figure A3: STED imaging of myosin and formin within actomyosin ring: *Co-staining of wound rings with antibodies against, activated form of myosin by p-MRLC-StarRed (left) and formin molecules by Dia2-AlexaFluor594 (middle). This shows differential distribution of myosin and formins within an acto-myosin ring. (merge: right).*

For this, we followed immunostaining protocol (3.7.1) and stained for p-MRLC and Dia2 to see any putative arrangements or colocalisations. We acquired STED images, although we did not see any specific localisation of the formin homolog, in the acto-myosin ring. This could be because of the high density of this protein, since there is a packed actin filament bundle across the acto-myosin ring. Another possibility is that we did have the correct antibody to identify

the epitope. We also stained for other formin homologs such as FHOD1 and FMNL1, although we did not see any specific localisations for them as well.

A.3.4 Cryptic lamellipodia and their role in long range flows (with Raghavan Thiagarajan)

In a separate project in the lab., we are looking at flows in epithelial cell monolayer.

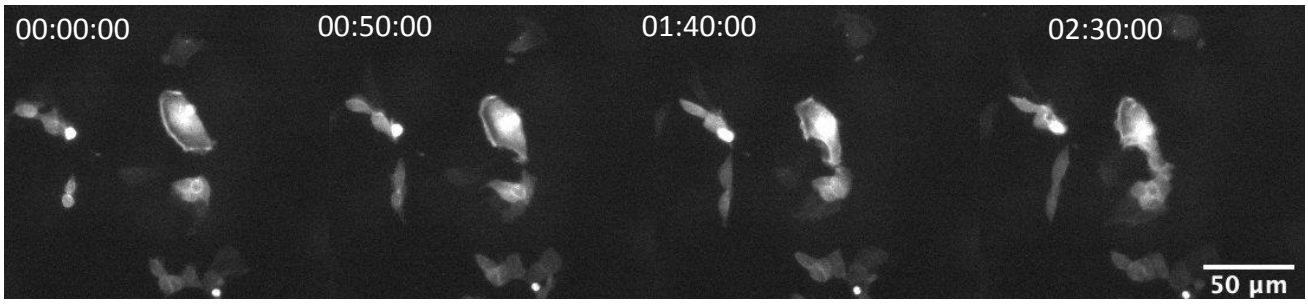

Figure A4: Cryptic lamelliopodia in a confluent epithelial monolayer: *Time evolution of a cryptic lamellipodia in MDCK E-cadherin (GFP) expressing cells, visualized by LifeAct-mCherry. Lamellipodia seen to be polarising to the left.*

MDCK epithelial cells are visualized to undergo pulsations in a confluent monolayer. These pulsations are of a time scale of ~7h and arise after 12h of confluency. Inhibition of ATPase activity (Blebbistatin 100µM for 12h) in these cells and subsequent washout leads to long range flows in the cell monolayer. We believe that, evaluation of the lamellipodial orientation will give us the putative flow direction. We are evaluating these results at the moment.

A.3.5 Inhibition of Rho-associated kinase (ROCK) and Rho

For inhibition of ROCK, drug *Y27632* was used with some preliminary results. ROCK inhibitor was incubated with the wound rings for ~ 1h with this drug, for both closed and open ring configuration myosin clusters were observed to disappear. Cases of open ring configurations, depicted ring closures without stalling (Movie 40).

For inhibition of an upstream effector Rho, *C3 transferase* was used. Preliminary results after inhibiting Rho proteins also depicted disappearance of myosin clusters at longer time scale of

incubation ~5h. Although occasional stalled rings as well as myosin cluster appearance was observed, in both open and closed ring configuration (Movie 41).

Above results and result from section 4.1.10.1 illustrates the rescued myosin cluster dynamics in a closed ring conformation could be an indicative of their phosphorylation state. We are looking further in this direction by trying to correlate these studies with FRET acquisition which will give a direct indicative of the amount of active Rho during these conditions.

BIBLIOGRAPHY

[1] T. E. Schroeder, “The contractile ring,” *J. Cell Biol.*, vol. 53, pp. 419–434, 1972.

[2] A. F. Huxley and R. Niedergerke, “Structural Changes in Muscle During Contraction: Interference Microscopy of Living Muscle Fibres,” *Nature*, vol. 173, no. 4412, pp. 971–973, 1954.

[3] H. Huxley and J. Hanson, “Changes in the Cross-Striations of Muscle during Contraction and Stretch and their Structural Interpretation,” *Nature*, vol. 173, no. 4412, pp. 973–976, 1954.

[4] H. E. Huxley, “The double array of filaments in cross-striated muscle.,” *J. Biophys. Biochem. Cytol.*, vol. 3, no. 5, pp. 631–48, 1957.

[5] V. Wollrab, R. Thiagarajan, A. Wald, K. Kruse, and D. Riveline, “Still and rotating myosin clusters determine cytokinetic ring constriction,” *Nat. Commun.*, vol. 7, no. 1, pp. 11860–11869, 2016.

[6] M. Rauzi, P.-F. Lenne, and T. Lecuit, “Planar polarized actomyosin contractile flows control epithelial junction remodelling,” *Nature*, vol. 468, no. 7327, pp. 1110–1114, Dec. 2010.

[7] M. Nishikawa, S. R. Naganathan, F. Jülicher, and S. W. Grill, “Controlling contractile instabilities in the actomyosin cortex.,” *Elife*, vol. 6, pp. 1–21, 2017.

[8] A. C. Martin and B. Goldstein, “Apical constriction: themes and variations on a cellular mechanism driving morphogenesis.,” *Development*, vol. 141, no. 10, pp. 1987–98, May 2014.

[9] E. Anon *et al.*, “Cell crawling mediates collective cell migration to close undamaged epithelial gaps.,” *Proc. Natl. Acad. Sci. United States Am.*, vol. 109, no. 27, pp. 10891–6, 2012.

[10] A. Ravasio *et al.*, “Gap geometry dictates epithelial closure efficiency,” *Nat. Commun.*, vol. 6, pp. 1–113, 2015.

[11] A. Jacinto, A. Martinez-Arias, and P. Martin, “Mechanisms of epithelial fusion and repair,” *Nat. Cell Biol.*, vol. 3, no. 5, pp. E117–E123, May 2001.

[12] E. Wagner and M. Glotzer, “Local RhoA activation induces cytokinetic furrows independent of spindle position and cell cycle stage.,” *J. Cell Biol.*, vol. 213, no. 6, pp. 641–9, Jun. 2016.

[13] O. Pertz, L. Hodgson, R. L. Klemke, and K. M. Hahn, “Spatiotemporal dynamics of

RhoA activity in migrating cells," *Nature*, vol. 440, no. 7087, pp. 1069–1072, 2006.

[14] W. M. Bement, C. A. Mandato, and M. N. Kirsch, "Wound-induced assembly and closure of an actomyosin purse string in Xenopus oocytes," *Curr. Biol.*, vol. 9, no. 11, pp. 579–587, Jun. 1999.

[15] M. Tamada, T. D. Perez, W. J. Nelson, and M. P. Sheetz, "Two distinct modes of myosin assembly and dynamics during epithelial wound closure," *J. Cell Biol.*, vol. 176, no. 1, pp. 27–33, 2007.

[16] S. R. K. Vedula *et al.*, "Microfabricated Environments to Study Collective Cell Behaviors," *Methods Cell Biol.*, vol. 120, pp. 235–252, 2014.

[17] A. Zumdieck, K. Kruse, H. Bringmann, A. A. Hyman, and F. Jülicher, "Stress generation and filament turnover during actin ring constriction," *PLoS One*, vol. 2, no. 8, pp. 1–6, 2007.

[18] S. R. a. Naganathan, S. Fürthauer, M. Nishikawa, F. Jülicher, and S. W. Grill, "Active torque generation by the actomyosin cell cortex drives left-right symmetry breaking," *Elife*, vol. 3, p. e04165, 2014.

[19] M. Mayer, M. Depken, J. S. Bois, F. Jülicher, and S. W. Grill, "Anisotropies in cortical tension reveal the physical basis of polarizing cortical flows," *Nature*, vol. 467, pp. 617–623, 2010.

[20] C. M. Simon, E. M. Vaughan, W. M. Bement, and L. E. -Keshet, "Pattern formation of Rho GTPases in single cell wound healing," vol. 24, no. 3, pp. 421–432, 2013.

[21] K. Dasbiswas, F. S. , Shiqiong Hu, S. A. Safran, and and Alexander D. Bershadsky, "Ordering of myosin II filaments driven by mechanical forces: experiments and theory," *Philos. Trans. R. Soc. B Biol. Sci.*, vol. 373, pp. 1–16, 2018.

[22] D. V. Köster *et al.*, "Actomyosin dynamics drive local membrane component organization in an in vitro active composite layer," *Proc. Natl. Acad. Sci.*, vol. 113, no. 12, pp. 1645–1654, 2016.

[23] A. C. Paré *et al.*, "A positional Toll receptor code directs convergent extension in Drosophila," *Nature*, vol. 515, no. 7528, pp. 523–527, 2014.

[24] F. Jülicher and S. Eaton, "Emergence of tissue shape changes from collective cell behaviours," *Semin. Cell Dev. Biol.*, vol. 67, pp. 103–112, 2017.

[25] J. Howard, *Mechanics of Motor Proteins and the Cytoskeleton*, 1st ed. Sinauer Associates Inc., 2001.

[26] D. Mizuno, C. Tardin, C. F. Schmidt, and F. C. Mackintosh, "Nonequilibrium mechanics of active cytoskeletal networks.," *Science (80-.).*, vol. 315, pp. 370–373, 2007.

[27] G. T. Eisenhoffer *et al.*, “Crowding induces live cell extrusion to maintain homeostatic cell numbers in epithelia,” *Nature*, vol. 484, pp. 546–551, 2012.

[28] C.-P. Heisenberg and Y. Bellaïche, “Forces in Tissue Morphogenesis and Patterning,” *Cell*, vol. 153, pp. 948–962, 2013.

[29] C. Jamora and E. Fuchs, “Intercellular adhesion, signalling and the cytoskeleton,” *Nat. Cell Biol.*, vol. 4, no. 4, pp. E101–E108, Apr. 2002.

[30] S.-T. Sit and E. Manser, “Rho GTPases and their role in organizing the actin cytoskeleton,” *J. Cell Sci.*, vol. 124, pp. 679–683, 2011.

[31] B. Kost and N. H. Chua, “The Plant Cytoskeleton: Vacuoles and Cell Walls Make the Difference,” *Cell*, vol. 108, pp. 9–12, 2002.

[32] U. S. Eggert, T. J. Mitchison, and C. M. Field, “Animal Cytokinesis: From Parts List to Mechanisms,” *Annu. Rev. Biochem.*, vol. 75, pp. 543–566, 2006.

[33] L. Blanchoin, R. Boujemaa-Paterski, C. Sykes, and J. Plastino, “Actin dynamics, architecture, and mechanics in cell motility.,” *Physiol. Rev.*, vol. 94, no. 1, pp. 235–63, 2014.

[34] D. A. Lauffenburger and A. F. Horwitz, “Cell migration: A physically integrated molecular process,” *Cell*, vol. 84, pp. 359–369, 1996.

[35] S. L. Rogers and V. I. Gelfand, “Membrane trafficking, organelle transport, and the cytoskeleton,” *Curr. Opin. Cell Biol.*, vol. 12, pp. 57–6, 2000.

[36] T. Chen, T. B. Saw, R.-M. Mège, and B. Ladoux, “Mechanical forces in cell monolayers,” *J. Cell Sci.*, vol. 131, pp. 1–11, 2018.

[37] W. M. Bement, G. Ian Gallicano, and D. G. Capco, “Role of the cytoskeleton during early development,” *Microsc. Res. Tech.*, vol. 22, pp. 23–48, 1992.

[38] T. Lecuit, P.-F. Lenne, and E. Munro, “Force Generation, Transmission, and Integration during Cell and Tissue Morphogenesis,” *Annu. Rev. Cell Dev. Biol.*, vol. 27, no. 1, pp. 157–184, 2011.

[39] B. Alberts, A. Johnson, J. Lewis, M. Raff, K. Roberts, and P. Walter, *Molecular biology of the Cell*, 4th ed. Garland Science, 2007.

[40] M. A. Jordan and L. Wilson, “Microtubules as a target for anticancer drugs,” *Nat. Rev. Cancer*, vol. 4, pp. 253–265, 2004.

[41] G. Cooper, *The cell: a molecular biology approach.*, 2nd ed. ASM Press, 2000.

[42] T. D. Pollard and W. E. Earnshaw, *Cell Biology*, 1st ed. Saunders, 2002.

[43] T. D. Pollard, “Rate Constants for the Reactions of ATP-and ADP-Actin with the Ends of Actin Filaments,” *J. Cell Biol.*, vol. 103, no. 6, 1986.

[44] S. Ono, “Mechanism of Depolymerization and Severing of Actin Filaments and Its Significance in Cytoskeletal Dynamics,” *Int. Rev. Cytol.*, vol. 258, pp. 1–82, 2007.

[45] A. J. Ehrlicher, “The Forces Behind Cell Movement The Forces Behind Cell Movement,” *Int. J. Biol. Sci.*, vol. 3, pp. 303–317, 2017.

[46] T. D. Pollard, L. Blanchoin, and R. D. Mullins, “Molecular mechanisms controlling actin filament dynamics in nonmuscle cells,” in *Annual Review of Biophysics and Biomolecular Structure*, vol. 29, 2000, pp. 545–576.

[47] K. Kruse and D. Riveline, *Spontaneous Mechanical Oscillations. Implications for Developing Organisms*, 1st ed., vol. 95. Elsevier Inc., 2011.

[48] A. Munjal and T. Lecuit, “Actomyosin networks and tissue morphogenesis,” *Development*, vol. 141, pp. 1789–1793, 2014.

[49] M. Vicente-Manzanares, X. Ma, R. S. Adelstein, and A. R. Horwitz, “Non-muscle myosin II takes centre stage in cell adhesion and migration.,” *Nat. Rev. Mol. Cell Biol.*, vol. 10, no. 11, pp. 778–90, 2009.

[50] F. Jiilicher’ and J. Prost’, “Cooperative Molecular Motors,” 1995.

[51] J. Prost, F. Jülicher, and J. F. Joanny, “Active gel physics,” *Nat. Phys.*, vol. 11, pp. 111–117, 2015.

[52] K. Kruse, J. F. Joanny, F. Jülicher, J. Prost, and K. Sekimoto, “Asters, Vortices, and Rotating Spirals in Active Gels of Polar Filaments,” vol. 92, no. 7, pp. 1–4, 2004.

[53] J. F. Joanny, F. Jülicher, K. Kruse, and J. Prost, “Hydrodynamic theory for multi-component active polar gels,” *New J. Phys.*, vol. 9, pp. 1–17, 2007.

[54] H. N. Higgs and E. S. Chhabra, “The many faces of actin: matching assembly factors with cellular structures.,” *Nat. Cell Biol.*, vol. 9, pp. 1110–1121, 2007.

[55] A. B. Verkhovsky, “Orientational Order of the Lamellipodial Actin Network as Demonstrated in Living Motile Cells,” *Mol. Biol. Cell*, vol. 14, pp. 4667–4675, 2003.

[56] D. Bray, *Cell Movements : From Molecules to Motility*, 2nd ed. Garland Science, 2000.

[57] T. Vicsek and A. Zafeiris, “Collective motion,” *Phys. Rep.*, vol. 517, pp. 71–140--, 2012.

[58] E. M. E. Purcell, “Life at low Reynolds number,” *Am. J. Phys.*, vol. 45, no. 1, p. 3, 1977.

[59] R. Aditi Simha and S. Ramaswamy, “Hydrodynamic fluctuations and instabilities in ordered suspensions of self-propelled particles,” *Phys. Rev. Lett.*, 2002.

[60] J. F. Joanny and J. Prost, “Active gels as a description of the actin-myosin cytoskeleton,” *HFSP J.*, vol. 3, no. 2, pp. 94–104, 2009.

[61] F. Wottawah *et al.*, “Optical rheology of biological cells,” *Phys. Rev. Lett.*, vol. 94, pp. 1–4, 2005.

[62] A. S. Streng, D. de Boer, J. van der Velden, M. P. van Dieijen-Visser, and W. K. W. H. Wodzig, "Posttranslational modifications of cardiac troponin T: An overview," *J. Mol. Cell. Cardiol.*, vol. 63, p. 2013, 2013.

[63] Y. Tanaka-Takiguchi *et al.*, "The elongation and contraction of actin bundles are induced by double-headed myosins in a motor concentration-dependent manner," *J. Mol. Biol.*, vol. 341, no. 2, pp. 467–476, 2004.

[64] J. M. Belmonte, M. Leptin, and F. Nédélec, "A theory that predicts behaviors of disordered cytoskeletal networks," *Mol. Syst. Biol.*, vol. 13, pp. 941–954, 2017.

[65] M. A. Chesarone and B. L. Goode, "Actin nucleation and elongation factors: mechanisms and interplay," *Curr. Opin. Cell Biol.*, vol. 21, no. 1, pp. 28–37, 2009.

[66] J. N. Jodoin *et al.*, "Stable Force Balance between Epithelial Cells Arises from F-Actin Turnover," *Dev. Cell*, vol. 35, no. 6, pp. 685–697, 2015.

[67] B. M. Gumbiner, "Regulation of cadherin-mediated adhesion in morphogenesis," *Nat. Rev. Mol. Cell Biol.*, vol. 6, pp. 622–634, 2005.

[68] K. Goodwin, S. J. Ellis, E. Lostchuck, T. Zulueta-Coarasa, R. Fernandez-Gonzalez, and G. Tanentzapf, "Basal Cell-Extracellular Matrix Adhesion Regulates Force Transmission during Tissue Morphogenesis," *Dev. Cell*, vol. 39, pp. 611–625, 2016.

[69] S. L. Haigo and D. Bilder, "Global tissue revolutions in a morphogenetic movement controlling elongation.," *Science (80-.).*, vol. 331, no. 6020, pp. 1071–1074, Feb. 2011.

[70] M. V. Hunter, D. M. Lee, T. J. C. Harris, and R. Fernandez-Gonzalez, "Polarized E-cadherin endocytosis directs actomyosin remodeling during embryonic wound repair," *J. Cell Biol.*, vol. 210, no. 5, pp. 801–816, 2015.

[71] A. Padmanabhan, H. T. Ong, and R. Zaidel-Bar, "Non-junctional E-Cadherin Clusters Regulate the Actomyosin Cortex in the C. elegans Zygote," *Curr. Biol.*, vol. 27, pp. 103–112, 2017.

[72] P. Agarwal and R. Zaidel-Bar, "Principles of Actomyosin Regulation In Vivo.," *Trends Cell Biol.*, vol. 29, no. 2, pp. 150–163, Feb. 2019.

[73] S. J. Heasman and A. J. Ridley, "Mammalian Rho GTPases: New insights into their functions from in vivo studies," *Nature Reviews Molecular Cell Biology*, vol. 9, no. 9. pp. 690–701, Sep-2008.

[74] A. Hall, "Rho family GTPases," *Biochem. Soc. Trans.*, vol. 40, pp. 1378–1382, 2012.

[75] A. L. Bishop and A. Hall, "Rho GTPases and their effector proteins.," *Biochem. J.*, vol. 348, no. 2, pp. 241–255, 2000.

[76] T. R. Arnold, R. E. Stephenson, and A. L. Miller, "Rho GTPases and actomyosin:

Partners in regulating epithelial cell-cell junction structure and function," *Exp. Cell Res.*, vol. 358, no. 1, pp. 20–30, 2017.

[77] W. M. Bement, A. L. Miller, and G. Von Dassow, "Rho GTPase activity zones and transient contractile arrays," *BioEssays*, vol. 28, pp. 983–993, 2006.

[78] S. Schonegg, A. A. Hyman, and W. B. Wood, "Timing and mechanism of the initial cue establishing handed left-right asymmetry in Caenorhabditis elegans embryos," *Genesis*, vol. 52, no. 6, pp. 572–580, 2014.

[79] T. Iskratsch, H. Wolfenson, and M. P. Sheetz, "Appreciating force and shape — the rise of mechanotransduction in cell biology," *Nat. Rev. Mol. Cell Biol.*, vol. 15, pp. 825–833, 2014.

[80] N. Wang, J. P. Butler, and D. E. Ingber, "Mechanotransduction across the cell surface and through the cytoskeleton," *Science (80-.).*, vol. 260, no. 5111, pp. 1124–1127, 1993.

[81] D. Pinheiro *et al.*, "Transmission of cytokinesis forces via E-cadherin dilution and actomyosin flows," *Nature*, vol. 545, no. 7652, pp. 103–107, May 2017.

[82] J. J. West *et al.*, "An Actomyosin-Arf-GEF Negative Feedback Loop for Tissue Elongation under Stress," *Curr. Biol.*, vol. 27, no. 15, pp. 2260–2270, Aug. 2017.

[83] T. D. Pollard and J.-Q. Wu, "Understanding cytokinesis: lessons from fission yeast.," *Nat. Rev. Mol. Cell Biol.*, vol. 11, no. 2, pp. 149–55, 2010.

[84] K. Röper, "Supracellular actomyosin assemblies during development.," *Bioarchitecture*, vol. 3, no. 2, pp. 45–9, 2013.

[85] W. M. Bement, "Actomyosin Rings: The Riddle of the Sphincter Dispatch," 2002.

[86] P. Martin and J. Lewis, "Actin cables and epidermal movement in embryonic wound healing.," *Nature*, vol. 360, no. 6400, pp. 179–83, Nov. 1992.

[87] T. Zulueta-Coarasa and R. Fernandez-Gonzalez, "Tension (re)builds: Biophysical mechanisms of embryonic wound repair," *Mech. Dev.*, 2016.

[88] A. C. Martin, "Pulsation and stabilization: Contractile forces that underlie morphogenesis," *Dev. Biol.*, vol. 341, no. 1, pp. 114–125, 2010.

[89] S. A. Gudipaty and J. Rosenblatt, "Epithelial cell extrusion: Pathways and pathologies," *Seminars in Cell and Developmental Biology*, vol. 67. Elsevier Ltd, pp. 132–140, 01-Jul-2017.

[90] S. Begnaud, T. Chen, D. Delacour, R.-M. Mège, and B. Ladoux, "Mechanics of epithelial tissues during gap closure," *Curr. Opin. Cell Biol.*, vol. 42, pp. 52–62, 2016.

[91] J. K. Klarlund, "Dual modes of motility at the leading edge of migrating epithelial cell sheets," *Proc. Natl. Acad. Sci.*, vol. 109, no. 39, pp. 15799–15804, Sep. 2012.

[92] A. Stathopoulos and D. Iber, “Studies of morphogens: keep calm and carry on,” *Development*, vol. 140, no. 20. Company of Biologists Ltd, pp. 4119–4124, 15-Oct-2013.

[93] Anne-Cécile Reymann *et al.*, “Actin Network Architecture Can Determine Myosin Motor Activity,” *Science (80-.).*, vol. 336, pp. 1310–1314, 2012.

[94] T. D. Pollard, “Mechanics of cytokinesis in eukaryotes.,” *Curr. Opin. Cell Biol.*, vol. 22, no. 1, pp. 50–6, Feb. 2010.

[95] V. Wollrab, “Active gels in vivo : Patterns and dynamics in cytokinetic rings and their functions in cell divison,” University of Strasbourg, 2014.

[96] D. and Riveline and A. Buguin, “Devices and methods for observing the cell division. WO/2010/092116,” 2009.

[97] V. and Wollrab and D. Riveline, “Devices and methods for observing eukaryotic cells without cell wall. WO/2013/135809,” 2012.

[98] V. Wollrab, D. Caballero, R. Thiagarajan, and D. Riveline, “Ordering Single Cells and Single Embryos in 3D Confinement: A New Device for High Content Screening.,” *J. Vis. Exp.*, no. 115, pp. 2–15, 2016.

[99] T. Masters, W. Engl, Z. L. Weng, B. Arasi, N. Gauthier, and V. Viasnoff, “Easy Fabrication of Thin Membranes with Through Holes. Application to Protein Patterning,” *PLoS One*, vol. 7, no. 8, pp. 1–7, Aug. 2012.

[100] D. Riveline, “Methods for observing cells with cell wall or invertebrate embryos with oblong eggshell. WO/2013/144302,” 2012.

[101] T. Watanabe, H. and Hosoya, and S. Yonemura, “Regulation of Myosin II Dynamics by Phosphorylation and Dephosphorylation of Its Light Chain in Epithelial Cells,” *Mol. Biol. Cell*, vol. 18, pp. 605–616, 2007.

[102] “Fission yeast : a laboratory manual,” Cold Spring Harbor Laboratory Press, 2016, p. 487.

[103] S. L. Forsburg and N. Rhind, “Basic methods for fission yeast,” *Yeast*, vol. 23, no. 3, pp. 173–183, 2006.

[104] E. Le Maout, S. Lo Vecchio, A. Bhat, and D. Riveline, “Directing cell migration on flat substrates and in confinement with microfabrication and microfluidics,” in *Methods in Cell Biology*, 1st ed., vol. 147, Elsevier Inc., 2018, pp. 109–132.

[105] D. Caballero, R. Voituriez, and D. Riveline, “Protrusion Fluctuations Direct Cell Motion,” *BPJ*, vol. 107, pp. 34–42, 2014.

[106] C. Spiegelhalter *et al.*, “From Dynamic Live Cell Imaging to 3D Ultrastructure: Novel

Integrated Methods for High Pressure Freezing and Correlative Light-Electron Microscopy. From Dynamic Live Cell Imaging to 3D Ultrastructure: Novel Integrated Methods for High Pressure Freezing an," vol. 5, no. 2, pp. 1–12, 2010.

[107] *Forces and Tension in Development*, 1st ed. Elsevier Inc., 2011.

[108] M. Rauzi, P.-F. Lenne, and T. Lecuit, "Planar polarized actomyosin contractile flows control epithelial junction remodelling," *Nature*, vol. 468, no. 7327, pp. 1110–1114, 2010.

[109] P. Bocchiaro and A. Zamperini, "The Role of Actin Remodelling Proteins in Wound Healing and Tissue Regeneration," in *Wound Healing - New insights into Ancient Challenges*, 2016, pp. 133–153.

[110] L. Hodgson, F. Shen, and K. Hahn, "Biosensors for characterizing the dynamics of rho family GTPases in living cells.," in *Current protocols in cell biology*, vol. Chapter 14, 2010.

[111] "Reciprocal regulation of actomyosin organization and contractility in nonmuscle cells by tropomyosins and alpha-actinins," 2019.

[112] J. Eyckmans and C. S. Chen, "3D culture models of tissues under tension.," *J. Cell Sci.*, vol. 130, no. 1, pp. 63–70, Dec. 2017.

[113] A. Sontheimer-Phelps, B. A. Hassell, and D. E. Ingber, "Modelling cancer in microfluidic human organs-on-chips," *Nat. Rev. Cancer*, vol. 19, no. 2, pp. 65–81, Feb. 2019.

[114] V. Wollrab, D. Caballero, R. Thiagarajan, and D. Riveline, "Ordering Single Cells and Single Embryos in 3D Confinement: A New Device for High Content Screening," *J. Vis. Exp.*, no. 115, Sep. 2016.

[115] T. Hayashi and R. Murakami, "Left-right asymmetry in Drosophila melanogaster gut development," *Dev. Growth Differ.*, vol. 43, no. 3, pp. 239–246, 2001.

[116] M. V. Danilchik, E. E. Brown, and K. Riegert, "Intrinsic chiral properties of the Xenopus egg cortex: An early indicator of left-right asymmetry," *Development*, vol. 133, no. 22, pp. 4517–4526, Nov. 2006.

[117] J. F. Beausang, H. W. Schroeder, P. C. Nelson, and Y. E. Goldman, "Twirling of actin by myosins II and V observed via polarized TIRF in a modified gliding assay," *Biophys. J.*, vol. 95, no. 12, pp. 5820–5831, Dec. 2008.

[118] D. Vavylonis, J.-Q. Wu, S. Hao, B. O'Shaughnessy, and T. D. Pollard, "Assembly mechanism of the contractile ring for cytokinesis by fission yeast.," *Science (80-.).*, vol. 319, no. 97, pp. 97–100, 2008.

[119] N. Levernier and K. Kruse, “Spontaneous formation of chaotic protrusions in a polymerizing active gel layer,” *BioRxiv*, pp. 1–5, 2019.

[120] A. Abbott, “Biology’s new dimension,” *Nature*, vol. 424, no. 6951, pp. 870–872, Aug. 2003.

[121] V. M. Weaver *et al.*, “Reversion of the malignant phenotype of human breast cells in three- dimensional culture and in vivo by integrin blocking antibodies,” *J. Cell Biol.*, vol. 137, no. 1, pp. 231–245, Apr. 1997.

[122] M. Anders, R. Hansen, R.-X. Ding, K. A. Rauen, M. J. Bissell, and W. M. Korn, “Disruption of 3D tissue integrity facilitates adenovirus infection by deregulating the coxsackievirus and adenovirus receptor.,” *Proc. Natl. Acad. Sci. U. S. A.*, vol. 100, no. 4, pp. 1943–8, Feb. 2003.

[123] S. K. Sia and G. M. Whitesides, “Microfluidic devices fabricated in Poly(dimethylsiloxane) for biological studies,” *Electrophoresis*, vol. 24, no. 21, pp. 3563–3576, Nov. 2003.

PUBLICATIONS

PUBLISHED:

E. Le Maout, S. Lo Vecchio, **A. Bhat**, and D. Riveline, "Directing cell migration on flat substrates and in confinement with microfabrication and microfluidics," *Methods in Cell Biology*, 1st ed., vol. 147, Elsevier Inc., 2018, pp. 109–132.

SUBMITTED:

How to orient cells in micro-cavities for high resolution imaging of cytokinesis and lumen formation.

Alka Bhat, Linjie Lu, Chen-Ho Wang, Simon Lo Vecchio, Riccardo Maraspini, Alf Honigmann, Daniel Riveline

CHAPTER

7

Directing cell migration on flat substrates and in confinement with microfabrication and microfluidics

Emilie Le Maout[*,†,‡,§,¶], **Simon Lo Vecchio**[*,†,‡,§,¶], **Alka Bhat**[*,†,‡,§,¶]
Daniel Riveline[*,†,‡,§,¶,1]

[*]*Laboratory of Cell Physics ISIS/IGBMC, CNRS and University of Strasbourg, Strasbourg, France*
[†]*Institut de Génétique et de Biologie Moléculaire et Cellulaire, Illkirch, France*
[‡]*Centre National de la Recherche Scientifique, UMR7104, Illkirch, France*
[§]*Institut National de la Santé et de la Recherche Médicale, U964, Illkirch, France*
[¶]*Université de Strasbourg, Illkirch, France*
[1]*Corresponding author: e-mail address: riveline@unistra.fr*

CHAPTER OUTLINE

Methods in Cell Biology, Volume 147, ISSN 0091-679X, https://doi.org/10.1016/bs.mcb.2018.06.006

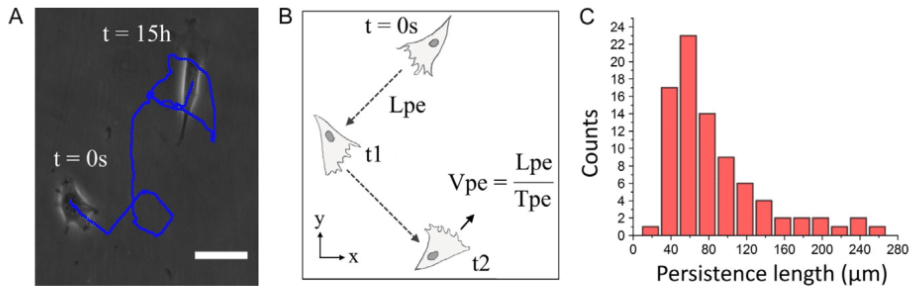

FIG. 1

Characterization of NIH3T3 fibroblast migration on a 2D flat substrate. (A) Typical trajectory of a cell moving randomly on a flat coverslip, the blue trace shows the trajectory. Scale bar 100 µm. (B) Schematics showing the migration of a cell, Lpe represents the persistence length, Tpe the persistence time and Vpe the persistence speed; pausing time and number of turns per unit time can also be measured. (C) Distribution of a parameter, here the persistence length, for NIH3T3 fibroblasts migrating on flat surface ($n = 84$ trajectories).

Indeed cell motion can be recapitulated on 2D flat coverslips or on Petri dishes: a polarized cell migrates in one direction, pauses, potentially changes polarity and migrates in another direction. Their typical motions over days are represented in Fig. 1. Five parameters can encode cell motility. Persistence length is the length traveled "straight" by the cell during a certain time with no pause. This time is called persistence time. Persistence speed is deduced from the ratio of these two values (see Fig. 1B). Next, cell pauses and this phase can be characterized by its duration time; the number of turn per unit time captures the changes in directions. Measurements of these five parameters can lead to interesting results to characterize cell motion in a generic way (see Fig. 1C; Caballero, Voituriez, & Riveline, 2014).

1.1 PETRI DISHES AND BOYDEN CHAMBERS: THEIR LIMITS

Experiments have been mainly performed so far in conditions which can be viewed as "artificial" compared to *in vivo* conditions. For example, cells are cultured and observed in flat Petri dishes (see Figs. 1A and 2A), and this method was kept probably for historical reasons (Petri, 1887). In this setup, cells have random shapes and this can alter their migration; also, they evolve on 2D flat substrates which constitutes an important difference with 3D physiological environments. At the stage of plating, cells can appear as single cells or as groups of cells with an ill-controlled number of cells per group. These varying initial conditions can lead to bias in the study of motility. Other assays using Boyden chambers, for example, can also generate artificial conditions (see Fig. 2C; Boyden, 1962): cells are placed in an upper chamber and are exposed to a membrane with cavities of controlled dimensions, typically 10 µm in diameter and 10 µm in depth. In the presence of chemical gradients between the top and bottom compartments, cells eventually migrate. However, the motion itself

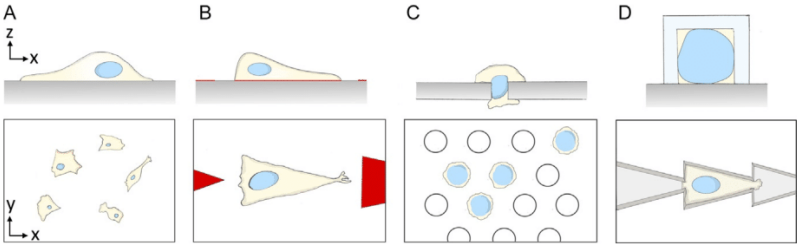

FIG. 2

Cell motility on different configurations. (A) Cell on Petri dish/flat 2D substrate. (B) Cell on 2D ratchet. (C) Cell on a "membrane" in a Boyden chamber experiment. (D) Cell in 3D confined ratchet. The nucleus is depicted in blue. In all panels, we represent *x–z* plane (top) and *x–y* plane (bottom).

is restricted to a small fraction of the cell size. This 10 μm cavity limits considerably the potential extrapolation to *in vivo* situations. As a result, with Petri dishes and Boyden chambers, the study of cell migration lacks control and the assays can be far from reproducing physiological conditions.

1.2 THE MICROFABRICATION REVOLUTION AND ITS IMPACTS

The usage of techniques developed through microfabrication and microfluidics (Whitesides, 2006) have opened a new era for the study of cell migration (Caballero et al., 2014; Cramer, 2010; Hawkins et al., 2009; Jiang, Bruzewicz, Wong, Piel, & Whitesides, 2005; Prentice-Mott et al., 2013). When studying 2D cell migration, the shape of cells can be imposed on surfaces through adhesive micro-contact printed proteins surrounded by cell repellent (see Fig. 2B; Théry & Piel, 2009). Cell symmetry and its effect on migration can be analyzed quantitatively and encoded in physical models (Fig. 5; Caballero et al., 2014; Hawkins et al., 2009). In addition, cells can be confined in 3D through the appropriate preparation of microchannels (see Fig. 2D); this can reproduce conditions where single cells are trapped in blood vessels with diameters smaller than cell dimensions. This configuration can also lead to controlled cell symmetries (see Figs. 7 and 8). In both cases, on flat 2D printed substrates and in 3D confined geometries, motions can be acquired in the presence of chemical gradients (Comelles et al., 2014; Prentice-Mott et al., 2013).

These developments have been possible because polydimethylsiloxane (PDMS)—the main material to prepare these assays—is biocompatible and easy to manipulate. The material is still liquid right after addition of the cross-linker and can be deposited on molds and cured in a 65 °C oven. The PDMS solid mold can be replicated with negative/positive combinations with up to nanometer resolutions in the reproduction of motifs (Qin, Xia, & Whitesides, 2010). Altogether, cell shapes and dimensions are now controlled with microfabrication, and these methods have shown to be essential for obtaining new standardized tests.

We report below experimental procedures to prepare these assays for the same cell type, i.e. NIH 3T3 fibroblasts. Any cell can be used, but the fact of probing the same cell line allows to identify changes in behaviors between experimental conditions set by the assay, such as speeds and directions.

1.3 DESIGNING THE MOTIFS: SCALING ARGUMENTS

In order to match the motility assays to each cell type, cell dimensions need to be determined first. The mean area of resting cells on flat coverslips allows to evaluate the optimal surface area needed to micro-contact print adhesive motifs on 2D flat surfaces. Cells will spread on these motifs with their spontaneous resting shape (Fig. 2B). In addition, measure of the mean cell diameter after trypsinization and before cells start spreading, helps to evaluate the cell volume and this can guide the design of motifs for 3D confinements (Fig. 2D). As reported above, the cell symmetry can also be modified: cells can adopt disk shapes (2D; Caballero et al., 2014) or move along straight channels (3D; Prentice-Mott et al., 2013), and their symmetry can be broken while keeping the projected area/volume constant in 2D/3D assays respectively. In fact, several studies have reported that the presence of asymmetric patterns in the environment can direct cell motion. This kind of motion has been named *ratchetaxis* (Caballero, Comelles, Piel, Voituriez, & Riveline, 2015). In 2D configuration, lines of periodic triangles can be generated to simplify the ratchetaxis motion along a single direction. For the 3D case, lines of periodic connected triangles can be generated to study the motion in confined environments with a local broken symmetry. In addition, the junction/gap between subsequent motifs can be controlled. In 2D, a cell on a motif will have different dynamics depending on the gap between neighboring motifs. In 3D confined situations, the opening width of connecting triangles will test different regimes in cell motility.

Altogether, cell area in 2D and cell volume in 3D will set rules for the design of the microfabricated unit. Gaps/junctions between motifs will test cell probing and confinement respectively. The sum of microfabricated unit length and junction's length can be integrated in a lattice unit or in cell dimension to compare between conditions and between cell types (L is about 100 μm for NIH 3T3 cells, see Fig. 1A). Cells trajectory can be then calculated as lattice unit/cell length dimensions. Symmetry/asymmetry will be generated by keeping constant area/volume in 2D/3D respectively.

Finally, the cell velocity should be taken into account for the design of experiments. Specifically, trajectories should be sufficiently long to acquire reliable statistics; this can be evaluated with cell velocity. For example, let us say that cells move at 10 μm/h speed with a typical cell dimension of 100 μm. If we want to follow the cell migration for 10 times the length of a cell (around 1000 μm), taking into account the frequent pauses on 2D flat surfaces (see Fig. 1A), this would require an acquisition of at least 24 h. In turn, the number of periodic lattice units should be prepared accordingly to allow cells to potentially move along this 1000 μm long trajectory.

With these simple orders of magnitude in mind, the masks containing the motifs can be designed for microfabrication.

2 MICROFABRICATION OF MOTIFS

2.1 DESIGNING THE MOTIFS

Design of the mask can be done using different softwares, e.g. Clewin (Freeware) or Autocad®. A light sensitive material called *photoresist* is used during microfabrication: it is spin-coated on a wafer before exposure of the wafer to UV light when substrate and mask are in close contact (Fig. 3).

Motifs are designed according to the type of photoresist, positive or negative. Here in our study, epoxy based photoresist SU-8 (MicroChem) was used. SU-8 being a "negative" photoresist becomes insoluble to the SU-8 developer when exposed to UV light. The unexposed regions will be stripped off during the development process leaving behind the micro-structures. Masks have to be prepared accordingly, in order

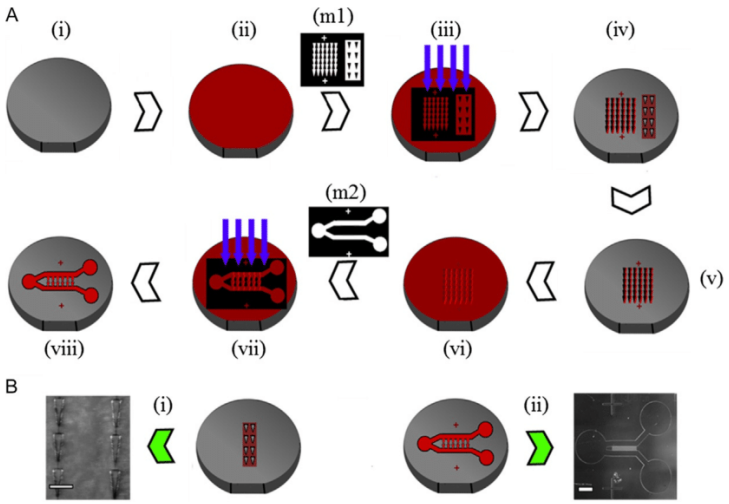

FIG. 3

Microfabrication for the study of 2D and 3D ratchetaxis. (A) Steps followed to obtain motifs. (i) Silicon wafer (ii) spin-coated with SU-8 (2005, 2025) according to the required height/depth. (iii) UV exposure of the spin-coated wafer through the desired mask (m1) for the first layer. (iv) Developed motifs of the first layer with 5 μm high connected triangles; left side of the wafer and 25 μm deep first layer of separated triangles; right side of the wafer. (v) Wafer with 5 μm high connected triangles (vi) spin-coated with photoresist; SU-8 2025 for 50 μm thickness. (vii) UV exposure of the spin-coated wafer through the desired mask (m2) for the second layer. (viii) Developed motifs of the second layer; connected triangles with the reservoir. (B) Developed resin motifs on a Si wafer of (i) 25 μm thick first layer of separated triangles (right side: holes on wafer; left side: image of the wafer, scale bar 100 μm); and (ii) 5 μm thick connected triangles with 50 μm thick reservoir (left side: pillars on wafer: right side, image of the wafer, scale bar 1 mm).

to fabricate either holes or pillars on the wafer. It is important to have dark motifs ("+" polarity) on the mask, so that the UV light cannot pass through, in turn fabricating holes on the wafer. Similarly, for fabricating pillars, transparent motifs ("−" polarity) have to be designed, which would allow the UV light to pass through the motifs, cross-linking the exposed photoresist. Structures fabricated in such a way have excellent thermal and mechanical stability.

After the masks with the desired dimensions are printed, motifs are prepared through microfabrication (see Section 2.2.1.3).

2.2 MICROFABRICATION

2.2.1 Protocol

2.2.1.1 Materials

- Silicon wafers (Si-Mat, cat. PRIME/76.5 mm/381 mm)
- Wafer tweezers
- Chromium/plastic photomask (Selba) with printed motifs to micro-fabricate
- SU-8 photoresist (MicroChem cat. SU8/2025/0.5)
- SU-8 developer (Chimie Tech Services, cat. DevSU8/4)
- Acetone
- 2-Propanol
- Ethanol 70%

2.2.1.2 Equipment

- Mask aligner (SUSS MicroTec, cat. MJB3)
- Spin-coater (Laurell Technologies, cat. WS-400B-6NPP)
- Hot plates (65 °C and 95 °C)
- Disposable graduated dropper (to remove air bubbles)

2.2.1.3 Method

Two sets of motifs are required for the processes reported in Sections 3–5. Section 3: micro-contact printing requires one layer of the photoresist (25 µm). The depth is tuned to have an optimal aspect ratio: if the pillars are too high and the motif area is too small, pillars will bend during stamping and the quality of the printed patterns will not be optimum. Section 4: open microchannel configuration requires one layer of the photoresist (25 µm): height of the photoresist pillars is tuned to have an optimal aspect ratio, and PDMS should be high enough to trap cells (see Fig. 7A). Sections 4 and 5: closed microchannel configuration requires two layers; a first layer of 5 µm thickness and a second layer of 50 µm thickness. The first layer is the microchannel which confines the cells from the top, whereas the second layer constitutes the reservoir for cells and should be high enough to allow cell movement and positioning.

The following steps are performed in a clean room, if available (see Fig. 3):

1. Clean the silicon wafers with first acetone and then ethanol. Dry the wafer using a nitrogen stream after each solvent cleaning. Solvent cleaning insures

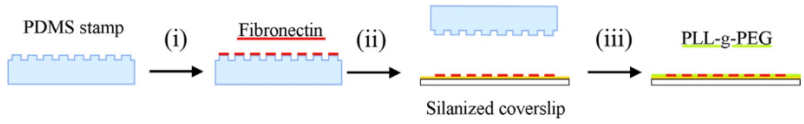

FIG. 4

Micro-contact printing procedure: (i) Incubation of the PDMS stamp with fibronectin. (ii) Stamping. (iii) Passivation with PLL-g-PEG.

complete removal of oils and organic residues from the surface of silicon wafers; while they do remove contaminants, solvents themselves actually leave residues on the surface of wafers as well. For this reason, a two-solvents method is implemented to ensure that the wafer is contaminant-free. After this step, heat the wafers at 200 °C for 15–30 min for a complete removal of humidity from the wafer surface.

2. Spin-coat the first photoresist layer according to the target thickness. To obtain separated triangular patterns for micro-contact printing (see Fig. 4) and open micro-channels (see Fig. 7), pour the photoresist (SU-8 2025) on the wafer and remove air bubbles with the aid of a plastic dropper. Set a two-step spinning process on the spin-coater. Spin at 500 rpm for 10 s with an acceleration of 100 rpm/s during the first step to homogenize the layer over the wafer. Next, spin the wafer containing the resin at 3000 rpm for 30 s with acceleration of 300 rpm/s for the second step. This should result in a photoresist layer of 25 µm thickness (see Fig. 3A (ii)).
3. To obtain the first layer for the closed connected triangular microchannel (see Fig. 8), a 5 µm thick layer is required. After repeating step (2) using the desired photoresist (SU-8 2005), spin at 3000 rpm for 30 s with acceleration of 300 rpm/s for the second spin step. This should result in a photoresist thickness of 5 µm (see Fig. 3A (ii)).
4. After obtaining the evenly spread photoresist, pre-bake has to be done to ensure a firm attachment of the photoresist to the wafer. For a 25 µm thick layer, this step has to be done during 5 min at 95 °C and for a 5 µm thick layer during 2 min at 95 °C.
5. After pre-bake, make a firm contact between the wafer and the mask containing the respective motifs. A defective contact will lead to ill-defined motifs (see Troubleshooting: Tr.1; Fig. 10A). The masks should have negative polarity for 25 µm thick layer (Separated Triangles) to give holes and positive polarity for 5 µm thick layer (Connected Triangles) to obtain pillars on photoresist (SU-8) layer. After tight contact with the mask (see Fig. 3A (m1)) cross-link the photoresist by exposing the wafer to UV irradiation with a dose of 150 mJ/cm^2 for 25 µm thick Separated Triangles and 105 mJ/cm^2 for 5 µm thick Connected Triangles (see Fig. 3A (iii)). The time of exposure will depend on the power/wavelength of the device (e.g., mask aligner) for the UV light exposure.

6. As soon as the exposure is over, for Separated Triangles: follow a post-bake of 1 min at 65 °C and then 5 min at 95 °C; and for Connected Triangle: 3 min at 95 °C. An image of the mask should be visible on the (SU-8) photoresist coating.
7. After post-bake, develop the structures by immersing them in the SU-8 developer solution, while gently agitating the container; 4 min for 25 µm thick Separated Triangles and 1 min for 5 µm thick Connected Triangles layer. This would strip off the non-cross-linked resin, leaving behind the required motifs (see Fig. 3A (iv)). Finally, rinse the surface with 2-propanol to remove the leftover photoresist.
8. Dry the wafer containing motifs, using a nitrogen stream after rinsing with 2-propanol.
9. After preparing a 5 µm thick layer of Connected Triangles (see Fig. 3A (v)), a second layer has to be prepared in order to obtain a microchannel of connected triangles with a reservoir for cells on either side of the Connected Triangles, in order to introduce cells in microchannels (see Fig. 8B).
10. The second layer (for reservoir) is recommended to be 50 µm thick to facilitate the entry of cells with the cell culture media. For this purpose, follow step (2) and spin the wafer containing the resin (SU-8 2025) at 1700 rpm for 30 s with an acceleration of 300 rpm/s for the second spin step (see Fig. 3A (vi)).
11. Then follow a pre-bake of 6 min at 95 °C.
12. Before the next step of UV exposure for cross-linking, check on the silicon wafer that the mask for the second layer containing motif for reservoir (see Fig. 3A (m2)) is perfectly aligned with the developed first layer of Connected Triangles. For alignment purpose, it is recommended to design masks with two crosses each, on both mask 1 (containing microchannel motif) and mask 2 (containing the reservoir motif) exactly at the same position. During microfabrication and alignment process, both crosses should superimpose between the first photoresist (SU-8) layer and the second mask to ensure optimal alignment of the first and second layers (see Troubleshooting: Tr. 2)
13. Once the alignment is performed, secure the tight contact between the wafer and the mask (for reservoir). Cross-link the photoresist by exposing the wafer to UV irradiation with a dose of 150–155 mJ/cm^2 for a 50 µm layer of reservoir (see Fig. 3A (vii)).
14. As soon as exposure is over, follow a post-bake of 1 min at 65 °C and then 6 min at 95 °C. After post-bake at 95 °C, an image of the mask should be visible on the photoresist coating.
15. Next, develop the structures by immersing the sample in the SU-8 developer solution while gently agitating the container for 5 min. This would strip off the non-cross-linked resin, leaving behind motifs (see Fig. 3A (viii)). Finally, rinse the surface with 2-propanol to remove the leftovers of photoresist.
16. After the silicon wafers are ready with motifs (with one or two layers), do a "hard bake" step at 150 °C for a couple of minutes. This is useful for annealing any surface cracks that may have appeared after development; this step is relevant to all layer thicknesses.

17. After obtaining the motifs for Separated Triangles (25 µm thick layer) and Connected Triangles (first layer: 5 µm, second layer: 50 µm), cover the wafers with PDMS (cross-linker:prepolymer [1:10]).
18. Remove all air bubbles through desiccation, and finally cure overnight at 65 °C on a leveled surface.
19. Once cured, peel off the PDMS, the chip is ready.

3 RECTIFYING CELL MOTION WITH ASYMMETRICAL PATTERNS: MICRO-CONTACT PRINTING OF ADHESIVE MOTIFS

3.1 THE DESIGN OF PATTERN

The scaling arguments are presented in Caballero et al. (2014) for this assay.

3.2 MICRO-CONTACT PRINTING

3.2.1 Protocol

In this section, we detail the protocol for printing adhesive motifs on a glass coverslip. We use fluorescent fibronectin to visualize motifs with microscopy (other proteins could also be used). Poly-L-lysine-g-polyethylene glycol (PLL-g-PEG) is used for surface passivation (see Fig. 4).

3.2.1.1 Materials

- "Piranha" solution (sulfuric acid: hydrogen peroxide [7:3])
- Glass coverslips, N°1–25 mm diameter
- 3-(Mercapto)propyltrimethoxysilane
- Phosphate-buffered saline 1 × (PBS)
- 10 µg/mL Rhodamine labeled Fibronectin (FN) (Cytoskeleton, cat. FNR01-A) in PBS
- 0.1 mg/mL PLL-g-PEG diluted in HEPES 10 mM (SuSoS AG, cat. SZ33-15)
- PDMS (Dow Corning, cat. DC184-1.1)
- Milli-Q Water
- Ethanol 70%
- Parafilm

3.2.1.2 Equipment

- Plasma Cleaner (Diener Electronic, cat. ZeptoB)
- Oven
- Sonicator
- Vacuum pump
- Desiccator

3.2.1.3 Methods

1. Clean the coverslips inside "Piranha" solution during 10 min (this step should be performed cautiously under a hood). Bubbles will form, check that coverslips stay immersed throughout the process. Carefully rinse the glass coverslips

with Milli-Q water. Then, sonicate one by one each coverslip in beakers during 5 min and dry them with a nitrogen stream. Finally, put them in an oven at 65 °C for 10 min.

2. Place the "Piranha" cleaned coverslips inside the desiccator with a small Petri dish filled with 100 µL of 3-(mercapto)propyltrimethoxysilane. Generate a vacuum, then close the pump and let the silane deposit on substrates for 1 h.
3. Place the silanized coverslips for at least 90 min at 65 °C (up to 4 h); note that non-bound silane is very sensitive to temperature and humidity.
4. Meanwhile, cut the PDMS to have 1 cm × 1 cm stamps; sonicate them for 5 min in ethanol and dry them with a nitrogen stream.
5. Activate the surface of each stamp with oxygen plasma (air can also be used). This step will make sure that the surface is hydrophilic and suitable for protein incubation and binding. Be sure that patterns face up during activation.
6. Incubate activated stamps with a 100 µL drop of 10 µg/mL solution of Rhodamine labeled FN for 1 h.
7. After incubation, remove the drop with a pipette and quickly dry the stamp with a nitrogen stream. It should take only few seconds. You can also let the stamp dry at room temperature for about 5 min. This step is critical and differences in drying will impact the overall quality of patterns (see Troubleshooting: Tr.3 and Tr.4).
8. Put the stamp (face with the patterns down) on the silanized coverslip with a 50 g weight on top of it. Wait for 30 min and gently remove weight and stamp from the coverslip. Store the patterned glass coverslips in PBS at 4 °C. At this point, patterns can be stored up to one week, even if immediate usage is recommended.
9. Deposit a 100 µL drop of PLL-g-PEG on a piece of parafilm and put the patterned face of the coverslip onto the drop. Incubate for 20 min. This step will passivate the surface and will decrease adhesion of cells outside the patterns.

3.2.2 2D cell migration experiment

The cells should be carefully placed on the micro-contact printed motifs. Proper washing allows to generate samples with cells exclusively on motifs. Cells should be plated at low density. This will help prevent them to migrate along the same path and in turn potentially "collide." Such phenomenon would interfere with cells trajectories. Finally, low serum condition allows to keep standard cell motility while preventing cell division during migration.

3.2.2.1 Materials

- NIH3T3 cells (or other migratory fibroblasts)
- Dulbecco's Modified Eagle Medium (DMEM) 4.5 g/L glucose 1% Penicillin–streptomycin
- Bovine Calf Serum (BCS)
- Leibovitz's (L-15) medium
- Trypsin–EDTA
- Cell counter

- Pipettes
- 5 mL Petri dishes (60 mm in diameter)

3.2.2.2 Equipment

- Epifluorescence microscope with phase contrast and temperature control
- Sterile hood
- Incubator with CO_2
- Centrifuge

3.2.2.3 Methods

At this stage, all steps should be performed under a sterile hood with a laminar flow.

1. Trypsinize a 5 mL Petri dish with adherent cells 3 min, and add 3 mL of DMEM 10% BCS.
2. Centrifuge cells at 500 rpm during 3 min and re-suspend the pellet in 5 mL of DMEM 10% BCS.
3. Count cells and place 2000 cells on the micro-patterned coverslip.
4. Incubate cells for 30 min at 37 °C with 5% CO_2. Wash out the sample to remove non-adherent cells, and replace medium by L-15 with 1% BCS. This low serum condition will ensure standard cell motility while reducing cell division during the 48 h experiments.
5. Go to the microscope and image patterns and cells (see Troubleshooting: Tr.5) (Fig. 5).

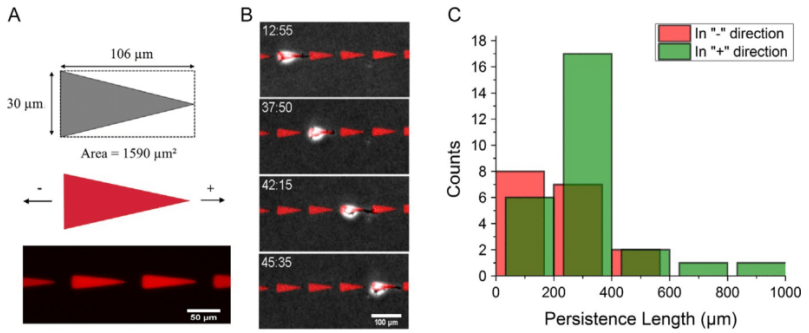

FIG. 5

(A) Pattern characteristics and dimensions (up) and motifs printed on a surface with micro-contact printing (bottom). Patterns are stamped with rhodamine labeled fibronectin. For clarity, tip direction is set as "+" and triangle base direction as "−" (middle). (B) Sequence of a NIH3T3 cell moving on triangles separated by 22 µm gaps. $T=0$ corresponds to the beginning of acquisition (shortly after plating). Migration is directed toward the "+" direction in this sequence; Scale bar 50 µm. Time in hh:mm. (C) Persistence length distribution of NIH3T3 cells migrating in "+" direction and in "−" direction. Motion is directed, or *rectified*, to the + direction on average.

4 CONTROL OF CELL MIGRATION IN CONFINED 3D ENVIRONMENT

4.1 THE DESIGN OF PATTERN

Along the scaling arguments (see Section 1), we measured cell volumes after trypsinization. We obtained a mean diameter for individual rounded cells of $D_{cell} = 14.4 \pm 1.6\,\mu m$ ($n = 388$ cells, s.d.), which corresponds to a mean volume of $V_{cell} = 1560 \pm 520\,\mu m^3$. Nuclei were stained on spread cells using Hoechst, and their volume and height were measured. The mean volume was $V_{nucleus} = 740 \pm 180\,\mu m^3$ ($n = 199$ nuclei, s.d.) and the mean height $H_{nucleus} = 8.5 \pm 1.4\,\mu m$ ($n = 199$ nuclei, s.d.). Altogether, we used V_{cell}, $V_{nucleus}$, $H_{nucleus}$ to design the 3D triangle channel motif: each triangular motif has the volume of a NIH3T3 fibroblast ($1500\,\mu m^3$). Taking into account these values, we selected the height of the microchannel of 5 µm to allow confinement of cell and nucleus. We calculated the *xy* area for each triangle to be $300\,\mu m^2$. After selecting an angle of 16° similar to the angle used in triangles on 2D ratchetaxis and to further confine the nucleus, we selected an opening width of 4 µm between connected ratchets. Using the following parameters (area: $300\,\mu m^2$, angle: 16° and opening width: 4 µm), base and length of a ratchet were calculated. They are equal respectively to 14 µm and 34 µm (see Figs. 7 and 8). In ratchetaxis experiments, we used this motif in a closed microchannel configuration, where cells were confined from the top and sides (see Fig. 8); and in open microchannel configuration, cells were confined only from the sides (see Fig. 7).

In order to have a large number of trajectories per experiment, we designed a mask with 50 rows of connected triangles. For the closed configuration, two layers of SU-8 are required. The first layer contains connected ratchets of 5 µm height. The second layer allows to fabricate the cells reservoir of 50 µm height. In order to generate chemical gradients, the second layer has a Y-shaped channel of 50 µm height (see Figs. 3 and 9B). For the open microchannel configuration, a layer of 25 µm height SU-8 is required in order to trap cells (see Fig. 7A).

4.2 CONFINED OPEN MICROCHANNEL CONFIGURATION

4.2.1 Protocol

4.2.1.1 Materials

- Masks/silicon wafer
- PDMS
- Glass coverslips (N°1–25 mm diameter)
- Chlorotrimethylsilane (Sigma, cat. 92360)
- 2 mL Petri dish (35 mm in diameter)

4.2.1.2 Equipment

- Plasma cleaner
- Tweezer
- Blade

- Oven
- Spin-coater
- Vacuum pump
- Desiccator

4.2.1.3 Methods

1. Pour PDMS (cross-linker:prepolymer [1:10]) on a silicon wafer. Remove air bubbles by placing the wafer into desiccator for 1 h. Cure at 65 °C for at least 4 h.
2. Cut PDMS with a blade and remove the PDMS 1 stamp from the wafer (see Fig. 6A (i)).
3. Activate the surface of PDMS stamp 1 with oxygen plasma. Put it inside the desiccator with a small Petri dish filled with 100 µL of chlorotrimethylsilane. Generate a vacuum, then close the pump and let the silane deposit on the substrate for 30 min.
4. Pour PDMS (cross-linker:prepolymer (1:10)) on PDMS 1 placed on Petri dish. Check that patterns are "face up." Remove air bubbles by placing the wafer into the desiccator for 1 h. Cure at 65 °C for at least 4 h (see Fig. 6A (ii)).
5. Cut PDMS with a blade and remove the PDMS stamp 2 from the Petri dish containing PDMS stamp 1.
6. Activate with oxygen plasma the surface of PDMS stamp 2. Put it inside the desiccator with a small Petri dish filled with 100 µL of chlorotrimethylsilane. Generate a vacuum, then close the pump and let the silane deposit on the substrate for 30 min.
7. Spin liquid PDMS on PDMS stamp 2. Set a two-step spinning process on the spin-coater. Spin at 500 rpm for 10 s during the first step to homogenize the PDMS layer over the PDMS stamp 2. The speed used in the second step will

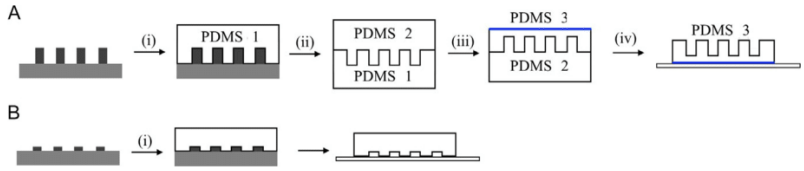

FIG. 6

Schematics of the method to obtain closed (A) and open (B) microchannel configuration. (i) PDMS is poured on SU-8 wafers and cured 4 h at 65°C. In closed configuration, microchannels are 5 µm height. (ii) After activation of PDMS and coverslip with oxygen plasma, they are both bonded together. In open configuration, microchannels are 25 µm height. (ii) PDMS 1 is cut, activate with oxygen, treated with chlorotrimethylsilane and PDMS is poured on it and cured 4 h at 65 °C. (iii) PDMS 2 is cut, activated with oxygen, treated with chlorotrimethylsilane and PDMS is spin-coated on top of PDMS 2 at 2000 rpm to obtain 40 µm PDMS layer. (iv) After curing at 65 °C for 4 h and activation with oxygen plasma, PDMS 3 is bonded to a coverslip and incubated overnight at 65 °C to consolidate the bonding. PDMS 2 is then peeled off.

define the height of PDMS stamp 3. Spin-coating at a speed of 2000 rpm allows the spreading of PDMS at a height of approximately 40 µm. Cure at 65 °C for at least 4 h (see Fig. 6A (iii)).

8. Activate both coverslip and PDMS stamp 3 (see Fig. 6A (iv); blue side) with oxygen plasma. Bind the blue surface side of PDMS stamp 3 to the coverslip. Incubate them at 65 °C overnight to secure the binding between the PDMS stamp 3 and the glass coverslip.
9. With a tweezer, gently peel off the PDMS stamp 2 from the PDMS stamp 3 (which is attach to the coverslip).

4.2.2 Cell migration experiment

4.2.2.1 Materials

- NIH3T3 cells (or other migratory fibroblasts)
- DMEM 4.5 g/L glucose 1% Penicillin–streptomycin
- BCS
- L-15 medium
- Trypsin–EDTA
- Cell counter
- Pipettes
- 5 mL Petri dishes (60 mm in diameter)

4.2.2.2 Equipment

- Epifluorescence microscope with phase contrast and temperature control
- Sterile hood
- Incubator with CO_2
- Centrifuge

4.2.2.3 Methods

At this stage, all steps should be performed under a sterile hood with a laminar flow. We report now how to place cells in the sample.

1. Before the experiment, activate the surface of the stamp with oxygen plasma. This step will make the surface hydrophilic and will facilitate media distribution within the sample. Place the open microchannel sample under UV for 10 min sterilization.
2. Trypsinize a 5 mL Petri dish with adherent cells 3 min and add 4 mL of DMEM 10% BCS. Count cells.
3. Centrifuge cells at 500 rpm during 3 min and re-suspend cells in DMEM 10% BCS at a density of 100,000 cells/mL.
4. Place 100 µL of the cell suspension on the open microchannel configuration.
5. Incubate 30 min at 37 °C with 5% CO_2. Wash out the sample to remove non-adherent cells and replace the medium with L-15 containing 1% BCS.
6. Go to the microscope and acquire cell migration with a 10 min interval.

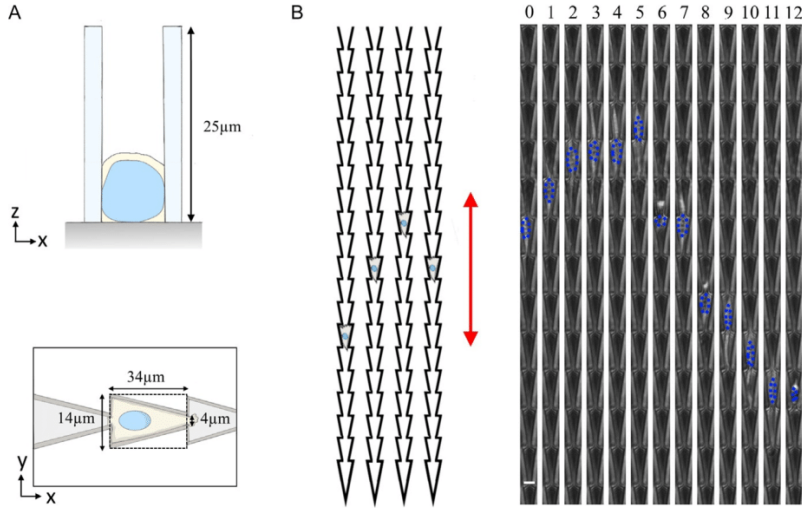

FIG. 7

(A) Dimension of the triangular 3D open configuration, *xz* plane (top) and *xy* plane (bottom). (B) Left: Schematic of the experimental setup. Cells are seeded in the middle of open ratchet microchannel. Right: Time-lapse images of a NIH3T3 fibroblast migrating in an open ratchet microchannel configuration. Blue dots outline the nucleus over time. Scale bar 10 µm, time in hour.

In open ratchet microchannel configuration, cells seeded in channels migrate longer and preferentially in the "+" direction after probing in both directions (see a typical example Fig. 7B (manuscript in preparation)).

4.3 CONFINED CLOSED MICROCHANNEL CONFIGURATION

4.3.1 Protocol

4.3.1.1 Materials

- Masks/silicon wafer
- PDMS
- Glass coverslips (N°1–25 mm diameter)
- Holes puncher

4.3.1.2 Equipment

- Plasma cleaner
- Tweezer
- Blade
- Oven

4.3.1.3 Methods

1. Pour PDMS (cross-linker:prepolymer (1:10)) on a silicon wafer. Remove air bubbles by placing the wafer in the desiccator for 1 h.
2. Cure at 65 °C for at least 4 h.
3. Cut PDMS with a blade and remove the PDMS stamp from the wafer (see Fig. 6B (i)).
4. Punch holes in the reservoirs with a 0.75 mm diameter puncher.
5. Use adhesive tape to remove dusts and PDMS residues deposited on the motifs.
6. Activate the coverslip and PDMS stamp with oxygen plasma. Bind PDMS to the coverslip (see Fig. 6A (ii′)).
7. Incubate the chip at 65 °C overnight to secure the binding between the PDMS stamp and the glass coverslip.

4.3.2 Cell migration experiment

At this stage, all steps should be performed under a sterile hood with a laminar flow. To place cells in the sample, we follow this protocol.

4.3.2.1 Materials

- NIH3T3 fibroblasts (or other migratory fibroblasts)
- Trypsin–EDTA
- DMEM 4.5 g/L glucose 1% Penicillin–streptomycin
- Leibovitz's L-15 medium
- BCS
- Pipettes
- Petri dishes
- Eppendorf micro-loader (Eppendorf, cat. 5242956003)

4.3.2.2 Equipment

- Laminar flow hood
- Incubator
- Centrifuge
- Epifluorescence microscope with phase contrast and temperature control
- Metallic holder

4.3.2.3 Method

1. Activate the chip with oxygen plasma to make it hydrophilic. Fill in the PDMS chip with L-15 with 10% BCS.
2. Trypsinize a 5 mL Petri dish with adherent cells for 3 min, and add 4 mL of DMEM 10% BCS. Count cells.
3. Centrifuge for 3 min at 500 rpm. Cells will form a pellet. Remove the supernatant and re-suspend cells in L-15 10% BCS at a density of 30 million cells/mL.

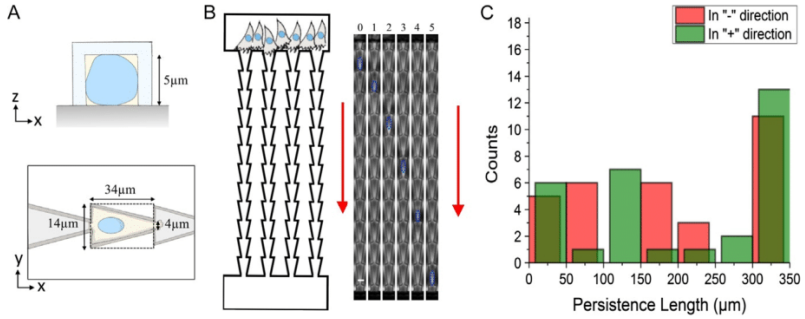

FIG. 8

Dimension of the triangle 3D confined motifs. (A) Schematic of a ratchet unit with its dimensions, *xz* axis (top) and *xy* axis (bottom). (B) Left: Schematics of the experimental setup. Cells are seeded in one side of the channel allowing the entry and migration of the cells in the "+" direction (red arrow). Right: Time-lapse images of a NIH3T3 fibroblast migrating in a ratchet microchannel in the "+" direction (red arrow). Blue dots outline the nucleus over time. Scale bar 10 µm, time in hours. (C) Persistence length distributions of cells migrating in "+" direction and in "−" direction. Experiments in (B) were repeated with cells plated on the other side of the channel. Altogether, the confined configuration forces cells to follow the polarity set at the entry of channels (in preparation).

4. With an Eppendorf micro-loader, inject 20 µL of cells suspension into one inlet (see Fig. 8B). Slowly aspirate L-15 medium from the second inlet to allow accumulation of cells at the entry of channel.
5. Immerse the PDMS chip in L-15 containing 10% BCS.
6. Incubate for 2 h at 37 °C to let cells adhere and spread.
7. Transfer the chip into sterile holder and start the time-lapse acquisition with a 10 × objective and 10 min interval. Note that due to the presence of a thin layer of PDMS in the optical path, phase contrast images might not be optimal. To improve the phase contrast, use an objective with a numerical aperture of a minimum 0.40.

5 CONTROL OF CELL MIGRATION IN 3D WITH CHEMOTAXIS

With this setup, the motion of cells can be challenged by a chemical gradient when the sample is closed (see Fig. 9B). We report now the protocol.

5.1 PROTOCOL

5.1.1 Materials

- Masks/silicon wafer
- PDMS
- Glass coverslips (N°1–25 mm diameter)
- Holes puncher

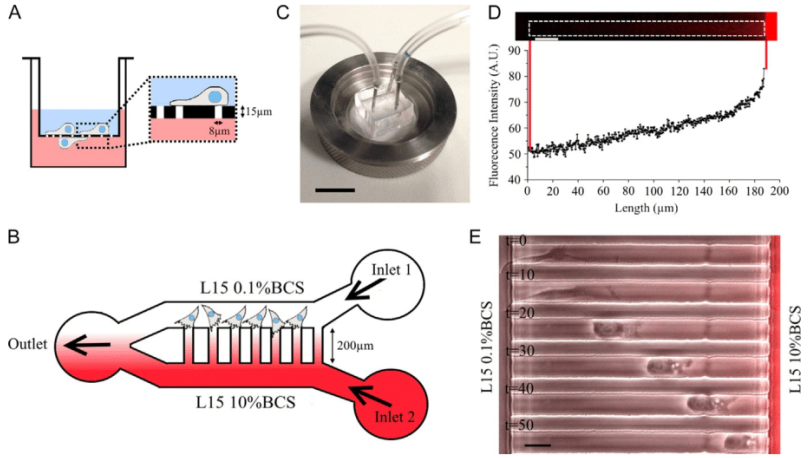

FIG. 9

Boyden and microfluidics experiments to study chemotaxis. (A) Schematic of a Boyden chamber. Typically, a Boyden chamber is composed of two chambers separated by a 15 μm thickness membrane with 8 μm pores (Boyden, 1962). Cells are seeded in the upper chamber in medium without chemo-attractant. The lower chamber is filled with medium containing the chemo-attractant. After incubation for 12 h, migration is stopped and migrating cells which crossed the membrane are counted. (B) Schematic of the microfluidic chip used to follow cell migration in response to a chemical gradient. Cells are seeded in the microfluidics chamber. Gradient is formed in the micro-channels by connecting two syringes, one with the chemo-attractant and fluorescent dye and the other one without. A syringe pump is necessary to form stable gradient up to 24 h. (C) Image of the device. Scale bar 1 cm. (D) Top: Fluorescent image of the microchannel and the chemical gradient visualized with fluorescent dye. Bottom: Corresponding fluorescent intensity profile along the microchannel. Scale bar 20 μm. (E) Time-lapse images of a NIH3T3 fibroblast migrating in a microchannel in a gradient of 10% serum. Scale bar 20 μm, time in minutes.

5.1.2 Equipment

- Plasma cleaner
- Tweezer
- Blade
- Oven

5.1.3 Methods

1. Pour PDMS (cross-linker:prepolymer (1:10)) on a silicon wafer. Remove air bubbles by placing the wafer in the desiccator for 1 h.
2. Cure at 65 °C for at least 4 h.
3. Cut PDMS with a blade and remove the PDMS stamp from the wafer (see Fig. 6A (i)).

4. Punch holes in the inlets–outlet with a 0.75 mm diameter puncher.
5. Use adhesive tape on the motifs to remove any residual dusts and/or PDMS residues.
6. Activate the coverslip and PDMS stamp with oxygen plasma. Bind PDMS to the coverslip (see Fig. 6A (ii)).
7. Incubate the chip at 65 °C overnight to secure the binding between the PDMS stamp and the glass coverslip.

5.2 CELL MIGRATION EXPERIMENT

At this stage, all steps should be performed under a sterile hood with a laminar flow. To place cells in the sample, we follow this protocol.

5.2.1 Materials

- NIH3T3 fibroblasts (or other migratory fibroblasts)
- Trypsin–EDTA
- DMEM 4.5 g/L glucose 1% Penicillin–streptomycin
- Leibovitz's L-15 medium
- BCS
- Petri dishes
- Eppendorf micro-loader
- Tetramethylrhodamine isothiocyanate–Dextran, molecular weight 20 kDa (Sigma, cat. 73766)
- 1 mL syringe (Henke-Sass Wolf Soft-Ject, cat. 5010-A00V0)
- 20Gx1″ needle (Terumo 0.9 × 25 mm Luer)
- 23Gx1″ needle (Terumo 0.6 × 25 mm Luer)
- Tygon tubing (Saint Gobain, cat. AAD04103)

5.2.2 Equipment

- Laminar flow hood
- Incubator
- Centrifuge
- Epifluorescence microscope with phase contrast and temperature control
- Metallic holder
- Syringe pump

5.2.3 Method

1. Activate the chip with oxygen plasma to make it hydrophilic. Fill in the PDMS chip with L-15 with no BCS (0% BCS).
2. Trypsinize a 5 mL Petri dish with adherent cells 3 min, and add 4 mL of DMEM containing 10% BCS. Count cells.
3. Centrifuge for 3 min at 500 rpm. Cells will form a pellet. Remove the supernatant and re-suspend cells in L-15 0% BCS at a density of 30 million

cells/mL. Cells are re-suspended in L-15 0% BCS in order to starve cells prior stimulation to the serum gradient.

4. With an elongated tip, inject 20 µL of cell suspension into the outlet. Slowly aspirate L-15 medium from inlet 1 to allow accumulation of cells at the channels entry (see Fig. 9B).
5. Immerse the PDMS chip in L-15 0% BCS.
6. Incubate for 2 h at 37 °C to let cells adhere and spread.
7. Transfer the chip into the sample holder.
8. To form the serum gradient, two 1 mL syringes are prepared with L-15 0.1% BCS or L-15 containing 10% BCS and fluorescent dextran, enabling visualization of the chemical gradient.
9. Connect syringes to syringe needles (23Gx1″) and Tygon tubing which have previously been rinsed with L-15.
10. Make sure that there are no bubbles into the tubing during experiment. This can prevent a good flow and detach cells if bubbles enter the microfluidic device (see Troubleshooting: Tr.6; Fig. 10F).

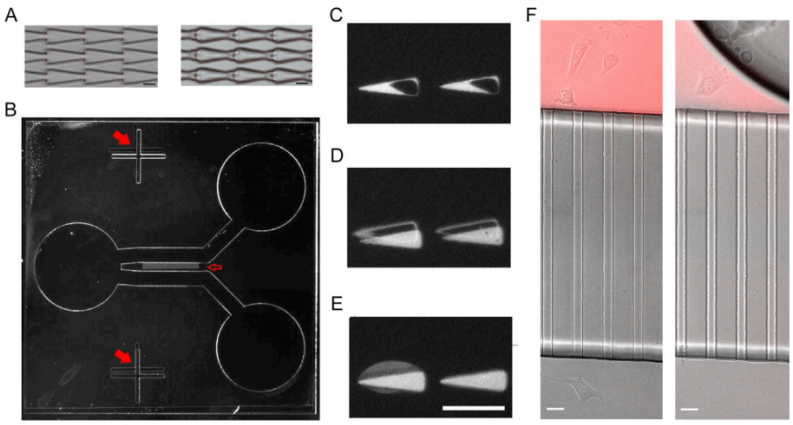

FIG. 10

Issues during microfabrication (A and B), micro-contact printing process (C, D, and E) and microfluidics experiments (F). (A) Images of two wafers. Left: Image of connected ratchet microchannel properly defined. Right: Image of ill-defined connected ratchet microchannel due to poor contact between SU-8 on wafer and mask. Scale bar 20 µm. (B) Image of a wafer where first and second layers are misaligned. Filled red arrows show non-aligned crosses, empty red arrow shows that micro-channels are not connected to the main channel at the bottom side. Scale bar 100 µm. (C) Patterns with over-dried stamp. (D) Double stamping. (E) Wet patterns. (F) Appearance of bubbles during chemical gradient experiment in microchannel. Chemical gradient is removed in the presence of bubble. Scale bar 20 µm.

11. Connect tubing to the two inlets of the chip by using cut syringe needles (20Gx1″). The outer diameter of the needles (0.9 mm) is slightly larger than the diameter of the punched holes (0.75 mm). This allows to make sure that upon insertion the connection is sealed securely (see Fig. 9C).
12. Place syringes on the pump. Flow the two solutions at a rate of 10 µL/h. After few minutes, a stable gradient forms into microchannels which can be visualized with fluorescent dextran as seen in Fig. 9D and E.

Conclusion: With this method, chemical gradients can be generated in closed configurations—but not in open configurations. They can be imposed in competition or in cooperation with other external cues such as confinement and ratchetaxis. The net results can be reported through the analysis of trajectories like in the other examples presented above.

6 TROUBLESHOOTING

Many issues can appear in the preparation of samples, during the microfabrication, micro-patterning, or even during acquisition under the microscope. We follow the order of their appearance below.

6.1 MICROFABRICATION

Tr.1: During microfabrication process, a critical step is to obtain well defined structures, for example, triangles should have sharp edges. Ill-defined structures will appear, if there is not a firm contact maintained between SU-8 and mask (see step in Figs. 3 (iii) and 10A). To prevent this, make sure that the contact is tight enough. This can also happen during the development step when motifs are under or overdeveloped. To avoid this, immerse back the wafer in SU-8 developing solution for 30 s, rinse with isopropanol and check the motifs.

Tr.2: If two layers are required, they need to be perfectly aligned. A misalignment is observed when crosses on the wafer of layer 1 do not overlap with crosses on the mask for the layer 2 (see Fig. 10B filled arrows). This results in disconnected structures from the first and second SU-8 layers (see Fig. 10B empty arrow). To prevent this, be patient and pay attention during alignment step that both crosses are aligned. During the design of the mask, it is possible to insert more asymmetric motifs in both masks (for the layers 1 and 2) along the motifs to make sure that there is optimal alignment, before UV exposure.

6.2 MICRO-CONTACT PRINTING

Tr.3: Drying time critically depends on humidity, the ambient temperature in the room and on patterns characteristics (area, aspect ratio and spacing between motifs). It can vary from 2 min to 6 min depending on the design. Drying the stamps with a nitrogen stream can prevent these problems, but this method is more difficult to

control. Drying too much the stamp will impede fibronectin transfer to the glass surface (Fig. 10C). On the other hand, a stamp too wet gives ill-defined patterns (Fig. 10E). This is the most critical step.

Tr.4: Double stamping (Fig. 10D) usually happens when the stamp moves while applying pressure or when it touches again the coverslip while removing it. Using two tweezers to remove the stamp (one on the coverslip, the other one holding the stamp) is a good solution to carefully release the PDMS stamp from the coverslip.

Tr.5: Cell death during acquisition might happen for the following reasons:

- Coverslips are not well rinsed after "piranha" treatment.
- Stability of PLL-g-PEG: it is recommended not to use the diluted solution after 2–3 weeks.
- Cells are too confluent on the plate, prior deposition on patterns: contact inhibition might affect cell motility and prevent motion leading to death on the motifs (especially for large gap distances).

6.3 MICROFLUIDICS

Tr.6: While imaging, air bubbles can affect the stability of chemical gradients (see Fig. 10F), and can lead to detachment of cells from the coverslip. Typically, this type of experiments cannot be analyzed. To prevent this, make sure that there are no bubbles in the tubing while preparing them and before starting experiment.

Tr.7: Even after the sealing of PDMS stamps to the coverslip, sometimes detachment can occur. A proper binding is particularly important for generating the chemical gradient. In this situation, check that plasma binding is properly achieved. Also, check if PDMS and coverslips are clean and without dusts, which if present could prevent proper sealing.

Optimal z-focus: In order to image cells during typical timescales relevant for reliable measures, i.e., days, cells need to remain within the same focal plane. When acquiring for longer time periods at 37 °C, microscopes might exhibit some drift due to thermal gradients, in particular along the z-direction. A good solution involves placing the entire experimental set-up in an environment with temperature control ahead of time, prior the experiment to secure a good mechanical stability. Alternatively, feedback loops to control the objective-sample distance can be used to keep focus throughout acquisition. Also, μm size beads can be deposited on the sample, and images can be realigned after experiments using these fiducial markers.

7 CONCLUSION

The methods reported in this article show how cell migration can be controlled specifically for a quantitative study. Their implementations do not require large and expensive equipment and these assays can be used in any laboratories. Designs of 2D and 3D cellular controls have allowed to reveal new modes of migrations

(Bergert et al., 2015; Caballero et al., 2015; Liu et al., 2015). With such setups, more migration modes could appear and the associated signaling networks could be studied. Finally, these microfabrication techniques could also open potential new methods for diagnosis at cellular scales in diseases where migration is impaired, in cancer for example (Mitchell, Jain, & Langer, 2017).

REFERENCES

Bergert, M., Erzberger, A., Desai, R. A., Aspalter, I. M., Oates, A. C., Charras, G., et al. (2015). Force transmission during adhesion-independent migration. *Nature Cell Biology*, *17*(4), 524–529.

Boyden, S. (1962). The chemotactic effect of mixtures of antibody and antigen on polymorphonuclear leucocytes. *Journal of Experimental Medicine*, *115*(3), 453–466.

Caballero, D., Comelles, J., Piel, M., Voituriez, R., & Riveline, D. (2015). Ratchetaxis: Long-range directed cell migration by local cues. *Trends in Cell Biology*, *25*(12), 815–827.

Caballero, D., Voituriez, R., & Riveline, D. (2014). Protrusion fluctuations direct cell motion. *Biophysical Journal*, *107*(1), 34–42.

Comelles, J., Caballero, D., Voituriez, R., Hortigüela, V., Wollrab, V., Godeau, A. L., et al. (2014). Cells as active particles in asymmetric potentials: Motility under external gradients. *Biophysical Journal*, *107*(7), 1513–1522.

Cramer, L. P. (2010). Forming the cell rear first: Breaking cell symmetry to trigger directed cell migration. *Nature Cell Biology*, *12*(7), 628–632.

Hawkins, R. J., Piel, M., Faure-Andre, G., Lennon-Dumenil, A. M., Joanny, J. F., Prost, J., et al. (2009). Pushing off the walls: A mechanism of cell motility in confinement. *Physical Review Letters, 102*, 058103-1–058103-4.

Helvert, S. V., Storm, C., & Friedl, P. (2018). Mechanoreciprocity in cell migration. *Nature Cell Biology*, *20*(1), 8–20.

Jiang, X., Bruzewicz, D. A., Wong, A. P., Piel, M., & Whitesides, G. M. (2005). Directing cell migration with asymmetric micropatterns. *Proceedings of the National Academy of Sciences of the United States of America*, *102*(4), 975–978.

Liu, Y. J., Le Berre, M., Lautenschlaeger, F., Maiuri, P., Callan-Jones, A., Heuzé, M., et al. (2015). Confinement and low adhesion induce fast amoeboid migration of slow mesenchymal cells. *Cell*, *160*, 659–672.

Mitchell, M. J., Jain, R. K., & Langer, R. (2017). Engineering and physical sciences in oncology: Challenges and opportunities. *Nature Reviews. Cancer*, *17*, 659–675.

Petri, J. R. (1887). Eine kleine Modification des Koch'schen Plattenverfahrens. *Centralblatt für Bakteriologie und Parasitenkunde*, *1*, 279–280.

Prentice-Mott, H. V., Chang, C.-H., Mahadevan, L., Mitchison, T. J., Irimia, D., & Shah, J. V. (2013). Biased migration of confined neutrophil-like cells in asymmetric hydraulic environments. *Proceedings of the National Academy of Sciences of the United States of America*, *110*(52), 21006–21011.

Qin, D., Xia, Y., & Whitesides, G. M. (2010). Soft lithography for micro- and nanoscale patterning. *Nature Protocols*, *5*(3), 491–502.

Théry, M., & Piel, M. (2009). Adhesive micropatterns for cells: A microcontact printing protocol. *Cold Spring Harbor Protocols*, *4*(7), 1–12.

Whitesides, G. M. (2006). The origins and the future of microfluidics. *Nature*, *442*, 368–373.

Submitted: Methods in Cell Biology

How to orient cells in micro-cavities for high resolution imaging of cytokinesis and lumen formation.

Alka Bhat,[1-5] Linjie Lu,[1-5*] Chen-Ho Wang,[6*] Simon Lo Vecchio,[1-5] Riccardo Maraspini,[6] Alf Honigmann,[6] Daniel Riveline[1-5]

Affiliations:

[1]Laboratory of Cell Physics ISIS/IGBMC, CNRS and University of Strasbourg, Strasbourg, France
[2]Institut de Génétique et de Biologie Moléculaire et Cellulaire, Illkirch, France
[3]Centre National de la Recherche Scientifique, UMR7104, Illkirch, France
[4]Institut National de la Santé et de la Recherche Médicale, U964, Illkirch, France
[5]Université de Strasbourg, Illkirch, France
[6] Max Planck Institute of Molecular Cell Biology and Genetics, Dresden, Germany

* Equal contributions

Correspondence to Alf Honigmann and Daniel Riveline

Abstract: Imaging dynamics of cellular morphogenesis with high spatial-temporal resolution in 3D is challenging, due to the low spatial resolution along the optical axis and photo-toxicity. However, some cellular structures are planar and hence 2D imaging should be sufficient, provided that the structure of interest can be oriented with respect to the optical axis of the microscope. Here, we report a 3D microfabrication method which positions and orients cell divisions very close to the microscope coverglass. We use this approach to study cytokinesis in fission yeasts and polarization to lumen formation in mammalian epithelial cells. We show that this method improves spatial resolution on range of common microscopies, including super-resolution STED. Altogether, this method could shed new lights on self-organization phenomena in single cells and 3D cell culture systems.

Keywords: Biological Physics, Microfabrication, Super-resolution STED, Cytokinesis, Cell Polarization, Organoids.

Introduction

Cells have been cultured traditionally on Petri dishes (Petri, 1887) where they can grow easily. In addition, adherent cell culture facilitates microscopy observation within single or a couple of focal planes. This 2D approach has become the standard method to culture and to observe

cells and multicellular systems, in basic research, in drug discovery, and in medicine for diagnosis.

However, this method is not optimal for many reasons [120] . Cells are artificially ‘forced’ to spread on planar and flat surfaces, potentially inducing artificial shapes and pathological signaling pathways compared to environments encountered in physiological conditions (Weaver, Petersen, Wang, Larabell, Briand, Damsky et al., 1997) (Anders, Hansen, Ding, Rauen, Bissell, Korn, et al., 2003). Cells evolve more physiologically in 3D environments, and classical Petri dishes may not reproduce faithfully this condition. However, 3D cell culture methods, in which cells are typically embedded in hydrogels, pose new challenges to our standard microscope observation techniques. In 3D and sometime also in 2D cell culture many structures/organelles will be ill-oriented with respect to the plane of observation for cells. Placing these organelles within the focal plane of objectives could lead to gain in resolutions in space and in time. These limitations have generated the need to design 3D structures closer to physiological conditions.
In this context, microfabrication has allowed to prepare 3D environments which are compatible with cell growth and organ designs [113] [112]. Shapes in 3D are generated with micrometer resolution using protocols which can be performed with simple training (see Figure 1). We reported since 2009 (Riveline & Buguin, 2009) (Wollrab & Riveline, 2012) (Riveline, 2012) [114] the preparation of cavities, where cells can be placed vertically with respect to the coverglass. In these 3D configurations, cell division occurs also in a direction perpendicular to the long axis of the cell, but structures such as cytokinetic rings can be seen with unprecedented resolutions. In standard coverslips, rings are perpendicular to the plane of acquisition of objectives: each plane of image capture gives two points, and full rings visualization requires multiple z-stacks acquisitions and 3D reconstruction. In contrast, in these cavities, cytokinetic rings can be seen ‘en face’ in a single focal plane of acquisition (see Figure 2). Any close to planar cellular structures with such orientations can in principle be imaged with this device and this method.

In this paper, we describe our different procedures and strategies to orient cell structures with 3D microfabrication. We also go one step further and prepare 3D cavities, which are optimized for super-resolution microscopy. We benchmark our system by imaging the cytokinetic rings in fission yeast and in mammalian cells, as well as the polarization and lumen formation in mammalian MDCK cells after the first cell division. The gain in resolution due to the positioning close to the coverglass and the orientation along the optical axis is significant in time and in space (see Figure 3). For example, clusters of myosin could be resolved with this method with resolution of 200nm with conventional confocal microscopy. They were visualized either by inverted microscope or by having cells imaged directly from below with no interface (Figure 3B). Through-hole cavities allowed us the usage of super-resolution STED microscopy for cytokinetic rings and lumen (Figure 3B.ii and Figure 4) with high NA objectives and minimal optical aberrations. The gain in temporal resolution is also important since organelles can be imaged within sub-seconds in their planes of evolution (see Figure 3C). For example, we reported thanks to this method that myosin clusters were still during cytokinesis in the cell framework. This unexpected observation and its analysis and comparisons with

theory and other systems led to the conclusions that myosin clusters generate stress which is associated to the ring constriction in mammalian cells. This supported the notion that myosin clusters dynamics and their self-organizations can serve as generic readouts in cells and in model systems to track and predict changes in shapes [5]. Altogether, these results show that cells inserted vertically in cavity can resolve spatial and temporal cues not accessible so far.

We report below the steps for preparation of 3D micro-patterns by taking the following outline. We start by describing the design and preparation of masks (I), and continue by the fabrication of motifs (II and III). We then explain how to place cells within cavities (V). Troubleshooting is reported in part VI.

I. Design of mask for optimized cavity preparation.

Masks will serve as support to expose and protect resins from light during the process. In their designs, motifs and inter-distances need to be carefully rationalized.

For each cellular system, cavity dimensions need to be matched to cell dimensions. The first step consists of measuring the distribution of cell diameter right after trypsinization for mammalian cells, and plating cells on a coverslip coated with fibronectin (typically 10µg/ml for 1 hour at room temperature). Distributions for cell diameter can be very sharp like for fission yeasts, and broader for mammalian cells. The mean value is a good starting point for selecting the disk dimension to be prepared on masks.

In addition to cavity diameter, the inter-distance between motifs is important. Inter-distance determines number of cavities per sample. In addition, as reported below, low inter-distance secures a satisfactory filling percentage of cells in cavities. However, this inter-distance should not be too low in order to secure firm attachment of the elastomer stamp. A rule of a thumb consists in taking inter-distance at least twice the cavity size.

After the designed motifs are printed and ready on a photomask, microfabrication process of the motifs follows. The mask prepared in our case had diameters of 17µm through 22µm with an inter-distance of 30µm for mammalian cells or 5µm for fission yeast. Photomasks can be designed using software such as Clewin (Freeware) or Autocad®. Disks are plain or transparent depending on the type of photoresist used in the next steps.

II. Microfabrication of motifs on Si wafer.

After the photomask is ready, a light sensitive epoxy-based material (photoresist) is used to obtain motifs on Si wafer. The photoresist (SU-8 in our case) is spin-coated on the wafer with specific coating time and speed to obtain the target height for cavities. In this part, we report SU-8 pillars which are fabricated on Si wafers.
The average diameters for HeLa and MDCK cells were measured to be ~20µm and ~15µm respectively. Therefore, the chosen diameter/height in our case were 22µm/25µm and

17µm/12µm for Hela cells and MDCK cells respectively. The preparation of cavities for fission yeasts is reported in this reference (Riveline, 2012) with special conical shapes to secure firm anchorage of cells.

Materials

- Silicon wafers
- Wafer tweezers
- Chromium/plastic photomask (with printed motifs to microfabricate)
- SU-8 photoresist (2010 and 2025)
- SU-8 developer
- Acetone
- 2-propanol
- Ethanol

Equipment

- Mask aligner (as UV source)
- Spin-coater
- Hot plates (65 °C and 95 °C)
- Disposable graduated dropper (for the removal of bubbles)

Steps for photolithography (Containing steps common to the co-authored article E. Le Maout, *et.al* Directing cell migration on flat substrates and in confinement with microfabrication and microfluidics," *Methods in Cell Biology*, 1st ed., vol. 147, Elsevier Inc., 2018, pp. 109–132).

1. To ensure that the silicon wafer is contaminant free, it is first cleaned with acetone. It is then dried with a nitrogen stream and followed by similar treatment with ethanol and drying process. Solvent cleaning ensures complete removal of oils and organic residues from the wafer surface. After solvent cleaning, it is advisable to heat up the wafers at 200°C for 10-20 minutes for complete removal of humidity from the surface of wafer.
2. To obtain the targeted height, pour the photoresist (SU-8 2025 for 25µm, and SU-8 2010 for 10µm) on the wafer and remove air bubbles with the help of a plastic dropper. Set a two-step spinning process on the spin-coater. Spin at 500rpm for 10s with an acceleration of 100 rpm/s during the first step to homogenize the layer over the wafer for attaining both 25µm and 12µm height. For a height of 25µm, spin the wafer containing resin at 3000rpm for 30s with acceleration of 300 rpm/s for the second step (*WS-650-23 Spin Coater; Laurell Technologies corporation*, centrifuge and rotor details kept throughout for microfabrication). For a height of 12µm, spin the wafer containing the resin (SU-8 2010) at 3500rpm for 30s with acceleration of 1000rpm/s. This should result in a homogeneous photoresist layer of the required thickness.
3. After obtaining the photoresist evenly spread, pre-bake has to be done to ensure a firm attachment of the photoresist to the wafer. This step has to be performed for 5min at 95°C.
4. After pre-bake, make a firm contact between the wafer and the mask containing the respective motifs. A defective contact will lead to ill-defined motifs. After tight contact with the mask, cross-link the photoresist by exposing the wafer to UV irradiation with a dose of

150 mJ/cm^2. The time of exposure will depend on the power of the device (e.g. mask aligner) for the UV light exposure (see Figure 1A.i).

5. As soon as the exposure is over, follow a post-bake of 1min at 65°C and then 5min at 95°C. An image of the mask should appear on the SU-8 photoresist coating.
6. After post-bake, develop the structures by immersing them in the SU-8 developer solution, while gently agitating the container for around 4min. This will strip off the non-crosslinked resin, leaving behind the motifs. Finally, rinse the surface with 2-propanol to remove the left-over photoresist.

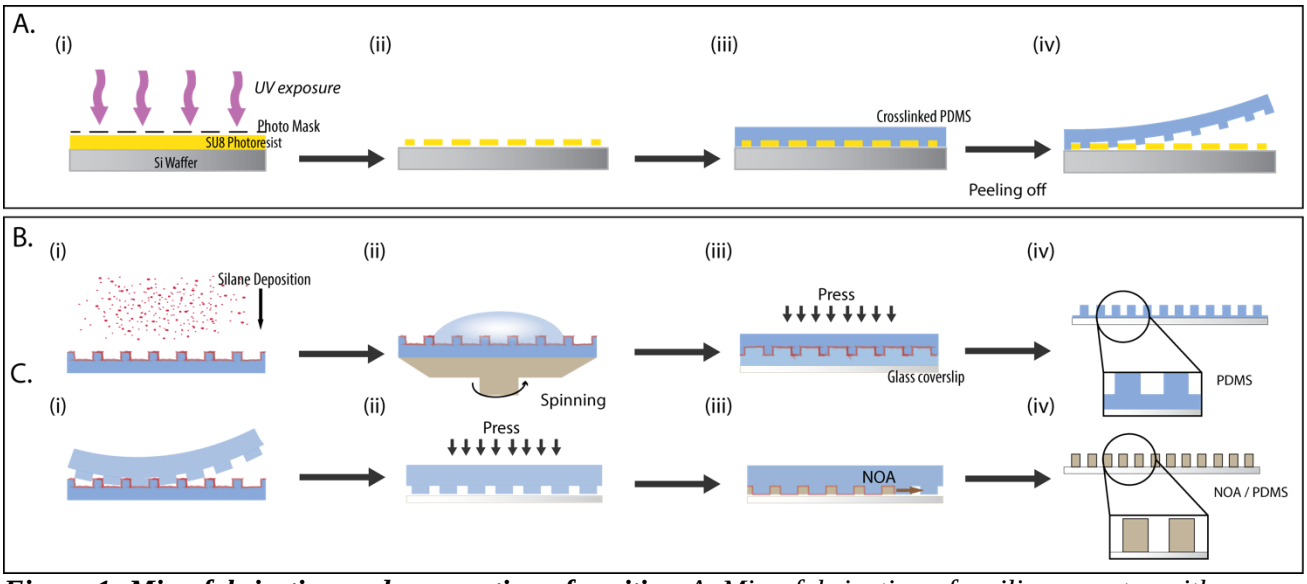

Figure 1: Microfabrication and preparation of cavities. *A. Microfabrication of a silicon master with photoresist SU-8 (A.; (i)) to obtain SU-8 pillars (A.; (ii)). Un-crosslinked PDMS is poured over the silicon master (A.; (iii)) and peeled off to give PDMS cavities (A.; (iv)). B. PDMS cavity preparation with polymer (PDMS) layer at the bottom by first silanizing the PDMS cavities with TMCS (B.; (i)) followed by spin-coating a drop of PDMS (B.; (ii)) to obtain uniform thin layer and crosslinking at 65°C O/N. The assembly is plasma-bonded with a glass coverslip and pressed uniformly (B.; (iii)). Crosslinked PDMS is peeled off from the assembly revealing cavities with PMDS layer at the bottom (B.; (iv)). C. PDMS cavities without polymer layer at the bottom is prepared using UV crosslinking polymer NOA-74 by first using the silanized PDMS master 1 (B.; (i)) with holes and pouring non-crosslinked polymer over it, and the sample is allowed to polymerize at 65°C O/N. After polymerization, the PDMS mold with pillars is peeled off from the assembly (C; (i)) and plasma bonded to a glass coverslip (C.; (ii)). The assembly is exposed to TMCS for silanization. Next, the assembly is incubated with NOA-74 (C.; (iii)) and polymerized under UV-A light for minimum 4 hours. PDMS mold with pillars is peeled off carefully from the glass coverslip revealing through-hole cavities (C.; (iv)). Same process can be used to obtain both PDMS and NOA through-hole cavities.*

7. White left-over seen over the wafers during 2-propanol treatment is an indicator for residual un-crosslinked resin. Repeat step 6 until rest of the non-crosslinked resin is stripped off the wafer completely.
8. Rinse with 2-propanol and dry the wafer containing motifs using a nitrogen air stream.
9. After the silicon wafers are ready with desired motifs, do a ‘hard bake’ step at ~150°C for 10 minutes. This is useful for annealing any surface cracks that may have appeared after

development; this step is relevant to all layer thicknesses. Structures fabricated in such a way have excellent thermal and mechanical stability (see Figure 1A.ii).

10. After obtaining the motifs, cover the wafers with PDMS (crosslinker: base [1:9]) (see Figure 1A.iii).
11. Remove all air bubbles through desiccation, and finally cure it overnight at 65°C on a leveled surface.
12. Once the elastomer is cured, peel off the PDMS block containing the desired cylindrical pillars with appropriate height (see Figure 1A.iv).

III. Process for cavity preparation

Cavities are prepared using polymers such as PDMS (heat-crosslinking polymer) or NOA-74 (UV- crosslinking polymer). Different steps are taken to achieve cavities with a thin polymer layer at the bottom, as well as through-hole cavities with no bottom polymer layer.

Materials

- NOA-74 (Norland products Inc.)
- PDMS (Base and crosslinker; Sylgard 184 Silicone Elastomer)
- Tweezers
- UV-A chamber (for polymer crosslinking)
- Oven (at 65 °C)
- Desiccator
- Sonicator
- 70% ethanol solution

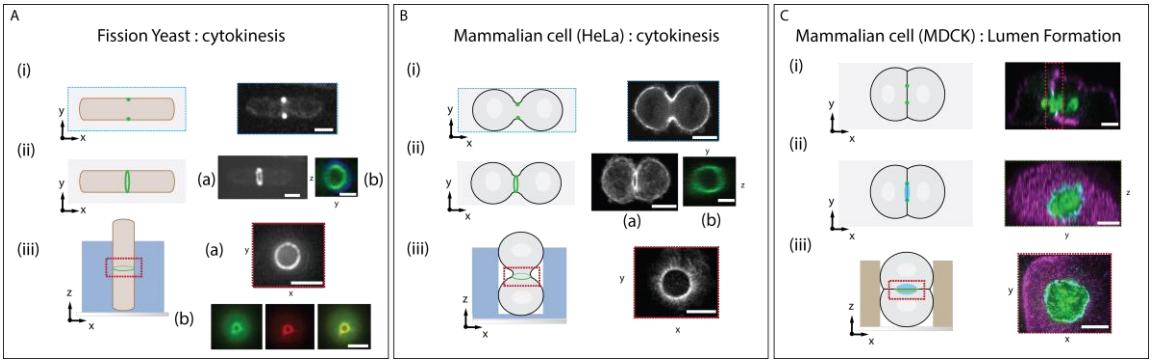

Figure 2: Orienting cells lead to optimal resolutions in space for a variety of cellular systems. *A. Fission yeast cytokinetic ring (tagged-myosin regulatory light chain RLC) visualized on a flat surface (glass coverslip), single plane imaging shows two points in the 'xy' plane corresponding to the ring (A. (i); scale bar 3µm). Reconstitution of ring with 'z' planes projections showing blurred tilted ring (A. (i); scale bar 3µm). Reconstitution of 'yz' planes, (A. (iib); scale bar 3µm) showing a blurred ring and with sectional cut 'en face' (green: pxl1 red for the ring: blankophor for the cell wall). Vertical cells (A. (iiia); scale bar 3µm) allow to reveal myosin clusters around the ring perimeter (Riveline, 2009). Also new structures appear such as arms, and concentric rings (A. (iiib); scale bar 3µm) (green: Pxl1 and*

red: Rlc1). B. Mammalian cell (HeLa) cytokinetic ring (tagged-myosin heavy chain MHC) visualized on a flat surface (B. (i); scale bar 10µm) with 'xy' plane showing two point accumulations. Reconstitution of 'z' planes projections showing blurred tilted ring (B. (iia); scale bar 10µm). Reconstitution of 'yz' planes, (B. (iib); green: myosin; scale bar 5µm) showing a deformed blurred ring with maximal projection and with sectional cut 'en face'. To visualize the full ring perimeter, cells are oriented vertically with respect to the plane of visualization inside cavities (B. (iii); scale bar 5µm), revealing myosin clusters around the ring perimeter. C. Lumen formation in MDCK doublets, cultured on glass coverslip (with Matrigel) after 24h visualized by confocal microscopy in single plane, showing two points accumulation (light blue:ZO1; lumen). Reconstitution of 'yz' planes showing a blurred and deformed lumen contour with sectional cut 'en face' for MDCK doublets. (C.; (ii)). Gain in information as well as in resolution is achieved after seeding cells inside through-hole NOA-74 cavities showing resolved and undistorted lumen contour (light blue: ZO1, magenta: E-cadherin, green: podocalyxin) Scale bars 3µm.

(i) <u>Cavities with polymer layer at the bottom</u>:

PDMS base and the curing agent are mixed in a ratio of 9:1 (v/v). This liquid PDMS is poured over the silicon master obtained via photolithography (for HeLa and MDCK cells), and silicon master is obtained via deep reactive ion etching (for fission yeast, (Riveline, 2012).

1. Liquid PDMS poured over the silicon wafers is degassed (removing trapped air inside the liquid polymer) and cured at 65°C overnight.
2. After curing by heat, the PDMS layer is peeled off (see Figure 1A.iv) from the wafer surface. This peeled off layer is considered as Master 1 with holes in the PDMS block. This is used as replica mold to fabricate pillars used as final motifs for the preparation of cavity.
3. Next, PDMS block with pillars is plasma activated and subsequently passivated with chlorotrimethyl silane (TMCS) under a desiccator for 10min.
4. Small amount of uncured liquid PDMS (~50µl) is poured over the motifs with subsequent spin-coating (and vacuum to hold the PDMS block) with 500rpm for 10s (to homogeneously distribute the liquid PDMS drop) and 1700rpm for 45s to obtain the preferred height (~ 40µm) (see Figure 1B.ii). (*KW-4A Spin coater; SPI supplies*, centrifuge and rotor details kept throughout for Section III (i)). This thickness will be corresponding to the polymer layer at the bottom of glass coverslip.
5. This combination of uncured polymer over PDMS block (containing pillars) is then incubated at 65°C overnight for curing.
6. Cured PDMS block and glass coverslip #0 (100µm thickness) are activated under oxygen plasma. In addition, PDMS block is bonded with the glass coverslip (coated side down). This configuration is pressed for several seconds to ensure tight bonding between them (see Figure 1B.iii).
7. This coverslip-PDMS 'sandwich' is incubated at 65°C overnight. Longer exposure to heat helps the bonding to be stronger between PDMS and coverslip.
8. Next, coverslip is held on both sides of the PDMS block, while peeling it off carefully. This avoids the risk of coverslip breakage during the process.

9. Thin bottom layer of PDMS on the coverslip (~ 40µm) with cavities on top is revealed (see Figure 1B.iv) and Figure 3A.i).

Even though cells are oriented in the right orientation with a good match between cell and cavity dimensions, an elastomer layer at the bottom decreases resolution. This leads to loss in fluorescence as well as in spatial resolution.

A typical example is shown with cytokinetic ring of HeLa cells observed using such cavities with polymer layer at the bottom and an inverted setup: the ring is blurred (see Figure 3A.iia-b). This blurring effect is due to distortion of light caused by this thin PDMS layer at the bottom. Therefore, for such configurations, it is better to visualize these structures with an upright microscope (see Figure 3A.iiia-b) and this allowed to reveal regularly spaced (0.8µm) myosin clusters around the cytokinetic ring [5]. Visualizing cells in such configuration does not only increase *spatial* resolution, but also *temporal* resolution for capturing fast dynamics (e.g. for cytokinesis in HeLa cells; see Figure 3C.i-ii).

To be able to visualize structures with higher resolutions, cavities without any polymer layer at the bottom (see Figure 1C.iv and Figure 3B.i) are fabricated and cells are visualized using STED super-resolution microscopy (see Figure 3B.iia-b).

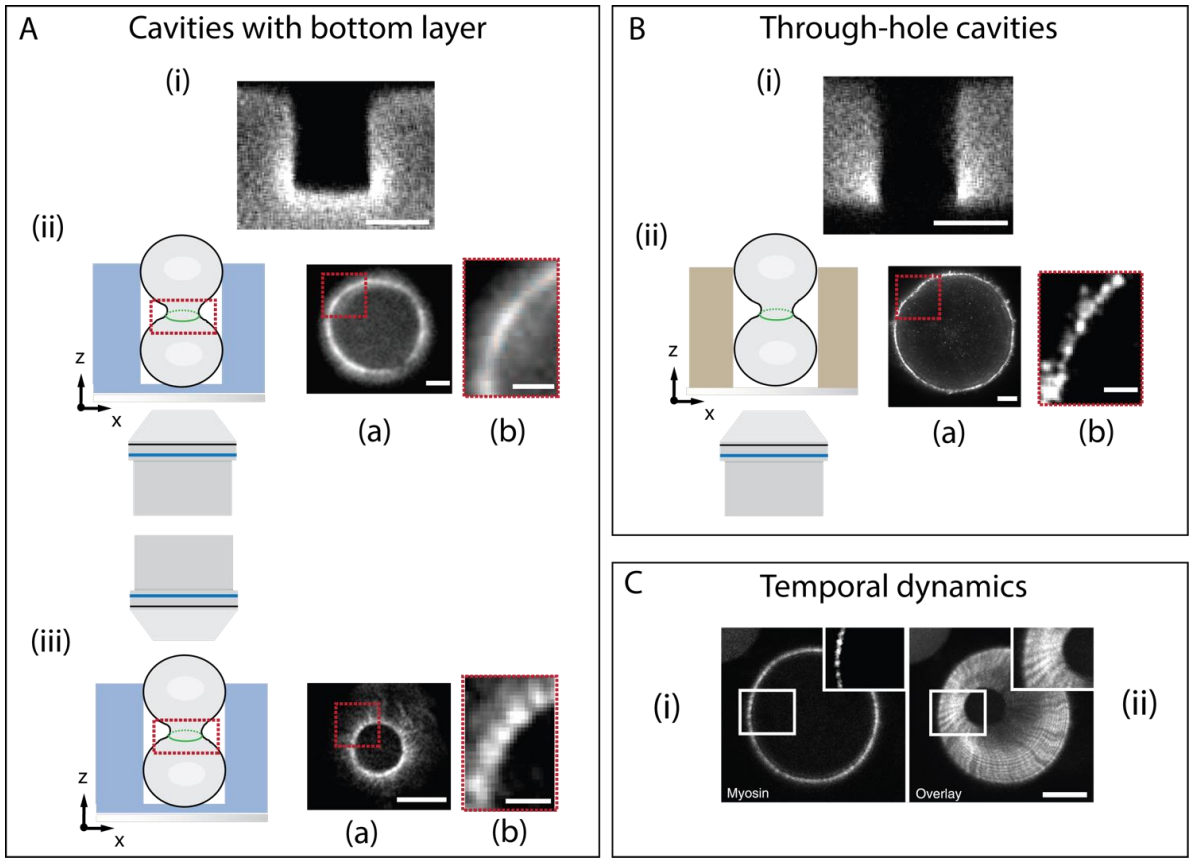

Figure 3: Gain in spatial and temporal resolutions in cavities; an example with myosin clusters of cytokinetic ring. *A. PDMS cavities with polymer (PDMS) layer at the bottom (A; (i) Scale bar 10 µm) is used. Synchronized cells are seeded inside cavities and visualized with an inverted set-up (A. (ii))*

showing a blurred cytokinetic ring (tagged-MHC) (A. (iia); scale bar 5µm); inset (red dashed lines) zoomed view showing a blurred portion of the ring (A. (iib); scale bar 3µm; Wollrab, 2014). To better resolve the cytokinetic ring inside a cavity with a PDMS layer at the bottom, imaging is done with an upright microscope (A. (iii)) avoiding the bottom polymer layer, revealing evenly spaced myosin clusters around the cytokinetic ring perimeter (A. (iiia); scale bar 5µm); inset (iib; red dashed lines; scale bar 1µm) zoomed view revealing the distance between clusters to be ~0.8µm. For further gain in resolution and optimized set-up usage, NOA-74 cavities without polymer layer at the bottom (B. (i) Scale bar 10 µm) are prepared. Synchronized cells are seeded inside cavities and visualized with an inverted setup (B. (ii)) using STED microscopy. Visualization of cytokinetic ring revealing individual myosin clusters (B. (iia); scale bar 5µm); inset (iib; red dashed lines; scale bar 1µm) zoomed view revealing myosin cluster inter-distance to be ~0.2 µm. C. Temporal resolution in cytokinetic ring (cluster) dynamics achieved by following the ring closure over time at high frame rate (10s), overlay of 25 frames, starting from the frame shown on the left (C. (i)) shows clusters moving radially (still clusters) throughout the ring closure (C. (ii)) scale bar 5µm) (Wollrab, 2016).

(ii) <u>Cavities without polymer layer at the bottom</u>.

Cells directly 'touching' the glass surface - without any polymer layer at the bottom - have a significant advantage to gain in resolutions during image acquisition. In addition, this configuration also provides higher freedom of objective working distance as well as the ease in using both upright and inverted microscope setups. Through-hole cavities are achieved with both polymers mentioned earlier, PDMS and NOA-74.

1. Steps from section III (i) steps 1 and 2 are repeated to obtain Master 1 (PDMS block with holes).
2. To obtain PDMS pillars (final motifs for cavity preparation), Master 1 is activated under oxygen plasma. Next, it is passivated with chlorotrimethyl silane (TMCS) under a desiccator for 20-30 mins (see Figure 1B.i). Post silanization PDMS is poured over the Master 1 (with holes), degassed and cured at 65°C overnight.
3. After curing, PDMS is peeled off the Master 1 (PDMS with holes) revealing PDMS block with pillars of target height.
4. To obtain cavities without PDMS layer at the bottom, first, blocks of PDMS with pillars (0.5cm X 0.5cm) are cut and sonicated (5min) with 70% ethanol to remove any dirt and residual silane.
5. These PDMS blocks (with pillars) are used for the preparation of cavities for fission yeast cells, as well as through-hole NOA-74 cavities for HeLa and MDCK cells.
6. Surfaces of PDMS pillars are activated under oxygen plasma, along with the glass coverslip on which pillars are to be bonded.
7. Activated PDMS block with pillars is now turned (activated side down) and put on top of the activated coverslip. The assembly is carefully pressed to ensure proper bonding. Inadequate boding would lead to non through-hole cavities (see Section VI and Figure 5D). Excessive strong bond will result in blocked cavities (see Section VI and Figure 5C). Care is taken that the pressure does not tilt these pillars (see Section VI, Figure 1C.ii and Figure 5A).

8. The assembly is then incubated for passivation with TMCS in a desiccator for 20-30 mins. Passivation is done to prevent irreversible bonding of PDMS pillars with the introduced polymer (NOA-74).
9. Post-passivation: the polymer (NOA-74) is introduced as a drop on one side of the assembly. Capillary action pulls the polymer into the assembly (see Figure 1C.iii). Speed of polymer flow throughout the assembly is dependent on height of the pillars as well as viscosity of the polymer. For example, NOA-74 is less viscous than PDMS and will 'travel' through the assembly quicker and more efficiently than PDMS. Desiccator can be used for 5-7 min for efficient and homogeneous filling of pillars, removing any air bubble trapped inside the assembly.
10. Polymer NOA-74 incubated assembly is then placed for curing (crosslinking) inside a chamber with UV-A source for minimum 4-6 hours.
11. After curing, pillars are carefully peeled off the surface of coverslip. Through-hole NOA-74 cavities are revealed, directly attached to the glass coverslip without any polymer layer at the bottom (see Figure 1C.iv and Figure 3B.i).

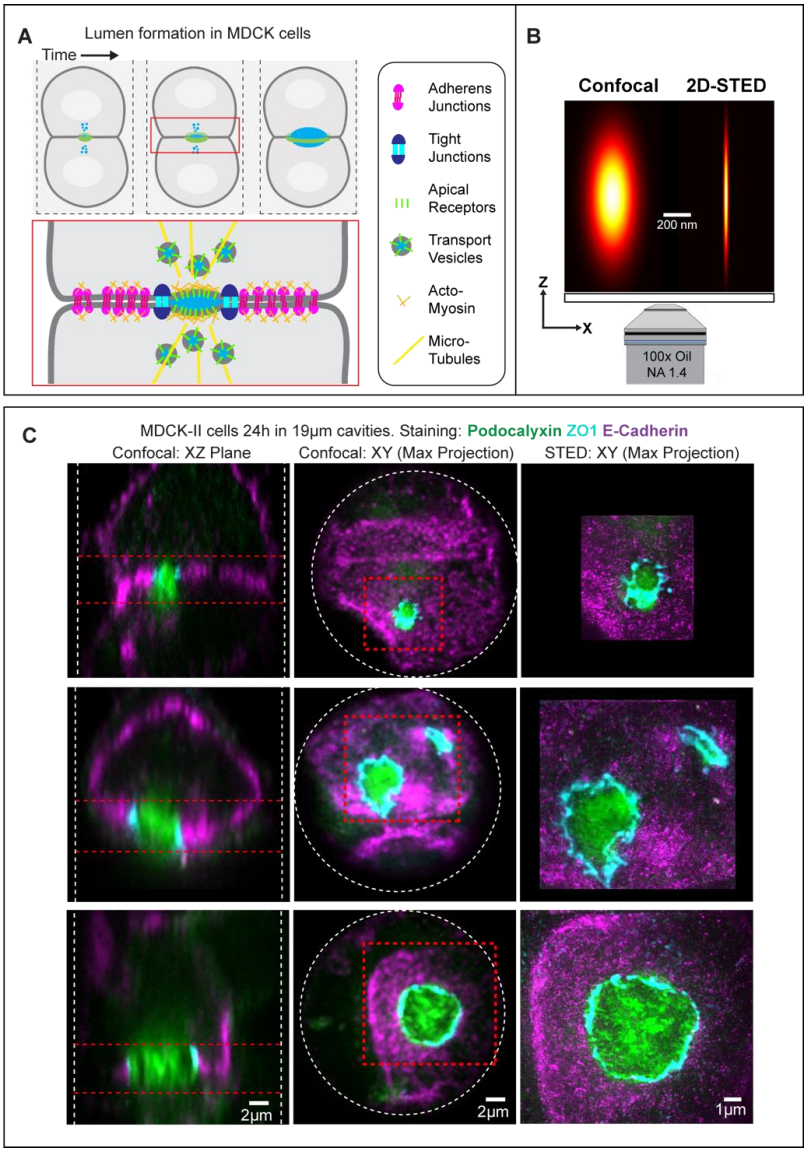

Figure 4: Visualisation 'en face' of MDCK lumen at the two cell stages in cavities with STED microscopy. *A. Sketch of the lumen initiation over time. Zoom shows the cell-cell adhesion interface and some of the key molecular components involved in organising the lumen. (B; (i)) Point spread function of confocal and 2D-STED, showing the 10 fold increase in XY resolution for STED but axial resolution is low. (B; (i)) Illustration of MDCK doublets inside through-hole NOA-74 cavities with lumen (inset; red). (C) Confocal and STED images of MDCK doublets cultured in through-hole NOA-74 cavities for 24h. Cells, which divided in the axial direction, allow to resolve the cell-cell adhesion interface with super-resolution at different stages of lumen expansion. Note that E-cadherin adhesion clusters are clearly resolved in lateral domain in the STED image. Additionally, the apical membrane protein podocalyxin appears to form protrusions in the STED image, which is consistent with micro-villi formation on the apical membrane.*

The same procedures 9-11 can be used to prepare PDMS cavities as well with no bottom layers. A typical example of cells inside such configuration, imaged with an inverted STED super-resolution microscope, is shown where myosin clusters can be observed at higher resolution (see Figure 3B.iia-b) revealing myosin clusters spaced at ~0.2μm intervals. Another example of oriented structures such as 'lumen' can also be visualized inside similar (PDMS) cavities without polymer layer at the bottom. (see Figure1C (iv) and Figure 4C; STED)

IV. Choosing the optimal polymer for the process: advantages and drawbacks of different polymers

As described above, two types of polymers, PDMS and NOA-74 are used. There are advantages and drawbacks for each polymer type. For imaging cells inside cavities, it is important to use a biocompatible polymers [123] (Masters, Engl, Weng, Arasi, Gauthier, Viasnoff, 2012).

Also, polymer viscosity can be critical to prepare cavities with small heights. Such configuration would require shorter PDMS pillars, plasma-bonded to coverslip. Incubation of this assembly with a comparatively lower viscosity polymer (80-95cP; NOA-74) is much easier than a polymer with higher viscosity (3500cP; PDMS). If a high viscosity polymer is required, polymer flooding with desiccation is needed. This helps to secure the process with an even distribution of the polymer.

Next, to obtain optimal resolution, the cured polymer with refractive index closer to glass coverslip (~ 1.52) must be chosen. This minimizes distortion of light due to passage through the polymer layer. Refractive indices of both PDMS (~1.41) and NOA-74 (~1.52) are close to glass, with NOA-74 being a better candidate.

Cured PDMS polymer forms strong attachment with glass coverslip. Such property is preferred when robust and long-lasting and/or permanent attachment with coverslip are required. If the polymer layer is to be detached from the surface, polymers with low modulus (NOA-74) are preferred. This allows complete detachment of the layer from the substrate, while keeping its original structure after sonication (10min).

V. Cell seeding and visualization

We next report the last steps prior observations:

Mammalian cells (HeLa and MDCK):

1. Small rectangular piece of PDMS is attached to the coverslip (with cavities) with a drop of un-crosslinked PDMS. This assembly is incubated inside the oven (65°C) for 4h. Such PDMS block will serve as a holder to handle the cavities with help of tweezers in the subsequent steps.
2. Cavities are plasma activated under oxygen plasma.
3. Cavities are further immersed in fibronectin (10 μg/ml) for 4h at room temperature.
4. Cylindrical PMMA piece is introduced inside 50ml tube.
5. Culture media is introduced into the tube until it forms a thin layer over the PMMA piece.
6. Coverslip with cavities is handled carefully with the help of tweezers, holding the rectangular
7. PDMS block attached to them. It is placed carefully inside the tube over the PMMA piece.
8. Harvested cells are centrifuged at 500rpm for 3min. Cell pellet is resuspended in 2ml of culture media and placed over coverslip inside the 50ml tube.
9. This assembly is centrifuged at 1500-2000rpm for 2min. The process is repeated three times. Between each repeat, media containing cells is carefully mixed to dissociate any cell clusters formed during the process of centrifugation. This step ensures a better filling percentage.
10. After the centrifugation steps, cavities are carefully removed and put into a metal holder with selected culture medium, and the sample is ready for acquisition.

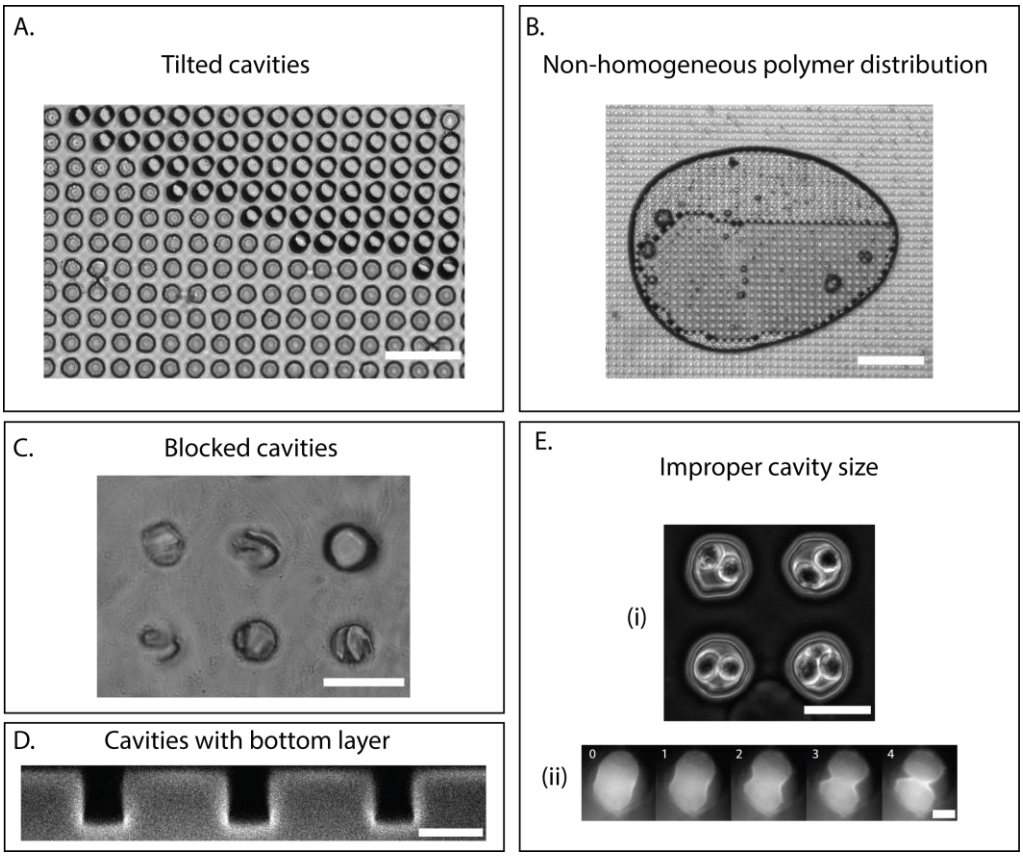

Figure 5: Issues and troubleshooting. *A. Tilted cavities due to inhomogeneous pressing of PDMS pillars on coverslip prior NOA-74 polymer incubation (scale bar 100µm). B. An air bubble trapped during polymer incubation leads to defects in samples. C. Strong plasma bonding between coverslip and PDMS pillars induces breakage of pillars while peeling them off from cavities. This leads to PDMS blocked NOA-74 cavities (scale bar 40µm). D. Weak plasma bonding between coverslip and PDMS pillars makes the cavities 'non through-hole' (scale bar 20µm). E. Error in matching average cell diameter and cavity dimension, when too large ((i); scale bar 40µm) leads to wrong orientation of dividing cells with respect to the visualization plane ((ii); scale bar 10 µm). (Wollrab, 2014).*

VI. Troubleshooting for cavity preparation.

We list below typical issues during protocols:

- **Tilted PDMS pillars leading to tilted cavities due to pressing during plasma bonding**

  Excessive pressing during plasma bonding (see section III. (ii), step 7.) of coverslip with PDMS pillars can result in tilted pillars (see Figure 5A). Consequently, cells and/or structures under observations would not appear at the correct focus and orientation, leading to poor image resolution.

- **Inhomogeneous cavity distribution due to trapped air bubble**

  In order to achieve homogeneous (NOA-74) prepolymer distribution, one should make sure to introduce the prepolymer on one side of the assembly as a small drop (~10-20µl) and left on the bench for the capillary action to fill the whole assembly. In contrast, polymer introduced from more than one sides could trap air bubble (see section III. (ii), step 9 and Figure 5B).

- **Blocked cavities with PDMS left behind**

  In case of excessive strong bond between coverslip and PDMS pillars (see section III. (ii), step 7.), peeling of PDMS pillars (after NOA-74 crosslinking) may leave PDMS blocked inside the cavities leading to obstructed cavities (see Figure 5C).

- **Polymer layer at the bottom inadequate plasma activation leading to poor bonding**

  Poor plasma bonding between coverslip and PDMS pillars (see section III. (ii), step 7.) could lead to insertion of NOA-74 prepolymer below PDMS pillars leading to non-through-hole cavities (see Figure 5D).

- **Wrong cavity size**

  Cavities should be designed according to the measured, average cell diameter of cells (see Section I). Failing to do so would lead to either horizontal (see Figure 5E.i) or tilted cells (see Figure 5E.ii) inside cavities. This would prevent

optimized microscopy and correct orientation of cells and structures under study.

VII. Conclusions.

This article reports strategies to prepare cavities optimized for orientation of cellular structures into the high-resolution plane of microscopes. Many cellular structures could be placed in the 'right' plane with our method. In fact, the usage of 3D environments for studying cells appear to be the natural way to reproduce situations encountered in physiological conditions. The cost is minimal as well as the need for specialized equipment. It is easy to foresee numerous applications of this new point of view in a literal sense to reveal new structures and dynamics with relevance for basic research and for medical applications.

Acknowledgements:
We thank the Riveline Lab and the Imaging Platform of IGBMC for discussions. This study was supported by the Human Frontier Science Program number RGP0050/2018. A.B. and SLV were also funded by the University of Strasbourg. This work with the reference ANR-10-LABX-0030-INRT has been supported by a French state fund through the Agence Nationale de la Recherche under the frame programme Investissements d'Avenir labelled ANR-10-IDEX-0002-02. C-H.W and R.M. were funded by the Max Planck Society (ELBE fellowship) and by the Deutsche Forschungsgemeinschaft (DFG, German Research Foundation) - Project Number 112927078 - TRR 83.

References:

[1] T. E. Schroeder, "The contractile ring," *J. Cell Biol.*, vol. 53, pp. 419–434, 1972.
[2] A. F. Huxley and R. Niedergerke, "Structural Changes in Muscle During Contraction: Interference Microscopy of Living Muscle Fibres," *Nature*, vol. 173, no. 4412, pp. 971–973, 1954.
[3] H. Huxley and J. Hanson, "Changes in the Cross-Striations of Muscle during Contraction and Stretch and their Structural Interpretation," *Nature*, vol. 173, no. 4412, pp. 973–976, 1954.
[4] H. E. Huxley, "The double array of filaments in cross-striated muscle.," *J. Biophys. Biochem. Cytol.*, vol. 3, no. 5, pp. 631–48, 1957.
[5] V. Wollrab, R. Thiagarajan, A. Wald, K. Kruse, and D. Riveline, "Still and rotating myosin clusters determine cytokinetic ring constriction," *Nat. Commun.*, vol. 7, no. 1, pp. 11860–11869, 2016.
[6] M. Rauzi, P.-F. Lenne, and T. Lecuit, "Planar polarized actomyosin contractile flows control epithelial junction remodelling," *Nature*, vol. 468, no. 7327, pp. 1110–1114, Dec. 2010.
[7] M. Nishikawa, S. R. Naganathan, F. Jülicher, and S. W. Grill, "Controlling contractile instabilities in the actomyosin cortex.," *Elife*, vol. 6, pp. 1–21, 2017.
[8] A. C. Martin and B. Goldstein, "Apical constriction: themes and variations on a cellular mechanism driving morphogenesis.," *Development*, vol. 141, no. 10, pp. 1987–98, May 2014.

[9] E. Anon *et al.*, “Cell crawling mediates collective cell migration to close undamaged epithelial gaps.,” *Proc. Natl. Acad. Sci. United States Am.*, vol. 109, no. 27, pp. 10891–6, 2012.
[10] A. Ravasio *et al.*, “Gap geometry dictates epithelial closure efficiency,” *Nat. Commun.*, vol. 6, pp. 1–113, 2015.
[11] A. Jacinto, A. Martinez-Arias, and P. Martin, “Mechanisms of epithelial fusion and repair,” *Nat. Cell Biol.*, vol. 3, no. 5, pp. E117–E123, May 2001.
[12] E. Wagner and M. Glotzer, “Local RhoA activation induces cytokinetic furrows independent of spindle position and cell cycle stage.,” *J. Cell Biol.*, vol. 213, no. 6, pp. 641–9, Jun. 2016.
[13] O. Pertz, L. Hodgson, R. L. Klemke, and K. M. Hahn, “Spatiotemporal dynamics of RhoA activity in migrating cells,” *Nature*, vol. 440, no. 7087, pp. 1069–1072, 2006.
[14] W. M. Bement, C. A. Mandato, and M. N. Kirsch, “Wound-induced assembly and closure of an actomyosin purse string in Xenopus oocytes,” *Curr. Biol.*, vol. 9, no. 11, pp. 579–587, Jun. 1999.
[15] M. Tamada, T. D. Perez, W. J. Nelson, and M. P. Sheetz, “Two distinct modes of myosin assembly and dynamics during epithelial wound closure,” *J. Cell Biol.*, vol. 176, no. 1, pp. 27–33, 2007.
[16] S. R. K. Vedula *et al.*, “Microfabricated Environments to Study Collective Cell Behaviors,” *Methods Cell Biol.*, vol. 120, pp. 235–252, 2014.
[17] A. Zumdieck, K. Kruse, H. Bringmann, A. A. Hyman, and F. Jülicher, “Stress generation and filament turnover during actin ring constriction,” *PLoS One*, vol. 2, no. 8, pp. 1–6, 2007.
[18] S. R. a. Naganathan, S. Fürthauer, M. Nishikawa, F. Jülicher, and S. W. Grill, “Active torque generation by the actomyosin cell cortex drives left-right symmetry breaking,” *Elife*, vol. 3, p. e04165, 2014.
[19] M. Mayer, M. Depken, J. S. Bois, F. Jülicher, and S. W. Grill, “Anisotropies in cortical tension reveal the physical basis of polarizing cortical flows,” *Nature*, vol. 467, pp. 617–623, 2010.
[20] C. M. Simon, E. M. Vaughan, W. M. Bement, and L. E. -Keshet, “Pattern formation of Rho GTPases in single cell wound healing,” vol. 24, no. 3, pp. 421–432, 2013.
[21] K. Dasbiswas, F. S. , Shiqiong Hu, S. A. Safran, and and Alexander D. Bershadsky, “Ordering of myosin II filaments driven by mechanical forces: experiments and theory,” *Philos. Trans. R. Soc. B Biol. Sci.*, vol. 373, pp. 1–16, 2018.
[22] D. V. Köster *et al.*, “Actomyosin dynamics drive local membrane component organization in an in vitro active composite layer,” *Proc. Natl. Acad. Sci.*, vol. 113, no. 12, pp. 1645–1654, 2016.
[23] A. C. Paré *et al.*, “A positional Toll receptor code directs convergent extension in Drosophila,” *Nature*, vol. 515, no. 7528, pp. 523–527, 2014.
[24] F. Jülicher and S. Eaton, “Emergence of tissue shape changes from collective cell behaviours,” *Semin. Cell Dev. Biol.*, vol. 67, pp. 103–112, 2017.
[25] J. Howard, *Mechanics of Motor Proteins and the Cytoskeleton*, 1st ed. Sinauer Associates Inc., 2001.
[26] D. Mizuno, C. Tardin, C. F. Schmidt, and F. C. Mackintosh, “Nonequilibrium mechanics of active cytoskeletal networks.,” *Science (80-.).*, vol. 315, pp. 370–373, 2007.
[27] G. T. Eisenhoffer *et al.*, “Crowding induces live cell extrusion to maintain homeostatic cell numbers in epithelia,” *Nature*, vol. 484, pp. 546–551, 2012.
[28] C.-P. Heisenberg and Y. Bellaïche, “Forces in Tissue Morphogenesis and Patterning,” *Cell*, vol. 153, pp. 948–962, 2013.

[29] C. Jamora and E. Fuchs, “Intercellular adhesion, signalling and the cytoskeleton,” *Nat. Cell Biol.*, vol. 4, no. 4, pp. E101–E108, Apr. 2002.
[30] S.-T. Sit and E. Manser, “Rho GTPases and their role in organizing the actin cytoskeleton,” *J. Cell Sci.*, vol. 124, pp. 679–683, 2011.
[31] B. Kost and N. H. Chua, “The Plant Cytoskeleton: Vacuoles and Cell Walls Make the Difference,” *Cell*, vol. 108, pp. 9–12, 2002.
[32] U. S. Eggert, T. J. Mitchison, and C. M. Field, “Animal Cytokinesis: From Parts List to Mechanisms,” *Annu. Rev. Biochem.*, vol. 75, pp. 543–566, 2006.
[33] L. Blanchoin, R. Boujemaa-Paterski, C. Sykes, and J. Plastino, “Actin dynamics, architecture, and mechanics in cell motility.,” *Physiol. Rev.*, vol. 94, no. 1, pp. 235–63, 2014.
[34] D. A. Lauffenburger and A. F. Horwitz, “Cell migration: A physically integrated molecular process,” *Cell*, vol. 84, pp. 359–369, 1996.
[35] S. L. Rogers and V. I. Gelfand, “Membrane trafficking, organelle transport, and the cytoskeleton,” *Curr. Opin. Cell Biol.*, vol. 12, pp. 57–6, 2000.
[36] T. Chen, T. B. Saw, R.-M. Mège, and B. Ladoux, “Mechanical forces in cell monolayers,” *J. Cell Sci.*, vol. 131, pp. 1–11, 2018.
[37] W. M. Bement, G. Ian Gallicano, and D. G. Capco, “Role of the cytoskeleton during early development,” *Microsc. Res. Tech.*, vol. 22, pp. 23–48, 1992.
[38] T. Lecuit, P.-F. Lenne, and E. Munro, “Force Generation, Transmission, and Integration during Cell and Tissue Morphogenesis,” *Annu. Rev. Cell Dev. Biol.*, vol. 27, no. 1, pp. 157–184, 2011.
[39] B. Alberts, A. Johnson, J. Lewis, M. Raff, K. Roberts, and P. Walter, *Molecular biology of the Cell*, 4th ed. Garland Science, 2007.
[40] M. A. Jordan and L. Wilson, “Microtubules as a target for anticancer drugs,” *Nat. Rev. Cancer*, vol. 4, pp. 253–265, 2004.
[41] G. Cooper, *The cell: a molecular biology approach.*, 2nd ed. ASM Press, 2000.
[42] T. D. Pollard and W. E. Earnshaw, *Cell Biology*, 1st ed. Saunders, 2002.
[43] T. D. Pollard, “Rate Constants for the Reactions of ATP-and ADP-Actin with the Ends of Actin Filaments,” *J. Cell Biol.*, vol. 103, no. 6, 1986.
[44] S. Ono, “Mechanism of Depolymerization and Severing of Actin Filaments and Its Significance in Cytoskeletal Dynamics,” *Int. Rev. Cytol.*, vol. 258, pp. 1–82, 2007.
[45] A. J. Ehrlicher, “The Forces Behind Cell Movement The Forces Behind Cell Movement,” *Int. J. Biol. Sci.*, vol. 3, pp. 303–317, 2017.
[46] T. D. Pollard, L. Blanchoin, and R. D. Mullins, “Molecular mechanisms controlling actin filament dynamics in nonmuscle cells,” in *Annual Review of Biophysics and Biomolecular Structure*, vol. 29, 2000, pp. 545–576.
[47] K. Kruse and D. Riveline, *Spontaneous Mechanical Oscillations. Implications for Developing Organisms*, 1st ed., vol. 95. Elsevier Inc., 2011.
[48] A. Munjal and T. Lecuit, “Actomyosin networks and tissue morphogenesis,” *Development*, vol. 141, pp. 1789–1793, 2014.
[49] M. Vicente-Manzanares, X. Ma, R. S. Adelstein, and A. R. Horwitz, “Non-muscle myosin II takes centre stage in cell adhesion and migration.,” *Nat. Rev. Mol. Cell Biol.*, vol. 10, no. 11, pp. 778–90, 2009.
[50] F. Jiilicher’ and J. Prost’, “Cooperative Molecular Motors,” 1995.
[51] J. Prost, F. Jülicher, and J. F. Joanny, “Active gel physics,” *Nat. Phys.*, vol. 11, pp. 111–117, 2015.
[52] K. Kruse, J. F. Joanny, F. Jülicher, J. Prost, and K. Sekimoto, “Asters, Vortices, and Rotating Spirals in Active Gels of Polar Filaments,” vol. 92, no. 7, pp. 1–4, 2004.
[53] J. F. Joanny, F. Jülicher, K. Kruse, and J. Prost, “Hydrodynamic theory for multi-

component active polar gels," *New J. Phys.*, vol. 9, pp. 1–17, 2007.
[54] H. N. Higgs and E. S. Chhabra, "The many faces of actin: matching assembly factors with cellular structures.," *Nat. Cell Biol.*, vol. 9, pp. 1110–1121, 2007.
[55] A. B. Verkhovsky, "Orientational Order of the Lamellipodial Actin Network as Demonstrated in Living Motile Cells," *Mol. Biol. Cell*, vol. 14, pp. 4667–4675, 2003.
[56] D. Bray, *Cell Movements : From Molecules to Motility*, 2nd ed. Garland Science, 2000.
[57] T. Vicsek and A. Zafeiris, "Collective motion," *Phys. Rep.*, vol. 517, pp. 71–140--, 2012.
[58] E. M. E. Purcell, "Life at low Reynolds number," *Am. J. Phys.*, vol. 45, no. 1, p. 3, 1977.
[59] R. Aditi Simha and S. Ramaswamy, "Hydrodynamic fluctuations and instabilities in ordered suspensions of self-propelled particles," *Phys. Rev. Lett.*, 2002.
[60] J. F. Joanny and J. Prost, "Active gels as a description of the actin-myosin cytoskeleton," *HFSP J.*, vol. 3, no. 2, pp. 94–104, 2009.
[61] F. Wottawah *et al.*, "Optical rheology of biological cells," *Phys. Rev. Lett.*, vol. 94, pp. 1–4, 2005.
[62] A. S. Streng, D. de Boer, J. van der Velden, M. P. van Dieijen-Visser, and W. K. W. H. Wodzig, "Posttranslational modifications of cardiac troponin T: An overview," *J. Mol. Cell. Cardiol.*, vol. 63, p. 2013, 2013.
[63] Y. Tanaka-Takiguchi *et al.*, "The elongation and contraction of actin bundles are induced by double-headed myosins in a motor concentration-dependent manner," *J. Mol. Biol.*, vol. 341, no. 2, pp. 467–476, 2004.
[64] J. M. Belmonte, M. Leptin, and F. Nédélec, "A theory that predicts behaviors of disordered cytoskeletal networks," *Mol. Syst. Biol.*, vol. 13, pp. 941–954, 2017.
[65] M. A. Chesarone and B. L. Goode, "Actin nucleation and elongation factors: mechanisms and interplay," *Curr. Opin. Cell Biol.*, vol. 21, no. 1, pp. 28–37, 2009.
[66] J. N. Jodoin *et al.*, "Stable Force Balance between Epithelial Cells Arises from F-Actin Turnover," *Dev. Cell*, vol. 35, no. 6, pp. 685–697, 2015.
[67] B. M. Gumbiner, "Regulation of cadherin-mediated adhesion in morphogenesis," *Nat. Rev. Mol. Cell Biol.*, vol. 6, pp. 622–634, 2005.
[68] K. Goodwin, S. J. Ellis, E. Lostchuck, T. Zulueta-Coarasa, R. Fernandez-Gonzalez, and G. Tanentzapf, "Basal Cell-Extracellular Matrix Adhesion Regulates Force Transmission during Tissue Morphogenesis," *Dev. Cell*, vol. 39, pp. 611–625, 2016.
[69] S. L. Haigo and D. Bilder, "Global tissue revolutions in a morphogenetic movement controlling elongation.," *Science (80-.).*, vol. 331, no. 6020, pp. 1071–1074, Feb. 2011.
[70] M. V. Hunter, D. M. Lee, T. J. C. Harris, and R. Fernandez-Gonzalez, "Polarized E-cadherin endocytosis directs actomyosin remodeling during embryonic wound repair," *J. Cell Biol.*, vol. 210, no. 5, pp. 801–816, 2015.
[71] A. Padmanabhan, H. T. Ong, and R. Zaidel-Bar, "Non-junctional E-Cadherin Clusters Regulate the Actomyosin Cortex in the C. elegans Zygote," *Curr. Biol.*, vol. 27, pp. 103–112, 2017.
[72] P. Agarwal and R. Zaidel-Bar, "Principles of Actomyosin Regulation In Vivo.," *Trends Cell Biol.*, vol. 29, no. 2, pp. 150–163, Feb. 2019.
[73] S. J. Heasman and A. J. Ridley, "Mammalian Rho GTPases: New insights into their functions from in vivo studies," *Nature Reviews Molecular Cell Biology*, vol. 9, no. 9. pp. 690–701, Sep-2008.
[74] A. Hall, "Rho family GTPases," *Biochem. Soc. Trans.*, vol. 40, pp. 1378–1382, 2012.
[75] A. L. Bishop and A. Hall, "Rho GTPases and their effector proteins.," *Biochem. J.*, vol. 348, no. 2, pp. 241–255, 2000.

[76] T. R. Arnold, R. E. Stephenson, and A. L. Miller, “Rho GTPases and actomyosin: Partners in regulating epithelial cell-cell junction structure and function,” *Exp. Cell Res.*, vol. 358, no. 1, pp. 20–30, 2017.
[77] W. M. Bement, A. L. Miller, and G. Von Dassow, “Rho GTPase activity zones and transient contractile arrays,” *BioEssays*, vol. 28, pp. 983–993, 2006.
[78] S. Schonegg, A. A. Hyman, and W. B. Wood, “Timing and mechanism of the initial cue establishing handed left-right asymmetry in Caenorhabditis elegans embryos,” *Genesis*, vol. 52, no. 6, pp. 572–580, 2014.
[79] T. Iskratsch, H. Wolfenson, and M. P. Sheetz, “Appreciating force and shape — the rise of mechanotransduction in cell biology,” *Nat. Rev. Mol. Cell Biol.*, vol. 15, pp. 825–833, 2014.
[80] N. Wang, J. P. Butler, and D. E. Ingber, “Mechanotransduction across the cell surface and through the cytoskeleton,” *Science (80-.).*, vol. 260, no. 5111, pp. 1124–1127, 1993.
[81] D. Pinheiro *et al.*, “Transmission of cytokinesis forces via E-cadherin dilution and actomyosin flows,” *Nature*, vol. 545, no. 7652, pp. 103–107, May 2017.
[82] J. J. West *et al.*, “An Actomyosin-Arf-GEF Negative Feedback Loop for Tissue Elongation under Stress,” *Curr. Biol.*, vol. 27, no. 15, pp. 2260–2270, Aug. 2017.
[83] T. D. Pollard and J.-Q. Wu, “Understanding cytokinesis: lessons from fission yeast.,” *Nat. Rev. Mol. Cell Biol.*, vol. 11, no. 2, pp. 149–55, 2010.
[84] K. Röper, “Supracellular actomyosin assemblies during development.,” *Bioarchitecture*, vol. 3, no. 2, pp. 45–9, 2013.
[85] W. M. Bement, “Actomyosin Rings: The Riddle of the Sphincter Dispatch,” 2002.
[86] P. Martin and J. Lewis, “Actin cables and epidermal movement in embryonic wound healing.,” *Nature*, vol. 360, no. 6400, pp. 179–83, Nov. 1992.
[87] T. Zulueta-Coarasa and R. Fernandez-Gonzalez, “Tension (re)builds: Biophysical mechanisms of embryonic wound repair,” *Mech. Dev.*, 2016.
[88] A. C. Martin, “Pulsation and stabilization: Contractile forces that underlie morphogenesis,” *Dev. Biol.*, vol. 341, no. 1, pp. 114–125, 2010.
[89] S. A. Gudipaty and J. Rosenblatt, “Epithelial cell extrusion: Pathways and pathologies,” *Seminars in Cell and Developmental Biology*, vol. 67. Elsevier Ltd, pp. 132–140, 01-Jul-2017.
[90] S. Begnaud, T. Chen, D. Delacour, R.-M. Mège, and B. Ladoux, “Mechanics of epithelial tissues during gap closure,” *Curr. Opin. Cell Biol.*, vol. 42, pp. 52–62, 2016.
[91] J. K. Klarlund, “Dual modes of motility at the leading edge of migrating epithelial cell sheets,” *Proc. Natl. Acad. Sci.*, vol. 109, no. 39, pp. 15799–15804, Sep. 2012.
[92] A. Stathopoulos and D. Iber, “Studies of morphogens: keep calm and carry on,” *Development*, vol. 140, no. 20. Company of Biologists Ltd, pp. 4119–4124, 15-Oct-2013.
[93] Anne-Cécile Reymann *et al.*, “Actin Network Architecture Can Determine Myosin Motor Activity,” *Science (80-.).*, vol. 336, pp. 1310–1314, 2012.
[94] T. D. Pollard, “Mechanics of cytokinesis in eukaryotes.,” *Curr. Opin. Cell Biol.*, vol. 22, no. 1, pp. 50–6, Feb. 2010.
[95] V. Wollrab, “Active gels in vivo : Patterns and dynamics in cytokinetic rings and their functions in cell divison,” University of Strasbourg, 2014.
[96] D. and Riveline and A. Buguin, “Devices and methods for observing the cell division. WO/2010/092116,” 2009.
[97] V. and Wollrab and D. Riveline, “Devices and methods for observing eukaryotic cells without cell wall. WO/2013/135809,” 2012.
[98] V. Wollrab, D. Caballero, R. Thiagarajan, and D. Riveline, “Ordering Single Cells and

Single Embryos in 3D Confinement: A New Device for High Content Screening.," *J. Vis. Exp.*, no. 115, pp. 2–15, 2016.
[99] T. Masters, W. Engl, Z. L. Weng, B. Arasi, N. Gauthier, and V. Viasnoff, "Easy Fabrication of Thin Membranes with Through Holes. Application to Protein Patterning," *PLoS One*, vol. 7, no. 8, pp. 1–7, Aug. 2012.
[100] D. Riveline, "Methods for observing cells with cell wall or invertebrate embryos with oblong eggshell. WO/2013/144302," 2012.
[101] T. Watanabe, H. and Hosoya, and S. Yonemura, "Regulation of Myosin II Dynamics by Phosphorylation and Dephosphorylation of Its Light Chain in Epithelial Cells," *Mol. Biol. Cell*, vol. 18, pp. 605–616, 2007.
[102] "Fission yeast : a laboratory manual," Cold Spring Harbor Laboratory Press, 2016, p. 487.
[103] S. L. Forsburg and N. Rhind, "Basic methods for fission yeast," *Yeast*, vol. 23, no. 3, pp. 173–183, 2006.
[104] E. Le Maout, S. Lo Vecchio, A. Bhat, and D. Riveline, "Directing cell migration on flat substrates and in confinement with microfabrication and microfluidics," in *Methods in Cell Biology*, 1st ed., vol. 147, Elsevier Inc., 2018, pp. 109–132.
[105] D. Caballero, R. Voituriez, and D. Riveline, "Protrusion Fluctuations Direct Cell Motion," *BPJ*, vol. 107, pp. 34–42, 2014.
[106] C. Spiegelhalter *et al.*, "From Dynamic Live Cell Imaging to 3D Ultrastructure: Novel Integrated Methods for High Pressure Freezing and Correlative Light-Electron Microscopy. From Dynamic Live Cell Imaging to 3D Ultrastructure: Novel Integrated Methods for High Pressure Freezing an," vol. 5, no. 2, pp. 1–12, 2010.
[107] *Forces and Tension in Development*, 1st ed. Elsevier Inc., 2011.
[108] M. Rauzi, P.-F. Lenne, and T. Lecuit, "Planar polarized actomyosin contractile flows control epithelial junction remodelling," *Nature*, vol. 468, no. 7327, pp. 1110–1114, 2010.
[109] P. Bocchiaro and A. Zamperini, "The Role of Actin Remodelling Proteins in Wound Healing and Tissue Regeneration," in *Wound Healing - New insights into Ancient Challenges*, 2016, pp. 133–153.
[110] L. Hodgson, F. Shen, and K. Hahn, "Biosensors for characterizing the dynamics of rho family GTPases in living cells.," in *Current protocols in cell biology*, vol. Chapter 14, 2010.
[111] "Reciprocal regulation of actomyosin organization and contractility in nonmuscle cells by tropomyosins and alpha-actinins," 2019.
[112] J. Eyckmans and C. S. Chen, "3D culture models of tissues under tension.," *J. Cell Sci.*, vol. 130, no. 1, pp. 63–70, Dec. 2017.
[113] A. Sontheimer-Phelps, B. A. Hassell, and D. E. Ingber, "Modelling cancer in microfluidic human organs-on-chips," *Nat. Rev. Cancer*, vol. 19, no. 2, pp. 65–81, Feb. 2019.
[114] V. Wollrab, D. Caballero, R. Thiagarajan, and D. Riveline, "Ordering Single Cells and Single Embryos in 3D Confinement: A New Device for High Content Screening," *J. Vis. Exp.*, no. 115, Sep. 2016.
[115] T. Hayashi and R. Murakami, "Left-right asymmetry in Drosophila melanogaster gut development," *Dev. Growth Differ.*, vol. 43, no. 3, pp. 239–246, 2001.
[116] M. V. Danilchik, E. E. Brown, and K. Riegert, "Intrinsic chiral properties of the Xenopus egg cortex: An early indicator of left-right asymmetry," *Development*, vol. 133, no. 22, pp. 4517–4526, Nov. 2006.
[117] J. F. Beausang, H. W. Schroeder, P. C. Nelson, and Y. E. Goldman, "Twirling of actin by myosins II and V observed via polarized TIRF in a modified gliding assay,"

Biophys. J., vol. 95, no. 12, pp. 5820–5831, Dec. 2008.
[118] D. Vavylonis, J.-Q. Wu, S. Hao, B. O'Shaughnessy, and T. D. Pollard, "Assembly mechanism of the contractile ring for cytokinesis by fission yeast.," *Science (80-.).*, vol. 319, no. 97, pp. 97–100, 2008.
[119] N. Levernier and K. Kruse, "Spontaneous formation of chaotic protrusions in a polymerizing active gel layer," *BioRxiv*, pp. 1–5, 2019.
[120] A. Abbott, "Biology's new dimension," *Nature*, vol. 424, no. 6951, pp. 870–872, Aug. 2003.
[121] V. M. Weaver *et al.*, "Reversion of the malignant phenotype of human breast cells in three- dimensional culture and in vivo by integrin blocking antibodies," *J. Cell Biol.*, vol. 137, no. 1, pp. 231–245, Apr. 1997.
[122] M. Anders, R. Hansen, R.-X. Ding, K. A. Rauen, M. J. Bissell, and W. M. Korn, "Disruption of 3D tissue integrity facilitates adenovirus infection by deregulating the coxsackievirus and adenovirus receptor.," *Proc. Natl. Acad. Sci. U. S. A.*, vol. 100, no. 4, pp. 1943–8, Feb. 2003.
[123] S. K. Sia and G. M. Whitesides, "Microfluidic devices fabricated in Poly(dimethylsiloxane) for biological studies," *Electrophoresis*, vol. 24, no. 21, pp. 3563–3576, Nov. 2003.

Alka Bhat

Les dynamiques d'agrégats de myosine et leurs rôles dans les fermetures d'epithelia

Résumé en français

Les agrégats de myosine ont été observés dans plusieurs systèmes : chez la *Drosophile*, *C. elegans*, ou encore dans des expériences avec des cytosquelettes reconstitués *in vitro*. Cependant, leur intégration dans un cadre général manque. En théorie, les filaments d'actine et les moteurs de myosine suivent des lois génériques d'auto-organisation. Des découvertes récentes du laboratoire montrent que la dynamique de ces agrégats à l'intérieur d'un anneau de cytokinèse sont en effet associés à des fonctions biologiques : la génération de stress lorsque leurs mouvements sont radiaux, et au transport lorsque leurs déplacements sont tangentiels. Dans ce travail de thèse, nous montrons que ces règles simples sont conservées lors du processus de cicatrisation par l'anneau d'acto-myosine dans les monocouches de cellules épithéliales. En utilisant la microfabrication, la biologie cellulaire, l'imagerie quantitative et la physique théorique, nous établissons que les agrégats radiaux et tangentiels sont respectivement associés à une fermeture locale ou à un arrêt de l'anneau. La conservation de ce mécanisme entre les systèmes uni- et multi-cellulaires suggère que la dynamique de ces agrégats de myosine pourrait être utilisée comme la lecture générique pour cartographier et prédire les changements de formes des embryons en développement.

Mots clés : physique cellulaire, agrégats de myosine, cytosquelette, acto-myosine, microfabrication, imagerie

Abstract in English

Myosin clusters have been reported in a variety of systems, such as *Drosophila*, *C. elegans*, and acto-myosin *in vitro* assays. However, their integration in a general framework is still lacking. In theory, actin filaments and myosin motors are predicted to follow generic rules of self-organisation. Recent findings from the laboratory reported that cluster dynamics within cytokinetic rings are associated with biological functions, *i.e.* stress generation when radial, and transport when tangential. In this study, we show that these simple rules hold as well for acto-myosin ring wound closure in epithelial monolayers. By using microfabrication, cell biology, quantitative imaging and theoretical physics, we report that radial and tangential clusters are related to local closures and stalled portions of rings, respectively. This conserved mechanism between single and multi-cellular system suggests that these myosin clusters dynamics could be used as generic read-out for mapping and predicting changes in shapes in developing embryos.

Keywords: cell physics, myosin clusters, cytoskeleton, acto-myosin, microfabrication, imaging